

Preventing Injuries of High Speed Marine Craft Operators

Incorporating Spinal Injury Models in the Analyses of Various Seat Suspension Principles

by

N. van den Nieuwenhuijzen

to obtain the degree of Master of Science
in Marine Technology in the specialization of Science
at the Delft University of Technology,
to be defended publicly on September 30, 2020 at 14:00.

Author Details

Student number: 4959167

Thesis Exam Committee

Dr. C.L. Walters,	TU Delft, Chairman
Dr. Ir. R.P. Notenboom,	Netherlands Defence Academy, Company Member
Ir. A.W. Vredeveltdt,	TNO Netherlands, Company Member
Dr. Ir. J.H. den Besten,	TU Delft, Staff Member
Dr. Ir. O.K. Bergsma,	TU Delft, Staff Member
Dr. H.C. Seyffert,	TU Delft, Staff Member

An electronic version of this thesis is available at <http://repository.tudelft.nl/>.

Abstract

On board of High Speed marine Craft (HSC), the crew and the passengers are exposed to high levels of Whole Body Vibrations (WBV) and large magnitude Repeated mechanical Shocks (RS) caused by the motions of the craft. The HSCs are typically 10 meters long, capable of reaching a maximum speed up to 50 knots and widely used by various maritime organizations. However, the operators and crew suffer from fatigue and injuries, leading to a reduced effectiveness and operational capacity of the marine craft. In an attempt to reduce the physical loads, passive Shock Mitigating Seats (SMS) can be installed. Numerous research has shown that an improperly designed SMS may amplify the wave impacts forces through phenomena such as bottoming out and dynamic amplification. Therefore, it is necessary to ensure that a suspension design works properly by testing the performance during wave impact events, before the seat is manufactured and installed onboard the craft. The problem is that it is difficult to determine the performance of the seats in both the design and off-design conditions with either sea trials or laboratory tests. This research focuses on the prevention of injuries and adverse health effects due to repetitive wave impacts by incorporating an injury model in the analyses of various suspension principles in the design of SMS.

In the current analyses of SMS either simplistic or specific models are used which restrict the application of these models to other suspension designs. Therefore, a computer program based on the finite element method is developed that allows realistic input accelerations in the surge, heave and pitch direction. The program incorporates highly non-linear elements, including the effect of bottoming. Additionally, the validity of the half-sine approximation for the wave impact excitation pulse was reviewed and concluded to be inappropriate for design purposes as it underestimates the probability of bottoming. Furthermore, the modified evaluation methods of ISO 2631 Part 5 using an optimized age-dependent coefficient based on gender in combination with a Weibull injury risk model were implemented to evaluate the resulting seat level accelerations.

A case study was conducted on a Fast Raiding Interception and Special forces Craft (FRISC) of the Royal Netherlands Navy (RNLN). A design based on a parallelogram of pinned truss elements in combination with a coil spring element was altered by replacing the coil spring with a gas-spring element. The design was analysed with dynamic simulations of full-scale measurements of wave impacts on a lifeboat of the Royal Sea Rescue Institution (KNRM). For the most severe wave impact of the acceleration record, the seat level acceleration was reduced from 17.7 [g] to 2.8 [g]. An operator of the age of 24 years who is exposed to the accelerations for half an hour a day, 30 days a year for two consecutive years was assumed. The probability of spinal injury was reduced for a male operator from 99.5% to 16.3% and for a female operator from 100.0% to 42.0%. These results illustrate the high risk of injury to which the HSC operators are exposed.

By incorporating highly non-linear elements and spinal injury models, the program and evaluation methods are capable of modelling various SMS suspension designs and analyse the performance. This can assist the seat designer, engineer or researcher with investigating suitable suspension designs before sea trials, experimental tests and prototype iterations. Therefore, the method offers the possibility to save time and reduce costs. Furthermore, the method can assist in defining new regulations in order to limit the exposure of the operators to physical loads and reduce the risk of spinal injury to an acceptable level.

Keywords: Shock Mitigating Seat, High Speed Marine Craft, Repetitive Wave Impacts, Suspension Principles, Half-Sine Approximation, Spinal Injury Models

Preface

Lectori salutem,

This thesis report contains the conducted research according to the requirements of the Master Marine Technology with the track Science of the Faculty of Maritime & Transport Technology at Delft University of Technology in order to obtain the degree of Master of Science.

The topic of the thesis research is shock mitigation seats on high speed marine craft, which will be further introduced in the first chapter. The topic concerns an ongoing problem in the work field of the Royal Netherlands Navy, my current employer, and other law enforcement agencies. With the research, I hope to have gained knowledge which can help solve the problem and deliver an useful contribution to Marine Technology Science. I would like to take the opportunity to thank those involved, whom made the research and the results possible.

First of all, I would like to thank my supervisor Dr. Ir. R.P. Notenboom of the Netherlands Defence Academy. For the second time, you supervised a thesis project of mine with great commitment and contributed to my academic development. I have greatly appreciated your guidance, willingness and feedback during the project. Also, I would like to thank Ir. A.W. Vredevelde of TNO Netherlands. Your expertise and knowledge in this field of science in combination with our discussions have been of great help to me. Furthermore, I would like to thank Dr. C.L. Walters of Delft University of Technology. You have challenged me to be critical and reflective on literature and my own work, which has been helpful to deliver a unique contribution to the Marine Technology Science. Finally, I would like to thank my family and friends for their enduring support in these challenging times.

*N. van den Nieuwenhuijzen
Den Helder, September 2020*

Contents

Abstract	iii
Preface	v
List of Figures	xi
List of Tables	xiii
Nomenclature	xv
1 Introduction	1
1.1 Background	1
1.2 Shock Mitigating Seats	2
1.3 Previous Research & Knowledge Gaps	2
1.4 Research Objective & Questions	4
1.5 Research Relevance	4
1.6 Outline Report	5
2 Computer Program	7
2.1 Program Method	7
2.2 Program Setup	8
2.2.1 Validation & Verification	9
2.3 Equations of Motion	9
2.3.1 Gravitation	11
2.3.2 Rayleigh Damping	11
2.3.3 Static Analysis.	11
2.3.4 Dynamic Analysis.	12
2.4 Mechanical Shock Mitigation.	13
2.4.1 Bottoming Out	14
2.4.2 Dynamic Amplification	14
2.5 Non-Linear Springs	17
2.5.1 Coil Spring Element.	17
2.5.2 Gas-Spring Element.	19
3 Injuries & Adverse Health Effects	27
3.1 Resulting Injuries	27
3.2 Human Tolerance to Shocks	28
3.3 Directives on Exposure to WBV & RS	29
3.3.1 ISO 2631 Part 1	31
3.3.2 ISO 2631 Part 5	32
3.4 Injury Criteria & Models	36
3.4.1 Eiband Tolerance Curves	36
3.4.2 Dynamic Response Index	37
3.5 Improvements of the ISO Evaluation Methods.	41
3.5.1 Metamodel of a Seated Person	41
3.5.2 Human Spine Ultimate Strength	41
3.6 Suitability of the Evaluation Methods	43

4	Wave Impact Accelerations	47
4.1	Wave Impact Excitation Pulse	47
4.1.1	Rigid Body Acceleration	48
4.1.2	Half-Sine Approximation	50
4.2	Full-Scale Wave Impact Measurements	51
4.2.1	KNRM Lifeboat Measurements	53
4.3	Application of the Half-Sine Approximation	54
4.3.1	KNRM Lifeboat Acceleration Record	54
4.3.2	Comparison of the Half-Sine Approximation & Measurements	58
4.3.3	Validity of the Half-Sine Approximation	64
4.4	Wave Impact Design Conditions	65
5	Case Study	69
5.1	Existing SMS Suspension Designs	69
5.2	Previously Analysed SMS	70
5.2.1	Previous Research Results	70
5.2.2	Seat A Model	71
5.2.3	Seat B Model	74
5.3	Proposed Design	79
5.3.1	Variation of the Geometrical Properties	80
5.3.2	Variation of the Human Weight	85
5.4	Analyses of the Proposed Design	85
5.4.1	Wave Impact Simulations	85
5.4.2	Probability of Injury	91
6	Conclusion & Recommendations	93
6.1	Conclusion	93
6.2	Limitations	95
6.2.1	Limitations of the Computer Program	95
6.2.2	Limitations of the Review on Injury Models	96
6.2.3	Limitations of the Study on Wave Impact Accelerations	96
6.2.4	Limitations of the Case Study	97
6.3	Implications	97
6.4	Recommendations	98
6.4.1	Current Implementation	98
6.4.2	Additional Research	98
	References	101
A	Root-Finding Algorithms	107
A.1	Newton-Raphson Method	107
B	Derivation of the Internal Forces for Standard Finite Elements	111
B.1	Non-Linear Beam Element	111
B.1.1	Axial Strain	111
B.1.2	Bending Strain	113
B.1.3	Internal Forces	116
B.2	Linear Beam Element	118
B.3	Non-Linear Bar Element	118
B.4	Linear Bar Element	119
B.5	Large Rotation Beam Element	119

C	Validation of Standard Finite Elements	123
C.1	Bar Element	123
C.1.1	Von Mises Truss	123
C.2	Beam Element	125
C.2.1	Beam Deflection Formulae	126
C.2.2	Portal Frame	130
C.2.3	Diamond Frame	132
C.3	Large Rotation Beam Element	136
C.3.1	Cantilever Beam	136
C.3.2	Diamond Frame	136
D	Derivation of the Internal Forces for Special Finite Elements	139
D.1	Damper Element	139
D.1.1	Non-Linear Damper	139
D.1.2	Linear Damper	140
E	Derivation of the Mass Matrices for the Finite Elements	141
E.1	Beam Element	141
E.2	Bar Element	142
E.3	Large Rotation Beam Element	143
E.4	Point Mass	144
E.5	Special Finite Elements	144
F	Validation of the Dynamic Program	145
F.1	Single DOF Mass-Spring-Damper Model	145
F.2	MATLAB ODE Solvers	148
F.3	Equations of Motion for Seat A	149
F.4	Validation of the Dynamic Program	152

List of Figures

1.1	FRISC of the Royal Netherlands Navy	1
2.1	Example of the phenomenon of bottoming out for an arbitrary SMS design	14
2.2	Example of the phenomenon of dynamic amplification for an arbitrary SMS design	15
2.3	Shock transmissibility curve for a half-sine excitation pulse	16
2.4	Zoomed in shock transmissibility curve for a half-sine excitation pulse	16
2.5	Coil spring element stiffness as function of the length	19
2.6	Coil spring element force-displacement curve	19
2.7	Gas-spring element in the global coordinate system	22
2.8	Gas-spring element force-displacement curve	25
3.1	ISO 2631 Part 5 flowchart for the calculation of the acceleration dose [1]	33
3.2	ISO 2631 Part 5 flowchart for the assessment of adverse health effects based on the acceleration dose [1]	36
3.3	Eiband tolerance curve for vertical accelerations [2]	37
3.4	Probability of spinal injury estimated from laboratory data compared to operational experience [3] [4]	39
3.5	Probability of injury for males and females as a function of the modified risk factor [5]	43
3.6	ISO 2631 Part 5 complete flowchart with limitations indicated in red	45
4.1	Wave impact sequence of events [6]	48
4.2	Vertical dynamic response of the craft and its different modes [6]	49
4.3	FFT of the vertical acceleration [6]	49
4.4	Normalized rigid body accelerations for multiple wave impacts [6]	50
4.5	Half-sine approximation of a wave impact [7]	50
4.6	Full-scale data wave impact duration against peak acceleration [7]	52
4.7	KNRM lifeboat of the Valentijn class [8]	53
4.8	KNRM lifeboat deck level acceleration record including three consecutive wave impacts [9]	54
4.9	Individual wave impacts from the KNRM lifeboat acceleration record	55
4.10	Half-sine approximation of the wave impacts from the KNRM lifeboat acceleration record	57
4.11	Acceleration response of models with different natural frequencies to the KNRM lifeboat acceleration record	59
4.12	Zoomed in acceleration response of models with different natural frequencies to the KNRM lifeboat acceleration record	60
4.13	Acceleration response of the SMS to various accelerations of the craft	61
4.14	Spring length of the model for various accelerations of the craft	63
4.15	Selection of full-scale data of wave impacts for the FRISC class	65
4.16	Total change in velocity contour lines for full-scale data of wave impacts for the FRISC class	66
5.1	Seat A	72
5.2	Schematic representation of seat A [10]	73
5.3	Seat A model	74
5.4	Seat B	75
5.5	C-shaped composite leaf spring seat model	78

5.6	Comparison of the resulting deformations for various models of C-shaped composite leaf spring suspension	78
5.7	Seat A model available stroke length for different values of L_{13}	81
5.8	Seat A model maximum height of the seat structure with respect to y_1	81
5.9	Seat A model undeformed structure for the extreme values of L_{13} and L_j	82
5.10	Seat A model natural frequency of three modes for different dimensions	84
5.11	Seat A model natural frequencies for different values of the mass	85
5.12	Seat level acceleration response in the vertical direction for suspension design seat A with different springs and settings	87
5.13	Seat level acceleration response in the horizontal direction for suspension design seat A with different springs and settings	87
5.14	Seat level acceleration response in the vertical direction per wave impact for suspension design seat A with different springs and settings	88
5.15	Seat level acceleration response in the horizontal direction per wave impact for suspension design seat A with different springs and settings	89
5.16	Spring length for the acceleration responses in time for suspension design seat A with different springs and settings	90
B.1	Deformed beam element	112
B.2	Deformed differential beam element due to bending	114
B.3	Relation between radius of curvature and arc length	114
B.4	Beam element in the global coordinate system	117
B.5	Bar element in the global coordinate system	119
C.1	Schematic representation of the Von Mises truss	123
C.2	Von Mises truss equilibrium path including snap-through behaviour	125
C.3	Schematic representation of the simplified suspension of seat B	126
C.4	Seat B suspension model application of virtual work method	127
C.5	Seat B suspension model free body diagrams	127
C.6	Seat B suspension model rotation of the rigid body	129
C.7	Seat B suspension model deformation for different values of h	130
C.8	Schematic representation of the portal frame	131
C.9	Portal frame load-deflection curves for different values of n	131
C.10	Portal frame deformation for different values of n	132
C.11	Schematic representation of the diamond frame	133
C.12	Diamond frame deformation for different types of loading	133
C.13	Diamond frame horizontal displacement of point B	134
C.14	Diamond frame vertical displacement of point C	134
C.15	Diamond frame rotation of point C	135
C.16	Diamond frame convergence study results	135
C.17	Cantilever beam deformation for different discretizations	136
C.18	Cantilever beam with end point load displacements	137
C.19	Diamond frame deformation for different beam elements	138
F.1	Single DOF mass-spring-damper model	145
F.2	Schematic representation of the simplified suspension of seat A	150
F.3	Seat A suspension model deformation	152
F.4	Seat A suspension model FFT of the vertical acceleration	154
F.5	Seat A suspension model acceleration of the seat in time	155
F.6	Seat A suspension model length of the spring in time	156
F.7	Seat A suspension model velocity of the seat in time	157
F.8	Seat A suspension model position of the seat in time	158

List of Tables

3.1	Survey results of self-reported injuries [11] [12]	28
3.2	DRI Guidelines for seated humans [3] [13]	38
3.3	Parameters for the CDRR [14] [13]	39
3.4	Recalculated parameters for the IRC [15]	40
3.5	Dynamic response limits for the IRC [15]	40
3.6	Coefficients for the modified risk factor R and Weibull injury risk model [5]	42
4.1	KNRM lifeboat acceleration record parameters of each wave impact	56
4.2	Critically damped mass-spring-damper model parameters for different natural frequencies	59
4.3	Acceleration response differences for various accelerations of the craft	62
4.4	Length of the spring for various accelerations of the craft	64
4.5	Parameters of the selected wave impact excitation pulses	66
5.1	Overview of commercial SMS suspension designs	70
5.2	Seat A dimensions [10]	73
5.3	Leaf spring Hexforce/Epikote material characteristics [16]	75
5.4	Proposed design model parameters	80
5.5	Peak accelerations of the seat level acceleration response per wave impact for suspension design seat A with different springs and settings	90
5.6	Shock transmissibility factors for the accelerations in the vertical direction per wave impact for suspension design seat A with different springs and settings	91
5.7	DRI values for the acceleration response in the vertical direction per wave impact for suspension design seat A with different springs and settings	92
5.8	Risk factor and probability of injury according to the ISO method and the modified ISO method for lumbar accelerations in both the horizontal and the vertical direction for suspension design seat A with different springs and settings	92
C.1	Von Mises truss critical load results	125
C.2	Von Mises truss critical displacement results	125
C.3	Seat B suspension model horizontal force displacement results	128
C.4	Seat B suspension model vertical force displacement results	129
C.5	Seat B suspension model bending moment displacement results	129

Nomenclature

Abbreviations

CF	Crest Factor
CLT	Classical Laminate Theory
DFT	Discrete Fourier Transform
DOF	Degree-of-Freedom
DRI	Dynamic Response Index
FBD	Free Body Diagram
FEA	Finite Element Analysis
FEM	Finite Element Method
FFT	Fast Fourier Transform
FRISC	Fast Raiding Interception and Special forces Craft
HSC	High Speed marine Craft
IRC	Injury Risk Criterion
ISO	International Organisation for Standardization
MBD	Multi-Body Dynamics
MTTV	Maximum Transient Vibration Value
NASA	National Aeronautics and Space Administration
NAVSEA	Naval Sea Systems Command
ODE	Ordinary Differential Equation
RIB	Rigid Inflatable Boat
RMS	Root-Mean-Square
RNLN	Royal Netherlands Navy
RNN	Recurrent artificial Neural Network
RS	Repeated mechanical Shocks
SMS	Shock Mitigating Seats
TF	Transmissibility Factor
VDV	Vibration Dose Value
WBV	Whole Body Vibrations

Subscripts

A_0	Cross-section of the gas cylinder	$[m^2]$
a_d	Deck level acceleration	$[m \cdot s^{-2}]$
a_p	Acceleration peak	$[m \cdot s^{-2}]$
a_s	Seat level acceleration	$[m \cdot s^{-2}]$
a_w	Frequency weighted acceleration	$[m \cdot s^{-2}]$
a_{RMS}	RMS acceleration	$[m \cdot s^{-2}]$
A_{iz}	Acceleration peaks in the vertical direction	$[m \cdot s^{-2}]$
a_{lz}	Lumbar acceleration response in the vertical direction	$[m \cdot s^{-2}]$
a_{sz}	Seat level acceleration in the vertical direction	$[m \cdot s^{-2}]$
C_p	Specific heat at constant pressure	$[J \cdot kg^{-1} \cdot K^{-1}]$
C_v	Specific heat at constant volume	$[J \cdot kg^{-1} \cdot K^{-1}]$
c_{crit}	Critical damping coefficient	$[N \cdot s \cdot m^{-1}]$
D_i	Accumulated damage	$[-]$
D_{kd}	Average daily acceleration dose in direction k	$[m \cdot s^{-2}]$
D_k	Acceleration dose in direction k	$[m \cdot s^{-2}]$

F_g	Gas-spring force	[N]
k_0	Normal spring stiffness	[N·m ⁻¹]
L_0	Undeformed length	[m]
L_R	Length of stiffness transition	[m]
L_0	Total stroke	[m]
L_{br}	Length of the bottom rod	[m]
L_{max}	Maximum length	[m]
L_{min}	Minimum length	[m]
L_{pr}	Length of the piston rod	[m]
L_s	Remaining stroke length	[m]
m_e	Effective mass	[kg]
M_P	Moment in point P	[N·m]
N_i	Number of cycles to failure	[-]
n_i	Number of cycles	[-]
p_0	Initial pressure inside the gas cylinder	[Pa]
P_x	Force in the direction of the x-axis	[N]
P_y	Force in the direction of the y-axis	[N]
P_{crit}	Critical load	[N]
Q_k	Stiffness matrix for ply k	[Pa]
Q_{crit}	Critical displacement	[m]
R_F	Damper force	[N]
S_e	Equivalent static compressive stress	[Pa]
S_{ed}	Daily equivalent static compressive stress	[Pa]
S_{ui}	Ultimate strength of the lumbar spine	[Pa]
t_0	Time of observation	[s]
t_d	Duration of daily exposure	[s]
t_k	Thickness for ply k	[m]
t_m	Period of measurement for the acceleration dose	[s]
T_n	Period of the natural frequency	[s]
T_e	Specific kinetic energy	[J]
U_a	Specific strain energy	[J]
U_e	Specific potential energy	[J]
V_0	Initial volume in the gas cylinder	[m ³]
β_{crit}	Critical deformed angle	[rad]
δ_{max}	Maximum displacement between the upper body and the pelvis	[m]
ϵ_a	Axial strain	[-]
ϵ_b	Bending strain	[-]
ω_n	Natural frequency	[rad]

Greek symbols

α	Angle	[rad]
α	Scale parameter	[-]
β	Shape parameter	[-]
ΔL	Elongation	[m]
Δt	Peak impact duration	[s]
ΔV	Total change in velocity	[m·s ⁻¹]
δ	Displacement between the upper body and the pelvis	[m]
δ	Ratio of spring stiffness transition	[-]
ΔL	Change in elongation over time	[m·s ⁻¹]
$\dot{\theta}$	Angular velocity	[rad·s ⁻¹]
ϵ	Strain	[-]

ϵ	Tolerance	[-]
γ	Heat capacity ratio	[-]
κ	Curvature	[m ⁻¹]
λ	Eigenvalue	[-]
λ	Force scale factor	[-]
μ	Arbitrary coordinate	[m]
Π	Potential energy	[J]
ρ	Density	[kg·m ⁻³]
ρ	Radius of curvature	[m]
σ	Stress	[Pa]
τ	Integration time constant	[s]
θ	Rotation	[rad]
θ	Slope	[rad]
ξ	Arbitrary coordinate	[m]
ζ	Damping ratio	[-]
ζ	Dimensionless displacement	[-]

Symbols

A	Cross-sectional area	[m ²]
b	Age of the person on which the exposure started	[year]
b	Width	[m]
C	Damping matrix	[N·s·m ⁻¹]
C	Specific damping matrix	[N·s·m ⁻¹]
c	Damping coefficient	[N·s·m ⁻¹]
c	Static stress due to gravitational force	[Pa]
D	Cumulative damage	[-]
dm	Differential mass element	[kg]
ds	Differential arc length element	[m]
E	Green-Lagrange strain matrix	[-]
E	Modulus of elasticity	[Pa]
F	Displacement gradient matrix	[-]
F	Potential function	[-]
F	Spring force	[N]
f	Continuous differentiable function	[-]
f	Natural frequency	[Hz]
G	Weight of the masses	[kg]
g	Gravitational constant	[m·s ⁻²]
H	Enthalpy	[J]
H	Force in the horizontal direction	[N]
h	Distance between parallel leaf springs	[m]
h	Initial height	[m]
I	Area moment of inertia	[m ⁴]
i	Year counter	[year]
J	Jacobian matrix	[N·m ⁻¹]
k	Coil spring stiffness	[N·m ⁻¹]
\mathcal{L}	Lagrangian	[J]
L	Length	[m]
L'	Deformed length	[m]
M	Moment	[N·m]
M	Specific mass matrix in the global coordinate system	[kg]
m	Specific mass matrix in the local coordinate system	[kg]

N	Number of exposure days per year	[-]
N	Number of nodes	[-]
n	Fraction of the force P	[-]
P	Force	[N]
p	Pressure	[Pa]
\hat{P}	Force unit load	[N]
\ddot{Q}	Acceleration in the global coordinate system	[m·s ⁻²]
\dot{Q}	Velocities in the global coordinate system	[m·s ⁻¹]
Q	Displacements in the global coordinate system	[m]
Q	Energy supplied to a system	[J]
q	Displacements in the local coordinate system	[m]
R	Gas constant	[J·K ⁻¹ ·mol ⁻¹]
R	Rayleigh dissipation function	[-]
R	Residue forces	[N]
R	Risk factor	[-]
R	Rotation matrix	[-]
R	Strain matrix	[-]
s	Arc length	[m]
T	Absolute temperature	[K]
T	Duration	[s]
T	Kinetic energy	[J]
T	Period	[s]
t	Thickness	[m]
t	Time	[s]
U	Eigenvector	[-]
U	Internal energy of a system	[J]
U	Potential energy	[J]
u	Shape function for the horizontal displacement	[m]
u	Velocity in the local horizontal direction	[m·s ⁻¹]
V	Force in the vertical direction	[N]
V	Volume	[m ³]
v	Shape function for the vertical displacement	[m]
v	Velocity in the local vertical direction	[m·s ⁻¹]
W	Work	[J]
\dot{x}	Change of the coordinate along the x-axis in time	[m]
x	Coordinate along the x-axis	[m]
\dot{y}	Change of the coordinate along the y-axis in time	[m]
y	Coordinate along the y-axis	[m]

1

Introduction

In this chapter, the topic of the thesis research is introduced and some background information is provided. Subsequently, the identified knowledge gaps, research questions and research relevance based on the literature study are described.

1.1. Background

On board of High Speed marine Craft (HSC), the crew and the passengers are exposed to high levels of Whole Body Vibrations (WBV) and large magnitude Repeated mechanical Shocks (RS). These physical loads result from the motions of the craft, such as slamming where the craft impacts a wave at high velocity after a lift off. Small HSC are typically 10 meters long and capable of reaching a maximum speed up to 50 knots [17]. These craft are widely used by various maritime organizations, because of their versatility and capability. An example of a HSC is the Fast Raiding Interception and Special forces Craft (FRISC), which is used by the Royal Netherlands Navy (RNLN) and other law enforcement agencies. In figure 1.1, the FRISC and the crew of marines are shown. The FRISC is a high speed marine craft with a length of 9.5 or 12 meters, which is highly manoeuvrable and is capable of reaching speeds up to 45 knots [18]. The craft is able to operate in a wide range of weather conditions, sea states and speeds. This makes the craft suited for a variety of operations such as search and rescue, reconnaissance, counter terrorism, anti-smuggling and anti-piracy.



Figure 1.1: FRISC of the Royal Netherlands Navy

However, the crew and passengers on board of the FRISCs suffer from fatigue and injuries, leading to a reduced effectiveness and operational capacity of the marine craft [12] [19] [17]. In a self-reported study of US Navy HSC operators [12], evidence of a significant injury problem was found. Of all operators that participated in this survey, 65% suffered from HSC-related injuries of which 89% occurred within the first two years of operation [12] [20]. Additionally, the injury rate of the HSC operators was compared to the average injury rate of US Navy personnel and the results showed that the injury rate of HSC operators is over five times higher than the Navy average [20]. In the survey, the most common injury locations were the lower back, knees and shoulders [12], which is confirmed by numerous other research [21] [20] [22] [17] [11] [10]. In another prior research [19], it was shown that the physical performance of passengers on board of Rigid Inflatable Boats (RIB) was reduced by up to 26 % after a 3 hour high-speed sea transit in rough sea conditions with unsuspending seats. The decrease in performance was argued to be a result of the passengers trying to compensate for the physical loads, leading to local muscle damage and fatigue in the legs [19] [11]. Many more test results and cases are known, where it becomes evident that the high levels of WBV and RS lead to severe adverse health effects and that, therefore improvement of the working environment is needed [11]¹ [12] [22].

1.2. Shock Mitigating Seats

In an attempt to reduce the physical loads on the crew, passive Shock Mitigating Seats (SMS) can be installed. Various SMS designs have been developed by commercial companies and can be bought 'off the shelf'. The SMS suspension design can be based on various suspension principles. The primary function of the seat is to reduce the effects of potentially hazardous shocks and vibrations by reducing the accelerations of the seat and the seat occupant [7] [26]. When the magnitude of the shock force transmitted through the seat suspension is less than the wave impact force at the base of the seat it is referred to as (mechanical) shock mitigation [26].

Numerous research has shown that an improperly designed seat may amplify the wave impacts forces [17] [11] [10] [16] [26] [26]. Therefore, it is necessary to ensure that a suspension design works properly by testing the performance during wave impact events, before the seat is manufactured and installed onboard the craft. The SMS models are developed for prescribed design conditions based on the expected operating conditions. The problem is that it is difficult to determine the performance of the seats in both the design and off-design conditions with either sea trials or laboratory tests. During sea trials, it is difficult to control the conditions such as sea state, weather, wave speed and position of the craft. In addition, it is expensive and time consuming to test the seats for a representative range of conditions. On the other hand, in laboratory tests, it is difficult to reproduce the complex motions of the sea and the craft [7]. A numerical dynamic analysis program may offer a solution as it is able to simulate the behaviour of various SMS suspension designs and only requires data of wave impact measurements [11]. The program would reduce the need for a lot of sea trials or laboratory tests. Therefore, such a program has the potential to save time and reduce costs by being able to make direct comparisons and assess possible design improvements of various suspension designs.

1.3. Previous Research & Knowledge Gaps²

The identified problem in the literature study consists of three parts. First of all, the applicability and the accuracy of the models used in prior research are discussed. Second, the input accelerations for the models and their validity is investigated. Third, the commonly used methods and injury models to evaluate the resulting seat accelerations are reviewed. In the following paragraphs, each of the parts is elaborately discussed.

In prior research [17] [11] [10] [16], the shock mitigating seats are analysed with either simplistic or spe-

¹Based on the multiple papers [23] [24] [25]

²This section is based on the literature study [27]

cific models which are mostly limited to a single Degree-Of-Freedom (DOF) and use the heave motion of a craft as input. In most studies [17] [11] [16], the SMS are modelled using a single DOF mass-spring-damper system. In another study [10], a rigid-body dynamics model was developed based on the equations of motion for a specific SMS design. With these models, the influence of variations of mass, spring stiffness and damper on the response are analysed. Based on these analyses, the designs would be altered in an attempt to improve the shock mitigating characteristics. However, the models used in previous research are restricted to one design or suspension principle only and only some of these models implement a non-linear coil spring element while the other models merely use linear elements. In the software from previous studies [10] [16] [17] [11], common elements such as a coil-spring and damper element were implemented, but only in the research of Stouten [16] and Vredeveltdt [10] the effect of bottoming was implemented while this is one of the major causes of poorly performing designs. The effect of bottoming was implemented by instantaneously increasing the spring stiffness when the coil spring reached a certain deformed length. Between the extreme lengths of the coil spring, the spring would have a constant spring stiffness and show linear behaviour. Realistic behaviour of the spring and the effect of bottoming may be increased by defining a more complicated stiffness-elongation curve for the element. This could lead to more realistic simulations of the behaviour of SMS when bottoming occurs. In none of the reviewed literature, a SMS suspension design with an integrated gas-spring element was analysed or modelled. To analyse a suspension design with a gas-spring, such an element has to be implemented in the computer program. The gas-spring element should also include the effect of bottoming. The application of a gas-spring in the suspension design could result in an improvement of the shock mitigating characteristics, because the gas-spring is able to absorb more energy than a coil spring for an equal stroke. Additionally, the gas-spring may prevent acceleration spikes resulting from bottoming in the response as the stiffness of a gas-spring increases gradually. In conclusion, SMS designs based on different suspension principles, which have coupled forward and vertical motions in combination with non-linear spring characteristics, can not be analysed with the previous models. Therefore, a numerical dynamic analysis program with multiple DOF is required [11] [26] that integrates highly non-linear elements such as a gas-spring. The application of the gas-spring may lead to new insights regarding the suspension design of SMS.

For both designing and testing of SMS, a simplified excitation pulse is often used to approximate the deck level accelerations in the heave direction experienced during wave impact events [28] [10] [16] [26] [29]. The approximation is known as the half-sine approximation and is used by numerous studies without much criticism while the validity of this approximation can be questioned. In comparison to full-scale experiments of wave impacts, the importance of peak acceleration levels is acknowledged and representative accelerations are used [6] [7]. However, the importance of wave impact durations seems to be neglected [30] [28] [29]. Incorrect values for these parameters could lead to an underestimation of the severity of the wave impacts, which in turn would lead to poor performance in operational conditions at sea. Therefore, both the half-sine approximation and the wave impact duration need to be investigated. To determine the validity of the half-sine approximation, various wave impact profiles can be generated with the half-sine approximation based on measured acceleration data from sea trials. The various wave impact profiles can be used as input to calculate the response of a SMS design and these responses can be compared in order to determine the validity of the half-sine approximation. To investigate the importance of the wave impact duration, data of full-scale measurements should be studied in order to determine whether the impact duration can be neglected.

Both a survey of self-reported injuries [12] and previous studies [19] [17] [11] [10] concluded that the operators of HSC are exposed to a greater than average risk of injuries and the most common anatomical location of injury is in the area of the lower back, knees and shoulders. In the reviewed literature of Olausson [17] [11], the resulting acceleration levels of the crew were compared to existing legislation on WBV and RS known as ISO 2631 part 1 and ISO 2631 part 5 [31] [1]. In the study of Vredeveltdt [10], a small overview was presented of existing legislation and on methods relating WBV and RS to spinal injury. Only in [10], [17] and [11], the resulting accelerations levels were compared to stated limits in legislation and directives on

WBV and RS. Additionally, most of the reviewed literature [17] [11] [10] [16] recommends further research in the relation between the physical loads and the resulting injuries of HSC operators in order to define suitable thresholds and acceptable limits. In the analyses and models from previous research, no injury model or model of the human body was implemented but the resulting seat level accelerations were processed using various injury criteria. However, the used injury criteria are often criticized for their suitability regarding the assessment of injuries and adverse health effects resulting from WBV and RS [32] [20] [33] [22] [17] [34] [35] [23] [11]. Therefore, an extensive study on commonly referenced standards and biomechanics literature was conducted in order to determine a suitable injury criterion/model to evaluate the probability of spinal injury resulting from WBV and RS. The most suitable of the reviewed models seem to be the dynamic response index and the evaluation methods from ISO 2631 Part 5. However, both evaluation methods still have their limitations. Therefore, possible improvements of these evaluation methods should be investigated by studying additional biomechanics literature.

1.4. Research Objective & Questions³

The main objective of the research is to prevent injuries of high speed marine craft operators resulting from repetitive wave impacts by incorporating an injury model in the analyses of various suspension principles in the design of shock mitigating seats.

Based on the main objective of this research, the following research question is formulated:

How can injuries experienced by the crew on high speed craft caused by wave impacts be modeled in the analyses of various suspension principles in the design of shock mitigating seats?

To answer the main research question, the following research questions need to be answered:

- How can the analyses of various suspension principles for shock mitigating seat designs be improved by integrating highly non-linear elements in the computer program such as a gas-spring element that includes the effect of bottoming?
- What simplified floor level acceleration pulse is a realistic representation of the accelerations experienced in wave impacts events at high speed?
- Which existing injury model is suitable to relate the physical loads experienced on high speed craft to the injuries of the crew, and how can this model be incorporated in the model?

1.5. Research Relevance⁴

The relevance of the research is an important aspect of the master thesis project. In the literature study, the relevance of the research was assessed from three different perspectives. These perspectives are; the industrial perspective, the user perspective and the scientific perspective. In this report, the main arguments of the relevance will be discussed briefly.

Industrial Perspective

Prior research has shown that the existing SMS do not mitigate the hazardous shocks and vibrations sufficiently. This leads to the conclusion that the suspension designs are lacking in performance and should be improved or altered. The proposed research will attempt to improve the analyses of various suspensions in the design of SMS by implementing highly non-linear elements, investigating the floor level accelerations during wave impact events and analysing the resulting accelerations with injury models. The improved analyses will contribute to an improvement of the design process, because the need for many iterations to optimize a design becomes unnecessary as less prototypes need to be produced and tested elaborately.

³This section is based on the literature study [27]

⁴This section is based on the literature study [27]

Therefore, the research has the possibility to save time and reduce costs when developing better products, which makes this research relevant from the industrial perspective.

User Perspective

The SMS is mostly used by governmental organisations such as the Navy, Army and other law enforcement agencies such as the Royal Sea Rescue Institution, coast guard and harbour police. The personnel of both governmental organisations and law enforcement agencies operate in dangerous conditions while performing certain tasks, where risk of life is possible. The physical loads to which the operators are exposed lead to a reduced effectiveness and operational capacity. These adverse effects are undesirable from both the ethical perspective and societal perspective. From an ethical perspective, it is not acceptable to have military personnel and officials carry out dangerous tasks while also suffering from severe adverse health effects due to their exposure to a poor working environment. From a societal perspective, it is not beneficial for the society if governmental organisations and law enforcement agencies are not able to perform their tasks as effectively due to poorly performing equipment and results in an increase of the deployment of personnel and material required in order to perform these tasks. In conclusion, the research is relevant from the user perspective as it contributes to the prevention of injuries by reducing the resulting physical loads to which the operators are exposed.

Scientific Perspective

In the last three decades, many experts and engineers within the maritime industry have focused on one specific component of HSC in the human machine interface, the operator and crew seating [26]. The shock mitigation seating is a continuously discussed topic among experts and to design a properly performing suspension is a challenge for many engineers. The experts and engineers are faced with a complex problem that requires understanding the dynamic interactions between a random sea surface and a craft moving at high speed at the interface of two fluids [26]. Additionally, the effect of prolonged exposure to the wave impacts on the human body in the short term and long term should be evaluated. The proposed research is relevant from the scientific perspective as it will deliver a useful contribution to help solving the problem by combining knowledge of various scientific fields and conduct research in three general aspects of the problem. The predominant scientific fields of which knowledge is required are; marine technology, biomechanics, structural engineering and mechanics. The three aspects in which further research will be conducted are wave impact deck level accelerations, various suspension principles for the mitigation of wave impact shocks and the relation between the physical loads and resulting injuries or adverse health effects.

1.6. Outline Report

The report is organized in four broad aspects of the problem, the computer program, injury models, wave impact excitation pulses and a case study. In this chapter the topic was already introduced and the research questions were presented. In chapter 2, the computer program is discussed and the equations of motion are derived. Additionally, the derivations for the coil spring element and the gas-spring element are presented. In chapter 3, the resulting injuries and adverse health effects of high speed craft operators are discussed. Furthermore, directives on the exposure to WBV and RS are described. Following from the directives, various evaluation methods and injury models are reviewed. In chapter 4, the excitation pulses of wave impacts are studied and an approximation for the excitation pulse is reviewed with data of full-scale experiments and measurements of a sea trial. In chapter 5, the computer program is used to analyse a SMS for a FRISC of the Royal Netherlands Navy. Finally, the research questions are answered based on the obtained results and the conclusion along with the recommendations are presented.

In addition to the main report, various appendices have been added. The appendices form an integral part in understanding the computer program. Any reader who is interested in or wants a deeper understanding of the computer program is encouraged to read through all appendices. In appendix A, some background

information of root-finding algorithms is given and the algorithm for the static analysis is described. In appendix B, the internal forces of the beam and bar elements are derived from the potential energy formulations. In appendix C, the beam and bar elements are validated with results from literature. In appendix D, the internal forces of the damper element are derived from the Rayleigh dissipation function. In appendix E, the mass matrices of all finite elements are derived from the kinetic energy formulations. In appendix F, the dynamic analysis part of the program is validated with analytical derivations.

2

Computer Program

In this chapter, the computer program is discussed. First, the possible theoretical methods for the program are reviewed and the program set up is described. Additionally, the equations of motion for the static analyses and dynamic analyses are derived. Furthermore, the physical causes of shock amplification in SMS are described. Finally, the internal forces for the coil spring element and gas-spring element are derived from the potential energy formulations.

2.1. Program Method¹

An approach for this research could be to use existing commercial computer programs. However, it would require effort and time to learn the program and mould the elements such that they have the desired behaviour. Therefore, generating a new computer program dedicated for the analyses of SMS is attractive and provides a good understanding of the theory behind the calculations and simulations. As the computer program is developed specifically for the analyses of SMS, the elements can be tuned to the requirements of the research. The only downside is that the development and validation of such a program may be time consuming, depending on the complexity of the program. In this research, the author has chosen to develop a new numerical dynamic analysis program which will be used to analyse SMS on HSC. The program can be based on several possible theoretical methods. The most common and suitable methods are either finite element method or rigid-body dynamics. Both methods have their advantages and disadvantages. Each of the methods will be discussed shortly and one will be chosen to develop the program.

Finite Element Analysis (FEA) is the modelling, simulation and analysis of a physical phenomenon based on the Finite Element Method (FEM). Many physical phenomena in engineering science are described in Partial Differential Equations (PDE). These PDE's are in general difficult to solve analytically. The FEM is a numerical method for solving these PDE's approximately. In order to determine the behaviour of a system or continuum, the continuum is discretized into many simple geometric shapes that are called finite elements and are connected by nodes. With the boundary conditions and material properties of each element, algebraic equations are derived. By assembling these algebraic equations of all elements, a system of equations results that represents the continuum. The FEM uses various mathematical methods to approximate a solution for the system of equations and thus determine the approximate behaviour of the system [36] [37]. Some advantages and disadvantages of the FEM are:

- FEM is able to model complex geometries.
- FEM can approximate the actual behaviour of mechanical systems.
- Experience and knowledge are needed to properly construct a FEM model.

¹This section is based on the literature study [27]

Rigid-body dynamics is a type of Multi-Body Dynamics (MBD) where the behaviour of a mechanical system is approximated by modelling the system as rigid bodies interconnected by joints, springs and dampers, but they are deformable if modelled as a flexible body. Each of the bodies may undergo various translational and rotational displacements. This method is able to accurately determine the behaviour of the total system and the behaviour of each individual body. As it is assumed that the bodies are rigid, these bodies will not deform by external forces. This assumption simplifies the analysis of the system as the number of variables that describe the behaviour of the system is reduced. Some advantages and disadvantages of rigid body dynamics are:

- Simplified analysis of the mechanical system due to reduced number of variables that describe the system.
- Compared to FEM the calculation times are much quicker. Therefore, it is easier to get faster insight in the behaviour of a mechanical system.
- Often when analysing a specific commercial design, joint properties are unknown and must therefore be determined using other methods such as experiments or models.

The numerical dynamics analysis program in this research will be based on the FEM. The main reasons for this choice are that the author has prior experience with the development of a computer program based on the FEM and that the program in this research should be able to model various complex SMS designs, while some specific properties are yet unknown due to lack of documentation or manufacturer's confidentiality. Experiments have been conducted in order to determine the properties of both springs and dampers, which could be implemented in a MBD model. However, when using the program to assess design improvements, the flexibility of the FEM is expected to be required in order to easily alter the (geometrical) properties of various elements or the construction of the suspension designs.

2.2. Program Setup²

In this research, two main programs are developed; the static analysis program and the dynamic analysis program.

The static analysis program must be able to solve the static equilibrium of a SMS given a static loading condition. The program can be used to derive force-displacement curves of various suspension designs. Any design parameter of the suspension design should be easily variable such that the influence of the design parameters can be investigated and any alterations analysed. The solution of the static equilibrium is used as the starting condition of the dynamic analysis program.

The dynamic analysis program must be able to simulate the behaviour of a SMS under complex accelerations. The accelerations can be prescribed and applied to any given location of the SMS. The program computes the response of the SMS and calculates the resulting accelerations of the person on the SMS. By comparing the resulting accelerations to the applied accelerations, the performance of the SMS can be analysed for a wide range of loading conditions.

For both programs, the following elements are implemented:

- Linear and non-linear bar element
- Linear and non-linear beam element
- Damper element (Rayleigh damping)
- Non-linear coil spring element

²This section is based on the literature study [27]

- Non-linear gas spring element

In addition, the following mathematical theories are implemented:

- Root-finding algorithm
- Numerical integration method

2.2.1. Validation & Verification

Once the program is developed, the results of the program should be examined to ensure the program works as is intended and the results of the simulations are correct. This process is divided in two processes which are called verification and validation. The process of validation establishes if the program satisfies the problem's requirements, while the the process of verification determines in the program works correctly [38]. Thus, the process of validation concerns "solving the right problem" and verification concerns "solving the problem right" [38].

In this research, for the validation of the computer program an step-by-step approach is taken. Each time a new element is programmed and implemented, the element will be validated by comparing the results of test cases with results from literature. Many fundamental structure problems are described in literature and can be used to validate the program. Once the results of the elements are validated within its range of applicability, more extensive problems can be confidently analysed. In addition, both static and dynamic results from full-scale experiments are available. These experiments can be simulated with the computer program if all required input data is known. The results of these simulations can then be compared to the experimental results. The results from the program may deviate from the experimental results as the program is based on the FEM and provides an approximation to the solution. Also, for the verification of the computer program a step-by-step approach is taken. The derivations for each element are made by hand and reproduced in MAPLE to check for any mistakes or errors. If a similar derivation exists in literature, then it is also compared to the literature. When the aforementioned checks are performed, the element is implemented in the MATLAB program and subsequently validated with fundamental problems from literature.

2.3. Equations of Motion

The equations of motion for a system are derived with the Euler-Lagrange Equation ³ based on the total Lagrangian approach. An advantage of the Euler-Lagrange equation compared to the Newton's laws is that the Euler-Lagrange equation for any system is expressed in generalized coordinates. A condition is that the generalized coordinates must fully describe the total system. As a result, the DOF is equal to the number of generalized coordinates.

The Euler-Lagrange equation is a combination of the equation of Leonhard Euler (1707-1783) and the potential function derived by Joseph-Louis Lagrange (1736-1813). The Euler equation is a second-order PDE from which solutions result that describe when a given functional is stationary. For the derivation of the Euler equation an integral of an arbitrary potential function is set up (2.1). This potential function describes a system as function of time. The potential function is a functional, because it is not only a function of time, but also the position of the masses as function time and the velocities of the masses as function time.

$$S = \int_{t_1}^{t_2} F(t, Q, \dot{Q}) dt \quad (2.1)$$

The purpose of the Euler equation is to find a function, which meets the preconditions, so that the integral of the functional has an extreme value. The integral should be minimized according to the principle of

³The general derivation of Euler-Lagrange is based on literature [39] [40] [41] [42]

stationary action formulated by William Rowan Hamilton (1805-1865). Solving the integral (2.1) results in the Euler equation (2.2).

$$\frac{d}{dt} \left(\frac{\partial F}{\partial \dot{Q}_i(t)} \right) - \frac{\partial F}{\partial Q_i(t)} = 0 \quad (2.2)$$

Lagrange formulated a potential function which can be combined with the Euler equation, see equation (2.3). The potential function is referred to as the Lagrangian [42].

$$\mathcal{L} = T - U \quad (2.3)$$

The Lagrangian describes the difference in kinetic energy (T) and potential energy (U). Substituting the Lagrangian in the Euler Equation results in

$$\frac{d}{dt} \left(\frac{\partial \mathcal{L}}{\partial \dot{Q}_i} \right) - \frac{\partial \mathcal{L}}{\partial Q_i} = 0 \quad (2.4)$$

With the Euler-Lagrange equation and expressing the kinetic energy and potential energy in generalized coordinates it is possible to derive the equations of motion for complex mechanical systems. If external forces are applied to the system, the Euler-Lagrange equation must be expanded with an extra term to account for work done by these forces.

$$\frac{d}{dt} \left(\frac{\partial \mathcal{L}}{\partial \dot{Q}_i} \right) - \frac{\partial \mathcal{L}}{\partial Q_i} = \frac{\partial W}{\partial Q_i} \quad (2.5)$$

The Euler-Lagrange equation presented in (2.5) is only suited for an undamped mechanical system. If damping is present within the system, another term must be added to the Euler-Lagrange equation. By substituting the Lagrangian and understanding that the potential energy of the system is not a function of the velocities of the masses nor that the kinetic energy of the system is a function of the position of masses, equation (2.5) simplifies to

$$\frac{d}{dt} \left(\frac{\partial T}{\partial \dot{Q}_i} - \frac{\partial U}{\partial \dot{Q}_i} \right) - \frac{\partial T}{\partial Q_i} + \frac{\partial U}{\partial Q_i} = P_i \quad (2.6)$$

$$\frac{d}{dt} \left(\frac{\partial T}{\partial \dot{Q}_i} \right) + \frac{\partial U}{\partial Q_i} = P_i \quad (2.7)$$

The Euler-Lagrange equation (2.7) represents an equation where the internal forces are equal to the external forces applied to the system. In order to derive the equations of motion for a mechanical system the total kinetic and potential energy of the system expressed in the generalized coordinates are required.

The total potential energy in the system is equal to summation of the potential energy per element. In this research, the potential energy is equal to the elastic strain energy. Gravitational potential energy is introduced later into the Euler-Lagrange equation.

$$U = \sum_e U_e \quad (2.8)$$

The total kinetic energy in the system is equal to the summation of the kinetic energy per element.

$$T = \sum_e T_e \quad (2.9)$$

For the Euler-Lagrange equation, the potential energy and kinetic energy are partially derived with respect to the generalized coordinates and summed [42].

$$\frac{\partial U}{\partial Q_i} = \sum_e \frac{\partial U_e}{\partial Q_i} \quad (2.10)$$

$$\frac{\partial T}{\partial \dot{Q}_i} = \sum_e \frac{\partial T_e}{\partial \dot{Q}_i} \quad (2.11)$$

The partial derivatives of the potential energy for the bar and beam elements are derived in appendix B and for the damper element in appendix D. In section 2.5, the partial derivatives of the potential energy for the coil spring element and gas-spring element are derived. The partial derivatives of the kinetic energy for all elements are derived in appendix E. All the elements are validated in appendices C and F by comparing simulation results with results from literature or other models.

2.3.1. Gravitation

As mentioned in the previous section, the potential energy formulation does not include the gravitational potential energy. However, gravitational forces are present in the simulations of the SMS and can not be neglected. Therefore, the vector G is defined which represents the weight of the masses. The weight is calculated by multiplying the global mass matrix with an acceleration vector. The acceleration vector has the gravitational acceleration on the indices for the vertical acceleration.

$$\vec{G} = [M]\vec{\ddot{Q}} \quad (2.12)$$

The gravitational forces are introduced in the Euler-Lagrange equation (2.7) by adding the vector to the external forces.

$$\frac{d}{dt} \left(\frac{\partial T}{\partial \dot{Q}_i} \right) + \frac{\partial U}{\partial Q_i} = P_i + G_i \quad (2.13)$$

2.3.2. Rayleigh Damping

Another term introduced to the Euler-Lagrange equation is the Rayleigh's dissipation function. This term only has a value when viscous damping is present within the system. Viscous damping is the resistance of a motion by a force whose magnitude is proportional to the velocity of the motion in the opposite direction [43] [44]. The Rayleigh's dissipation function is defined as [45] [42]

$$R = \frac{1}{2} \vec{\dot{Q}}^T [C] \vec{\dot{Q}} \quad (2.14)$$

Where $[C]$ is the damping matrix. The damping matrix is built similar to the global mass matrix. In this research, viscous damping is implemented in a structure by the use of a damper element. The derivation of the damper element is shown in appendix D. Rayleigh's dissipation function is implemented in the Euler-Lagrange equation (2.13) according to

$$\frac{d}{dt} \left(\frac{\partial T}{\partial \dot{Q}_i} \right) + \frac{\partial R}{\partial \dot{Q}_i} + \frac{\partial U}{\partial Q_i} = P_i + G_i \quad (2.15)$$

In the program, the damper force due to viscous damping is calculated with

$$\vec{R}_F = [C]\vec{\dot{Q}} \quad (2.16)$$

The damper force is implemented in the Euler-Lagrange equation similar to the gravitational force was. Therefore, equation (2.15) changes to

$$\frac{d}{dt} \left(\frac{\partial T}{\partial \dot{Q}_i} \right) + \frac{\partial U}{\partial Q_i} = P_i + G_i - R_i \quad (2.17)$$

2.3.3. Static Analysis

For the static analysis the Euler-Lagrange equation (2.17) simplifies as the derivative with respect to time and the velocity of the motion drops out. The result of this simplification is

$$\frac{\partial U}{\partial Q_i} = P_i + G_i \quad (2.18)$$

By rewriting the equation and bringing all terms to one side, the equilibrium equation is derived.

$$\frac{\partial U}{\partial Q_i} - P_i - G_i = 0 \quad (2.19)$$

Equation (2.19) presents a set of non-linear equations. As the potential energy is expressed in generalized coordinates with N number of nodes, the number of non-linear equations is equal to the number of nodes. If equation (2.19) is not equal to zero, no equilibrium is achieved and a residue (R) exists [46] [47].

$$R_i = \frac{\partial U}{\partial Q_i} - P_i - G_i \quad (2.20)$$

The system of non-linear equations must be solved such that the residue is minimized and in the ideal case becomes zero, because only then equilibrium is achieved. It is important to realise that for some structures the external forces are unknown as the node can be supported as roller, pinned or fixed. The external forces are in that case reaction forces on the support and these are unknown. If a node is supported then the displacement, depending on what type of support is known. Therefore, the residue vector is extended with an conditional vector Q_i^P to account for supported nodes. This vector describes for each node which DOF is free or fixed. If for a displacement direction of a node the prescribed value is equal to zero, then that DOF is fixed and the displacement in that direction is equal to zero.

$$R_i = \begin{cases} \frac{\partial U}{\partial Q_i} - P_i - G_i, & \text{if } Q_i^P \neq 0 \\ Q_i - Q_i^P, & \text{if } Q_i^P = 0 \end{cases} \quad (2.21)$$

The system of non-linear equations can now be solved using a numerical method to find the root of these functions [46] [47]. However, if a large load is applied under which the structure is likely to fail or deform drastically, the numerical iteration will need many iterations and may sometimes even be unable to solve the system of non-linear equations. Therefore, the equilibrium and residue equations are altered by defining the external forces in an alternative way. The external force will be scaled with the scaling factor λ .

$$P_i + G_i = \lambda (P_i + G_i) \quad (2.22)$$

The scale factor has a value between 0% and 100%, the number of increments between these values can be defined by the user. This method of gradually deforming the structure is known as load control [47]. Another method would be displacement control, which has advantages compared to load control in structures that show snap behaviour [47]. The new definition of the external forces substituted in equation (2.21) gives

$$R_i = \begin{cases} \frac{\partial U}{\partial Q_i} - \lambda (P_i + G_i), & \text{if } Q_i^P \neq 0 \\ Q_i - Q_i^P, & \text{if } Q_i^P = 0 \end{cases} \quad (2.23)$$

When a root finding algorithm is applied to the system of non-linear equations, the scale factor starts with the value of zero and each time the root finding algorithm solves the system of non-linear equations, the scale factor is increased and the algorithm continues. The result is that for each scale factor of the force a solution of displacements is known. This process allows the root-finding algorithm to have an increased change of convergence. Another advantage is that this process gives better insight in how a structure deforms under increasing external forces.

2.3.4. Dynamic Analysis

For the dynamic analysis, the total total Lagrangian approach is used. The partial derivatives of the kinetic energy result in a linear relation between the mass matrix and the accelerations.

$$\frac{d}{dt} \left(\frac{\partial T}{\partial \dot{Q}_i} \right) = [M] \ddot{Q} \quad (2.24)$$

Therefore, the Euler-Lagrange equation (2.17) simplifies to

$$[M] \ddot{Q} + \frac{\partial U}{\partial Q_i} = P_i + G_i - R_i \quad (2.25)$$

From this equation, the accelerations can be calculated according to

$$\vec{Q} = [M]^{-1} \left(-\frac{\partial U}{\partial Q_i} + P_i + G_i - R_i \right) \quad (2.26)$$

The equations of motion derived from the Euler-Lagrange equation are a set of second order ODE. For the dynamic analysis, the set is rewritten to two vectors of first order ODE.

$$Y = \begin{pmatrix} \vec{Q}_i \\ \dot{\vec{Q}}_i \end{pmatrix} \quad \text{and} \quad \dot{Y} = \begin{pmatrix} \dot{\vec{Q}}_i \\ \ddot{\vec{Q}}_i \end{pmatrix} \quad (2.27)$$

Where the vector \dot{Y} is the derivative of the vector Y . The advantage of rewriting the equations of motion to two vectors of first order ODE is that the equations only have to be integrated once in order to solve the solution. To solve these differential equations an numerical integration method from the MATLAB toolbox is used. MATLAB offers various ODE solvers for diverse problems. In appendix F, the various solvers are discussed and an appropriate ODE solver is chosen for the dynamic simulations.

When the accelerations are calculated using equation (2.26), these can not be simply substituted in the vector \dot{Y} . Similar as with the static analysis, the boundary conditions due to any supports must be implemented. This is done with the same conditional vector Q_i^P as in the static analysis. If for a displacement direction the prescribed value of the conditional vector is equal to zero, then the acceleration in that direction should be zero as well. The process should be performed every time step.

$$\ddot{Q}_i = \begin{cases} \ddot{Q}_i, & \text{if } Q_i^P \neq 0 \\ 0, & \text{if } Q_i^P = 0 \end{cases} \quad (2.28)$$

The same process to implement the boundary conditions can be used to apply prescribed accelerations to any displacement direction. A prescribed acceleration could for example be an excitation pulse applied to somewhere on the structure. In that case, the calculated acceleration should be replaced with the prescribed acceleration for each time step.

2.4. Mechanical Shock Mitigation

Prior research [17] [11] [10] [16] [26] has shown that improper design features of a SMS can lead to poor performance and in some cases even to shock amplification instead of shock mitigation. The causes of shock amplification are the phenomena of bottoming out and dynamic amplification. These phenomena should be prevented as they can lead to an increase of the probability of injuries and adverse health effects.

First, the phenomenon of bottoming out should be prevented. Bottoming out is the result of insufficient stroke length of the spring-damper combination and is primarily a function of the wave impact severity force [26]. During severe wave impacts, the stroke of the spring-damper combination is fully used and metal-to-metal contact will occur. This sudden mechanical shock in the suspension leads to seat level acceleration spikes, which can exceed the acceleration peak of the wave impact. The larger the force of the wave impact, the larger the required stroke of spring-damper combination is [10] [26].

Second, the phenomenon of dynamic amplification should be avoided. In this context, dynamic amplification means that the suspension will amplify the shock instead of mitigating it without the occurrence of bottoming [26]. Dynamic amplification is comparable to the resonance effect for vibrations where the response amplitude overshoots the input amplitude, but it is referred to as dynamic amplification for single shocks. The amplification is the result of the long duration of the input shock pulse relative to the natural period of the suspension design.

In the following sections, both of these phenomena will be explained and demonstrated with simulations of

a single DOF mass-spring-damper model which represents a SMS suspension. The model consists of two different point masses, a coil spring element and a damper element. Such a model is described in the first section of appendix F. For the simulations a half-sine pulse is used to represent the excitation pulse of wave impact. For now, it is assumed that this approximation is valid. The validity of this approximation will be investigated later in the report.

2.4.1. Bottoming Out

To demonstrate the effect of bottoming, the coil-spring is modelled such that when it reaches an extreme length the stiffness instantaneously increases. This method has been used by prior research to investigate the effect of bottoming [10] [16].

In figure 2.1, the deck level acceleration and seat level acceleration response for the model are shown. The seat level acceleration shows a large positive acceleration spike of approximately 21 [g] that exceeds the deck level acceleration with an acceleration peak of 4 [g]. The acceleration spike is the result of metal-to-metal contact indicating that the spring bottoms out. The acceleration spikes from bottoming are not associated with the wave impact force, but they are the result of relative motion and contact between the seat and the deck [26]. To reduce the probability of bottoming, the spring travel, spring stiffness and damping should be increased [10]. However, the increase of these parameters is not necessarily beneficial for the shock mitigating characteristics [9].

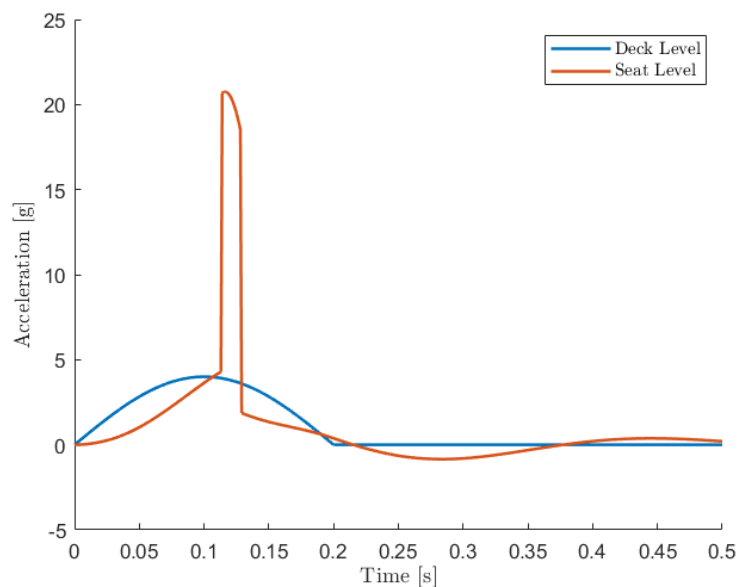


Figure 2.1: Example of the phenomenon of bottoming out for an arbitrary SMS design

2.4.2. Dynamic Amplification

For the demonstration of dynamic amplification, bottoming is not modelled in the coil spring element. In figure 2.2, the deck level acceleration and the seat level acceleration responses of two suspension designs are shown. The suspension designs have a different coil spring stiffness and damping coefficient resulting in different natural frequencies. The critical damping ratio of both suspensions was 25%. The figure shows that the response of both designs to the same deck level acceleration results in different seat level accelerations. The suspension with a natural frequency of 1.5 [Hz] successfully mitigates the half-sine pulse shock, while the suspension with a natural frequency of 2.5 [Hz] seems to amplify the peak acceleration without any evidence of bottoming. These results illustrate the phenomenon known as dynamic amplification.

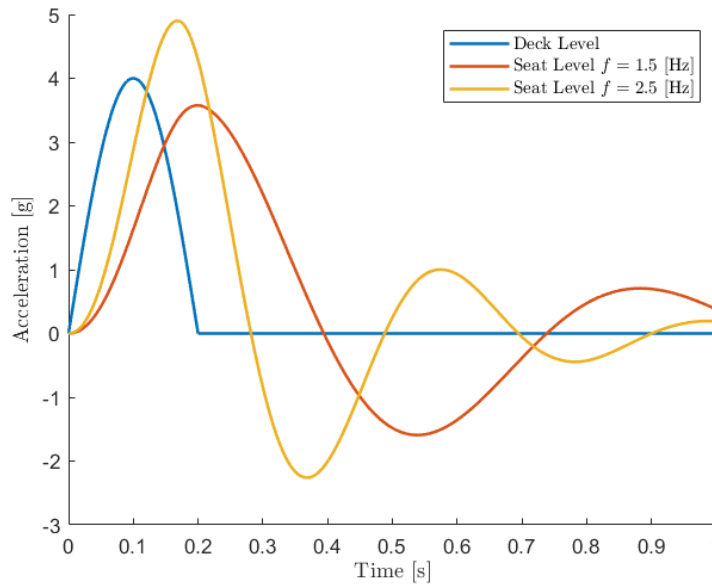


Figure 2.2: Example of the phenomenon of dynamic amplification for an arbitrary SMS design

In order to avoid dynamic amplification, the ratio of the shock pulse duration over the period of the natural frequency of the suspension design should result in a transmissibility factor which is less than one. The Transmissibility Factor (TF) is defined as the seat level peak acceleration response over the deck level peak acceleration according to

$$\text{TF} = \frac{\max(a_s(t))}{\max(a_d(t))} \quad (2.29)$$

Where $a_s(t)$ is the seat level acceleration and $a_d(t)$ the deck level acceleration. When the transmissibility factor exceeds a value of one, it is referred to as a pulse-period mismatch [26] and the acceleration levels are amplified. By analysing the natural frequencies of the suspension design and the periods of the wave impacts, it can be assessed whether the seat design falls within the mitigation/attenuation region (transmissibility < 1) or in the amplification region (transmissibility > 1). Another non-dimensional factor R is defined to compare the periods of the shock pulses and the periods of the natural frequencies. The factor R is defined as

$$R = \frac{T}{T_n} \quad (2.30)$$

Where T is the period of the excitation pulse and T_n is the period of the natural frequency of the suspension design. As the excitation pulse is a half-sine pulse, the duration of the half-sine is used as the period [26].

Based on multiple simulations with variable coil spring stiffnesses and damping coefficients, the shock transmissibility curves were derived for a half-sine pulse with an peak acceleration of 4 [g] and a duration of 200 [ms]. The natural frequency of the model varied from 0.1 [Hz] to 20.0 [Hz]. In figures 2.3 and 2.4, the shock transmissibility curves for the mass spring damper model with critical damping ratios ranging from 0 % to 125% are shown. The results are in agreement with literature and prior research [43] [48] [16] [26].

The figures 2.3 and 2.4 show that for an factor R value of approximately 0.27 [-] to 0.4 [-] the shock TF is lesser or equal to unity. These values of factor R correspond to models with an natural frequency up to approximately 1.35 [Hz] for 0% critical damping and 2.0 [Hz] for 125 % critical damping. These results indicate that it is desirable to have a suspension design with low natural frequencies for the mitigation of this specific shock pulse. The figures also show that the critical damping ratio has a significant influence of the

response of models with a natural frequencies above 4.0 [Hz]. The results indicate the critically damped or overdamped models do not amplify the shock pulse much compared to underdamped models as the shock TF is approximately equal to unity. These observations are important to consider when designing a SMS suspension. Note that the discussed results are based on a half-sine excitation pulse and may differ from other forms of excitation pulses.

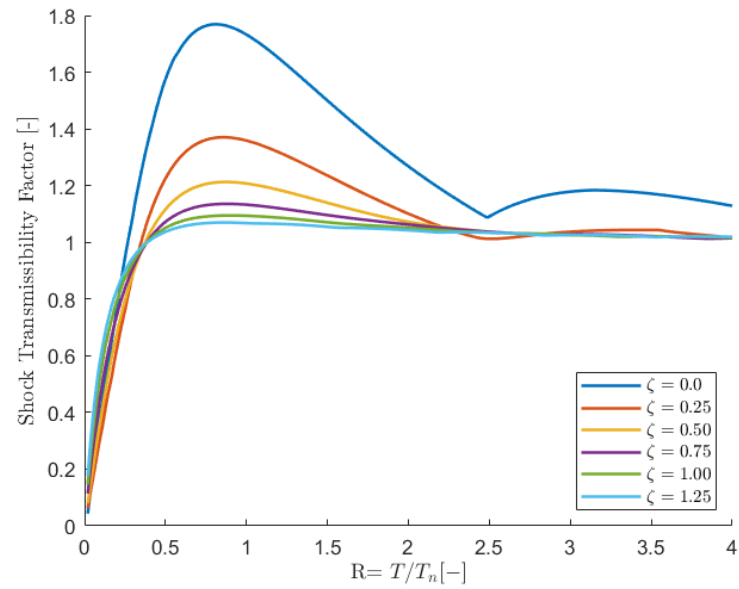


Figure 2.3: Shock transmissibility curve for a half-sine excitation pulse

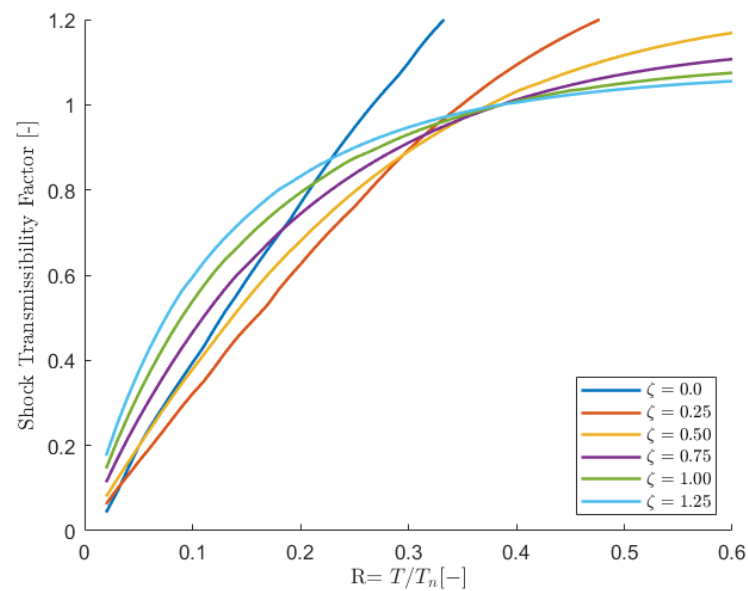


Figure 2.4: Zoomed in shock transmissibility curve for a half-sine excitation pulse

2.5. Non-Linear Springs

In this section, the internal forces of the coil spring element and the gas-spring element are derived from the potential energy formulations.

2.5.1. Coil Spring Element

A coil spring element stores mechanical energy and exerts a force on the nodes in the opposite direction of the elongation of the coil spring. The spring force F is approximately proportional with the elongation ΔL , except for very large compression or extension.

$$F = -kx \quad (2.31)$$

Where k is the coil spring stiffness. The coil spring stiffness is regarded as a constant value for a specific coil spring. The work done when extending or compressing the spring over a distance dx is

$$dW = Fdx \quad (2.32)$$

The total work done by the spring or energy stored in the spring is calculated by integrating the expression.

$$W = U_e = \int_{L_0}^{L'} Fdx = \frac{1}{2}k\Delta L^2 \quad (2.33)$$

Where ΔL is the elongation of the coil spring. The elongation of the coil spring is defined as

$$\Delta L = L' - L_0 \quad (2.34)$$

with L' is the deformed length and L_0 is the undeformed length. The deformed length of the coil spring is calculated with the horizontal and vertical displacements.

$$L' = \sqrt{(L + u_2 - u_1)^2 + (v_2 - v_1)^2} \quad (2.35)$$

The internal forces of the of coil spring element in the local coordinate system are calculated according to

$$\frac{\partial U_e}{\partial q_i} = k\Delta L \frac{\partial \Delta L}{q_i} \quad (2.36)$$

Where q is has the form of (u_1, v_1, u_2, v_2) . The internal forces in the local coordinate system are transformed to internal forces in the global coordinate system according to (B.44). Subsequently, these forces are summed for the complete system according to (B.45).

Bottoming of the Coil Spring

The coil spring force is approximately proportional with the elongation except for large compression or extension. This effect is also observed in the analyses of the SMS and known as the effect of bottoming. When the coil spring reaches its minimum or maximum length, the coil spring stiffness increase greatly as the stroke is fully used. This change in coil spring stiffness is not instantaneous, but near the limits of the stroke the stiffness already increases. Therefore, a function is derived in order to mimic this behaviour and transition the stiffness between two values.

Suppose that the transition function is

$$k(L) = a_0 + a_1L + a_2L^2 + a_3L^3 \quad (2.37)$$

With its derivative

$$\frac{dk}{dL} = a_1 + 2a_2L + 3a_3L^2 \quad (2.38)$$

Where L is the current length. The coefficients in the function can be determined with boundary conditions.

In the case of maximum compression, the minimum length L_{min} and the spring stiffness is k_{min} . At the length where the transition of the coil spring stiffness starts L_R , the coil spring has its normal stiffness k_0 . At both lengths, the gradient should be zero as the beyond these lengths the stiffness is constant.

$$L = \begin{cases} L_{min}, & k_{min} = a_0 + a_1 L_{min} + a_2 L_{min}^2 + a_3 L_{min}^3 \\ L_{min}, & 0 = a_1 + 2a_2 L_{min} + 3a_3 L_{min}^2 \\ L_R, & k_R = a_0 + a_1 L_R + a_2 L_R^2 + a_3 L_R^3 \\ L_R, & 0 = a_1 + 2a_2 L_R + 3a_3 L_R^2 \end{cases} \quad (2.39)$$

The length of the coil spring at which the stiffness starts transitioning is defined as

$$L_R = L_{min} + \delta(L_0 - L_{min}) \quad (2.40)$$

Where the δ is the ratio and can be given a value to represent realistic behaviour. Using the boundary conditions, the coefficients a_0, a_1, a_2 and a_3 can be determined. The coefficients are

$$\begin{aligned} a_0 &= \frac{3k_{min}L_{min}L_R^2 - L_R^3k_{min} + L_{min}^3k_0 - 3L_{min}^2L_Rk_0}{(L_{min} - L_R)^3} \\ a_1 &= \frac{6L_RL_{min}(k_0 - k_{min})}{(L_{min} - L_R)^3} \\ a_2 &= \frac{-3(L_{min} + L_R)(k_0 - k_{min})}{(L_{min} - L_R)^3} \\ a_3 &= \frac{2(k_0 - k_{min})}{(L_{min} - L_R)^3} \end{aligned} \quad (2.41)$$

In the case of the maximum elongation another transition function can be derived with the transition length defined as

$$L_R = L_{max} - \delta(L_{max} - L_0) \quad (2.42)$$

With the deformed length of the coil spring, the stiffness can be determined according to

$$k = \begin{cases} k_{min}, & \text{if } L \leq L_{min} \\ k(L), & \text{if } L_{min} < L < L_R \\ k_{max}, & \text{if } L \geq L_{max} \\ k(L), & \text{if } L_R < L < L_{max} \\ k_0, & \text{otherwise} \end{cases} \quad (2.43)$$

In figure 2.5 and figure 2.6, the discontinuous and continuous stiffness and spring force as function of the length are shown. In the figures the effect of bottoming is visible around spring lengths of $L = 0.25$ [m] and $L = 0.75$ [m]. At these length, the spring stiffness and spring force increases instantaneously. With the transition function, this discontinuity is removed and the function transitions more smoothly. All parameters for the transitional functions can be freely chosen within the program and varied per coil spring element.

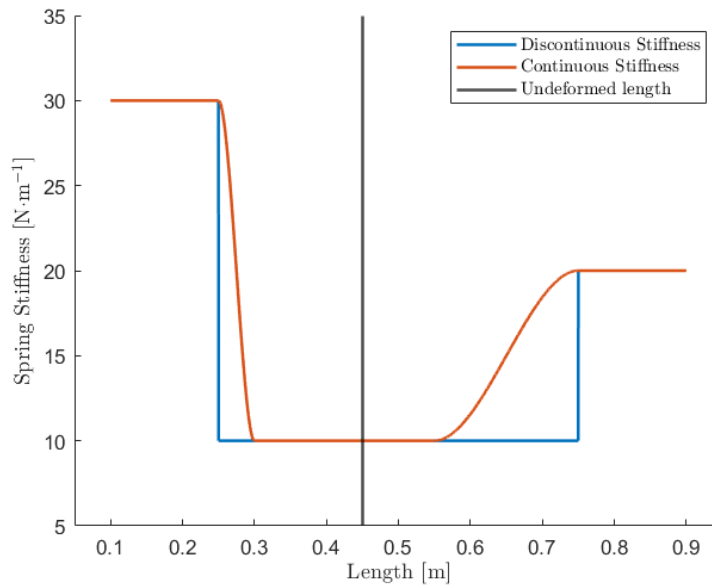


Figure 2.5: Coil spring element stiffness as function of the length

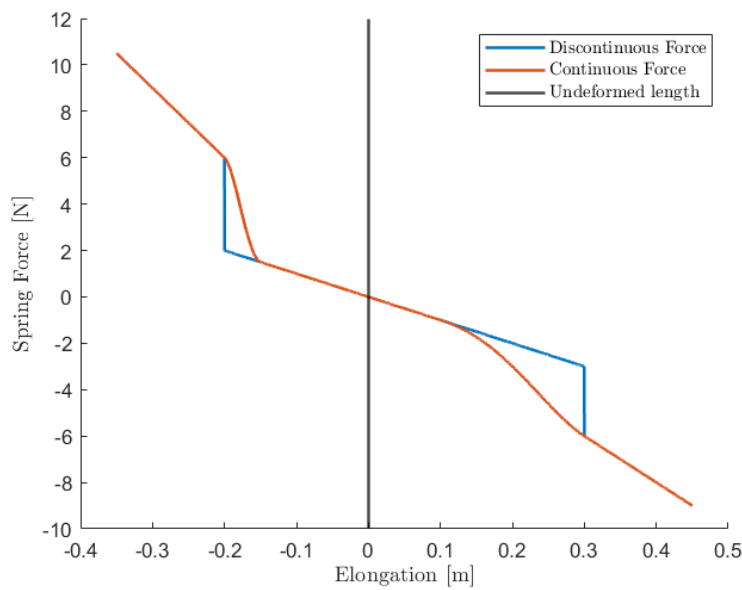


Figure 2.6: Coil spring element force-displacement curve

2.5.2. Gas-Spring Element

The gas-spring is a sealed cylinder containing pressurized gas. When an axial loading is applied to the gas-spring, the gas is compressed. In this research, the initial position of the piston is in the top position.

According to the first law of thermodynamics for a closed system, the internal energy (U) of a system is the sum of the energy (Q) supplied to the system and the work (W) done by the system on its surroundings.

$$dU = dQ - dW \quad (2.44)$$

The thermodynamic process of the gas-spring element is assumed to be an isentropic process. An isentropic process is both adiabatic and reversible. Adiabatic means that there is no heat transfer between the

system and its surroundings. Reversible work indicates that the work transferred by the system and the surroundings is frictionless. The reversible work is defined as

$$W = pdV \quad (2.45)$$

where p is the pressure and V is the volume. Then, the first law of thermodynamics (2.44) simplifies to

$$dU = -pdV \quad (2.46)$$

Assuming that the gas-spring contains an ideal gas, then the ideal gas law applies.

$$pV = RT \quad (2.47)$$

Where R is the gas constant and T is the absolute temperature of the gas. For an ideal gas, the change in internal energy and enthalpy are only a function of the specific heat at constant pressure, the specific heat at constant volume and the temperature [49].

$$dU = C_v(T)dT \quad (2.48)$$

$$dH = C_p(T)dT \quad (2.49)$$

The enthalpy (H) of the system is defined as

$$H = U + pV \quad (2.50)$$

Substituting the ideal gas law (2.47) gives

$$H = U + RT \quad (2.51)$$

Then, the change in enthalpy is

$$dH = dU + RdT \quad (2.52)$$

With the relations for change of the internal energy (2.48) and enthalpy (2.49), the equation (2.52) gives Mayer's relation which describes a relation between the specific heat at constant pressure and the specific heat at constant volume.

$$C_p(T) - C_v(T) = R \quad (2.53)$$

The heat capacity ratio is the ratio of the heat capacity at constant pressure and the heat capacity at constant volume. The equation for the heat capacity ratio is [49]

$$\gamma = \frac{H}{U} = \frac{C_p(T)}{C_v(T)} \quad (2.54)$$

In addition, it is assumed that the gas within the gas-spring is a calorically perfect gas. For an calorically perfect gas the heat capacity at constant pressure and the heat capacity at constant volume are constant for all temperatures. As a result the heat capacity ratio is constant.

Next, a pressure-volume relation for a isentropic process is derived. The derivative of the ideal gas law with respect to the temperature is

$$p \frac{dV}{dT} + V \frac{dp}{dT} = R \quad (2.55)$$

Rewriting this equation to

$$pdV + Vdp = RdT \quad (2.56)$$

Combining the equations (2.46) and (2.48) gives

$$-pdV = C_v dT \quad (2.57)$$

$$dT = \frac{-pdV}{C_v} \quad (2.58)$$

The result combined with equation (2.56) results in

$$pdV + Vdp = -\frac{R}{C_v}pdV \quad (2.59)$$

Substituting Mayer's relation (2.53) gives

$$pdV + Vdp = \left(\frac{C_v - C_p}{C_v}\right)pdV = (1 - \gamma)pdV \quad (2.60)$$

Simplifying and integrating the equation according to

$$\int \frac{1}{P}dP = -\gamma \int \frac{1}{V}dV \quad (2.61)$$

The integrals result in the natural logarithms.

$$\ln P + \gamma \ln V = \text{constant} \quad (2.62)$$

From which follows that for an isentropic process the following relation holds between the pressure and volume.

$$pV^\gamma = \text{constant} \quad (2.63)$$

The assumptions used for this derivation is that the process is adiabatic and reversible. In addition, the gas in the gas-spring is assumed to be a perfect gas.

The thermodynamic process is considered to be adiabatic, because when the gas-spring in the suspension of a SMS is compressed it occurs in such a short time frame that the gas-spring is unable to transfer much heat to its surroundings. If the compression would take a much longer period of time, then it would be able to transfer heat and the assumption of an isothermal process would be a better option.

The work done by the gas-spring is considered to be reversible, which means that the gas-spring is frictionless and does not dissipate energy. This assumption is considered to be valid for this research as the purpose of the gas-spring to deliver an opposing force against any motion and not to dissipate energy. As for the dissipation of energy, the damper element is implemented based on viscous damping.

A calorically perfect gas is a gas that obeys the ideal gas law and the specific heats at constant volume and pressure are constant and independent of temperature. This assumption is made to simplify the element. The value of the heat capacity ratio can be defined by the user, but is dependent of the gas present in the cylinder.

Non-Linear Gas-Spring

Figure 2.7, shows a gas-spring element with two nodal points in the global coordinate system.

The maximum and minimum length of the gas-spring are calculated according to

$$L_{max} = L_{pr} + L_0 + L_{br} \quad (2.64)$$

$$L_{min} = L_{pr} + L_{br} \quad (2.65)$$

Where L_{pr} is the length of the piston rod, L_0 is the total stroke and L_{br} is the length of the bottom rod. Regarding the geometry of the gas-spring, the following assumptions are made: $L_0 \leq L_{pr}$, $0 \leq L_{br}$, $L' \leq L_{max}$ and $L_s \leq L_0$. The length of the gas-spring is calculated with

$$L' = \sqrt{(L + u_2 - u_1)^2 + (v_2 - v_1)^2} \quad (2.66)$$

From this length, the remaining stroke is expressed as

$$L_s = L' - L_{pr} - L_{br} \quad (2.67)$$

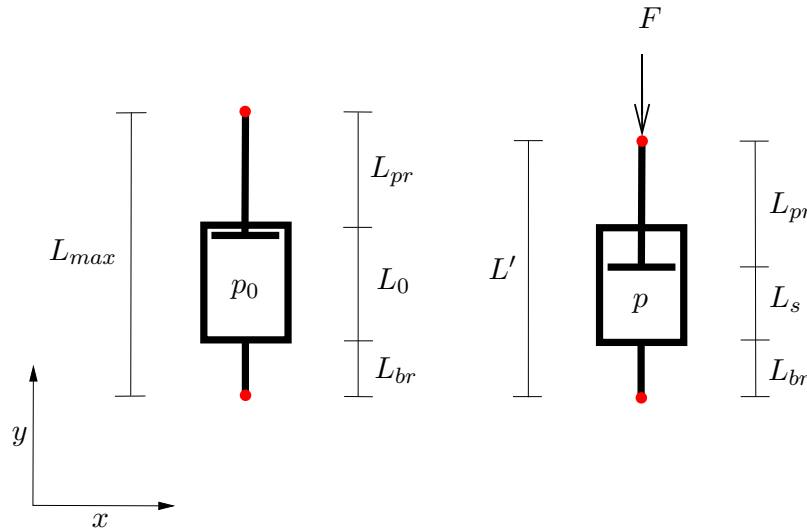


Figure 2.7: Gas-spring element in the global coordinate system

The initial volume in the gas cylinder is

$$V_0 = A_0 L_0 \quad (2.68)$$

Where A_0 is the cross-section of the cylinder. The remaining volume in time when compressed is

$$V = A_0 L_s \quad (2.69)$$

With the equation for an isentropic process (2.63) the pressure and force in time can be calculated and expressed as

$$p = p_0 \frac{V_0^\gamma}{V^\gamma} \quad (2.70)$$

$$F = F_0 \frac{L_0^\gamma}{L^\gamma} \quad (2.71)$$

In thermodynamics, the work is defined positive when the gas exerts force on its surroundings. However, in the application of the FEM program when the gas-spring is compressed energy is stored in the gas. Thus, when the gas exerts a force on its surroundings it reduces the potential energy of the gas.

$$U_e = -W \quad (2.72)$$

The potential energy stored in the gas-spring can be calculated according to the following equations.

$$U_e = - \int_{V_0}^V p dV = - \int_{V_0}^V p_0 \frac{V_0^\gamma}{V^\gamma} dV \quad (2.73)$$

$$U_e = - \int_{L_0}^{L_s} F dL = - \int_{L_0}^{L_s} F_0 \frac{L_0^\gamma}{L^\gamma} dL \quad (2.74)$$

Both equations produce the same result, which can be simplified to

$$U_e = - \frac{p_0 A_0 L_0^\gamma}{1-\gamma} (L_s^{1-\gamma} - L_0^{1-\gamma}) \quad (2.75)$$

The internal forces of the gas-spring in the local coordinate system are calculated according to

$$\frac{\partial U_e}{\partial q} = -p_0 A_0 L_0^\gamma L_s^{-\gamma} \frac{\partial L_s}{\partial q} \quad (2.76)$$

Where q is has the form of (u_1, v_1, u_2, v_2) . From the equation of the gas spring internal force it is visible that if $L_0 = L_s$, the gas-spring is over pressurized which generates an internal force equal to $p_0 A_0$. An external force applied to the gas-spring must overcome this force in order to compress the gas-spring.

Limits of the Gas-Spring

Similar as with the effect of bottoming of the coil spring element, the gas-spring element has limits which must be implemented in the FEM program. The limits shall be discussed before the solution is presented.

In contrast to the coil spring element, the gas-spring element is theoretically unable to bottom. This can be concluded based on a standard p-V diagram of a gas cylinder. As the volume of the cylinder decreases when compressed, the pressure in the cylinder starts increasing. When the volume in the cylinder approaches a value of zero the pressure inside will increase to infinite and show asymptotic behaviour. Therefore, no additional routine is implemented for bottoming in the case of compression.

As mentioned in the previous section, the initial position of the piston is in the top position. Thus when a tensile force is applied to the gas-spring, the piston is unable to move any further. In the case of tensile loading, it is assumed that the piston rod will deform. This may happen during dynamic simulations and it is similar to bottoming as the stiffness of the element increases instantaneously. Therefore, a routine will be implemented which will mimic this behaviour.

Another problem which arises when implementing equation (2.76). As the gas-spring is over pressurized, the applied external compressive load must overcome the initial force of the pressurized gas in order to compress the cylinder. This effect poses a problem for the numerical methods as it forms a discontinuity in the force-displacement curve.

The solution for above mentioned issues is to combine a custom coil-spring element with an adapted gas-spring element. The elements are modelled such that the behaviour of the gas-spring element is dominated by the coil spring element when $L_0 \leq L_s$ and is dominated by the gas-spring when $L_s \leq L_0$.

Gas-Spring Force

The force in the gas-spring is

$$\frac{\partial W}{\partial q} = -p_0 A_0 L_0^\gamma L_s^{-\gamma} \quad (2.77)$$

Two new lengths are defined as

$$\begin{aligned} L_{-\delta} &= L_0 - \delta L_0 \\ L_{+\delta} &= L_0 + \delta L_0 \end{aligned} \quad (2.78)$$

Where δ is ratio. A transition function is defined which describes the gas-spring force as function of the length.

$$F(L_s) = a_0 + a_1 L_s + a_2 L_s^2 + a_3 L_s^3 \quad (2.79)$$

With its derivative

$$\frac{dF(L_s)}{dL_s} = F'(L_s) = a_1 + 2a_2 L_s + 3a_3 L_s^2 \quad (2.80)$$

The coefficients of the transitional function can be determined with the boundary conditions. At $L_s = L_{+\delta}$, the force and the gradient should be zero. At $L_s = L_{-\delta}$, the force is and gradient are equal to

$$F(L_{-\delta}) = p_0 A_0 L_0^\gamma L_{-\delta}^{-\gamma} \quad (2.81)$$

$$F'(L_{-\delta}) = -\gamma p_0 A_0 L_0^\gamma L_{-\delta}^{-\gamma-1} \quad (2.82)$$

Using the boundary conditions, the coefficients are solved as

$$\begin{aligned}
 a_0 &= \frac{(L_{-\delta}F' - F)L_{+\delta}^3 + (3FL_{-\delta} - F'L_{-\delta}^2)L_{+\delta}^2}{(L_{-\delta} - L_{+\delta})^3} \\
 a_1 &= \frac{(2L_{-\delta}^2F' - 6FL_{-\delta})L_{+\delta} - F'L_{+\delta}^3 - F'L_{-\delta}L_{+\delta}^2}{(L_{-\delta} - L_{+\delta})^3} \\
 a_2 &= \frac{2L_{+\delta}^2F' + (3F - F'L_{-\delta})L_{+\delta} - F'L_{-\delta}^2 + 3FL_{-\delta}}{(L_{-\delta} - L_{+\delta})^3} \\
 a_3 &= \frac{F'(L_{-\delta} - L_{+\delta}) - 2F}{(L_{-\delta} - L_{+\delta})^3}
 \end{aligned} \tag{2.83}$$

The gas-spring force (F_g) as a function of the stroke length is

$$F_g = \begin{cases} 0, & \text{if } L_{+\delta} \leq L_s \\ F(L_s), & \text{if } L_{-\delta} < L_s < L_{+\delta} \\ \frac{\partial W}{\partial q}, & \text{if } L_s \leq L_{-\delta} \end{cases} \tag{2.84}$$

Coil Spring Stiffness

The spring stiffness as a function of the deformed length is derived similar to the derivation in section 2.5.1.

$$k(L') = \begin{cases} 0, & \text{if } L' \leq L_{max} \\ k(L'), & \text{if } L_{max} < L' < L_{+\delta} \\ k_+, & \text{if } L_{+\delta} \leq L' \end{cases} \tag{2.85}$$

where $L_{+\delta} = L_{max} + \delta L_{max}$.

Combining the coil spring and gas-spring

The internal forces of the gas-spring are calculated according to

$$\frac{\partial U_g}{\partial q} = F_g \frac{\partial L_s}{\partial q} \tag{2.86}$$

and the internal forces of the coil spring are calculated according to

$$\frac{\partial U_c}{\partial q} = k\Delta L \frac{\partial \Delta L}{q} \tag{2.87}$$

The total internal forces of the gas-spring element are a combination.

$$\frac{\partial U_e}{\partial q} = \frac{\partial U_g}{\partial q} + \frac{\partial U_c}{\partial q} \tag{2.88}$$

The internal forces in the local coordinate system are transformed to internal forces in the global coordinate system according to (B.44). Subsequently, these forces are summed for the complete system according to (B.45).

In figure 2.8, the force-displacement curve of the gas spring element is shown. In the figure, it is clear that when a tensile force is applied to the gas-spring it has a high stiffness and only small resulting deformations. When a compressive force is applied, the element will deform according to $pV^\gamma = \text{constant}$ after the threshold of initial force is reached.

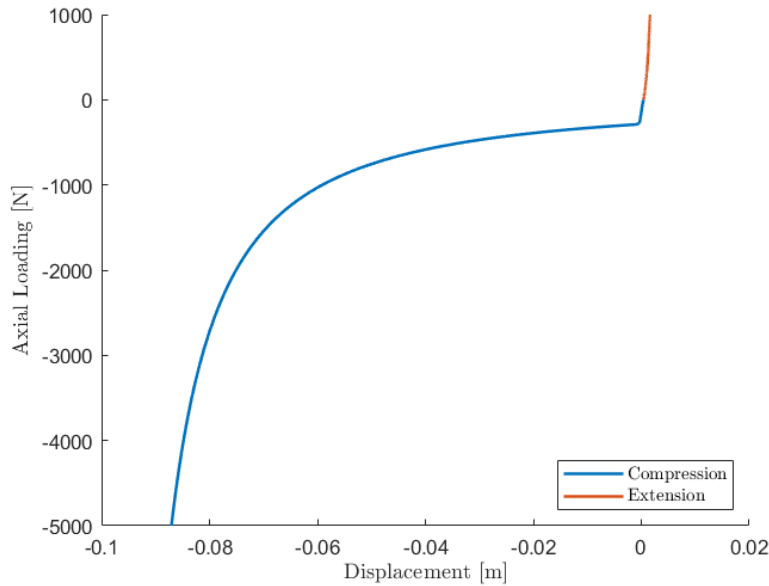


Figure 2.8: Gas-spring element force-displacement curve

For this example, the following parameters were used for the elements. The pressure inside the cylinder is $p_0 = 1.47 \cdot 10^5$ [Pa]. The cross-sectional area is $A_0 = 0.002$ [m²] and the initial stroke length is $L_0 = 0.1$ [m]. For the heat capacity ratio an value of $\gamma = 1.4$ [-] is used, which is the value for standard air [49]. The external load is applied in the axial direction in the range of $F = -5000$ to $F = 1000$ [N]. The ratios used to describe the transitional functions is $\delta = 0.005$ [m] and the stiffness of the coil spring is $K = 1.0 \cdot 10^5$ [N·m⁻¹].

3

Injuries & Adverse Health Effects

In this chapter, the relation between the injuries and adverse health effects of HSC operators and the physical loads from repetitive wave impacts is discussed. First, the reported injuries by the crew and passengers of HSC are presented. Then, the current directives on exposure to WBV and RS are discussed. Following from these directives, various evaluation methods and injury models are reviewed. Finally, the suitability of the evaluation methods and injury models is discussed.

3.1. Resulting Injuries¹

The crew on board of HSC are exposed to a great variety of health risks resulting from the physical loads experienced by the crew [11]. The physical loads are categorized as WBV and RS and have the possibility to cause various physical injuries. The resulting injuries are both acute and chronic [21] as these injuries reduce both the short-term and the long-term effectiveness of the personnel [12] [20]. Additionally, the RS are experienced as physically exhausting [50] [16]. Both in the research of Stouten [16] and Vredeveltdt [10], the RS are estimated to be more dangerous and are more likely to result in injuries and adverse health effects compared to WBV.

In research conducted by the United States Navy [12], special boat operators of HSC reported injuries and adverse health effects as a result of the working conditions on HSC. A self-report survey of injuries was administered to a total of 154 participants in order to obtain an overview of the resulting injuries. The mean age of the participants was 32.0 ± 5.9 years of whom the mean time of service was 12.0 ± 5.5 years of which the mean time as HSC operator was 4.7 ± 3.0 years. The mean body weight of the participants was 85.2 ± 10.3 [kg]. Of all the participants, 95 participants reported one injury, 11 participants reported two injuries and 5 participants reported three injuries.

The results of this survey are shown in table 3.1. In the table the number of injuries are shown per anatomical location. The column of 'sought medical attention' shows the number of persons that sought medical care of the total number of persons to whom the question was asked. For convenience, the results are also shown as a percentage.

Table 3.1 shows that the most common injuries locations are to the lower back, knees and shoulders. This observation is also confirmed by other studies [21] [22] [17] [11] [10]. The most common injury type was sprain/strain 49.3 %, disc problems 7.9 % and trauma 7.9 %. A disadvantage of the results shown in the table is that it gives no indication what type of injury is the most common for each anatomical location [11].

¹This section is based on the literature study [27]

Table 3.1: Survey results of self-reported injuries [11] [12]

Anatomical Location	No. Injuries	Sought Medical Attention	
Head	3	3 (3)	(100 %)
Neck and Upper Back	9	6 (9)	(67 %)
Shoulder	21	15 (20)	(75 %)
Elbow	2	1 (2)	(50 %)
Wrist	1	1 (1)	(100 %)
Hand	1	1(1)	(100 %)
Trunk	2	1(1)	(100 %)
Lower Back	50	40 (48)	(83 %)
Hip / Buttocks	6	6 (6)	(100 %)
Thigh	2	1 (2)	(50 %)
Knee	32	24 (32)	(75 %)
Leg	7	5 (7)	(71 %)
Ankle	10	9 (10)	(90 %)
Foot	3	1 (2)	(50 %)

All the injuries from the participants combined represented 722 years of service on HSC and exposure to WBV and RS. The injuries resulted in 145 days of hospitalization, 929 days of sick leave, 4223 days of limited duty, 4218 days of limited performance, 2294 days lost of mission training time and 4089 days lost of physical conditioning time [12]. The hospitalization rate for HSC operators was calculated to be 2687 per 100000 person-years of exposure. This rate was compared to the at the time overall US Navy hospitalization rate for similar injuries, which was only 479 per 100000 person-years of exposure. Based on the results, the authors concluded that the operators of HSC are at a greater than average risk to injuries and adverse health effects.

Several studies have shown that the physical loads also result in reduced physical performance, damage of the muscles and fatigue [51] [19]. In research [19], it was shown that the physical performance of passengers on Rigid Inflatable Boats (RIB) was reduced by up to 26 % after a 3 hour high-speed sea transit in rough sea conditions with unsuspended seats. The results were obtained by measuring the performance by numerous tests such as a shuttle run, push-ups and vertical jumps. Additional medical tests showed that the creatine kinase activity had increased after the transit, which indicated that the muscle were damaged [19]. This observation has also been made in previous large-scale tests [21]. In the literature [21] [52] [19], it was argued that the muscle damage is a result of the passengers trying to compensate for the physical loads they are exposed to by contracting their muscles. Adverse health effects, such as muscle damage and fatigue are suspected to even further increase the probabilities of both acute and chronic injuries due to a prolonged exposure to WBV and RS [11].

Unfortunately, the cause-effect relationship or correlation of the exposure to WBV and RS to the resulting injuries and adverse health effects is not yet clear and difficult to define [21] [20] [33] [34] [35] [11]. Nonetheless, in existing standards and directives, various evaluation methods are recommended which include allowable limits. These documents will be discussed in this chapter.

3.2. Human Tolerance to Shocks

Before existing standards and directives are reviewed, it is important to study the shock pulse key parameters and their influence on the human tolerance to shocks. In prior research by the National Space and Aeronautics Administration [2], five key parameters are identified for quantifying shock pulse severity [26].

In this research the human tolerance to rapidly applied accelerations was investigated using various test methods to simulate different acceleration pulses. The authors concluded that the human tolerance to rapidly applied accelerations depends on

- The magnitude of the acceleration pulse
- The duration of the acceleration pulse
- The shape of the acceleration pulse
- The direction in which the acceleration force is applied
- The change in acceleration with respect to time (also known as jerk)

A HSC experiences accelerations and motions in all six DOF. However, the largest recorded deck lever accelerations are always in the vertical direction [26]. Therefore, a first-step approach to ensure that a SMS design performs as required is to analyse its shock mitigating characteristics in the vertical direction. The magnitude of a shock pulse does not define the human tolerance to shocks, nor does the acceleration cause injury [26]. Stress resulting from the acceleration causes injury. Therefore, both the acceleration magnitude and the pulse duration should be taken into account when calculating the resulting stress in a specific part of the human body [2] [26].

Another relevant parameter for the human tolerance to shocks could be the natural frequency of the human body. The resonant frequency of a person in the seated posture is typically around 5 [Hz] [53] [13] and for a standing person around 12 [Hz] [54]. The natural frequency of a person in either a seated or standing posture has no significant relationship with the mass [55] [54] or height [54]. However, the tension of the muscles can have a significant influence of the resonant frequency [55]. It is unknown whether the natural frequencies of the human body (in particular of the spine) should be avoided. Some literature argues that there is no scientific proof that a single impact is able to start vibration of the spine [34] [35]. Even the repetitive nature of the wave impacts is not able to cause vibrations as these occur only approximately once per second [34] [35]. Other literature indicates that the resonant frequency of the body should be avoided, but provides no arguments or references on the reason why [13] [17]. No literature with convincing arguments on the importance of avoiding the natural frequencies of the human body and the influence on the human tolerance to shocks has been found.

3.3. Directives on Exposure to WBV & RS²

In literature, several standards for the human exposure to WBV and RS are found. The most commonly used and referenced are; ISO 2631 Part 1 [31], ISO 2631 Part 5 [1], European Union Directive 2002/44/EC [56], Annex 10 of 2000 HSC code, International Code for Safety on HSC [57] and Maritime Guidance Note 436 from the UK Maritime and Coastguard Agency [58] [34] [35]. Especially, the ISO 2631 Part 1 and Part 5 are widely referenced as these present methods and limits on the evaluation of the effects of WBV and RS and determine the probability of adverse health effects [56] [59] [21] [60] [61] [20] [62] [63] [33] [17] [5] [24] [23] [11] [10]. The standards are based on different methods in order to reduce or evaluate the adverse health effects resulting from the WBV and RS. However, only few directives describe limits of exposure to WBV and RS. A reason could be that it is difficult to formulate generally applicable tolerance limits as the tolerance level is heavily dependant on the limits and reaction of a person's body [10]. Another reason could be that is difficult to experimentally determine these tolerance levels as results from experiments with animals or crash dummy's are not one-to-one translatable with the human body [10].

The evaluation methods of ISO 2631 Part 1 and ISO 2631 Part 5 will be described in depth in the coming sections as these standards give extensive methods to evaluate WBV and RS in relation to the probability of adverse health effects. The other commonly referenced directives are briefly discussed below.

²This section is based on the literature study [27]

European Union Directive 2002/44/EC

The 2002/44/EC [56] is included in the law of all EU countries and applies to all professionally operated boats of these countries. The directive states minimum requirements for the protection of workers from risks or adverse health effects resulting from the exposure to mechanical vibrations. The directive defines limits, which indicate the maximum level of exposure to WBV one may subject crew or passengers to. The limits for the daily vibration exposure are expressed in action values and limit values and based on the root-mean-square value or the vibration dose value as described by ISO standard 2631 Part 1.

The daily exposure limit value standardised to an eight hour period is $1.15 \text{ [m}\cdot\text{s}^{-2}]$ or a vibration dose value of $21 \text{ [m}\cdot\text{s}^{-1.75}]$. The daily exposure action value standardised to an eight hour period is $0.5 \text{ [m}\cdot\text{s}^{-2}]$ or a vibration dose value of $9.1 \text{ [m}\cdot\text{s}^{-1.75}]$. If the action value is exceeded, the employer is obligated to establish or implement measures in order to reduce the exposure to vibrations and the associated risks. If the limit value is exceeded, the employer is obligated to take immediate action in order to reduce the exposure to vibration to a value below the limit value threshold [56]. In addition, the employer is obligated to identify the reasons why the exposure limit value has been exceeded.

In the case of sea and air transport, when it is not possible to comply with the stated daily exposure limit despite the technical and organisational measures taken, the boat builders or operators may opt to request for an exemption [56] [34]. The exemption can only be granted on national level and on the condition that every reasonably possible measure has been taken to minimize the exposure to WBV. In addition, only in the case of sea transport, vibrations exceeding 1 [Hz] have to be considered.

Maritime Guidance Note 436 from the UK Maritime and Coastguard Agency

The MGN 436 provides guidance on mitigating the effects of WBV and RS on HSC [58]. The guidance is provided by suggesting design improvements of the vessels and suitable postural positions for the crew on board to enable them to brace for wave impacts effectively. The directive only prescribes qualitative recommendations and no quantitative limits or thresholds.

Regarding the posture of crew members multiple recommendations are given. The design of the craft should allow any crew member to remain their postural stability during voyage and adequate design features such as seat, foot straps and hand holds should be provided. During voyage, an upright posture with the spine in neutral alignment should be maintained whilst facing the travel direction in order to reduce the stress on the spine and the risk of injury.

The directive indicates that the application of SMS as a way to reduce WBV and RS in order to reduce the likelihood of injury. It also states that when lateral forces are experienced, the seat should provide appropriate postural lateral stability and support. Furthermore, the SMS should be appropriate for the craft and its operational profile. The greater the crew is exposed to WBV and RS, the greater is the need for adoption of specifically designed shock mitigating equipment to cope with the level of exposure experienced.

Annex 10 of 2000 HSC code, International Code for Safety on HSC

The code defines requirements for the design and construction of HSC, the mandatory equipment on board as well as the operation conditions and maintenance for the equipment [57]. The aim of the code is to set general levels of safety for HSC which are equivalent to those of a conventional ship stated in the International Convention for the Safety of Life at Sea (SOLAS Convention) the 1974 version [64]. The stated levels of safety are intended to prevent equipment and structures from failure during events such as a collision or grounding.

3.3.1. ISO 2631 Part 1

In 1977, the International Organisation for Standardization (ISO) published the international standard ISO 2631 Part 1 [31]. The ISO standard is named 'Mechanical vibration and shock evaluation of human exposure to whole body vibration'. The ISO standard would be expanded with additional parts over time. In Part 1, the general requirements of the evaluation of human exposure to WBV are described and the methods for the measurement of periodic, random and transient WBV are defined. The considered frequency range for health and comfort is 0.5 [Hz] to 80 [Hz]. The described methods of evaluation do not apply to large magnitude single shocks such as in vehicle accidents.

The basis evaluation method is the frequency weighted Root-Mean-Square (RMS) acceleration. The frequency weighted RMS acceleration is calculated according to

$$a_{\text{RMS}} = \left(\frac{1}{T} \int_0^T a_w^2(t) dt \right)^{\frac{1}{2}} \quad (3.1)$$

Where $a_w(t)$ is the frequency weighted acceleration in $[\text{m}\cdot\text{s}^{-2}]$ and T is the duration in [s]. The weightings for the acceleration depend on the axis of vibration and are given in the ISO standard. The purpose of the frequency weighting method is to compensate and normalize for differences in the human susceptibility at various frequencies [65]. The frequency weighted acceleration for one direction is calculated with the weightings according to

$$a_w = \left(\sum_i (w_i a_i)^2 \right)^{\frac{1}{2}} \quad (3.2)$$

Furthermore, the crest factor is calculated in order to investigate if the weighted RMS acceleration is suitable for describing the severity of the vibration in relation to the effects on the human body. The Crest Factor (CF) is calculated as

$$\text{CF} = \left| \frac{\max(a_w(t))}{a_{\text{RMS}}} \right| \quad (3.3)$$

A note regarding the crest factor is that it does not indicate the severity of vibration, but only the ratio of shocks and vibrations [31] [34] [10]. For a vibration signal with a crest factor below or equal to 9, the weighted RMS acceleration is sufficient. However, for a vibration signal with a crest factor that exceeds the value of 9 this method is not sufficient and additional evaluation methods are recommended. Two of these additional evaluation methods are described; the running RMS and the fourth power Vibration Dose Value (VDV). Furthermore, newer editions of the ISO standard refer to the ISO 2631 Part 5 where more evaluation methods are described concerning the health of the lumbar spine. The running RMS evaluation method uses a short integration time constant (τ) in order to account for occasional shocks and transient vibrations. The running RMS is calculated according to

$$a_{\text{RMS}}(t_0) = \left(\frac{1}{\tau} \int_{t_0-\tau}^{t_0} a_w^2(t) dt \right)^{\frac{1}{2}} \quad (3.4)$$

Where τ is the integration time for the running average and t_0 the time of observation. From the running RMS, the Maximum Transient Vibration Value (MTTV) is calculated as

$$\text{MTTV} = \max(a_{\text{RMS}}(t_0)) \quad (3.5)$$

The ISO standard recommends an to use an integration time of $\tau = 1$ [s] to calculate the MTTV. The VDV is more sensitive for shocks within the acceleration record as it takes the fourth power as basis for averaging [31] and does not decay during periods of low value of vibration magnitude [65]. The VDV is calculated as

$$\text{VDV} = \left(\frac{1}{T} \int_0^T a_w^4(t) dt \right)^{\frac{1}{4}} \quad (3.6)$$

Where T is the duration of the period in [s]. Furthermore, the following ratio's are defined that approximately indicate when the additional evaluation methods need to be used in order to judge the effects of vibration on the human body.

$$\begin{aligned} \frac{\text{MTTV}}{a_w} &= 1.5 \\ \frac{\text{VDV}}{a_w T^{\frac{1}{4}}} &= 1.75 \end{aligned} \quad (3.7)$$

Note that the additional evaluation methods do not replace the basic evaluation method of the weighted RMS, but should be analysed and reported additionally.

Some important notes regarding the suitability of the ISO 2631 Part 5 evaluation methods are:

- The evaluation methods focus primarily on the assessment of vibrations and are based on mean values.
- The evaluation methods do not account for human spine dynamics and are not based on biomechanics literature.
- The values of the limits are defined without much argumentation and without any references to biomechanics literature.
- The evaluation methods do not take variability regarding gender, weight and age of the person into account.

3.3.2. ISO 2631 Part 5

In 2004, the ISO 2631 standard was expanded with ISO 2631 Part 5: Method for evaluation of vibration containing multiple shocks. The purpose of part 5 is to quantify WBV containing multiple shocks in relation to the health of the human body. Injury or adverse effects to the lumbar spine are the predominant health risks due to long term exposure to WBV and RS. Therefore, part 5 addresses the exposure to RS when a person is seated and focuses especially on the lumbar spine response.

The proposed evaluation method is the spinal response acceleration dose. This dose can be determined with three steps. First, the response of the human spine to the applied accelerations is calculated. Next, the number of acceleration peaks and the associated magnitudes are counted. Finally, the acceleration dose is calculated with a dose model that is stated to be related to the Palmgren-Miner fatigue theory [66].

The Palmgren-Miner rule or Miner rule is a method to calculate fatigue or damage accumulation based on a linear relation. The Palmgren-Miner rule is defined as [66] [67] [68] [69]

$$D = \sum_{i=1}^k D_i = \sum_{i=1}^k \frac{n_i}{N_i} \quad (3.8)$$

Where D_i is the accumulated damage, n_i is the number of cycles and N_i is the number of cycles to failure at stress level or loading condition i . The Palmgren-Miner rule is based on the following assumptions: [70] [71]

- The rate of damage accumulation is constant for each loading cycle.
- Damage only occurs when the resulting stress is higher than the fatigue limit.
- When the cumulative damage equals unity $D = 1$, the component is assumed to fail.

The drawbacks or limitations of the Palmgren-Miner rule are: [72] [67] [68] [73]

- The effects of and interaction between various load sequences are neglected such as in tests with high-low stress and low-high stress loading sequences.
- The rate of damage accumulation is independent of the loading conditions, while this behaviour is not observed in experiments.
- The average value of damage accumulation until failure is usually around unity, but may deviate strongly. Generally, the sum to failure for low-high stress tests is greater than unity, while for low-high stress tests it is less than unity.
- The accumulated damage induced by stresses below the fatigue limit are neglected.

To increase the accuracy of the Palmgren-Miner rule, numerous non-linear fatigue damage accumulation methods have been proposed [73]. For the prediction of multi-stress level fatigue life, a non-linear damage model known as the modified Palmgren-Miner rule was considered [72]. The modified Palmgren-Miner rule is defined as

$$D = \sum_{i=1}^k (D_i)^c = \sum_{i=1}^k \left(\frac{n_i}{N_i} \right)^c \quad (3.9)$$

Where the constant c is independent of the applied stress. Therefore, the modified Palmgren-Miner rule is a stress-independent model similar as the original Palmgren-Miner rule [72]. However, the constant c has a value that is greater than unity, which results in a non-linear trend in the fatigue life prediction [74] [5]. If the value of this constant is equal to unity, then the the modified Palmgren-Miner rule simplifies to the original Palmgren-Miner rule. Experimental data has shown that for Palmgren-Miner exponent for biological tissue can vary from a value of 5 to 20 [1] [5]. In the standard, a value of 6.0 is chosen for the Palmgren-Miner exponent.

In figure 3.1, the flowchart for the calculation of the acceleration dose according to the ISO 2631 standard part 5 is shown.

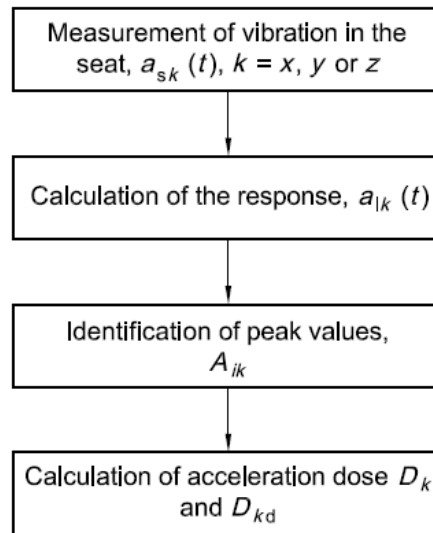


Figure 3.1: ISO 2631 Part 5 flowchart for the calculation of the acceleration dose [1]

For the calculation of the response of the human spine, predictive models are used. The spinal response in the vertical direction is represented by a non-linear Recurrent artificial Neural Network (RNN) model. The RNN model is to calculate to the lumbar acceleration response ($a_{lz}(t)$) to vertical accelerations applied at the seat surface ($a_{sz}(t)$). The response is based on a seated person in a upright relaxed posture with no

back support of the seat.

The RNN model is a computational algorithm that models an unknown system based on its input-output data. The input for the model consists of delayed samples of the seat acceleration ($a_{sz}(t-i+4)$) and the output of the lumbar acceleration response ($a_{lz}(t-i)$). Every output is a function of all previous inputs and outputs. Therefore, the RNN model is non-linear. The RNN model for vertical accelerations was trained with seat level vibrations and shocks in the magnitude range of -2.0 [$\text{m}\cdot\text{s}^{-2}$] to 4.0 [$\text{m}\cdot\text{s}^{-2}$] and a frequency of 0.5 [Hz] to 40 [Hz]. Ethical constraints limited the magnitude of the exposure to the volunteers to impacts greater than 4.0 [$\text{m}\cdot\text{s}^{-2}$] [20] [75]. In the tests used to train the RNN model, the volunteers were belted to the seat. This is not the case for all types of HSC or in certain operations [9]. The lumbar acceleration response from the RNN model is calculated with the following equations.

$$\begin{aligned} a_{lz}(t) &= \sum_{j=1}^7 W_j u_j(t) + W_8 \\ u_j(t) &= \tanh \left(\sum_{i=1}^4 w_{ji} a_{lz}(t-i) + \sum_{i=5}^{12} w_{ji} a_{sz}(t-i+4) + w_{j13} \right) \end{aligned} \quad (3.10)$$

Where W_j and w_{ji} are the coefficients for the equations, which are presented in the ISO standard [1]. The coefficients of the RNN model are specific to a sampling rate of 160 [Hz]. If the input data has a different sampling rate, then it must be resampled accordingly.

Next, the number of acceleration peaks (A_{iz}) and the associated magnitudes are counted. In the ISO standard, an acceleration peak is defined as the maximum absolute value of the lumbar acceleration response between two consecutive zero crossings. For the vertical direction, only the positive peaks should be counted as compression of the spine is of primary interest for the exposure severity.

Furthermore, the acceleration dose (D_k) in the direction k is calculated as

$$D_k = \left(\sum_i A_{ik}^6 \right)^{\frac{1}{6}} \quad (3.11)$$

Where A_{ik}^6 is the i^{th} peak of the lumbar acceleration response ($a_{lz}(t)$). For accelerations in the z direction, the RNN model is used while for the x and y direction another model is used. For the calculation dose, the ISO standard suggests to neglect peaks with a considerably lower (factor three or more) magnitude compared to the highest peak in the record as these will not have a significant contribution due to the 6^{th} power term. In addition to the acceleration dose, the average daily acceleration dose is defined, which may be useful to determine the assessment of health effects. The average daily acceleration dose is defined as

$$D_{kd} = D_k \left(\frac{t_d}{t_m} \right)^{\frac{1}{6}} \quad (3.12)$$

Where t_d is the duration of daily exposure and t_m is the period of measurement for the acceleration dose.

In the ISO standard, it is assumed that RS result in transient pressure changes at the lumbar vertebral endplates. Over time these pressure changes may result in adverse health effects due to material fatigue processes. Factors such as the number of peak compression of the lumbar spine and the associated magnitudes are identified as the key exposure factors. The Palmgren-Miner approach is applied to evaluate the effects of the internal pressure changes in the spine. The relation between the pressure changes and tolerance of the human spine can be used to assess the potential of adverse health effects. The assessment is based on a seated person in a upright position. A forward bending posture or twisted posture is likely to increase the adverse health effects.

A biomechanical model, based on experiments, has shown that a linear relationship exists between compressive stress in the spine and the peak acceleration response in the spine. The equivalent static compressive stress (S_e) is calculated with the acceleration dose according to

$$S_e = \left(\sum_k (m_k D_k)^6 \right)^{\frac{1}{6}} \quad (3.13)$$

Where the recommended values of the coefficient for the x , y and z directiona are $m_x = 0.015$ [MPa·s²·m⁻¹], $m_y = 0.035$ [MPa·s²·m⁻¹] and $m_z = 0.032$ [MPa·s²·m⁻¹]. Based on the equivalent static compressive stress, the daily equivalent static compression dose (S_{ed}) is defined as

$$S_{ed} = \left(\sum_k (m_k D_{kd})^6 \right)^{\frac{1}{6}} \quad (3.14)$$

With the daily equivalent static compression dose, a risk factor R can be defined which relates human response acceleration dose to the assessment of adverse health effects. This risk factor should be calculated sequentially taking the increased age and reduced strength during the exposure time into account. The factor is defined as

$$R = \left(\sum_{i=1}^n \left(\frac{S_{ed} \cdot N^{1/6}}{S_{ui} - c} \right)^6 \right)^{\frac{1}{6}} \quad (3.15)$$

Where N is the number of exposure days per year, n the number of years of exposure, i the counter indicating each year, S_{ui} is the ultimate strength of the lumbar spine for a person of age and c is a constant which presents the static stress due to gravitational force. A value of $c = 0.25$ [MPa] is normally used.

The value of the ultimate strength of the lumbar spine depends on the bone density of the vertebrae. This value normally decreases when the age of the person increases. Based on *in vitro* studies, the following relationship between the ultimate strength and the age has been derived.

$$S_{ui} = 6.75 - 0.066(b + i) \text{ MPa} \quad (3.16)$$

Where b is the age of the person at which the exposure has started. In figure 3.2, the flowchart for the assessment of adverse health effects from vibrations containing multiple shocks according to the ISO 2631 standard part 5 is shown.

For the assessment of adverse health effects for n years of exposure and for a lifetime of exposure assuming 240 days of exposure per year, the standard has suggested some limit values for the daily equivalent compression dose and the risk factor R . The values are set for a person who starts being exposed at the age of 20 years and is exposed until the age of 65 years, meaning that the person is exposed for 45 years. The limits are shown in figure 3.2. If the number of days per year of exposure differ from the 240 days, then the respective values of S_{ed} can be adjusted by multiplying the with the factor $\left(\frac{240}{N}\right)^{\frac{1}{6}}$.

Some important notes regarding the suitability of the ISO 2631 Part 5 evaluation methods are:

- The evaluation methods are based on spine dynamics, but only validated for seat level acceleration peaks up to 4 [g].
- The values of the limits are defined without much argumentation and without any references to biomechanics literature.
- The evaluation methods take variability regarding age and prolonged exposure into account, but not variability in weight or gender.

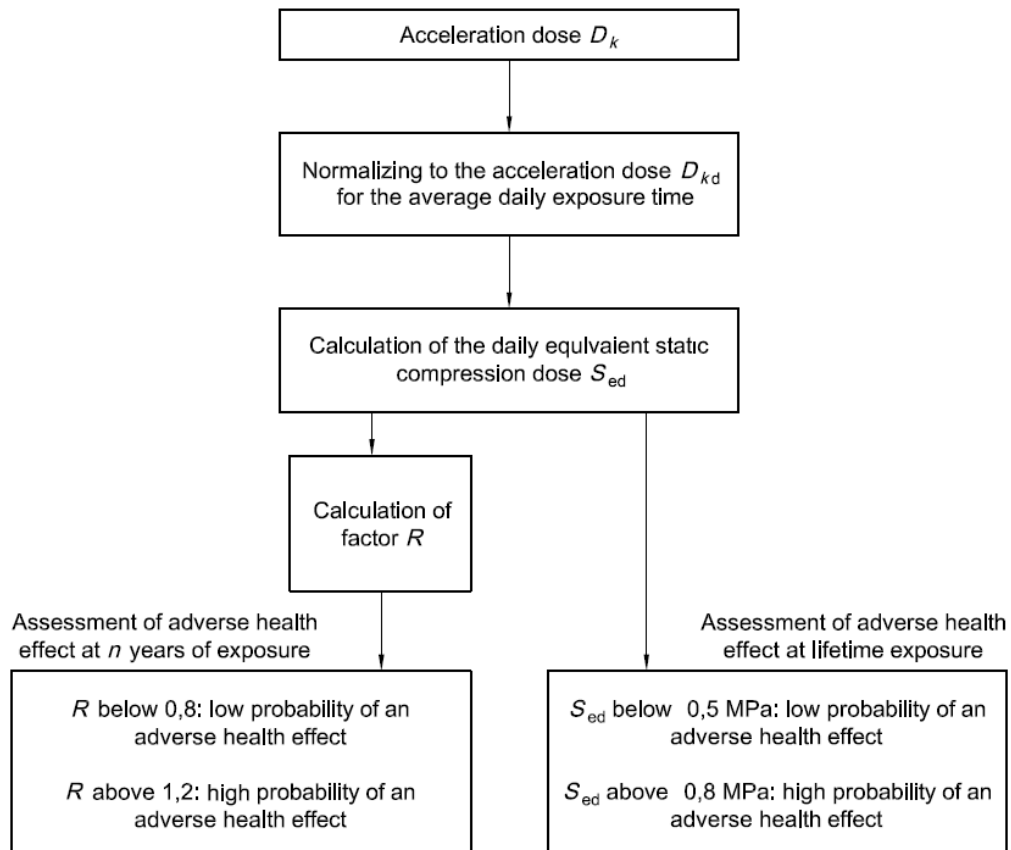


Figure 3.2: ISO 2631 Part 5 flowchart for the assessment of adverse health effects based on the acceleration dose [1]

3.4. Injury Criteria & Models³

In previous research [10], some injury models were reported besides the standards described in the previous section. These models are the Eiband tolerance curves and the dynamic response index. The Eiband tolerance curves are used in the previous research [10] to evaluate the resulting accelerations of the operator on the SMS. The curves are a somewhat older injury model, which is not referenced that often in more recent research [10] [26]. On the other hand, the dynamic response index is referenced far more in recent literature [13] [59] [21] [60] [61] [20] [62] [63] [10] [26]. Both of the injury models will be explained below, the Eiband tolerance curves more briefly compared to the dynamic Response index.

3.4.1. Eiband Tolerance Curves

In the late 50s at the National Aeronautics and Space Administration (NASA), Eiband wrote a memorandum on human tolerance to rapidly applied accelerations. The excitation pulse used in the experiments has the form of a trapezoidal pulse. Based on experiments with both humans and animals, Eiband derived multiple curves drawn as the acceleration force against the duration of the acceleration which indicate the severity of possible injuries, see figure 3.3. The tolerance curves are related to forces in the headward direction[2].

From literature and experience, it is known that the human tolerance to rapidly applied accelerations depends on the direction of the acceleration, the magnitude of the acceleration, the duration of the acceleration, the rate at which the acceleration and how the body is supported during exposure to the acceleration. Therefore, the effects of body restraint, acceleration direction, onset rate and plateau duration of the excita-

³This section is based on the literature study [27]

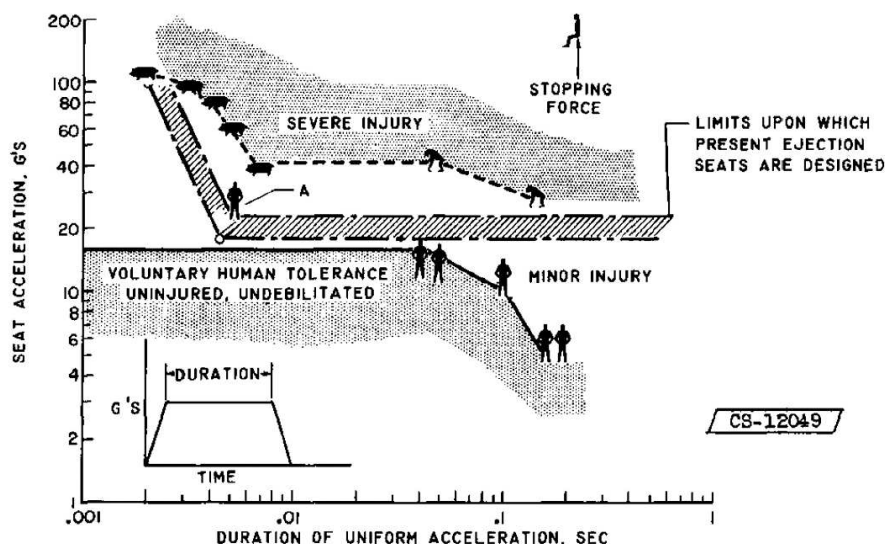


Figure 3.3: Eiband tolerance curve for vertical accelerations [2]

tion pulse are investigated. The primary variable for human tolerance to rapidly applied accelerations was concluded to be adequate torso and extremity restraint. When the conditions for adequate body restraint are met, the other parameters such as acceleration direction, onset rate and plateau duration determine the maximum tolerance and severity/limits of injury [2].

Based on the experiments, it was concluded that the magnitude of the human tolerance decreases as the plateau duration of the excitation pulse increases and that the magnitude of the human tolerance decreases as the onset rate increases. The human tolerance is lower when forces are applied parallel to the spine compared when two when the forces are applied perpendicular to the spine [2].

Some important notes regarding the suitability of the Eiband curves are:

- In the experiments of Eiband the human subjects are restraint to their seats, while the crew on the HSC are often not restraint on most SMS designs.
- The crew on board of the HSC are exposed to accelerations from multiple directions, while in the experiments only accelerations in one direction at a time are applied.
- The excitation pulse in the experiments of Eiband has a trapezoidal form. However, more recent research on SMS uses an excitation pulse with a half sine pulse form.
- The severe injury curves were drawn based on experiments with animals and due to differences in anatomical structure they are not one-to-one translatable to human curves. They can give a slight indication of the possible human tolerance curves for severe injuries.

3.4.2. Dynamic Response Index

In 1971, James W. Brinkley and John T. Shaffer published a technical report [3] based on previous research [76] in which they formulated a linear biomechanic model of the human torso, which measures the probability of spinal injury resulting from vertical shock load for a person in the seated posture. The model is known as the Dynamic Response Index (DRI), which is linearly proportional to the maximum compression of the human spine. In the model, the spinal injury is based on compressive spinal fracture due to the deformation of the spine as the upper body displaces relative to the pelvis [76].

The DRI is derived from a simple mechanical model, where the human spine is modelled as a lumped single DOF mass-spring-damper system [3]. The response of the model is computed by solving a second order differential equation, where spinal compression is the unknown variable and the forcing function is the seat level acceleration resulting from the vertical shock ($\ddot{a}(t)$). The second order differential equation is

$$\frac{d^2\delta}{dt^2} + 2\zeta\omega_n \frac{d\delta}{dt} + \omega_n^2\delta = \ddot{a}(t) \quad (3.17)$$

Where δ is the displacement between the upper body and the pelvis, ζ is the damping ratio, ω_n is the natural frequency. The coefficients for the equation were derived experimentally with compressive strengths of individual vertebrae. For the experiments, male aviators of the Air Force were tested with a mean age of 27.9 years. The natural frequency is 8.4 [Hz] and the damping coefficient is 0.224 [-] [76]. The dimensionless number DRI is defined as [3]

$$\text{DRI} = \frac{\delta_{\max}\omega_n^2}{g} \quad (3.18)$$

Where δ_{\max} is the maximum displacement due to the vertical shock and g is the gravitational constant. With the displacement, the lumbar force and the maximum lumbar force can be calculated by multiplying it with the stiffness (k) such that the force (F) is equal to $F = k\delta$. The DRI guidelines for ejection seats according to Brinkley are shown in table 3.2. In the current NATO standard [77], the maximum allowed value of the DRI is 17.7, which corresponds with an injury probability of 10 %.

Table 3.2: DRI Guidelines for seated humans [3] [13]

Risk of Injury	Probability of Injury [%]	DRI Value [-]
Low	0.5	15.2
Moderate	5.0	18.0
High	50.0	22.0

As the DRI guidelines for ejection seat shown in table 3.2 only provide limited guidance, the guidelines were expanded over a range of DRI values [4] with experiments of cadaver specimens. The results of these experiments are shown in figure 3.4. In the figure, the solid line represents the result obtained from the experiments in the laboratory. The dashed line represents the operationally experienced injury rates. In the figure, the operational injury rates show an increase in the DRI tolerance levels [4].

Some time later in the mid 1980's, the DRI was extended to all three translational axes [78]. The Combined Dynamic Response Ratio (CDRR) was defined [13]. The CDRR applied the DRI method to all three directions and combined them into one ratio. The CDRR is calculated according to

$$\text{CDRR}(t) = \sqrt{\left(\frac{\delta_x(t)}{S_x}\right)^2 + \left(\frac{\delta_y(t)}{S_y}\right)^2 + \left(\frac{\delta_z(t)}{S_z}\right)^2} \quad (3.19)$$

Where $\delta_x(t)$, $\delta_y(t)$ and $\delta_z(t)$ are the time dependant displacements in each translational direction and S_x , S_y and S_z are the maximum allowed displacements. Additional research [14] on the extended method and the kinematics of a seated person in the passenger compartment of lifeboat subjected to water impacts determined values for the natural frequency and damping ratio for all translational directions for a body mass of 75 [kg] The results of this research are shown in table 3.3. For the directions is it assumed that the person is directed with the face towards the bow of the lifeboat. The parameters/coefficients for the DRI are related to the specific test set up and extrapolation to other configurations may require additional testing or recalculation of the parameters [78] [15].

Some important notes regarding the suitability of the DRI are:

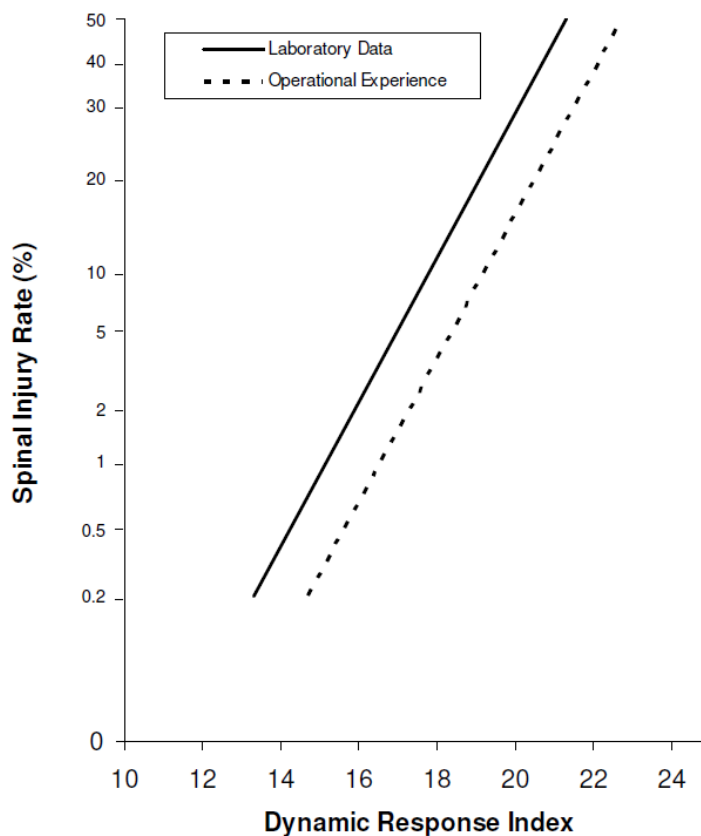


Figure 3.4: Probability of spinal injury estimated from laboratory data compared to operational experience [3] [4]

Table 3.3: Parameters for the CDRR [14] [13]

Translation	Natural frequency [Hz]	Damping ratio [-]
Surge	10.0	0.100
Sway	9.2	0.090
Heave	8.4	0.224

- The DRI is not validated for repetitive loading.
- The DRI does not take variability regarding gender, weight and age of the person into account.
- If the person carries additional equipment on the upper body, the natural frequencies and damping characteristics change. This invalidates the DRI model.
- The response of the human body is expected to be non-linear, which was also observed during *in vitro* studies. The DRI model may be too simplistic in this case [21] [59].
- For continuous vibrations with a frequency above 8.4 [Hz] the response decreases quadratic with the frequency. As a result, the DRI erroneously indicates that severe accelerations at high frequencies are permissible [53].

Recently (2017) conducted research at NASA [15] in cooperation with Brinkley reviewed the development of the Brinkley Dynamic Response Criterion (BDRC). In the research, the parameters from table 3.3 were recalculated with newer techniques and new injury risk levels were determined based on available injury

data. Instead of the CDRR, the Injury Risk Criterion (IRC) is used and calculated as

$$\text{IRC}(t) = \sqrt{\left(\frac{\text{DRI}_x(t)}{\text{DRI}_x^{\text{lim}}}\right)^2 + \left(\frac{\text{DRI}_y(t)}{\text{DRI}_y^{\text{lim}}}\right)^2 + \left(\frac{\text{DRI}_z(t)}{\text{DRI}_z^{\text{lim}}}\right)^2} \quad (3.20)$$

$$\text{DRI}_k(t) = \frac{\delta_k(t)\omega_n^2}{g} \quad (3.21)$$

Where $\text{DRI}_x(t)$, $\text{DRI}_y(t)$ and $\text{DRI}_z(t)$ are the time dependant dynamic responses and $\text{DRI}_x^{\text{lim}}$, $\text{DRI}_y^{\text{lim}}$ and $\text{DRI}_z^{\text{lim}}$ are the DRI limits for each axis. The recalculated parameters for the second order differential equation are shown in table 3.4 per direction. Again, it is assumed that the person is directed with the face towards the positive x-axis and is head is direction in the positive z-axis. The second order differential is now non-linear as the parameters change with the sign of the displacement. In table 3.5, the dynamic response limits are shown per direction. If the $\text{IRC} \geq 1.0$, then the IRC should be recalculated with the next highest set of limits of table 3.5. If $\text{IRC} \leq 1.0$, then the result is the risk level due to the acceleration.

Table 3.4: Recalculated parameters for the IRC [15]

Axis	Direction	Natural frequency [Hz]	Damping ratio [-]
x	-	8.91	0.040
x	+	10.0	0.200
y	-	9.23	0.070
y	+	9.23	0.070
z	-	7.50	0.240
z	+	8.42	0.224

Table 3.5: Dynamic response limits for the IRC [15]

Axis	Direction	Low ($\leq 0.5\%$)	Medium (0.5 % to 5.0 %)	High (5.0 % to 50.0 %)
x	-	$-28.0 \leq \text{DRI}_x \leq 0.0$	$-35.0 \leq \text{DRI}_x \leq -28.0$	$-46.0 \leq \text{DRI}_x \leq -28.0$
x	+	$0.0 \leq \text{DRI}_x \leq 35.0$	$35.0 \leq \text{DRI}_x \leq 40.0$	$40.0 \leq \text{DRI}_x \leq 46.0$
y	-	$-15.0 \leq \text{DRI}_y \leq 0.0$	$-20.0 \leq \text{DRI}_y \leq -15.0$	$-30.0 \leq \text{DRI}_y \leq -20.0$
y	+	$0.0 \leq \text{DRI}_y \leq 15.0$	$15.0 \leq \text{DRI}_y \leq 20.0$	$20.0 \leq \text{DRI}_y \leq 30.0$
z	-	$-13.4 \leq \text{DRI}_z \leq 0.0$	$-16.5 \leq \text{DRI}_z \leq -13.4$	$-20.4 \leq \text{DRI}_z \leq -16.4$
z	+	$0.0 \leq \text{DRI}_z \leq 15.2$	$15.2 \leq \text{DRI}_z \leq 18.0$	$18.0 \leq \text{DRI}_z \leq 22.8$

Some important notes regarding the suitability of the IRC are:

- The method assumes that the body of the person is belted to the seat such that it experiences the same translations and rotations as the seat.
- The BDRC method has only been validated for shock pulses with a duration up to 0.5 [s].
- Very specific instructions for the seating and restraints must be met in order for the BDRC to be valid. This heavily limits the applicability of the BDRC method to other configurations such as SMS on HSC.
- The method is based on experiments with primarily male military volunteers and most of them were younger than 30 years. Therefore, differences in sex, fitness and age are most likely not taken into account.

3.5. Improvements of the ISO Evaluation Methods⁴

In the next sections, various research on the possible improvements of the ISO 2631 standard are discussed.

3.5.1. Metamodel of a Seated Person

In the early 2000s, research on low-order dynamics metamodel for the prediction of vertical impacts to the human spine was conducted in a joint effort by the center of applied biomechanics from the university of Virginia and the USA naval surface warfare center [79] [60] [61] [20] [62] [63]. The relative performance of conventional injury evaluation methods used by the naval architecture community was assessed using measurement data from various sea trials. The analysed evaluation methods are from the standard ISO 2631 Part 5.

In the research, a numerical model was presented, based on a Madymo (TNO, Inc.) lumped mass system. The model is a lumped mass simulation of a 50th percentile male in a seated posture. The parameters for the 50th percentile male are based on biomechanics literature [80] [81]. The model was developed to evaluate the response of seated humans to different wave impact conditions. With measurements of a SMS Mk V Special Operations Craft equipped with both an isolated seat and a non-isolated seat the model was validated. Multiple wave impact excitation pulses were chosen of which some were within the validated range of ISO 2631 Part 5 and some outside the range. The acceleration peaks of the chosen wave impacts had magnitudes varying from 0 [g] to 14 [g] [62] [63].

The simulations of the metamodel were compared with the simulations of the RNN model from ISO 2631 Part 5 [1]. For wave impacts with a peak acceleration below 4 [g], the RNN model from ISO 2631 Part 5 correlated well with the metamodel. For wave impacts with a peak acceleration above 4 [g], the results increasingly diverged and the metamodel produced higher accelerations in the lumbar spine response than the RNN model from ISO 2631 Part 5 [62]. The results indicate that the RNN model from ISO 2631 Part 5 may not be valid outside its region and suggest the possible need to replace the RNN model with the model based on the Madymo simulation in order to predict the loads in the lumbar spine more accurately. During the sea trials, information from the HSC operators indicate that the current tolerance limits provided by ISO 2631 Part 5 for the daily equivalent static compressive dose and the risk factor R are conservative [20].

The authors regarded the ISO 2631 Part 5 as the best injury criterion available at the time as it is developed for repetitive loading and is based on the biomechanics of the spine [61] [20]. No suitable criterion exists at the time of the research which is able to predict the likelihood of spinal injuries from HSC operations [60] [61] [62]. Based on military career assumptions, the reference values for injury in ISO 2631 Part 5 are too low for HSC operators. It is recommended that the injury reference values are adjusted to reflect the physical fitness of military personnel. The results suggested that the RNN model from ISO 2631 Part 5 may not be valid outside its validated range as it substantially under predicts the spinal acceleration response for wave impacts with larger amplitudes. Within the designs range for seat level accelerations from 0 [g] to approximately 4 [g], the method is valid, but it was noticed to regularly predict incorrect response amplitudes and incorrect signs [62]. As a result, the RNN model from ISO 2631 Part 5 should not be used outside of its validated range and with caution in its design range.

3.5.2. Human Spine Ultimate Strength

In more recent research [5], a large-scale experiment of the human lumbar spine tolerance to repetitive compressive loading was conducted to evaluate and improve existing guidelines (especially ISO 2631 Part 5) for the exposure of the human body to WBV and RS. The current method in the ISO 2631 Part 5 to calculate the ultimate strength of the spine is solely a function of the age and is developed on the basis of single cycle compression tests. The method is not validated for cycling loading with experiments.

⁴This section is based on the literature study [27]

For the research, fatigue tests from literature for a total of 77 male and 28 female cadaveric spinal segments were used. The mean age of the male specimens were 53 ± 19 years and for the female specimens 58 ± 20 years. The results from the experiments showed that the factors such as the number of cycles, the loading conditions, sex and age have a significant contribution to the lumbar strength and the probability of bony failure. Therefore, the effects of the number of cycles, the loading conditions, sex and age were taken into account when calculating the ultimate strength of the spine. A modified version of the ISO 2631 Part 5 risk factor R was developed, which incorporates the effects of age, stress and number of cycles by deriving an optimized age-dependent coefficient (G_{age}) based on gender.

Using the optimized age-dependent coefficient, the method to calculate the ultimate strength of the lumbar spine becomes

$$S_{\text{ui}} = 6.75 - G_{\text{age}}(b + i) \text{ MPa} \quad (3.22)$$

Where b is the age of the person at which the exposure has started. With the resulting ultimate strength of the lumbar spine, the risk factor R could be determined. In addition, an univariate Weibull survival analysis was performed which resulted in an model that relates the exposure to risk of injury and incorporates the R factor. The expression of the injury risk model is

$$\Pi = 1 - e^{-\left(\frac{R}{\alpha}\right)^\beta} \quad (3.23)$$

Where α and β are the scale and shape parameter respectively, which are also based on gender. The coefficients for the modified risk factor R and the Weibull injury risk model are shown in table 3.6. In figure 3.5, the injury risk curves as a function of the risk factor R for males and females are shown.

Table 3.6: Coefficients for the modified risk factor R and Weibull injury risk model [5]

Sex	G_{age}	α^*	β^*
Male	0.0520	1.613 (1.460, 1.809)	2.799 (2.168, 3.511)
Female	0.0378	0.959 (0.854, 1.093)	3.709 (2.509, 5.207)

* α and β shown with 95% confidence intervals

The modified risk factor R was compared to the standard R factor from ISO 2631 Part 5. The comparison highlighted the differences in age and the need for different models between sexes. Furthermore, it showed that the standard method in the ISO 2631 Part 5 underestimates the risk of injury for young adults and overestimates the risk for older persons. A limitation of the modified model, as with the ISO 2631 model, is that the models do not include healing over the course of time, which is expected to have a significant contribution [5].

The modified R factor and Weibull injury risk model were applied to experimental measurements from other research [20] and predicted a spinal injury risk value of 38% for crew and passengers of HSC [5], which is in agreement reported high risk of injuries in literature [12].

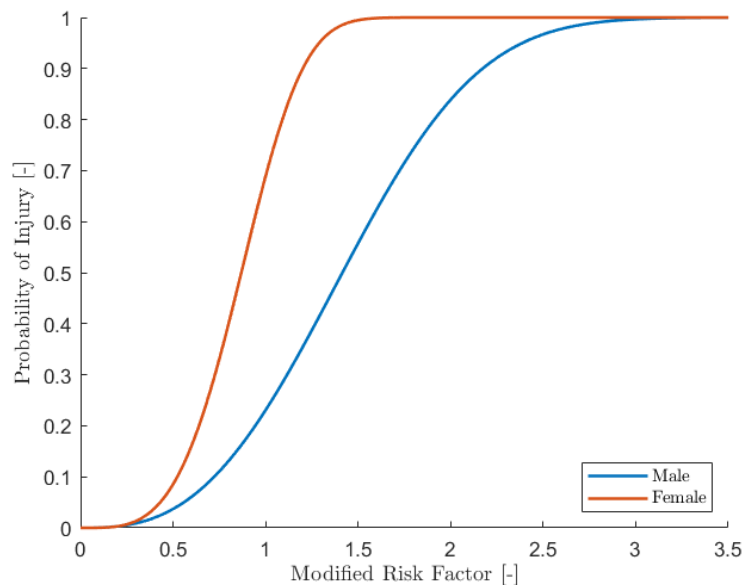


Figure 3.5: Probability of injury for males and females as a function of the modified risk factor [5]

3.6. Suitability of the Evaluation Methods⁵

In the previous sections, the most commonly referenced standards, methods and injury models to evaluate spinal injury resulting from WBV and RS on HSC have been discussed. In this section, the suitability of these methods will be discussed.

Based on the literature review, the following criteria are deemed unsuitable to evaluate spinal injury resulting from WBV and RS on HSC; the acceleration RMS and VDV from ISO 2631 Part 1. These evaluation methods are not validated with biomechanics literature [20] and therefore do not account for human spine dynamics [32]. Additionally, the RMS and VDV values are based on mean values and thus neglect/underestimate the risk of shocks with large peak accelerations [34] [35] [17]. According to some literature, these methods are suitable for the evaluation of WBV only [34]. Furthermore, the limit values stated in the ISO 2631 standard Part 1 based on discomfort, not on injury boundaries or injury criteria [20] [11]. The suitability of the limits based on discomfort and their relation to injury are questioned in literature as well [32] [33] [22] [17] [34] [35] [23] [11]. The methods can be used to predict physical fatigue, but not to define limits for safe exposure to wave impacts [34] [35].

Based on the reviewed literature, the two existing injury criteria to assess spinal injury which seem to be appropriate are the dynamic response index and the evaluation methods from ISO 2631 Part 5 [20] [22]. Both of these methods are based on the biomechanics of the spine and have been validated with experiments [3] [20]. However, both evaluation methods still have their limitations [60]. For both methods, the main limitations and drawbacks will be discussed next.

Limitations of the DRI

The main limitation of the DRI is that the criteria does not account for or is validated for repetitive loading while the spinal injuries of HSC operators are often the result of multiple wave impacts over a longer period of time. Additionally, the DRI does not take into account any recovery of the muscles or spine [21]. Furthermore, the DRI is based on compressive spinal fracture, while research as shown that the injuries resulting from exposure on HSC are often related to intervertebral disc injuries [60]. Finally, the DRI does

⁵This section is based on the literature study [27]

not take variability regarding gender, weight and age of the person into account. In addition, the weight of additional equipment on the upper body changes the natural frequencies and damping characteristics, which invalidates the DRI. Although the original DRI is limited to a single DOF, various studies have shown that the method can be extended to multiple DOF [78] [13] [15].

Limitations of ISO 2631 Part 5

In figure 3.6, the total flowchart of the evaluation methods of ISO 2631 Part 5 including the limitations in various stages is shown. The three stages with limitations are the calculation of the lumbar acceleration response with the RNN model, the calculation of the risk factor R and the defined limits for probability of injury.

The main limitation of the RNN model is that it is not validated for wave impacts with a seat level acceleration peaks larger than 4 [g] [20] [34] [35] while seat level acceleration peaks exceeding 10 [g] have been reported [13] [10] [16] [9]. For wave impacts with seat level acceleration peaks larger than 4 [g], the model substantially under predicts the spinal acceleration response [62]. In contrast to the DRI, the evaluation methods from ISO 2631 Part 5 are developed for repetitive loading and incorporate accelerations in the surge and sway direction in addition to the heave direction, which is important as additional accelerations in these directions increase the probability of spinal injury [34] [1]. However, the RNN model does not take into account the rotation of the spine or moments acting on the spine that may increase the probability of lumbar spine injury even more [60].

The risk factor for the probability of injury has no proven correlation with injury risks [35] and the defined limits seem to be on the conservative side [20] [34] [35] [22]. Furthermore, the risk factor does not take variability regarding weight and gender into account. Other research [5] has shown that the method to assess the ultimate strength of the lumbar spine for the R factor is not validated for cyclic loading nor does it differentiates in number of cycles, loading conditions and gender. The results of the research showed that the method from ISO 2631 Part 5 underestimates the risk of injury for young adults and overestimates the risk for older persons.

Conclusion

Based on the limitations of both evaluation methods, the ISO 2631 Part 5 evaluation method is most likely the best suitable injury criterion to evaluate spinal injuries as a result of WBV and RS for wave impacts with an acceleration peak below 4 [g]. The evaluation methods of ISO 2631 Part 5 could be improved by using the metamodel from literature [21] [60] [61] [20] [62] [63] instead of the RNN model presented in the standard. The metamodel has been validated for wave impacts with acceleration peaks of 0 [g] to 14 [g] [62] [63]. Unfortunately, the metamodel is not published and the literature does not provide any equations representing the model which can be implemented in the computer program and used in this research. Alternatively, the modified R factor and the Weibull injury risk model [5] could be used to improve the accuracy of the evaluation method of ISO 2631 Part 5, which are fully described in the literature [5].

Therefore, two options remain for the implementation of an injury model in this research. The first option is to implement the evaluation methods from ISO 2631 Part 5 including the modified R factor and the Weibull injury risk model. The second option is to implement the dynamic response index which can be used to evaluate spinal injury for the full range of wave impacts described in literature [7], but is only valid for individual shocks. In this research both of these options will be implemented in order to enable a comparison of the risk values resulting from the different injury models.

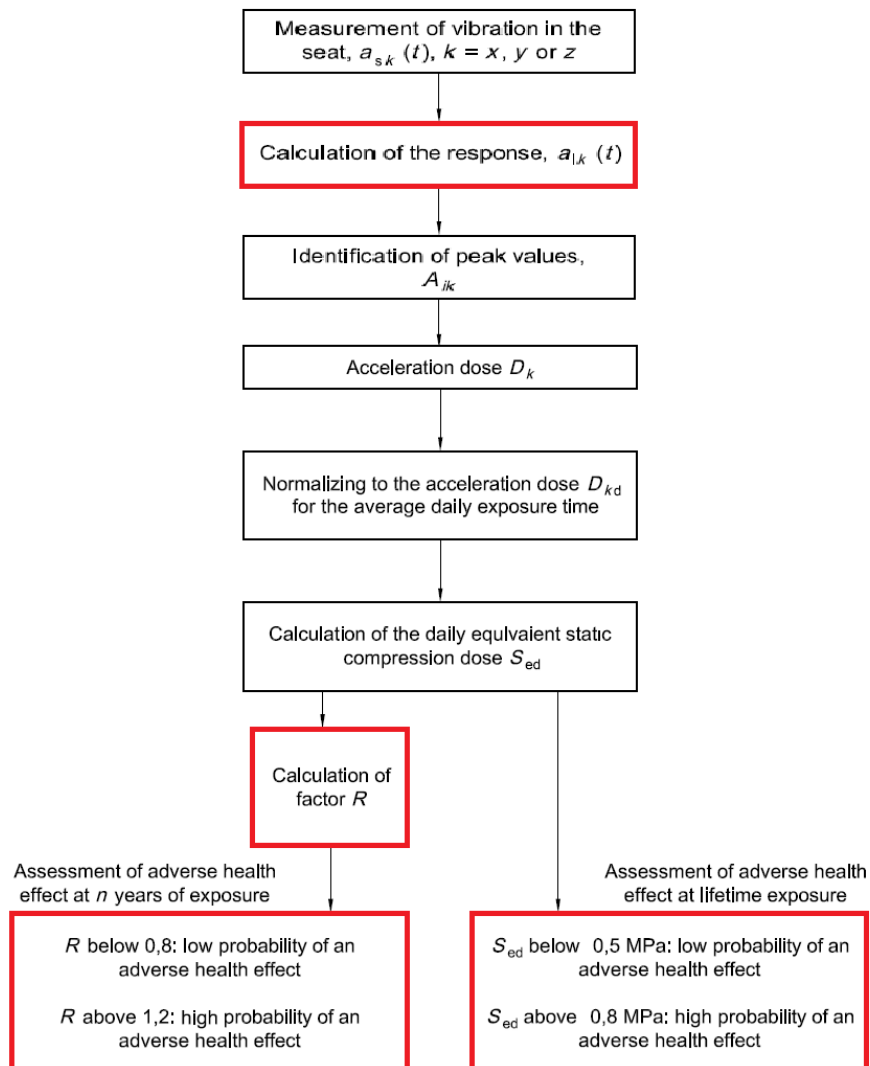


Figure 3.6: ISO 2631 Part 5 complete flowchart with limitations indicated in red

4

Wave Impact Accelerations

In this chapter, the wave impact excitation pulse will be discussed. First, the acceleration period for a wave impact is identified in an acceleration record and the half-sine approximation is explained. Then, full-scale data of wave impacts and measurements of a sea trial are presented. With the available acceleration data and a simple mass-spring-damper model, the validity of the half-sine approximation is reviewed.

It is time consuming and involves high costs to assess the performance of the SMS in both the design and off-design conditions with either sea trials and laboratory tests. An alternative is to run multiple simulations using a computer program with measurements of various sea trials as input. This is still not an ideal situation as the simulations would be dependant on the available data. Therefore, an excitation pulse is assumed which should represent a realistic wave impact and could be used as input. The parameters defining this excitation pulse can be easily changed to resemble various wave impacts events.

4.1. Wave Impact Excitation Pulse¹

In a publication made by the materials department of the United States Navy [6], the Naval Sea Systems Command (NAVSEA), an approach is presented to quantify the amplitude and duration of a wave impact load for small HSC. A mathematical model of a single DOF, the vertical direction, is used to determine the relationship between the wave impact loads and the resulting acceleration response on the craft. In this research, mechanical shocks are defined as accelerations with a duration of 100 [ms] or more, while vibrations are defined as accelerations with a duration of 50 [ms] or less.

In figure 4.1, the sequence of events for a typical wave slam event for a HSC are shown. The top figure shows the unfiltered vertical acceleration response curve for an individual wave impact [82]. The middle figure is the vertical velocity time trace, which is derived by integrating the acceleration curve [82]. The bottom figure shows the vertical displacement curve, which is derived by integrating the velocity curve [82].

In figure 4.1 at time A, the vertical acceleration is approximately -0.9 g, which is similar to a condition of free fall. Based on the linear decrease in velocity between time A and B and the drop in height in the same interval, the movement of the craft is considered to be a combination of heave and pitch motion. At time B, the craft impacts the wave where the force of the impact results a large peak in the vertical acceleration. At the same time, the velocity is at a minimum and the slope changes from negative to a positive one. From time B to time C, the craft moves into the water, the velocity goes to zero and the acceleration decreases. At time C, the displacement of the craft is at a minimum, the velocity is equal to zero and the acceleration has a value of approximately 1.0 g. The time C is considered to be the end of the wave impact

¹This section is based on the literature study [27]

event. From time C to D, the combination of buoyancy, hydrodynamic lift, thrust and drag result in a net positive acceleration. From time D to E, the gravity begins to overcome the combination of forces and another wave impact begins [6].

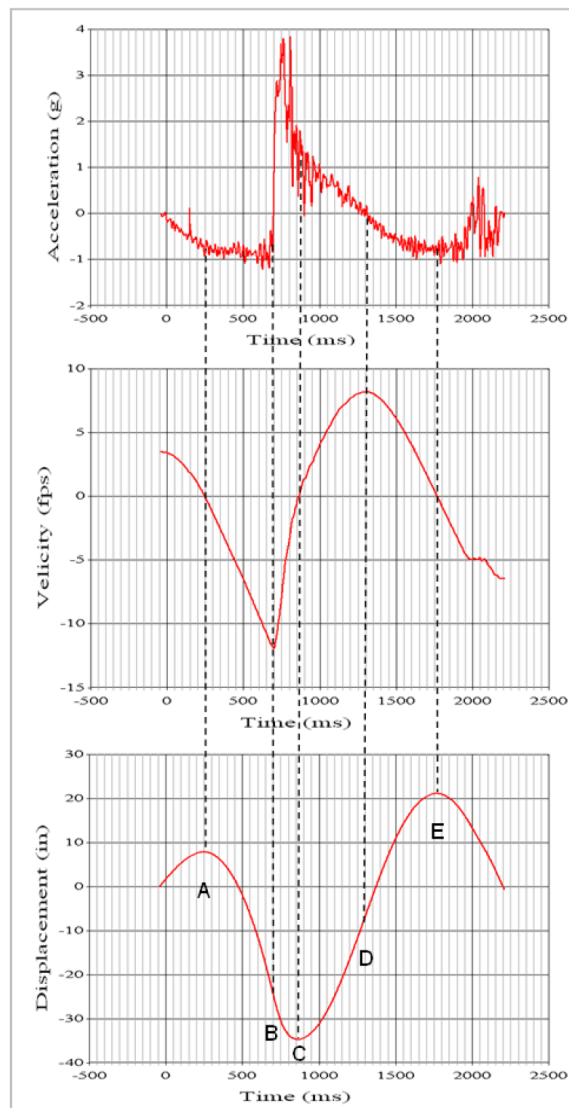


Figure 4.1: Wave impact sequence of events [6]

4.1.1. Rigid Body Acceleration

Due to the sensitivity of accelerometers, the measured acceleration time signal consists of rigid body accelerations and flexural motions [6]. The flexural motions are structural vibrations due to the wave impact or due to operating machinery. During wave impacts, the flexural motions and structural vibrations are not of primary interest. Therefore, accelerometers are typically placed at relative stiff locations to reduce the vibration content in the signal, but even then they are sensitive enough to measure accelerations of the millimeter vibrations of plating. These accelerations can have equal or greater magnitude than the heave accelerations of the craft due to the wave impact [6]. In figure 4.2, the linear superposition of the rigid body accelerations and the flexural motions is shown [6] [83].

As already mentioned, the rigid body acceleration caused by the wave impact is of primary interest and

the structural vibrations are not. The rigid body accelerations characterize the wave impact and can be obtained by removing the flexural motions and structural vibrations from the record. These can be removed by using a low-pass filter [84] [85] [86].

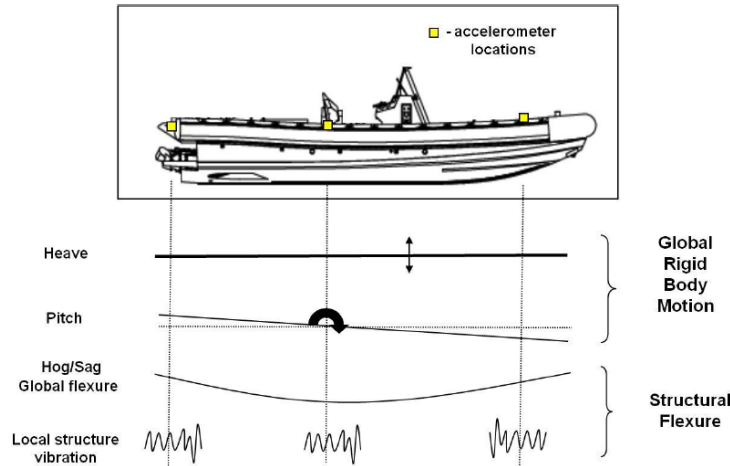


Figure 4.2: Vertical dynamic response of the craft and its different modes [6]

The appropriate frequency for the filter can be determined with a Fourier analyses. In figure 4.3, the Fourier spectrum of a random acceleration response is shown. The Fourier spectrum shows that dominant frequency is at 2 [Hz], while some vibration content is visible as well at 25, 40 and 55 [Hz]. These frequencies are a result of the flexural motions and structural vibrations, which should be removed from the acceleration time record. Separating the unfiltered acceleration record in the different response modes is known as modal decomposition [6].

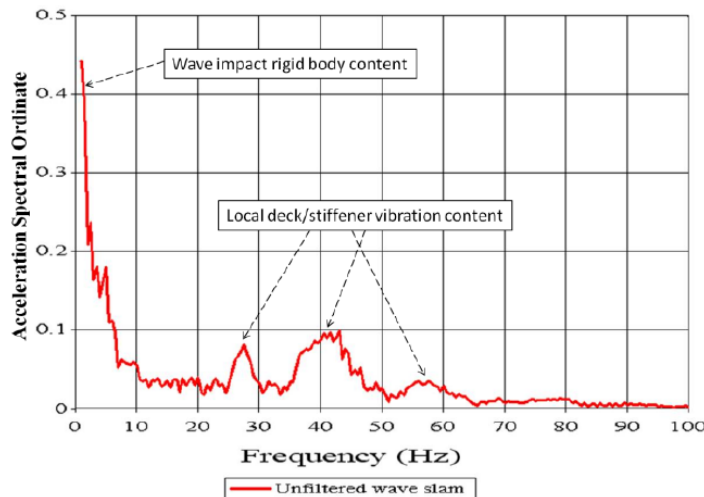


Figure 4.3: FFT of the vertical acceleration [6]

The modal decomposition is done by applying a low-pass filter to the acceleration record. Based on experiments with multiple sets of data for craft with a length of less than 30 [m] the authors concluded that a low-pass filter with a cut-off frequency of 10 [Hz] removes the flexural motions and structural vibrations sufficiently [6]. This experiment confirms earlier studies which also applied a similar cut-off frequency [86]

[87]. This cut-off frequency can always be checked by a Fourier analysis to each acceleration record. Note that this method of filtering may not be appropriate for all type of analysis on craft acceleration data.

4.1.2. Half-Sine Approximation

In figure 4.4 the rigid body accelerations per wave impact are normalized with the peak acceleration within that record. Each color represents a single wave impact from the record. The numbers in the upper right corner indicate the time in seconds when the wave impact occurred in the wave record. The magnitude of the original peaks varied from 1.9 g to 5.3 [g], with durations varying from approximately 165 to 220 . The amplitude of the acceleration of a single wave impact response depends primarily on speed, craft weight and wave parameters [83]. The sequence of the wave encounters and the time between each wave impact is random.

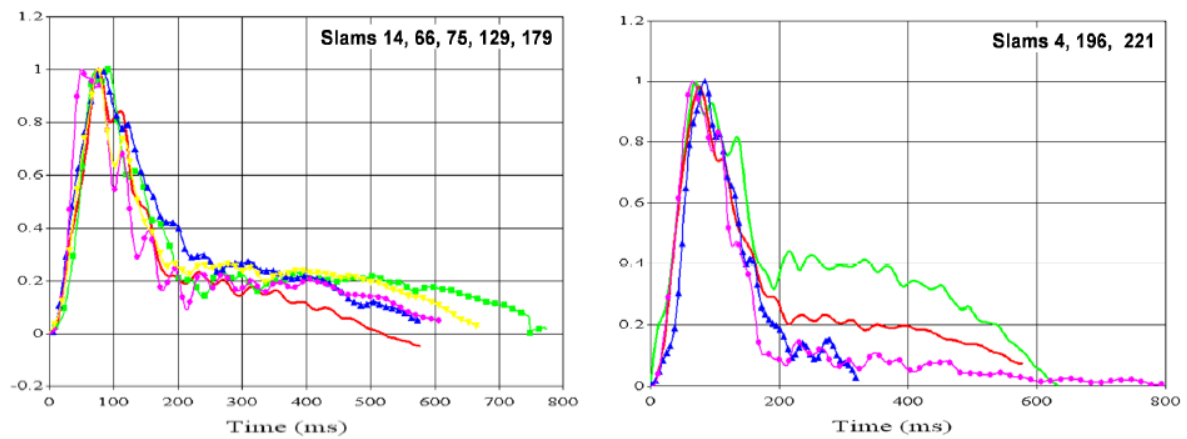


Figure 4.4: Normalized rigid body accelerations for multiple wave impacts [6]

After performing multiple tests and measuring the vertical accelerations and studying previous research [88] [13], the authors concluded that the excitation pulse of the rigid body acceleration can be simplified to a half-sine pulse as is shown in figure 4.5.

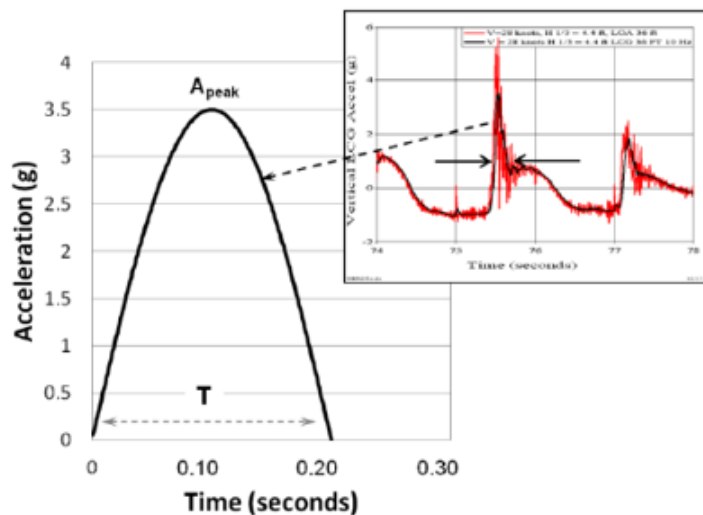


Figure 4.5: Half-sine approximation of a wave impact [7]

Both the peak acceleration and the peak duration of the excitation pulse of the rigid body acceleration

should be used to define the pulse of the half sine approximation. In addition, the change in velocity for the half sine pulse should be approximately equal to the change in velocity due to the wave impact. Only when these conditions are satisfied the half-sine approximation is claimed to be valid. Other important conclusions and recommendations drawn are: [6]

- The acceleration response of a single wave impact is deterministic [82], because the effects of a wave impact are damped out before the next wave impact occurs. This means that every wave impact is independent of other wave impacts. In addition, the acceleration response for a wave impact is unique and repeatable, when the set of load conditions for that wave impact remain constant.
- Due to the sensitivity of accelerometers, the measured acceleration time signal consists of rigid body accelerations and flexural motions [7]. The rigid body accelerations can be obtained by applying a response mode decomposition to the unfiltered acceleration record [6]. The decomposition can be done by using a low-pass filter [84][85][86]. The appropriate frequency for the filter can be determined with a Fourier analysis.
- In a wave impact event for HSC, multiple phases can be distinguished by studying the acceleration response, the velocity time history and the absolute vertical displacement [82]. It is important to distinguish these phases to correctly quantify the duration of the wave impact period.
- The shape of the rigid body acceleration pulse during the wave impact phase can be simplified to a half-sine pulse [88] [13]. The integral of the half sine pulse acceleration over time is the change in velocity due to the wave impact. This parameter is useful for quantifying the severity of a wave impact. The duration of the half-sine pulse follows from the wave impact phase.

The half-sine approximation is used in numerous studies and research [28] [10] [16] [26] [29] to simulate an wave impact in both computer simulations and testing facilities. In these studies, the half-sine pulse is used to design, develop and test SMS. However, not much attention is paid to the validity of the approximation or whether the parameters describing the pulse are chosen correctly. The research described in the next section on full-scale data measurements of wave impacts may indicate or provide correct values for the approximation of the wave impacts.

4.2. Full-Scale Wave Impact Measurements²

In research conducted by Coe et al. [7], the development of an laboratory test standard for the performance of various SMS is described. All authors are member of ISO TC108 SC4 WG18, which is the international technical group that is responsible for the standardization of laboratory evaluation of marine shock mitigating seats. The paper aims to provide help in selecting the most suitable design by testing multiple designs under controlled and repeatable conditions when all seats are exposed to the same excitation. The shape, peak amplitude and duration of the wave impact pulse are key parameters during testing. In this research, an acceleration pulse shape was defined, based on the results from the publication of NAVSEA [6]. The duration of the half-sine pulse was estimated based on the filtered acceleration data. The wave impact consists of the impact dominated phase and the hydrodynamic lift and buoyancy phase. In contrast to the publication of NAVSEA [6], this paper studied the vertical heave acceleration and the fore-aft surge acceleration to distinguish these phases. In the publication of NAVSEA [6], the acceleration response, velocity time history and the absolute vertical displacement were studied. Another publication of NAVSEA [30], recommends to use the acceleration response, velocity time history and the absolute vertical displacement in combination with the fore-aft surge acceleration to identify the impact duration. The combination of these methods seems a reliable approach to more likely determine the impact duration accurately.

In addition, the researchers gathered an extensive set of data during a large amount of head-sea trials in rough water. In these sea trials, the wave impact duration versus the peak acceleration was measured

²This section is based on the literature study [27]

for individual wave impacts on crafts from various weight classes. The results of these measurements are shown in figure 4.6. As an example, the FRISC has a weight of maximum 8000 [kg] [18]. Thus, the FRISC belongs to the weight class which is shown as blue circles 14000–18000 [lb] (≈ 6350 – 8165 [kg]). According to the data, this weight class experiences the largest magnitude peak accelerations of all examined weight classes.

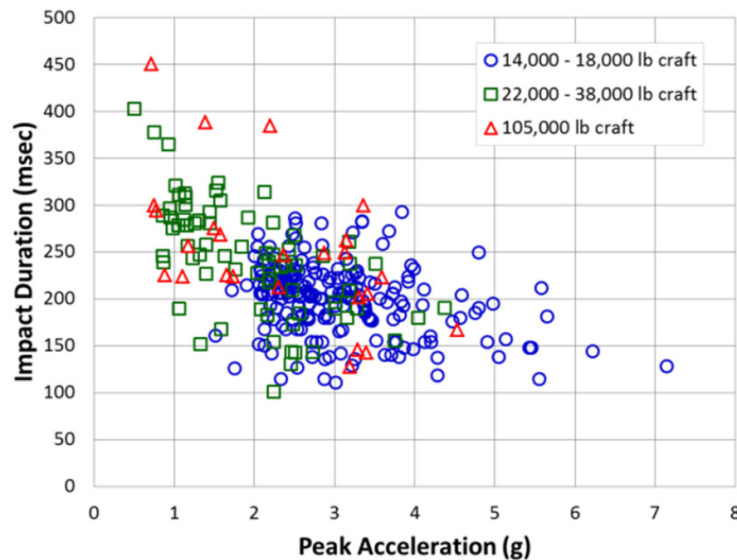


Figure 4.6: Full-scale data wave impact duration against peak acceleration [7]

The data in figure 4.6 indicates that the shortest duration of the impact is approximately 100 , regardless of the peak acceleration or weight class. Lower accelerations durations (2 to 50) are argued to be the result of large amplitude vibrations of unfiltered data that crossed the zero axis during the impact period. In the article a number of variables are discussed, which explain the variation in the impact duration of a given peak acceleration. These variables are craft weight, impact angle, wave height, speed, deadrise and the location of the impact [7] [30]. Based on these results, it is suggested that a minimum duration of 100 should be used to define a pulse shape [7] [30].

In later publications made by NAVSEA [28] [26] [29], laboratory test requirements for SMS are discussed and presented. For testing, six threshold levels are defined which resembles the severity of the wave impacts for different HSC classes. The peak acceleration increases per each threshold level. For a military class craft, the peak acceleration amplitude values of 3.0, 4.0, 5.0, 6.0, 8.0 and 10.0 [g]. The impact duration of the excitation pulse is defined as 100 for every peak acceleration independent of class type [28] [26] [29].

In one publication [26], the impact duration of 100 [ms] is chosen for testing as controlling long duration pulses requires a reconfiguration of the test apparatus. Additionally, the time and costs to test for multiple impact durations was considered costs prohibitive. The impact duration of 100 [ms] was chosen as the largest peak accelerations are observed for this duration according to Coe et al. [7]. Other publications [28] [29], define the impact duration of 100 [ms] without any argumentation. Although the existence of wave impacts with longer impact durations is acknowledged, the various impact durations seem to be neglected in the testing requirements. This decision seems contrary to the results presented by figure 4.6 as other combinations of impact duration and peak acceleration are measured as well and may result in more severe wave impacts.

4.2.1. KNRM Lifeboat Measurements

During the period of this research, full scale measurements of wave impacts have been conducted by TNO in corporation with the KNRM. The wave impacts were measured during sea trials on the lifeboat 'Edith Grondel', which is a boat of the Valentijn 2000 class. The boat is one of the seventeen vessels in her class built by Habbeke Shipyard. The lifeboat is designed such that it is fully self-righting. Self-righting is the ability of a vessel when it is capsized to the upright position without intervention. The lifeboat has a overall length of 11.0 [m], a beam length of 3.52 [m], a draft of 0.7 [m] and a weight of 10000 [kg]. The vessel is able to reach speeds up to 35 knots and sustain full power output for 6 hours [89] [8]. In figure 4.7, one of the vessels of the Valentijn class is shown.



Figure 4.7: KNRM lifeboat of the Valentijn class [8]

The accelerometers on the craft had a sample rate of 5000 [Hz]. The accelerometers were placed at the starboard side and port side of the craft on the base of two suspension seats. The raw data was smoothed with an moving average filter with the number of data points to average set at 77. The raw data was also filtered with low pass filtering techniques as these were often reported in literature [31] [1] [6] [7]. For example, a Butterworth low pass filter with a cutoff frequency of 20 [Hz] and 60 [Hz]. The results showed that the filtering technique was satisfactory in extracting the rigid body accelerations [9].

In figure 4.8, the acceleration record of three consecutive wave impacts is shown. Before each wave impact the figure clearly shows an acceleration level of -1.0 [g], indicating that the craft is in free fall. Upon impact with the wave, the acceleration levels increase to approximately 2.3 [g]. Immediately after the wave impact peak, the effects of buoyancy, hydrodynamic lift including propulsion are visible and result in a positive acceleration.

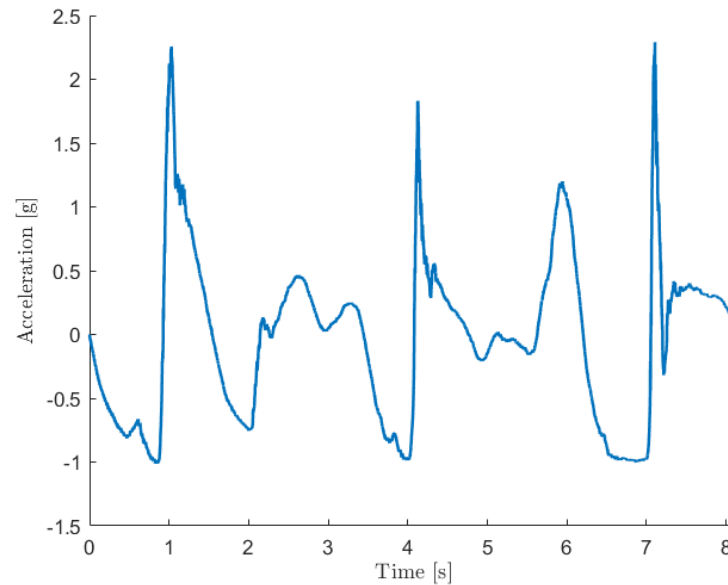


Figure 4.8: KNRM lifeboat deck level acceleration record including three consecutive wave impacts [9]

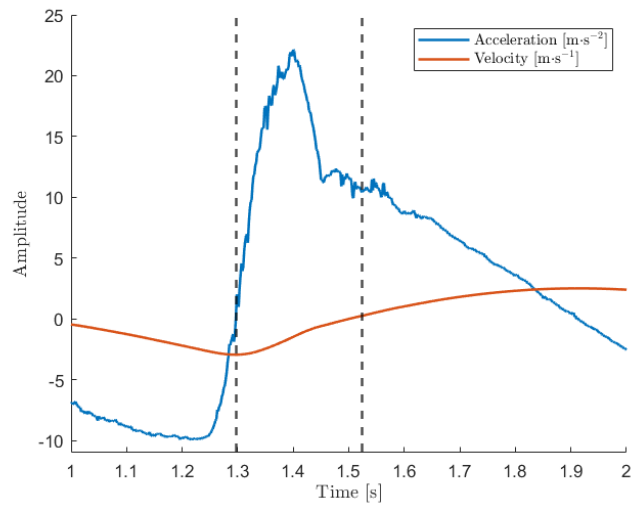
4.3. Application of the Half-Sine Approximation

In this section, the half-sine approximation will be applied to the KNRM lifeboat acceleration record. Subsequently, the validity of the half-sine approximation will be reviewed by analysing the response of a single DOF mass spring damper model to various excitation pulses.

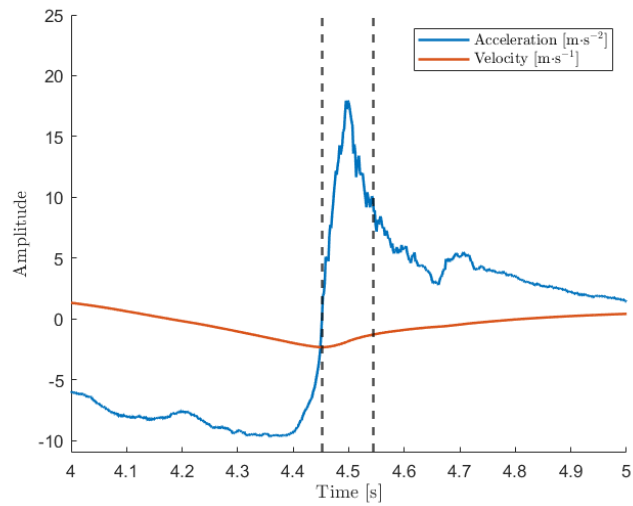
4.3.1. KNRM Lifeboat Acceleration Record

To study the wave impacts of the KNRM lifeboat acceleration record more closely, the individual wave impacts are extracted from the acceleration record. In figure 4.9, the wave impact deck level accelerations are shown per plot in combination with the vertical velocity. In addition, vertical dashed lines are drawn that indicate the phase of the wave impact. In table 4.1, the parameters for the wave impacts and the half-sine approximation of the wave impact are shown. The half-sine approximation and the acceleration record are shown in figure 4.10.

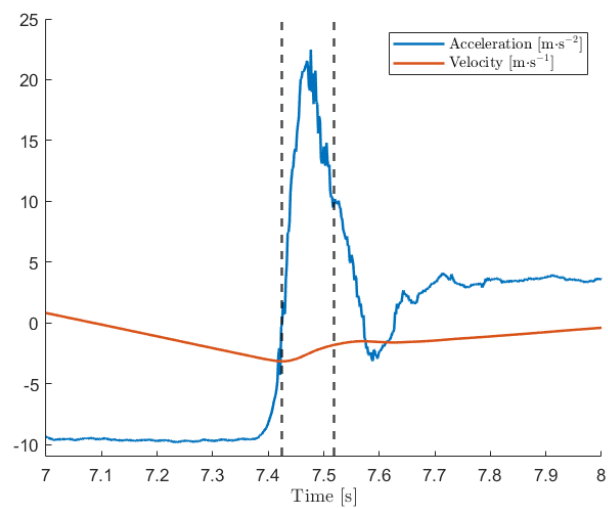
The wave impact phase is partially based on the description in section 3.1 by NAVSEA [6]. The starting point in time of the wave impact is defined when the velocity is at a minimum as shown in figure 4.9. However, the end point in time is not based on the method including the vertical velocity and vertical displacement as described by NAVSEA [6]. This method was used at first, but it would result in ambiguous results as the impact duration would exceed the experimental data found by Coe et al. [7]. This may be the result of the unknown initial position and initial velocity at the start of the acceleration record, which results in a total shift of the amplitude for both the position and velocity in time. Therefore, the end of the wave impact duration is based on the magnitude of the accelerations levels. The end of the wave impact dominated phase is when the acceleration has a value of approximately 1.0 [g] [6]. With this definition and a trial-and-error approach, the results in table 4.1 were obtained. In the last column, the error of the change in velocity for the half sine and measured acceleration excitation pulse is shown. The magnitude of these errors does not exceed a value of 1.0 [%], which is deemed to be sufficiently accurate to meet the conditions of the approximation. For further research on wave impacts it is recommended to study the fore-aft acceleration in combination with the vertical acceleration in order to define the wave impact phase. The combination of the acceleration records in both directions provides better insight in the the sequence of events for a wave impact event [6] [7].



(a) Wave impact one



(b) Wave impact two



(c) Wave impact three

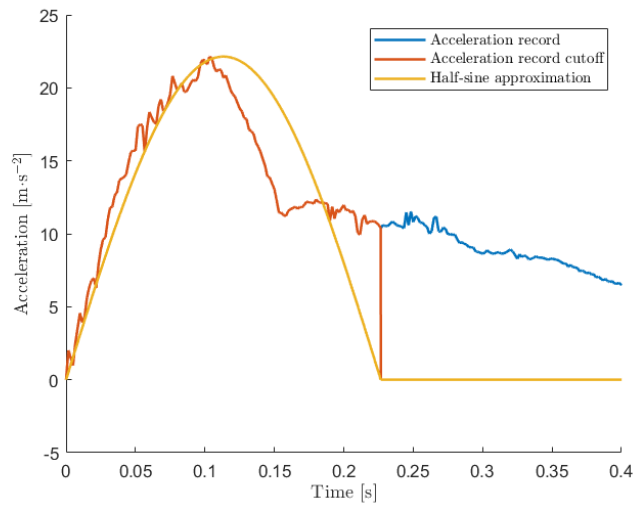
Figure 4.9: Individual wave impacts from the KNRM lifeboat acceleration record

Table 4.1: KNRM lifeboat acceleration record parameters of each wave impact

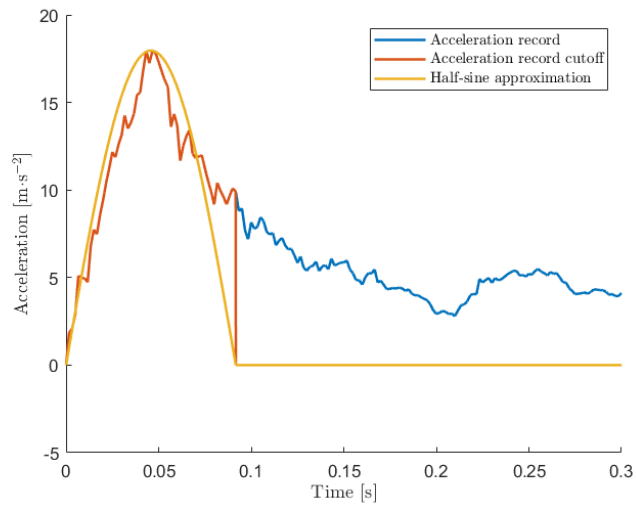
Wave Impact	Peak acceleration [g]	Impact Duration [ms]	Δv measured [$\text{m}\cdot\text{s}^{-1}$]	Δv half-sine [$\text{m}\cdot\text{s}^{-1}$]	Δv error [%]
1	2.257	226.667	3.195	3.195	-0.011
2	1.831	91.667	1.040	1.048	0.790
3	2.291	93.333	1.341	1.335	-0.434

In figure 4.10, the original acceleration record, the cutoff (beyond the impact phase) acceleration record and the half-sine approximation of the wave impact are shown. The figure shows that the curve of the half-sine pulse is smooth compared to the acceleration record, which is not unexpected as the acceleration record is the filtered rigid body acceleration of the measured acceleration. Additional filtering or smoothing of the rigid body acceleration would increase the smoothness. Before the acceleration peak, the slope (or jerk) of the half-sine pulse seems to approximate the average slope of the acceleration record quite well for wave impact one and wave impact three. The approximation for wave impact two is less accurate as the jerk of the half-sine pulse larger than the jerk of the acceleration record. As a result of the difference in the jerk, the time of the acceleration peak deviates more than for wave impact one and wave impact three. Past the acceleration peak, the half-sine pulse deviates strongly compared to the acceleration record. For wave impact one, the acceleration record quickly decreases to around $10 \text{ [m}\cdot\text{s}^{-2}]$ from which the acceleration value remains about constant. For wave impacts two and three, the curve of the half-sine pulse follows the acceleration record more closely. At the end of the impact duration, the half-sine pulse has a value of zero while in the acceleration record a positive acceleration is observed. The positive acceleration is the result of a combination of buoyancy, hydrodynamic lift, thrust and drag [6]. These forces result in a positive acceleration, but do not belong to the wave impact phase according to the definition of the wave impact phases [6].

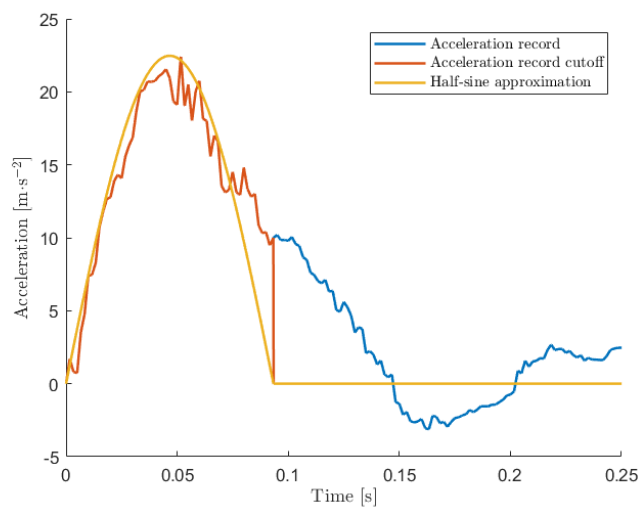
Compared to the data of Coe et al. 4.6, the severity of the wave impacts is not that extreme as both peak acceleration and impact duration are in the lower values of the data range. For wave impact two and three, the impact duration is slightly below the minimum threshold of 100 [ms]. Therefore, they can not be compared to similar wave impacts measured by Coe et al. An important note is that the lifeboat vessel of the KNRM has a mass of 10000 [kg] and thus belongs in the weight class of the green circles 22000–38000 [lb] (≈ 9980 – 17235 [kg]). However, the data points for the 14000–18000 [lb] craft (FRISC) and 22000–38000 [lb] craft overlap partially. More specifically, the overlap mostly within the data region with a peak acceleration of 2 to 4 [g] and with a duration of 100 to 250 [ms]. Wave impact one from table 4.1 fits within this region and is therefore assumed to be suited for analysis of SMS on a FRISC as well.



(a) Wave impact one



(b) Wave impact two



(c) Wave impact three

Figure 4.10: Half-sine approximation of the wave impacts from the KNRM lifeboat acceleration record

4.3.2. Comparison of the Half-Sine Approximation & Measurements

The half-sine approximation is extensively used for simulations in previous research [10] [16] and for determining criteria for shock mitigation tests and impact loading conditions [7] [13] [90] [91] [92] [93] [94]. However in recent literature [29], a value for the wave impact duration is stated which contradicts with full-scale data of wave impacts [7] shown in figure 4.6. The values for the peak acceleration agree across literature [7] [29]. In the publication of NAVSEA [29], an impact duration of 100 [ms] is taken for every peak acceleration level without any further argumentation. The literature [7] on experimental data from full scale tests shows that impact duration varies from 100 [ms] up to 450 [ms]. When a single value for the impact duration is chosen to represent the wave impacts across different peak acceleration levels, the severity of the wave impact may be seriously underestimated.

To review the validity of the half-sine approximation from literature [6], the response for both the wave impacts with the KNRM lifeboat and the half-sine approximation of the same wave impacts will be compared. For the comparison, the response of a three different single DOF mass-spring-damper models will be used. Such a model is described in the first section of appendix F. The models consist of two different masses, a linear coil spring element and a damper element. Each of the mass-spring-damper models is tuned to a specific natural frequency (f). In combination with a assumed damping ratio (ζ) the stiffness of the coil spring can be determined as the masses of the system are usually known. The damping ratio ζ describes at what rate the oscillations decay from one excitation to the next one. This ratio is usually defined as [44]

$$\zeta = \frac{c}{c_{crit}} = \frac{c}{2 \cdot \sqrt{k \cdot m_e}} \quad (4.1)$$

Where c is the damping coefficient, c_{crit} is the critical damping coefficient and m_e is the effective mass of the system. For a mass-spring-damper system with two masses, the effective mass is calculated as

$$m_e = \frac{m_1 m_2}{m_1 + m_2} \quad (4.2)$$

The damping ratio depends on the damping present in the system. Without damping the system would oscillate indefinitely. If the damping ratio is less than one, the system is underdamped and the motion is oscillatory until it decays completely [44]. If the damping ratio in the system is greater than one, the system is overdamped and the mass would return to its starting position without oscillating [44]. When the damping ratio is equal to one, the damping is equal to the critical damping coefficient and the system returns to its starting position with minimal amount of time required. This form of damping in the system is known as critically damped.

In practice, it is observed that the SMS usually have a critically damped or slightly overdamped system with a frequency around 2 [Hz] [9], which is confirmed by literature [95] [17] [11] [10]. This type of damping in the system is preferred in contrast to an underdamped system, because it results in lower shock transmissibility factors for dynamic amplification as shown in section 2.4.2. Additional reasons are that the person on the seat is less afflicted by long lasting oscillations after a wave impact and that a seat is designed to mitigate a shock from its initial position. Therefore, the seat should return to the initial position in the minimum amount of required time, which is the case for a critically damped system.

For the simulations, three models are generated with natural frequencies of 1.0 [Hz], 2.0 [Hz] and 3.0 [Hz]. The two masses in the system represent the craft and the seat with the occupant. The mass of the craft is $m_{craft} = 10000$ [kg], which resembles the lifeboat of the KNRM. The mass of the seat and the occupant (in this case a RNLN marine with its equipment) is $m_{seat} = 140.0$ [kg] [9]. Then, the effective mass results in $m_e = 138.067$ [kg]. The stiffness of the coil spring for the various models can be calculated with

$$k = \omega^2 m_e = (2\pi f)^2 m_e \quad (4.3)$$

It is assumed that the systems are critically damped and thus the damping coefficient can be calculated according to

$$c = c_{crit} = 2\sqrt{k m_e} \quad (4.4)$$

In table 4.2, the coil spring stiffness and damping coefficient for each mass-spring-damper model are shown.

Table 4.2: Critically damped mass-spring-damper model parameters for different natural frequencies

Natural Frequency [Hz]	Spring Stiffness [$\text{N}\cdot\text{m}^{-1}$]	Damping Coefficient [$\text{N}\cdot\text{s}\cdot\text{m}^{-1}$]
1	$5.451 \cdot 10^3$	$1.735 \cdot 10^3$
2	$2.180 \cdot 10^4$	$3.470 \cdot 10^3$
3	$4.906 \cdot 10^4$	$5.205 \cdot 10^3$

In figures 4.11 and 4.12, the acceleration response of the seat is shown for all three models. The acceleration applied at the base of the seat is the acceleration record from the sea trials with the KNRM lifeboat. The effect of bottoming is neglected in these simulations, thus the resulting accelerations may not be feasible in practice. The results do show what the influence of the natural frequencies is on the acceleration response.

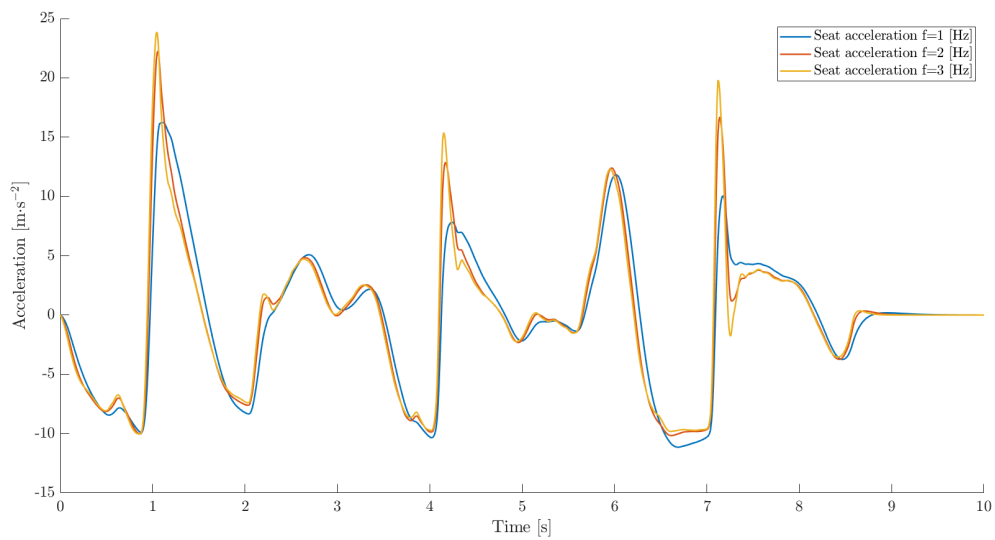


Figure 4.11: Acceleration response of models with different natural frequencies to the KNRM lifeboat acceleration record

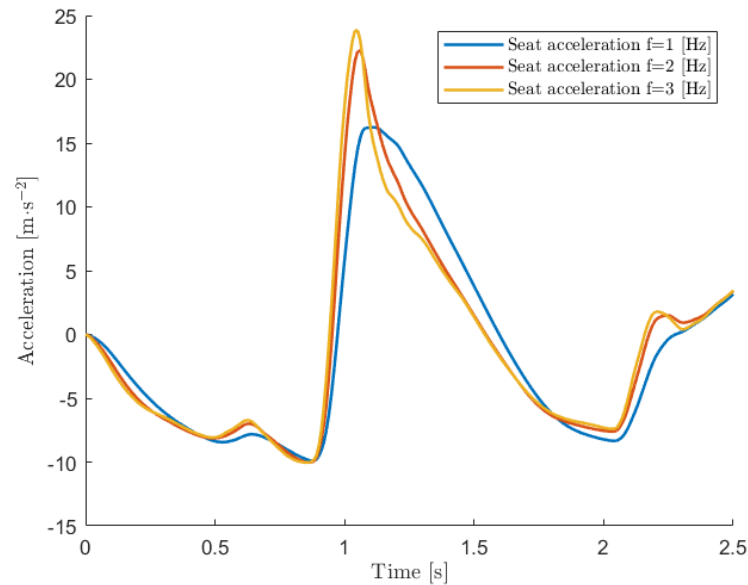
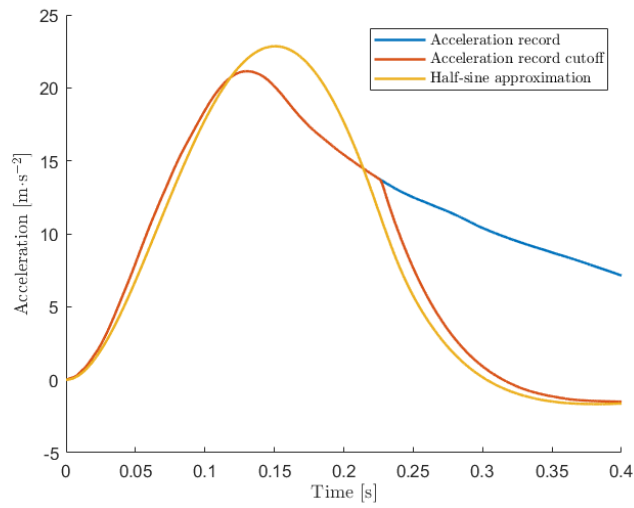


Figure 4.12: Zoomed in acceleration response of models with different natural frequencies to the KNRM lifeboat acceleration record

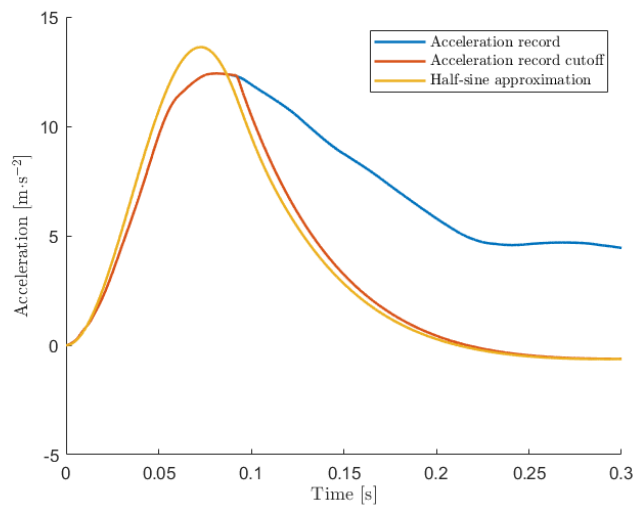
The results in figures 4.11 and 4.12 show that the the model with a natural frequency of 1 [Hz] mitigates the three present wave impacts in the signal. For increasing natural frequencies of the system, the acceleration response increases as well. The shock mitigation in terms of reducing the acceleration peak deteriorates, indicating that a critically damped system with low natural frequencies is desirable when the acceleration peaks of the wave impacts need to be mitigated. For a low natural frequency, the spring stiffness and damping coefficient have lower values resulting in a larger motion or required stroke of the spring. This increases the probability of bottoming, which may result in acceleration spikes as shown in section 2.4.1, appendix F and previous research [10] [16] [26].

From the acceleration record in figure 4.8, the three individual wave impacts were obtained and approximated using the half-sine approximation as shown in figure 4.10. In figure 4.13, the acceleration responses of the critically damped mass-spring-damper model with a natural frequency of 2 [Hz] for all excitation pulses of figure 4.10 are shown. The excitation pulses are used as deck level accelerations and are applied to the mass of the craft. The response is the resulting seat level acceleration. In the figure 4.13, the response to the original acceleration record is easily identifiable as both the half-sine pulse and the cutoff acceleration record deviate drastically from the response to the original acceleration record. This is a result of the positive accelerations beyond the impact phase which originate from a combination of buoyancy, hydrodynamic lift, thrust and drag [6]. These forces do not belong to the wave impact phase [6].

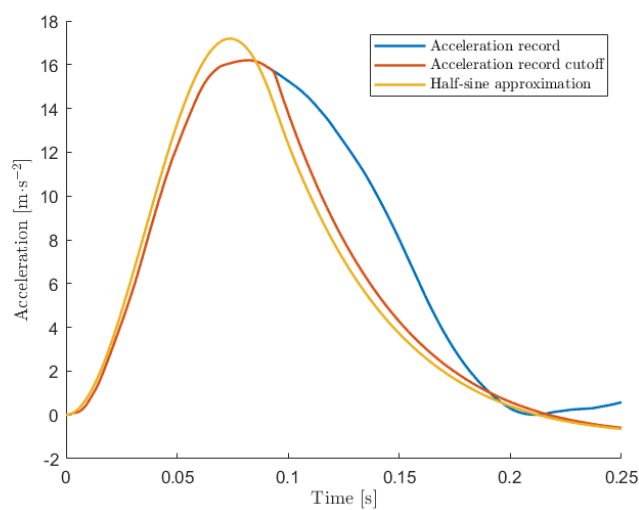
For the validation of the half-sine approximation, the differences in the response between the half-sine pulse and the cut off acceleration record interesting. The parameters for the half-sine pulse are chosen such that the total change in velocity is equal to the cut off acceleration record as is described in section 4.2.1. The parameters of the wave impacts are shown in table 4.1.



(a) Wave impact one



(b) Wave impact two



(c) Wave impact three

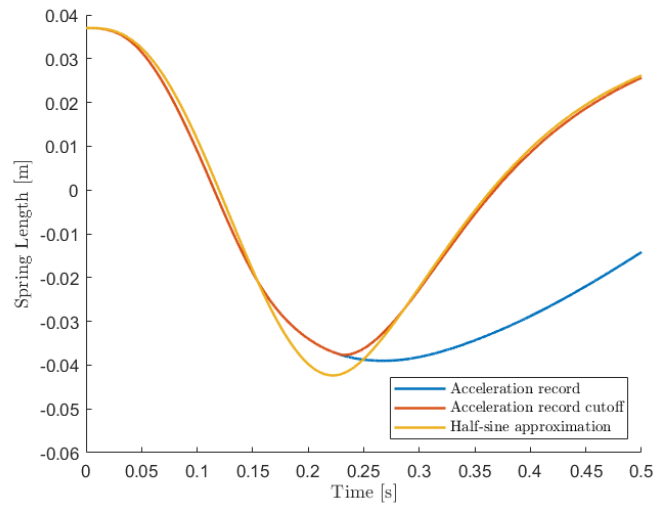
Figure 4.13: Acceleration response of the SMS to various accelerations of the craft

The figure 4.13 shows that for all three wave impacts the peak acceleration response of the half-sine pulse is larger than the peak acceleration response of the cut off acceleration record. For wave impact one, the peak acceleration response of the half-sine pulse even exceeds the peak acceleration of the craft, indicating that the shock is not mitigated. Due to the differences in the slope of the excitation pulses before the peak acceleration, the response for the cut off acceleration record tends to lag behind the response for the half-sine pulse as shown for wave impact two and wave impact three. Despite the lag in the responses, the overall shape of the response to the half-sine approximation and the response to the cutoff acceleration record are quite similar. The time at which the cutoff acceleration record varies from the original record is also clearly visible as at this moment in time the response instantaneously deviates. In table 4.3, the differences in the response for the peak acceleration value and occurrence of the peak acceleration in time are shown. The results in table 4.3 show that the maximum error of the acceleration peak in the acceleration response is less than 10 %, while the maximum absolute value of the error for the time of the acceleration peak is less than 16 %.

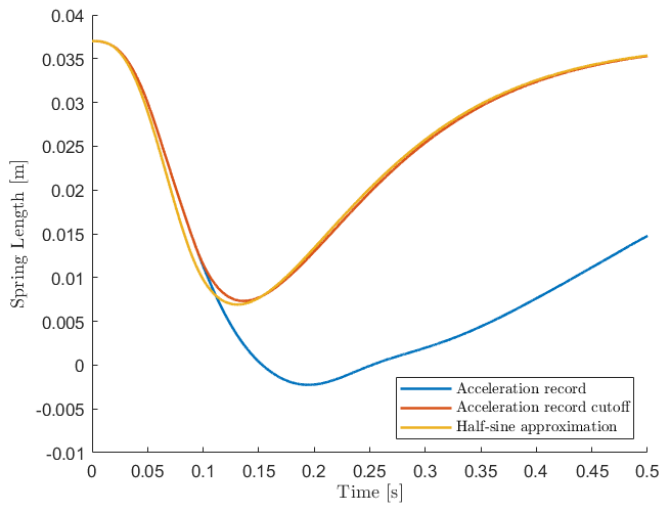
Table 4.3: Acceleration response differences for various accelerations of the craft

Wave Impact	Record acceleration [$\text{m}\cdot\text{s}^{-2}$]	Half-sine acceleration [$\text{m}\cdot\text{s}^{-2}$]	Acceleration error [%]	Record time [s]	Half-sine time [s]	Time error [%]
1	21.139	22.851	8.101	0.130	0.151	15.668
2	12.416	13.620	9.670	0.081	0.073	-10.578
3	16.201	17.190	6.104	0.082	0.074	-10.437

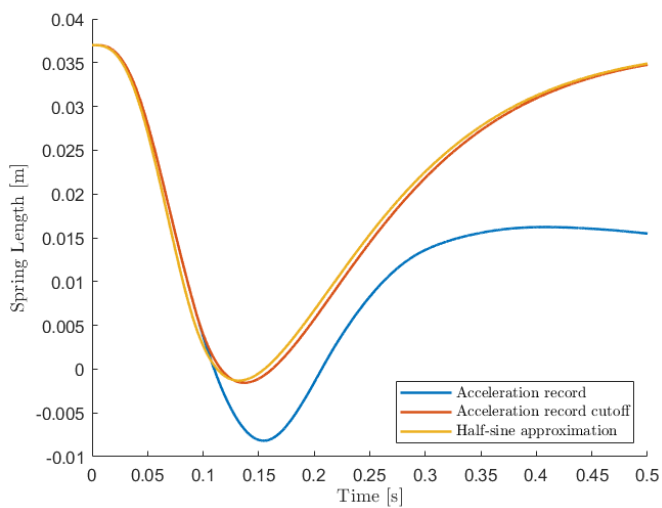
Another method to review the validity of the half-sine approximation is to study the displacement associated with the responses to the excitation pulses. The displacement can be important in order to determine the probability of bottoming. In figure 4.14, the spring length of the coil spring for all excitation pulses from figure 4.9 are shown. In figure 4.14, it is visible that the spring length has negative values for each wave impact. This shows that the mass of the craft has passed the mass of the seat. This result indicates that the suspension has bottomed out as a negative coil spring length is not possible. For these simulations the effect of bottoming is neglected for simplicity. Bottoming would increase the complexity of analysing and comparing the responses as large magnitude acceleration spikes would be present in the response.



(a) Wave impact one



(b) Wave impact two



(c) Wave impact three

Figure 4.14: Spring length of the model for various accelerations of the craft

In figure 4.14, the spring length for the original acceleration record is also clearly identifiable as the required stroke for wave impact two and wave impact three is much larger than the for the other acceleration inputs. This is the result from the remaining positive accelerations due to a combination of buoyancy, hydrodynamic lift, thrust and drag beyond the impact phase. The results of the response show a lag between the spring length for the cutoff acceleration record and the half-sine pulse, which is the result from the difference in the jerk before the acceleration peak. Overall, the response in spring length seems quite comparable for the cut off acceleration record and the half-sine pulse. In table 4.4, the differences in minimum spring length and occurrence of this length in time are shown. The results in table 4.4 show that the largest error of the minimum spring length is approximately 16 % and that the largest error of the occurrence in time for the minimum spring length is less than 5 %.

Table 4.4: Length of the spring for various accelerations of the craft

Wave Impact	Record minimum spring length [cm]	Half-sine minimum spring length [cm]	Spring length error [%]	Record time [s]	Half-sine time [s]	Time error [%]
1	-3.770	-4.235	12.341	0.233	0.222	-4.514
2	0.734	0.692	-5.626	0.136	0.131	-4.033
3	-0.156	-0.131	-16.018	0.137	0.132	-3.579

4.3.3. Validity of the Half-Sine Approximation

Based on the results from figures 4.13 and 4.14 and tables 4.3 and 4.4, the half-sine approximation is concluded to be a reasonable approximation for the wave impact phase with some minor manageable deficiencies. When comparing the responses to the cut off acceleration and the half-sine pulse, it was observed that the response for the half-sine pulse has a larger acceleration peak with an average error of 7.968 % as shown in 4.13. Between both responses a lag in time is noticed, which depends on the jerk of the acceleration record and the half-sine pulse. In contrast to the peak acceleration error, the results do not indicate a clear average error in time as shown in table 4.3.

The length of the spring for in the responses to the cut off acceleration and the half-sine pulse seems moderately comparable in terms of the minimum spring length. The error in the spring length does not indicate a clear average error as shown in table 4.4. For the occurrence of the minimum spring length in time, more clear results have been found. The average error in time is -4.402 %. An important note is that the effect of bottoming was neglected in these simulations and the results for the acceleration of the seat and the length of the spring may differ in practice.

An important note of the half-sine approximation is that by the definition of the wave impact phase, the positive acceleration as a result of the combination of buoyancy, hydrodynamic lift, thrust and drag is ignored. According to literature [6], these forces do not belong to the wave impact phase according to the definition, but in the simulations the influence of the resulting positive acceleration was not minor. The ignored resulting craft accelerations are below the threshold of $10 \text{ [m}\cdot\text{s}^{-2}]$, but they have a significant influence on the required stroke during the excitation period. The accelerations result in larger compression of the spring, which increases the required stroke and the probability for bottoming. Therefore, the half-sine approximation should not be used blindly without considering the remaining acceleration after the wave impact phase.

In conclusion, the half-sine approximation is a reasonable approximation of the wave impact phase only, but it underestimates the probability of bottoming as it ignores any accelerations beyond the wave impact phase. For laboratory testing purposes, the half-sine approximation offers some advantages as the method allows to easily and quickly generate various wave impacts by altering the two half-sine shape pa-

rameters; peak acceleration and impact duration. For designing purposes, it is recommended to disregard this approximation and use full-scale measurement data as the half-sine approximation underestimates the probability of bottoming.

4.4. Wave Impact Design Conditions

In this research, the wave impact excitation pulses will be based on the measurements on the KNRM lifeboat and on the full-scale data of Coe et al. [7] in combination with the half-sine approximation. In the figure 4.6, the wave impacts for three different weight classes measured at the longitudinal center of gravity are shown. As the FRISC belongs within the weight class of 14000 – 18000 [lb] (\approx 6350 – 8165 [kg]), these measurement results will be used to define various wave impact excitation pulses. Using the most extreme points of the cluster of data points, a trapezoid can be drawn as shown in figure 4.15. Most of the data points for the weight class fit within this trapezoid, except for some measured wave impacts with peak acceleration below 2 [g], but these wave impacts are not described as uncomfortable by HSC operators [26].

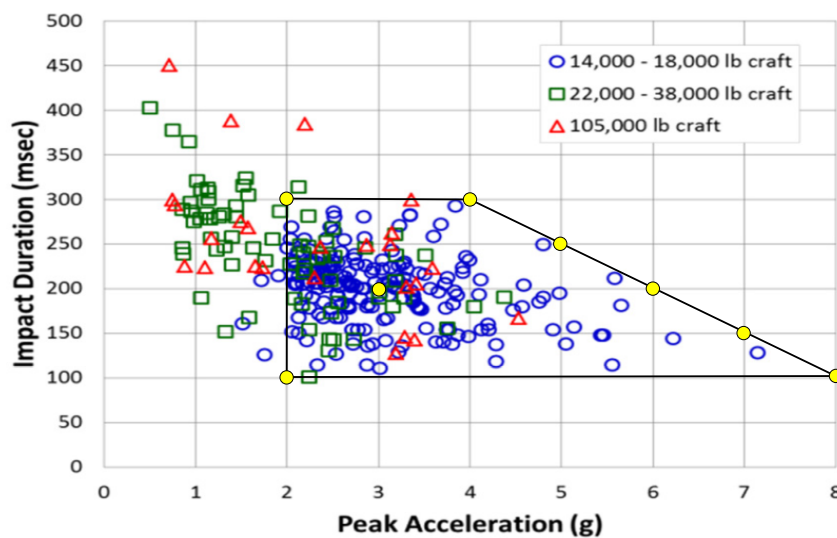


Figure 4.15: Selection of full-scale data of wave impacts for the FRISC class

In research conducted by the NLDA [10], an excitation pulse with a peak acceleration of 4 [g] and a impact duration of 200 [ms] was used. In research conducted by the TUD [16], four different excitation pulses were used with peak accelerations of 3.9, 4.8, 5.6 and 7.1 [g] in combination with impact durations of 290, 250, 210 and 135 [ms]. Based on previous research conducted by the NLDA [10] and TUD [16], a total of eight critical wave impacts excitation pulses are defined for the simulations and analysis in this research. The wave impact excitation pulses are shown in the first two columns of table 4.5. The selected wave impact excitation pulse parameters describe the most diverse wave impacts from the measurements, but also includes most of the excitation pulses used by previous research and studies[10] [16]. Instead of a excitation pulse with a peak acceleration of 4 [g] and a impact duration of 200 an pulse with a peak acceleration of 3 [g] and a impact duration of 200 is chosen. The reason for this is that based on the data points in the figure 4.15, the wave impacts at impact durations of 200 with lower peak accelerations are more common. Prior research has shown that the periods/frequencies of the excitation pulses as well as the eigenfrequencies of the SMS should be analysed [10] [16]. This was confirmed in section 2.4.2, where the phenomenon of dynamic amplification was described. It is important to identify the periods/frequencies of the excitation pulses in order to prevent a pulse-period mismatch and dynamic amplification. The selected wave impacts have durations that vary from 100 [ms] to 300 [ms] as can be seen from table 4.5.

Table 4.5: Parameters of the selected wave impact excitation pulses

Peak Acceleration [g]	Impact Duration [msec]	Change in Velocity [m·s ⁻¹]
2	100	1.249
2	300	3.747
3	200	3.747
4	300	7.494
5	250	7.807
6	200	7.494
7	150	6.558
8	100	4.996

In the literature, the severity of the wave impact is defined by the change in velocity due to the wave impact [7]. The half-sine pulse of a wave impact is described by both the acceleration peak and the peak duration. For a half-sine pulse, the area under the pulse can be simply calculated by integrating a sine function over half the period, which results in

$$\Delta v = \frac{a_p(2\Delta t)}{\pi} \quad (4.5)$$

Where a_p is the peak acceleration in [m·s⁻²] and Δt is the peak impact duration in [s]. With this equation, a contour plot can be generated which indicates the change in velocity for all combinations of peak accelerations and impact durations. The contour plot is shown in figure 4.16. In this figure, the contour lines display the change in velocity with increments of $\Delta V = 1.0$ [m·s⁻¹]. Figure 4.16 shows that the wave impact with a peak acceleration of 5 [g] and impact duration of 250 [ms] results in the most severe change in velocity of $\Delta v = 7.81$ [m·s⁻¹]. For all other selected wave impacts, the change in velocity is shown in the third column of table 4.5.

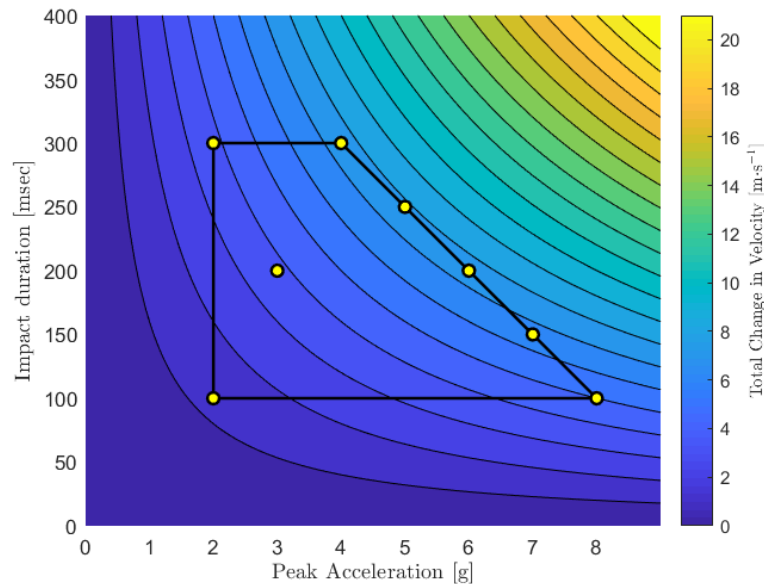


Figure 4.16: Total change in velocity contour lines for full-scale data of wave impacts for the FRISC class

The contour plot in figure 4.16 shows that if the impact duration is set to 100 [ms], more severe wave impacts with a larger change in velocity are neglected. The larger change in velocity can be realised with an impact

duration of 100 [ms], but this requires that the peak acceleration is increased. The required magnification may result in wave impacts that are not found during full-scale experiments. Additionally, the increase can result in less accurate analyses of the resulting (probability of) injury as the shape of the excitation pulse is altered. This alteration also changes the response of the seat (with respect to dynamic amplification) which has influence on the human tolerance to shocks as described in section 3.2. Therefore, it is recommended to not only test and simulate wave impacts with a duration of 100 [ms], but to vary both the impact duration and peak acceleration. The advantage is that the seat can be tested and designed for more effectively as the excitation pulses represent a wide range of realistic wave impacts. The disadvantage is that this may require a reconfiguration of the test apparatus and may involve high costs.

5

Case Study

In this chapter, the developed computer program and the results from previous chapters are used for a case study. The case study concerns two SMS designs which have been analysed in previous research. Both SMS are considered as an option for the application on a FRISC of the Royal Netherlands Navy.

5.1. Existing SMS Suspension Designs

In prior research and studies conducted by the NLDA [10] and TUD [16] two type of SMS suspension designs have been analysed, which are referred to as seat A and seat B. However, other types of suspension designs are also commercially available. In this section, the suspension designs of various companies within the SMS industry are briefly discussed.

Before, various existing suspension designs are discussed it is important to understand what the functions of SMS are. According to Coe et al. [7] and confirmed by other literature [10] the functions are:

- The seat should help the person remain in place while a craft is sailing and manoeuvring
- The seat should place the person in a stable position relative to any controls if applicable
- The seat should provide a comfortable contact surface. while avoiding any uncomfortable concentrations of pressure
- The seat should reduce the effects of any uncomfortable or potentially hazardous shocks and vibrations that would otherwise be experienced by the person

This shows that the mitigation of hazardous levels of RS or WBV is not the only function a SMS has. The other functions of a SMS may impose restrictions on the design. An example is that the operator on a SMS should stay in a relative stable position to any controls. In practice, this means that the movement of the operator on the seat is restricted when controls are mounted stationary on the deck of the craft. Further restrictions may be present from an operational view or other reason. Another example is that for the FRISC in the RNLN, the operators and crew on board must be able to quickly move from the seats without the need for unlocking many safety measures such as belts or straps. The ease of use of the SMS is also an important aspect for some operations. If the settings of the suspension design are adjustable, then they should be relative easy and adaptable in a short time [10]. Many more of such restrictions may exist and variations across different HSC types are likely to depend on the intended use of the craft.

Various SMS suspension designs are commercially available for HSC. Therefore, the suspension designs of SMS for military craft of five companies are compared. The results of this comparison are shown in table

5.1. In the table, three different types of suspension designs are identified. The three types are a parallelogram, fixed or pinned leaf spring and a rail with a gas-spring. The main difference besides the available stroke is the need for an additional spring or damper element.

Table 5.1: Overview of commercial SMS suspension designs

Seat	Suspension principle	Stroke [mm]	Additional spring	Additional damper
A	Parallelogram of pinned truss elements	150	Yes	Yes
B	Fixed parallel leaf spring	150	No	Yes
C	Fixed/pinned parallel leaf spring	200	No	Yes
D	Rail with gas cylinder	203/254	No	No
E	Rail with gas cylinder	203	No	No

In the design based on the rail with a gas cylinder, no additional damper is needed as the gas-cylinder functions as a gas-spring and a damper. This suspension design offers the longest available stroke length of the designs. In the suspension design based on fixed or pinned leaf spring, only an additional damper is needed. An disadvantage of this design seems to be that the spring-stiffness is non-adjustable. In the suspension design based on the parallelogram of truss elements, both an additional spring and damper are needed. This suspension design offers the shortest available stroke, but can be easily adjusted by altering the geometric properties of the parallelogram. An advantage of this suspension design is that the spring and damper can be relatively easily altered by swapping these elements for others.

In previous research only seat A and seat B were analysed. These designs will be discussed more in depth in the coming sections. The program developed in this research is able to model all five SMS from table 5.1. However, a disadvantage is that the characteristics of the suspension design are unknown. This includes characteristics such as geometrical properties and properties of the springs and dampers. These characteristics are kept confidential by the manufacturers, but can be determined using measurements and experiments as is done in previous research.

5.2. Previously Analysed SMS

In this section, the results from previous research on the SMS for the FRISC are discussed. Additionally, the models for both SMS designs are presented.

5.2.1. Previous Research Results

In previous research conducted at the NLDA [10], seat A was analysed by a bachelor student. In another research conducted at the TUD, the suspension of seat B was redesigned and analysed by a master student. With the use of their models, the influence of the following design parameters was investigated: spring preload, mass, spring stiffness, damping and length of the spring/damper combination [10] [16]. In this section, the most important results and recommendations from both studies will be summarised and discussed.

An increase of the spring preload shows that bottoming occurs after a longer period of time and at a higher acceleration level, which results in a smaller peak acceleration. When the spring preload is increased, the seat has an increased probability of reaching the spring limit in extension. In the analyses, the magnitude of the positive acceleration remained larger than the magnitude of the resulting negative acceleration. When the spring reaches its limit in extension, the person on the seat would either fly off or receive a jerk when the person is belted on the seat. Both cases can be unsafe or uncomfortable, thus the negative acceleration levels should be minimized as well [76].

An increase of the mass of the person results in an increased probability of bottoming as a larger stroke length is required. As the bottoming occurs earlier in time, the resulting acceleration peaks are increased. The increase of the seat mass also increases the inertia, which results in an increase of the lag between the motion of the seat and the base of the seat. A decrease of the mass of the person may cause the weight of the seat to not be large enough to overcome the preload of the spring. This means that a portion of the spring preload must be overcome by the accelerations. Another important aspect when varying the mass of the system is the influence on the eigenfrequencies. An increase of the mass results in lower eigenfrequencies. The eigenfrequencies of the system are important as dynamic amplification must be avoided in order to prevent large accelerations in the response of the seat. Dynamic amplification can also be prevented by the application of damping elements.

A decrease of the spring stiffness results in an increased compression of the spring and an increased probability of bottoming. As bottoming occurs at lower accelerations levels for a decreased spring stiffness, the resulting acceleration peak for bottoming is higher. The spring stiffness also influences the eigenfrequencies of the system. An increased spring stiffness results in higher eigenfrequencies. An important consideration of the spring is to what extent the stiffness of the spring is increased when the seat bottoms. The magnification of the spring stiffness strongly influences the resulting peak accelerations of the seat and the overshoot of the spring length. The magnification factor should therefore be correctly estimated.

An increase of the damping coefficient results in a decrease of the lag between the motion of the seat and the base as the relative motions between these are increasingly counteracted by the damper. Therefore, the probability of bottoming decreases and the time before bottoming occurs is increased. This results in a lower peak acceleration when bottoming does occur. The damping also influences the dynamic amplification of the system.

As mentioned previously, for a decreased spring stiffness, decreased damping coefficient or increased seat mass an increased stroke length is required in order to prevent bottoming. The length of the spring/damper combination was altered by increasing and decreasing the minimum spring length. Altering the minimum spring length does not result in a change of the behaviour of the suspension, but it does effect the probability of bottoming. An increase of the minimum spring length results in larger probability of bottoming and bottoming occurring earlier in time which results in larger acceleration peaks. A decrease of the minimum spring length decreases the probability of bottoming.

The most important conclusions and recommendations drawn are: [10]

- The effect of bottoming is predominantly responsible for the extreme accelerations experienced by the crew. Therefore, it is recommended to investigate ways of preventing the effect of bottoming.
- To reduce the probability of bottoming the spring travel, spring stiffness and damping coefficient should be increased.
- To improve the shock mitigating characteristics of seat A, the spring stiffness and damping should be decreased while the spring travel is sufficiently increased in order to prevent bottoming.
- The seat mass, spring stiffness and damping coefficient influence the eigenfrequencies of the system. The eigenfrequencies of the system and of the excitation pulses should be analysed in order to prevent dynamic amplification.

5.2.2. Seat A Model

In figure 5.1, seat A is shown. The picture of the seat shows the parallelogram of pinned truss elements and the combination of a coil spring and damper. The damper is a hydraulic damper with a progressive return stroke. The height of the seat can be adjusted to the length of a crew member by moving the the

spring-damper combination lower connection on the base of the seat. The location of the connection can be altered by a rotary knob. According to the manufacturer, the height of the seat can be adjusted with a maximum of 0.5 [m]. The coil spring is pre-loaded such that the initial position of the seat is always in the top position. The preload of the seat is adjustable to the weight of the crew member with specific tools. In addition, a handle is mounted on the top of the seat and the seat is covered with a layer of shock absorbing foam rubber for comfort and a layer of anti-slip material on top. The suspension of the seat is made of anodized aluminum and steel [10]. Depending on the model, the total mass of the seat is 21.5 [kg] or more.



Figure 5.1: Seat A

The model of seat A is based on a the model used in previous research [10]. A schematic representation of this model is shown in figure 5.2. The suspension is described by the points 1 to 6. Point 0 represents the center of gravity for the base of the seat and point 7 the center of gravity for the seat which includes the mass of the person. In table 5.2, the values for the parameters describing the suspension are shown. In the model of the seat, the location of point 5 is adjustable by altering the value of length L_j . As the spring is pre-loaded, the initial position of the seat is at the maximum length of L_{56} .

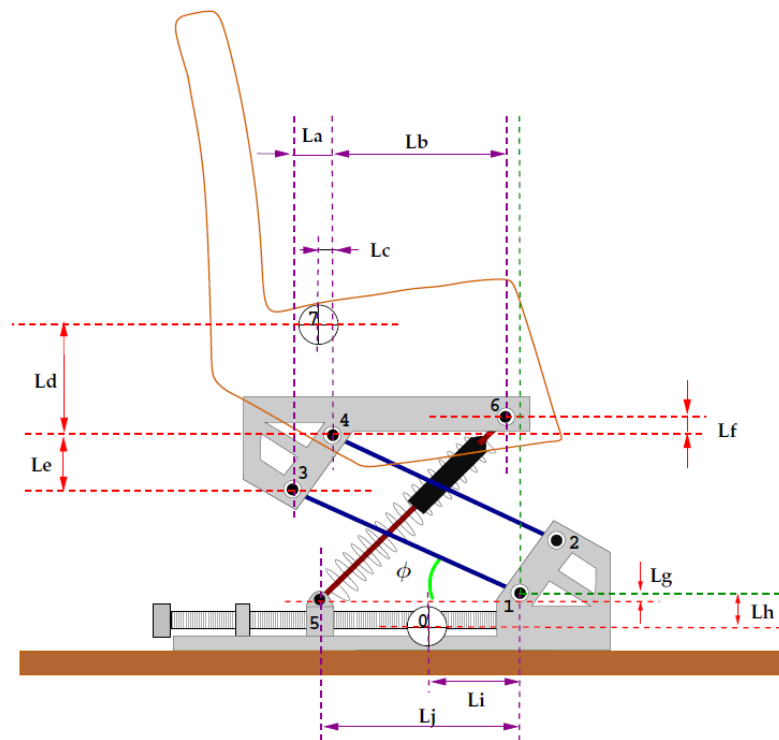


Figure 5.2: Schematic representation of seat A [10]

Table 5.2: Seat A dimensions [10]

Lengths	Value [m]
L_a	0.08
L_b	0.102
L_c	0.03
L_d	0.38
L_e	0.104
L_f	0.05
L_g	0.013
L_h	0.06
L_i	0.15
L_j (max)	0.215
L_j (min)	0.075
L_{13}	0.252
L_{56} (max)	0.304
L_{56} (min)	0.233

In figure 5.3, the FEM model of seat A is shown. In this figure the values of the variable lengths are $L_j = 0.145$ and $L_{56} = 0.304$. The jockey seat is modelled with nine non-linear bar elements and a combination of a damper with an coil-spring element. The connections between all elements are modelled as hinges, but the rotation of the nodes is restricted. The center of gravity (point 0) for the base of the seat is not modelled as this will not be used during any simulations in this research. The center of gravity (point 7) for the seat and the person is modelled and fixed to the seat by two triangular constructions. The bar elements are implemented as massless. The mass of the system is manually divided of the nodes by the use of point masses.

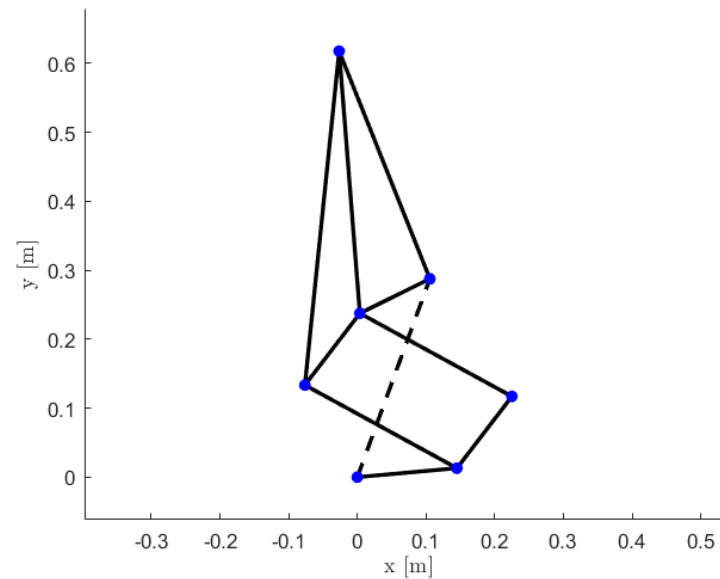


Figure 5.3: Seat A model

5.2.3. Seat B Model

In figure 5.4a, seat B is shown. In the figure 5.4b the redesigned suspension design of seat B is shown. Both seats are based on a parallel leaf spring, which is clamped on both ends. Damping in the suspension is not based on friction, but achieved by a separate piston damper. A clear advantage of the suspension design is the simple geometry. However, this advantage is not without some disadvantages. The disadvantages are; the height of the seat is not variable, the leaf spring stiffness is not adjustable and the leaf spring is not pre-loaded. The seat plus base has a weight of 24 [kg] and the seat without base a weight of 17 [kg]. Furthermore, the seat is covered with extra padding and it is shaped such that the operator is seated with an upright body posture. The main differences with the redesigned suspension design is the number and shape of the leaf springs. The alteration significantly improves the maximum allowed compression.

The plates for the leaf spring are made of a thermoset composite [16]. The glass fibres used are Hexforce 7581 and the resin used is Epikote 04908. The material characteristics for the composite are shown in table 5.3. After analysis in both MATLAB and ABAQUS, the layup $[(0/90)_4(\pm 45)_2(0/90)_4(\pm 45)_2(0/90)_4]_S$ was selected for the leaf spring. The dimensions per plate are a length of 600 [mm], a width of 150 [mm] and a thickness of 7.23 [mm].



Figure 5.4: Seat B

Table 5.3: Leaf spring Hexforce/Epikote material characteristics [16]

Type	Parameter	Value	Unit
Longitudinal modulus	E_1	24	GPA
Transverse in-plane modulus	E_2	23	GPA
In-plane shear modulus	G_{12}	3.52	GPA
Out-of-plane shear modulus	G_{23}	2.51	GPA
Out-of-plane shear modulus	G_{13}	2.24	GPA
Major in-plane Poisson's ratio	ν_{12}	0.14	-
Thickness per ply	t	0.23	mm

The developed program in this research is not able to model various plies of a composite. Therefore, the macro mechanical properties of the plate are calculated with the Classical Laminate Theory (CLT). The basis of the CLT is the classical plate theory, which for homogeneous plates is based on the Kirchhoff hypothesis [96] [97]. The Kirchhoff assumptions for a homogeneous plate are: [96] [97]

- Deflections of the mid-surface are small compared to the thickness.
- The mid-plane is unstrained when subjected to pure bending.
- Plane sections normal to the mid-plane remain normal after bending
- Transverse normal stresses to the mid-plane are in-extensible and may be neglected in stress-strain relations.

For an anisotropic laminate consisting of N stacked orthotropic plies, the total thickness is defined as

$$t = \sum_{k=1}^N t_k \quad (5.1)$$

Where t_k is the thickness of the k -th layer. The middle surface has coordinate $z=0$, thus the k -th layer has a coordinate which is $z_{k-1} \leq z \leq z_k$ while the outer plies have $z_0 = -\frac{t}{2}$ and $z_N = \frac{t}{2}$. With the coordinates the resultant force per unit length are calculated as

$$\vec{N} = \begin{pmatrix} N_x \\ N_y \\ N_{xy} \end{pmatrix} = \int_{-\frac{t}{2}}^{\frac{t}{2}} \begin{pmatrix} \sigma_x \\ \sigma_y \\ \tau_{xy} \end{pmatrix} dz = \sum_{k=1}^N \left(\int_{z_{k-1}}^{z_k} \begin{pmatrix} \sigma_x \\ \sigma_y \\ \tau_{xy} \end{pmatrix}_k dz \right) \quad (5.2)$$

and the resultant moments per unit length as

$$\vec{M} = \begin{pmatrix} M_x \\ M_y \\ M_{xy} \end{pmatrix} = \int_{-\frac{t}{2}}^{\frac{t}{2}} \begin{pmatrix} \sigma_x \\ \sigma_y \\ \tau_{xy} \end{pmatrix} z dz = \sum_{k=1}^N \left(\int_{z_{k-1}}^{z_k} \begin{pmatrix} \sigma_x \\ \sigma_y \\ \tau_{xy} \end{pmatrix}_k z dz \right) \quad (5.3)$$

The composite laminate constitutive relations relate the forces and moments to the strains and curvature using the ABD matrix. The relations are derived using the classical plate theory and are defined as

$$\begin{pmatrix} \vec{N} \\ \vec{M} \end{pmatrix} = \begin{bmatrix} [A] & [B] \\ [B] & [D] \end{bmatrix} \begin{pmatrix} \vec{\epsilon} \\ \vec{\kappa} \end{pmatrix} \quad (5.4)$$

Where \vec{N} is the forces vector, \vec{M} the moments vector, $\vec{\epsilon}$ the strains vector and $\vec{\kappa}$ the curvatures vector. The coefficients in the ABD matrix can be calculated according to

$$\begin{aligned} [A] &= \sum_{k=1}^N [\bar{Q}_k] (z_k - z_{k-1}) \\ [B] &= \sum_{k=1}^N [\bar{Q}_k] \frac{z_k^2 - z_{k-1}^2}{2} \\ [D] &= \sum_{k=1}^N [\bar{Q}_k] \frac{z_k^3 - z_{k-1}^3}{3} \end{aligned} \quad (5.5)$$

Where the reduced transformed stiffness matrix of ply k $[\bar{Q}_k]$ is the product of the transformation matrix $[T_k]$, the stiffness matrix $[Q_k]$ and the strain matrix $[R]$. The strain matrix is required to transform from tensorial strain ϵ_{12} to engineering shear strain $\gamma_{12} = 2\epsilon_{12}$.

$$[\bar{Q}_k] = [T_k]^{-1} [Q_k] [R] [T_k] [R]^{-1} \quad (5.6)$$

The matrices are defined as

$$\begin{aligned} [Q_k] &= \begin{bmatrix} \frac{E_1}{1 - \nu_{12}\nu_{21}} & \frac{\nu_{12}E_2}{1 - \nu_{12}\nu_{21}} & 0 \\ \frac{\nu_{12}E_2}{1 - \nu_{12}\nu_{21}} & \frac{E_2}{1 - \nu_{12}\nu_{21}} & 0 \\ 0 & 0 & G_{12} \end{bmatrix} \\ [T_k] &= \begin{bmatrix} \cos^2 \theta & \sin^2 \theta & 2 \sin \theta \cos \theta \\ \sin^2 \theta & \cos^2 \theta & -2 \sin \theta \cos \theta \\ -\sin \theta \cos \theta & \sin \theta \cos \theta & \cos^2 \theta - \sin^2 \theta \end{bmatrix} \\ [R] &= \begin{bmatrix} 1 & 0 & 0 \\ 0 & 1 & 0 \\ 0 & 0 & 2 \end{bmatrix} \end{aligned} \quad (5.7)$$

Where θ is the orientation of the ply in the x-y plane of the coordinate system. The chosen layup of $[(0/90)_4(\pm 45)_2(0/90)_4(\pm 45)_2(0/90)_4]_S$ has some advantages which can be used to simplify the ABD matrix. The layup is symmetrical and therefore unwanted membrane/bending coupling is eliminated, meaning

that the matrix $[B] = 0$ [98]. Additionally, the layup is balanced as for every ply with a positive angle or orientation, there is also a mirrored ply. Therefore, the layup is considered to be balanced and thus eliminates stretching/shearing coupling $A_{16} = A_{26} = 0$ [98]. Furthermore, many plies with a orientation of $\theta = 0^\circ$ are placed as far away as possible from the neutral axes. This placement improves the bending stiffness D_{11} of the composite [98]. With the data from table 5.3, the ABD is calculated. The result is

$$\begin{aligned} [A] &= \begin{bmatrix} 1.637 \cdot 10^8 & 0.367 \cdot 10^8 & 0.0 \\ 0.367 \cdot 10^8 & 1.637 \cdot 10^8 & 0.0 \\ 0.0 & 0.0 & 0.384 \cdot 10^8 \end{bmatrix} [\text{N}\cdot\text{m}^{-1}] \\ [B] &= \begin{bmatrix} 0.0 & 0.0 & 0.0 \\ 0.0 & 0.0 & 0.0 \\ 0.0 & 0.0 & 0.0 \end{bmatrix} [\text{N}] \\ [D] &= \begin{bmatrix} 747.667 & 157.668 & 0.0992 \\ 157.668 & 746.477 & 0.0992 \\ 0.0992 & 0.0992 & 165.588 \end{bmatrix} [\text{N}\cdot\text{m}] \end{aligned} \quad (5.8)$$

From the ABD matrix, the stiffness and the bending stiffness can be calculated using the width of the plate $b = 0.15$ [m] according to

$$\begin{aligned} EA &= \int_0^b A_{11} dy = A_{11}b \\ EI &= \int_0^b D_{11} dy = D_{11}b \end{aligned} \quad (5.9)$$

Some important notes regarding the resulting values and descriptions in the research [16].

- Contradicting values regarding the dimensions of the plates have been reported in the research. This concerns dimensions such as laminate thickness and ply thickness. It remains unclear which of the reported values is correct.
- The author conducted static displacement tests and compared the results with a finite element model in ABAQUS, but has failed to report any macro mechanical properties of the produced leaf spring or an ABD matrix of the composite. Therefore, it is not possible to validate the obtained results in the above calculation.

Although there are some uncertainties and limited data is available, some static simulations have been performed with the C-shaped composite leaf spring suspension. In figure 5.5a, the model of the redesigned seat B is shown. For the model, the large rotation beam elements are used. The model is based on the geometric properties used in the ABAQUS model of Stouten [16] and the discussed composite leaf spring. Figure 5.5b shows the deformed C-shaped composite leaf spring suspension. For the analysis, a load of 2000 [N] to 2500 [N] was applied to the node where the seat is normally mounted. In figure 5.6, the results of the static analysis and the results from the research of Stouten are shown [16]. Stouten presented three force-displacement curves which are derived or calculated with an analytical deviation, a finite element model in ABAQUS and with experiments on the produced prototype. The other curves in the figure represent the static simulations of the C-shaped composite leaf spring suspension with a varying number of elements.

The results in figure 5.6 show that when the number of elements for the leaf spring is increased, the results converge to a solution. This is expected and discussed in appendix C for another structure. The curves show that as the number of elements increases the deflection increases too. However, as the deflection increases the program was unable to calculate the deflection to a load of 2500 [N]. This behaviour was unexpected, but it is suspected to be the result of deficiencies in the model. More specifically, in the joint where the double leaf springs are connect to each other. For this joint, several assumptions had to be made which may have lead to the deficiency in the model.

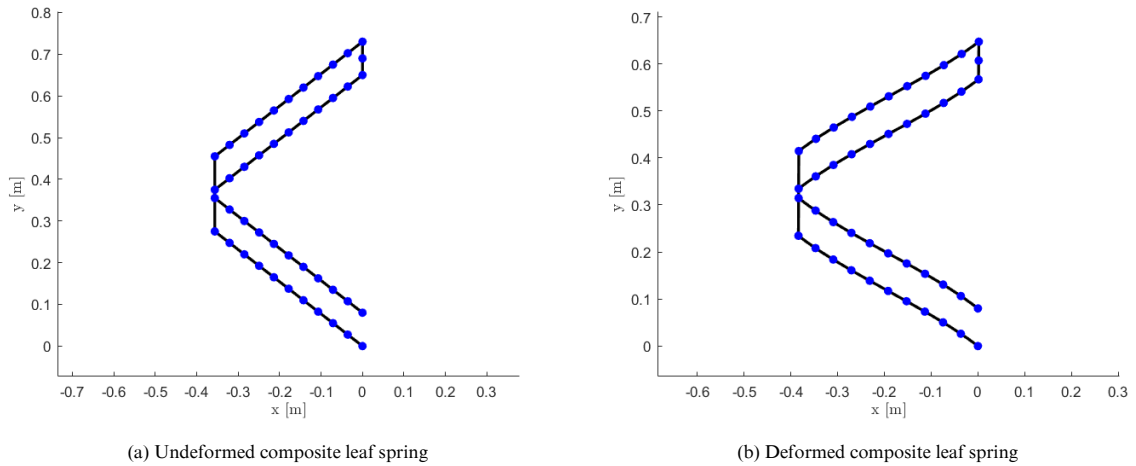


Figure 5.5: C-shaped composite leaf spring seat model

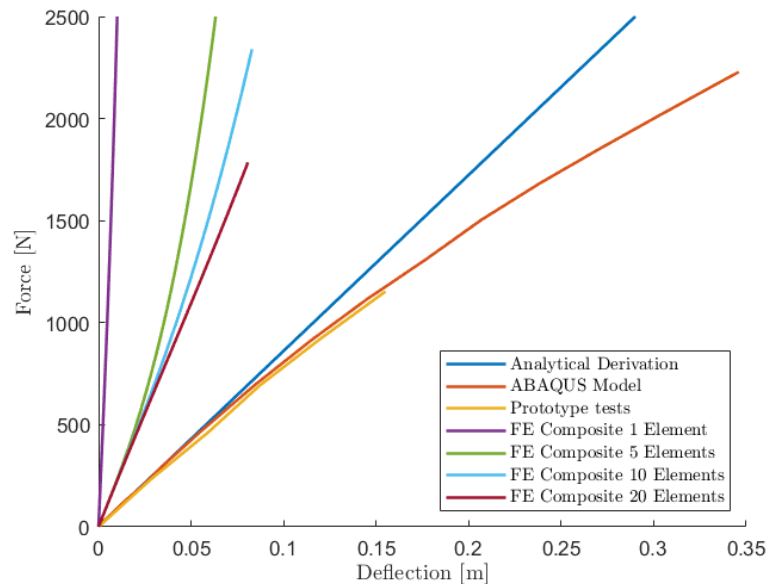


Figure 5.6: Comparison of the resulting deformations for various models of C-shaped composite leaf spring suspension

Furthermore, the results obtained with the static simulations differ drastically from the results presented by Stouten [16]. Not only the values differ, but also the gradient of the curve. The curves presented by Stouten are degressive, while the results from the static simulations are progressive. The difference could be caused by several reasons:

- Inaccurate model of the produced prototype as contradicting geometrical properties are reported.
- Either the CLT is inappropriate to calculate the macro mechanical properties of the plate or the used Hexforce/Epikote material characteristics are not accurate enough.
- The bending stiffness calculated via the ABD matrix includes the Poisson ratio and thus the Poisson effect, while this effect is not taken into account in the beam elements of the finite element program.

Based on the obtained results with the C-shaped composite leaf spring suspension model, the following actions are recommended.

- Investigation of the geometrical properties of the suspension.
- Investigation of the macro mechanical properties of the leaf spring plates.
- Investigation of a method to accurately model the macro mechanical behaviour of the suspension in combination with another convergence study. Special attention should be given to the modelling of the joint that connects the leaf springs.

5.3. Proposed Design

In this section, a new design is proposed based on of the previously analysed designs. Subsequently, the proposed design is described and geometrical variations are analysed.

In this research, the author has chosen to continue the case study with an in depth analyses of seat A. The choice to further analyse seat A over seat B is supported by the following arguments:

- Currently, all the FRISC of the RNLN are equipped with seat A. From the perspective of the RNLN, specifically the materials department DMO, it is more beneficial to implement another element in or to slightly alter the design of the current seats than to replace all seats with another seat design. An replacement of all seats would involve high costs compared to implementing an alteration.
- The standard and altered seat B are not accurately described in the previous research [16], which means that a lot of assumptions have to be made regarding geometrical properties or macro mechanical behaviour. This would lead to a less accurate model and in turn to a less meaningful case study. On the other hand, seat A is very well described in previous research [10].

Based on the suspension design of seat A described in section 5.2.2, a new design is proposed which integrates a gas-spring instead of a coil spring element. The gas spring may prevent acceleration spikes resulting from bottoming as the stiffness of the gas-spring increases gradually. The parameters for the proposed design model are shown in table 5.4. Most of the parameters are based on values used in prior research [10]. A damper is not yet included in the model, because first the undamped response will be analysed. However, the mass of the damper is included as this will be important for the response. For the gas-spring, the maximum and minimum length are based on the extreme lengths of the coil spring. Furthermore, a diameter of 0.05 [m] and a circular cross-section are assumed. The initial pressure of the gas-spring is such that when no occupant is seated, the piston inside the gas cylinder is in the top position. The gas spring k represents the stiffness of the element when it bottoms out in extension. The non-linear bar elements are regarded as very stiff elements, which is realised with large values for the modulus of elasticity and cross-sectional area.

Table 5.4: Proposed design model parameters

Parameter	Value	Unit
Gravity constant	9.81	[m·s ⁻²]
Mass seat	18	[kg]
Mass of person on seat	70	[kg]
Mass truss elements	2	[kg]
Mass damper element	2	[kg]
Mass gas-spring element	2	[kg]
Mass total	94	[kg]
Non-linear bar E	$1.0 \cdot 10^7$	[N·m ⁻²]
Non-linear bar A	1.0	[m ²]
Non-linear bar ρ	0.0	[kg·m ⁻³]
Gas-spring L_{pr}	0.233	[m]
Gas-spring L_0	0.071	[m]
Gas-spring L_{max}	0.304	[m]
Gas-spring L_{min}	0.233	[m]
Gas-spring p_0	1.299	[bar]
Gas-spring A_0	0.001963	[m ²]
Gas spring γ	1.4	[-]
Gas spring δ	0.05	[-]
Gas spring k	$36.0 \cdot 10^4$	[N·m ⁻¹]

5.3.1. Variation of the Geometrical Properties

In this section, geometrical variations and their influence on the natural frequencies is investigated. For the analyses, two geometrical parameters will be varied. These are the length of the truss elements (L_{13}) and the length between the lower mounting point of the spring-damper combination and the mounting point of the truss elements (L_j). For an illustration of the model, see figure 5.2.

First, the influence of the parameters on the available stroke will be analysed. In figure 5.7, the length of the gas-spring damper combination is shown against the angle of point 1 for various lengths of the truss elements of the parallelogram. The black lines in the figure indicate the extreme lengths of the gas-spring damper combination. When the angle of point 1 is equal to zero, then the seat is at the same height as the base. The figure shows that for a length of $L_{13} = 0.202$ [m] with $L_j = 0.215$ [m], this will occur before the gas-spring damper combination has reached its minimum length. This result indicates that seat may impact the deck before the gas-spring damper combination is able absorb all the energy of the excitation pulse. Therefore, this design configuration is deemed as unsuitable. For all other combinations of L_{13} and L_j , this effect will not happen as is shown in figure 5.7. In the case that the gas-spring damper combination is replaced with other elements that allow even more spring travel the available height (or travel) of the seat before it impacts the deck becomes important. Therefore, for the same combinations of L_{13} and L_l the maximum height of point 3 of the seat is shown in figure 5.8. In figure 5.9, four of the undeformed structures for extreme values of L_{13} and L_j are shown. In the figures it is clearly visible that for the lengths of $L_{13} = 0.202$ [m] and $L_{13} = 0.352$ [m] the motion of the seat is approximately circular and that during excitation the seat will accelerate in the horizontal direction in addition to the vertical direction.

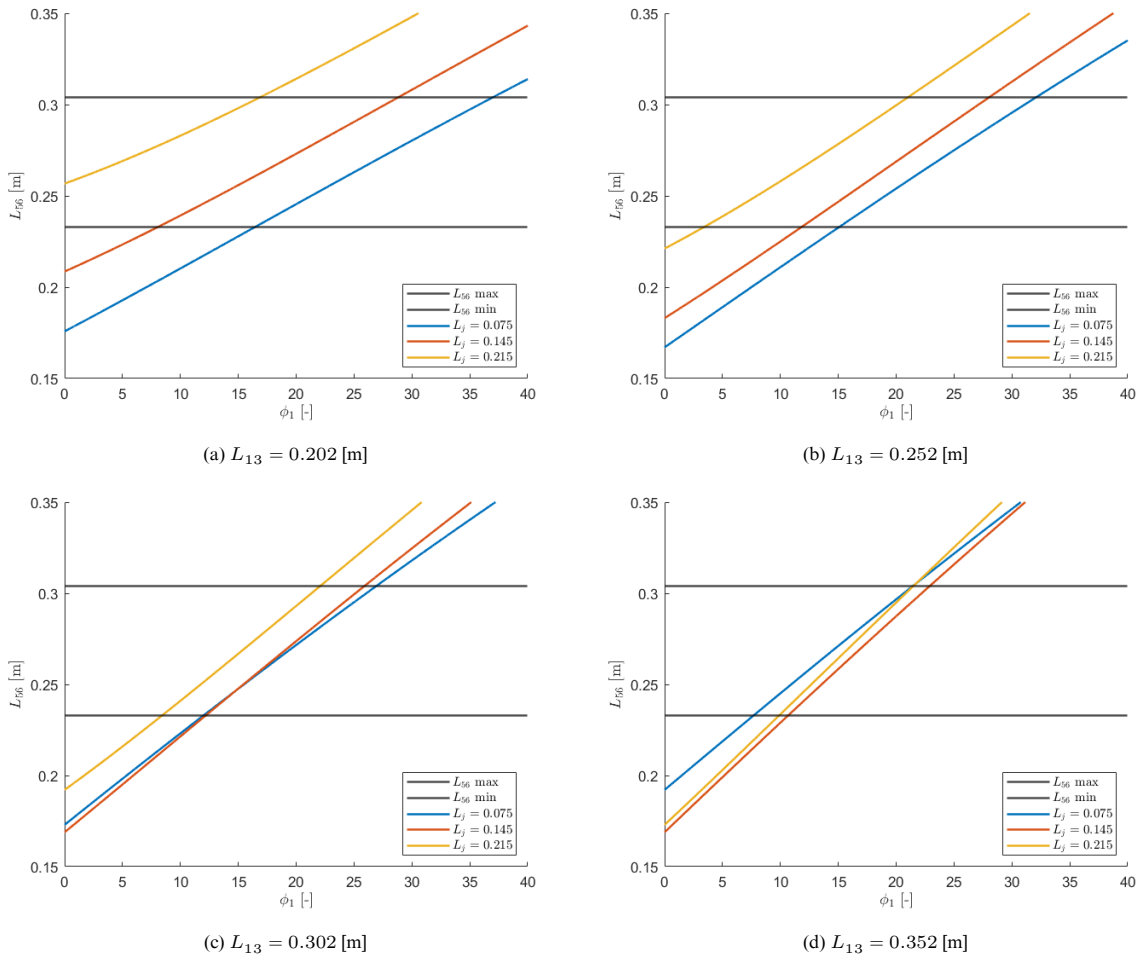


Figure 5.7: Seat A model available stroke length for different values of L_{13}

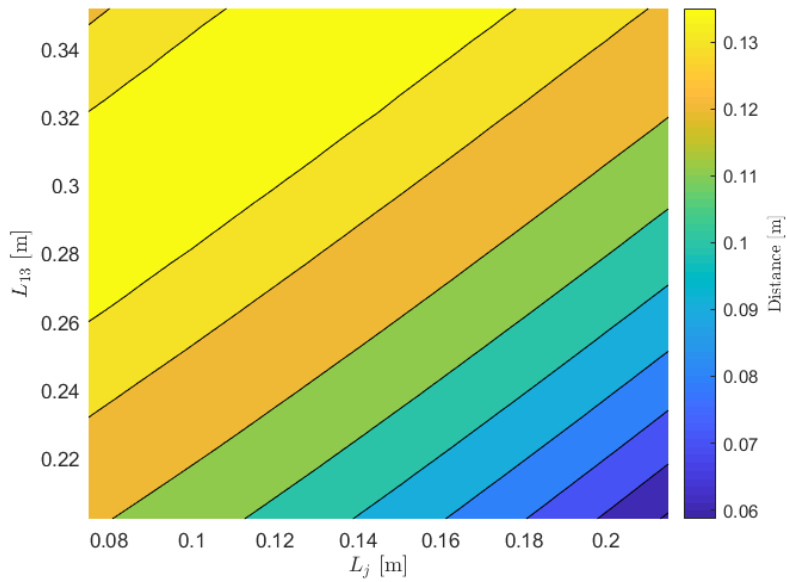


Figure 5.8: Seat A model maximum height of the seat structure with respect to y_1

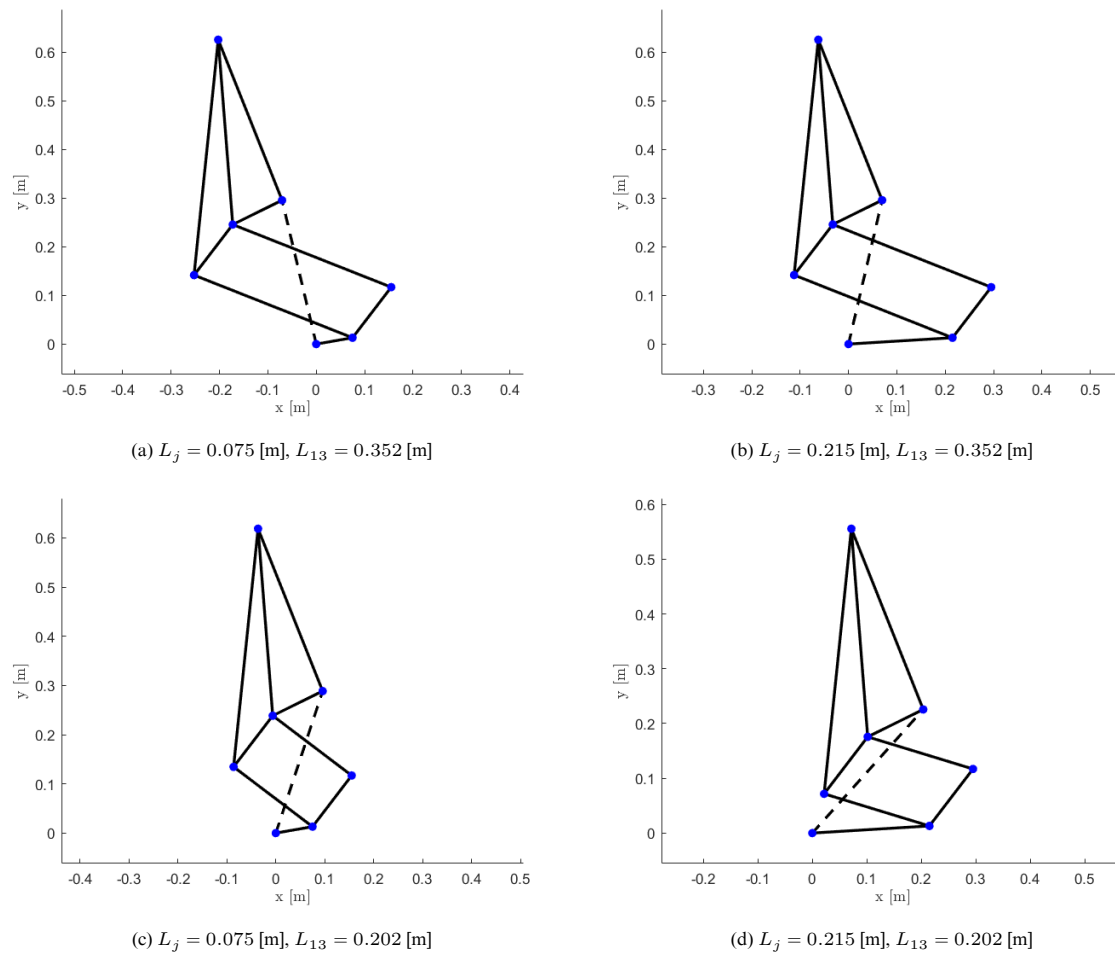


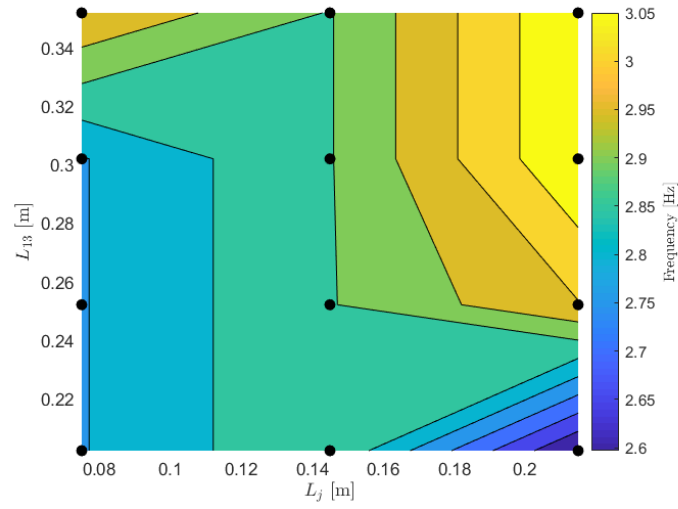
Figure 5.9: Seat A model undeformed structure for the extreme values of L_{13} and L_j

In prior research, it was recommended to analyse the natural frequencies of SMS suspension designs in order to prevent the phenomenon of dynamic amplification [10] [16]. Therefore, the natural frequencies of the proposed suspension design are analysed while varying the geometrical parameters L_{13} and L_j . The natural frequencies are calculated by analysing the undamped response of the suspension design after it was released from a non-equilibrium state with the Fast Fourier Transform (FFT). This process was also applied during the validation of the dynamic program in appendix F. The FFT is a MATLAB algorithm that computes the Discrete Fourier Transform (DFT) of a signal. For all simulations, the non-equilibrium state is when the seat is undeformed and no occupant is seated. At the start of the simulation the mass of the human body is added to the seat which will result in a deformation and a oscillating response in time. An important note is that the stiffness of a gas-spring depends on the compression. Therefore, different natural frequencies may be found with this method when the human weight is varied.

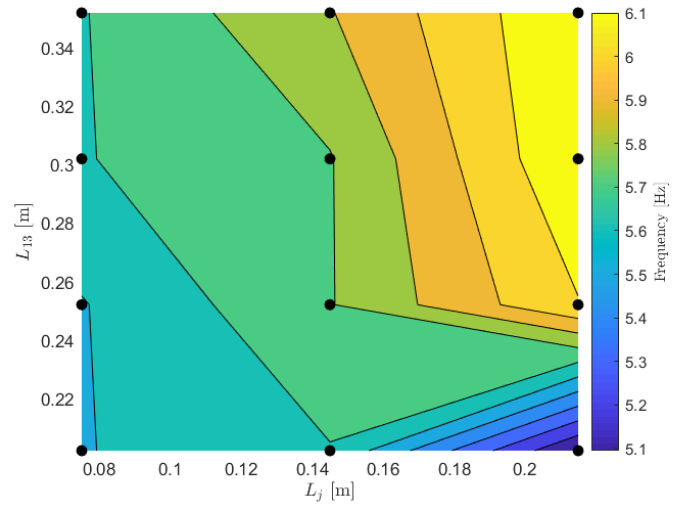
In figure 5.10, the first three natural frequencies as a function of both L_{13} and L_j are shown by means of a contour plot. The black dots in these figures indicate for which combinations of the parameters dynamic simulations were conducted. The contours in the plots from figure 5.10 are not smooth as the number of simulations for these plots is limited for the sake of time. Contour plots are able to quickly and easily provide insight in the influence of parameters, but the contours are not necessarily true and depend heavily on the number of simulations. Therefore, the results from figure 5.10 should not be used blindly or without thorough consideration. The results show that the first mode of the natural frequency varies from 2.6 [Hz] to 3.05 [Hz]. These natural frequencies are considered viable as similar values for the natural frequencies

are commonly reported in literature [95] [17] [11] [10].

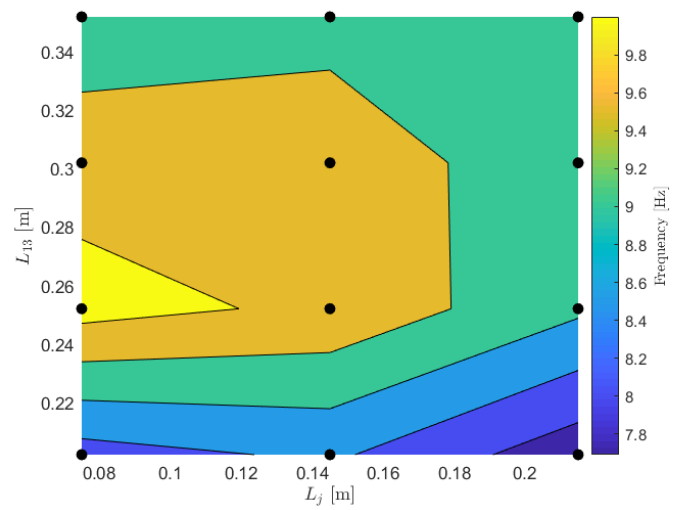
In practice, the parameter L_j is variable and used to adjust the height of the seat. Thus, the only option is to change the length of the truss elements L_{13} to improve the design of the seat. Based on figures 5.7 and 5.8, it seems desirable to increase the length of the truss elements in order to increase the available height of the seat with respect to the base. An additional benefit is that the another spring-damper combination can be implemented with a smaller minimum length. This would further increase the available stroke and reduce the probability of bottoming. This is best shown in figure 5.7 for $L_{13} = 0.302$. However, changing the length of the truss elements influences the natural frequencies as shown in figure 5.10. Increasing the length of the truss elements results in generally higher first mode natural frequencies. This is also true for the second mode and only partly for the third mode. It is difficult to determine whether the small increase in the natural frequencies results in a better or worse performance of the designs. This depends on the duration of the excitation pulses as shown in section 2.4.2. The seat designer should take this into account by designing a suspension based on the expected operating conditions.



(a) First mode



(b) Second mode



(c) Third mode

Figure 5.10: Seat A model natural frequency of three modes for different dimensions

5.3.2. Variation of the Human Weight

In this section, the influence of the human weight on the natural frequencies for a single suspension design is investigated. For the suspension design, the following values were used for the parameters with a variable length $L_{13} = 0.252$ [m] and $L_j = 0.145$ [m]. The natural frequencies are again determined with the FFT of a dynamic simulation.

In figure 5.11, the first three natural frequency modes are plotted for a representative range of human masses. Note for these calculations and prior research [10] [16] that part of the weight exerts a force directly on the deck via the feet. Thus the values used for the mass do not represent the full mass of the human body. The figure shows that although the mass increases, the first and second natural frequency mode increase as well. This behaviour was not expected as for a single DOF incorporating a coil-spring with a constant stiffness, the natural frequencies would decrease. However, as the gas spring is increasingly compressed for an increasing mass, the stiffness of the element increases non-linear. Therefore, it is suspected that the increase of the stiffness of the gas-spring is larger than the increase of the mass. As a result the natural frequencies of the suspension design are increased.

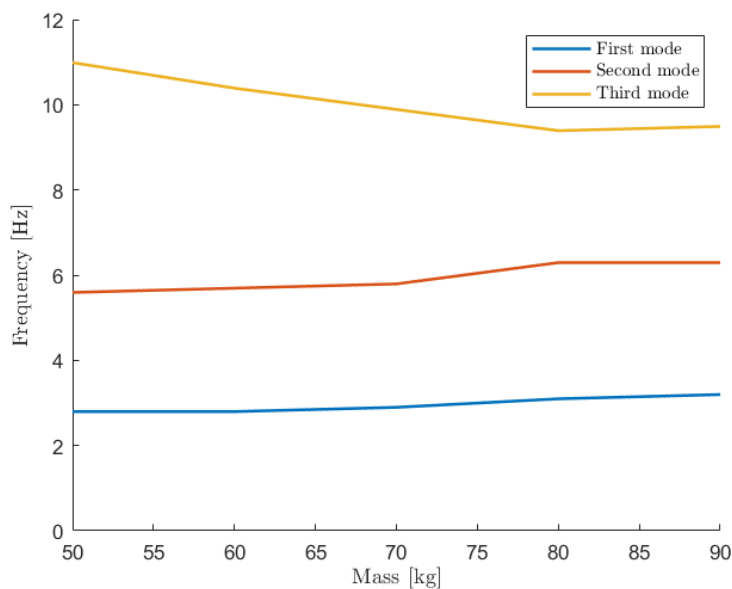


Figure 5.11: Seat A model natural frequencies for different values of the mass

5.4. Analyses of the Proposed Design

In this section, the proposed design further analysed with dynamic simulations with a full-scale wave impact acceleration record. The response of the proposed design will be compared to the response of the original suspension of seat A. Additionally, the resulting seat level accelerations are analysed with the dynamic response index and the modified evaluation methods of ISO 2631 Part 5.

5.4.1. Wave Impact Simulations

For the dynamic simulations, the full-scale acceleration record of the KNRM from figure 4.8 is used as input. Multiple simulations of suspension design seat A with the variable lengths of $L_{13} = 0.252$ [m] and $L_j = 0.145$ [m] and with different springs plus settings will be performed. First, the original suspension design of seat A integrating the coil spring is analysed. Subsequently, multiple simulations of the proposed design with gas-spring element are made in which the initial pressure is adjusted as a percentage of the

weight of the operator. The increments for the percentages of the weight of the operator is 25 % per setting. In figures 5.12 and 5.13, the craft acceleration (i.e. deck level acceleration) and the seat level accelerations in the vertical and horizontal direction for the total record are shown. In figures 5.14 and 5.15, the same seat level accelerations are zoomed in and shown per wave impact. Furthermore, the spring length in time for the simulations is shown in figure 5.16.

In figures 5.12 and 5.13, acceleration spikes are clearly visible in the seat level acceleration record. These large magnitude spikes are the result of bottoming as is shown in figure 5.16. As the springs are compressed, the spring length approaches the extreme length and increases in stiffness. In figure 5.14, it is visible that the suspension design has the largest amplification of the deck level acceleration for the first and third wave impact. The suspension design integrating a gas-spring with an initial pressure that only compensates for the weight of the seat does mitigate the deck level acceleration of the first and third wave impact more, but on the other hand amplifies the deck level acceleration of the second wave impact more. Furthermore, the results from figure 5.14 show that when the initial pressure of the gas-spring is increased, the amplification of the deck level accelerations reduces and the shock mitigating characteristics improve. This indicates that a gas-spring element which is correctly adjusted to account for the weight of the operator may be a viable option in suspension design A. However, when the initial pressure only compensates the weight of the seat, then the shock mitigating characteristics are just slightly better. The figures 5.13 and 5.15 show that the magnitude of the seat level acceleration in the horizontal direction increases and decreases with the magnitude of the acceleration spikes in the vertical direction. The reason for this is that the motion of the seat is somewhat circular due to the parallelogram of pinned truss elements and therefore once the suspension bottoms the horizontal and vertical motion and acceleration of the seat are reversed. If the suspension has poor shock mitigating characteristics, then this will occur more severely as is shown by the large magnitude seat level accelerations.

An important observation regarding the seat level acceleration and the deck level acceleration is that the oscillations and vibrations resulting from the shock pulse are almost completely damped out before the next wave impact occur as shown best by figures 5.12, 5.13 and 5.16. This indicates the response of the suspension to each consecutive wave impact can be regarded as independent. Furthermore, it is observed in figure 5.16, that for lower initial pressures not only the initial compression is increased, but that the oscillating motions in between the wave impacts are increased. This behaviour is expected as for a larger initial pressure, the stiffness of the gas-spring is increased and will not vary a lot in spring length for low accelerations levels. The initial pressure also influences the position of the piston during low acceleration levels. For larger initial pressures, the piston is forced against the cylinder wall in the top position.

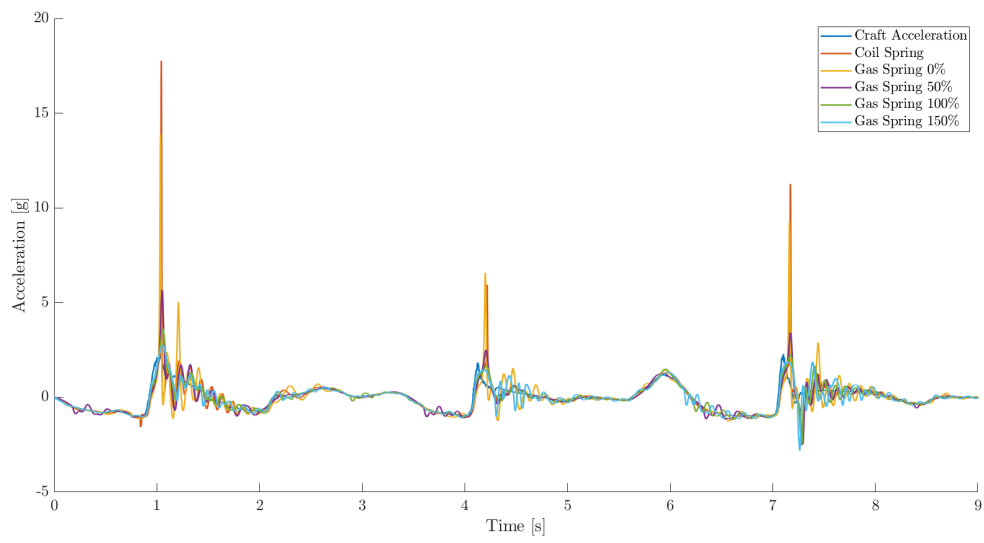


Figure 5.12: Seat level acceleration response in the vertical direction for suspension design seat A with different springs and settings

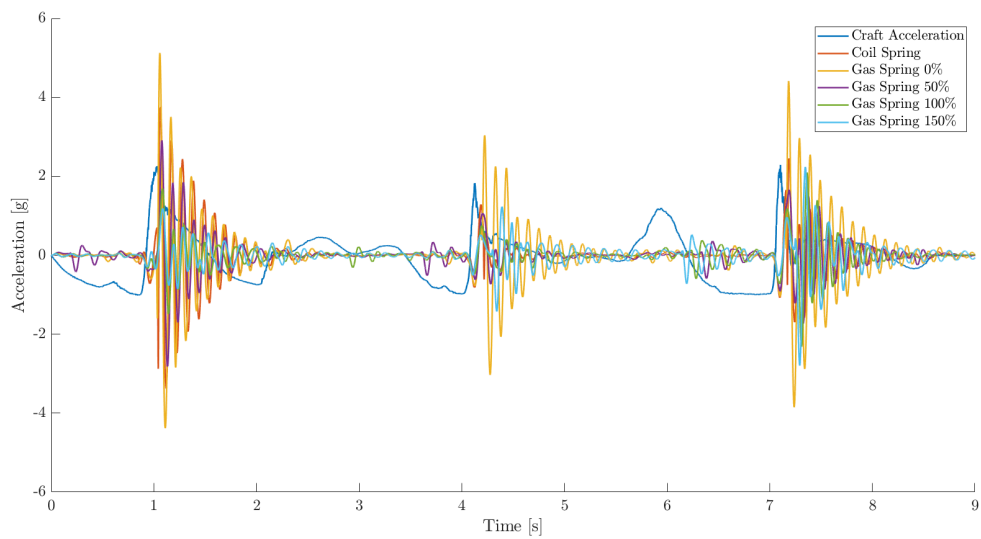
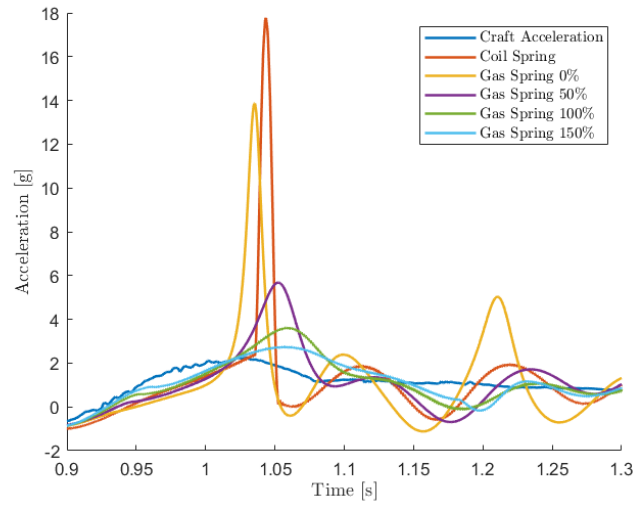
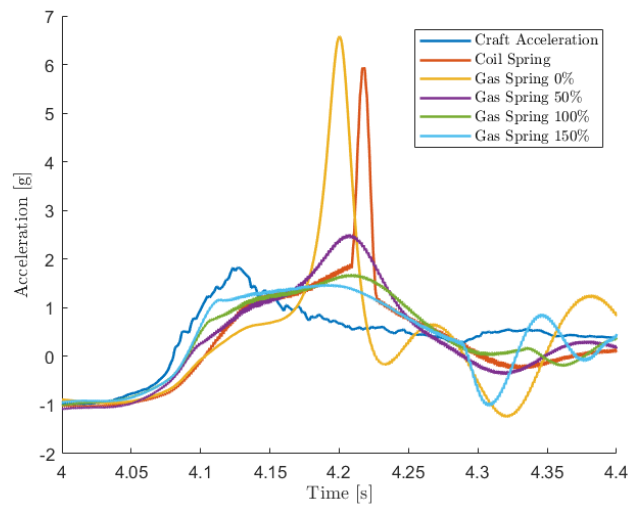


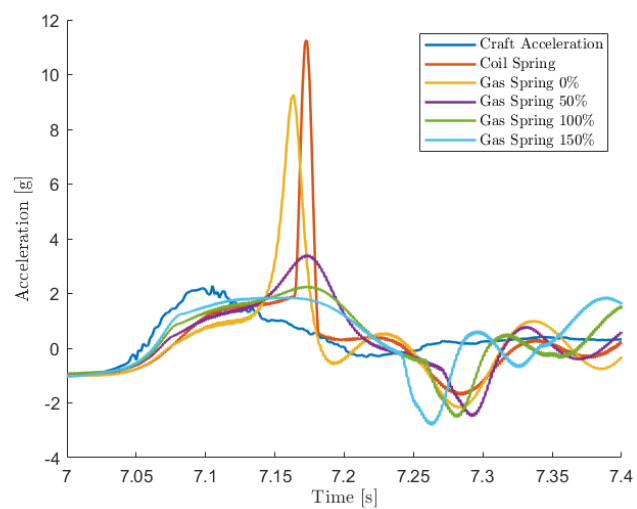
Figure 5.13: Seat level acceleration response in the horizontal direction for suspension design seat A with different springs and settings



(a) Wave impact one

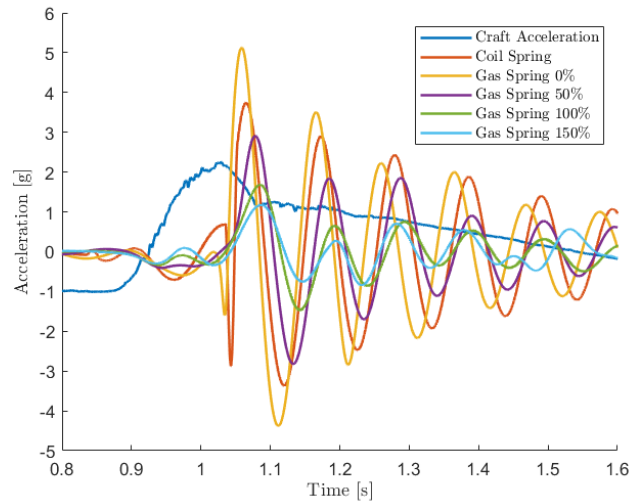


(b) Wave impact two

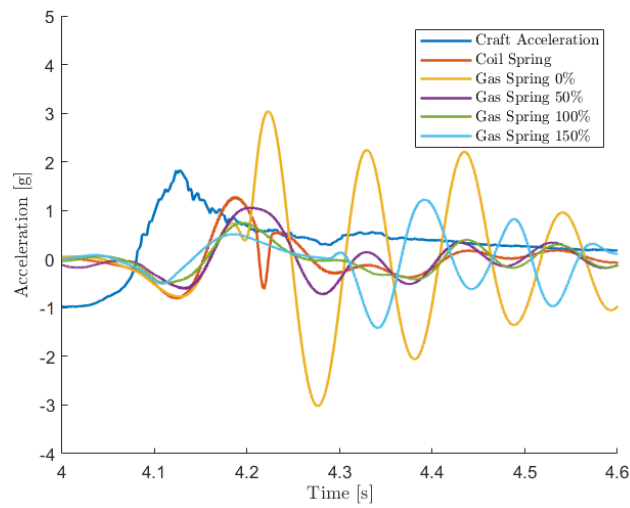


(c) Wave impact three

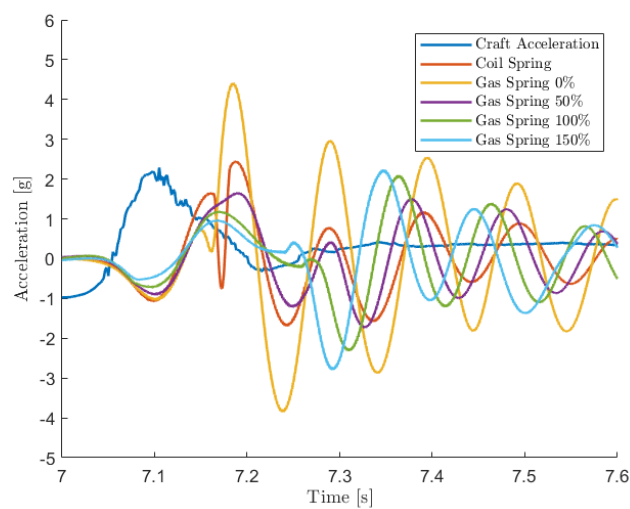
Figure 5.14: Seat level acceleration response in the vertical direction per wave impact for suspension design seat A with different springs and settings



(a) Wave impact one



(b) Wave impact two



(c) Wave impact three

Figure 5.15: Seat level acceleration response in the horizontal direction per wave impact for suspension design seat A with different springs and settings

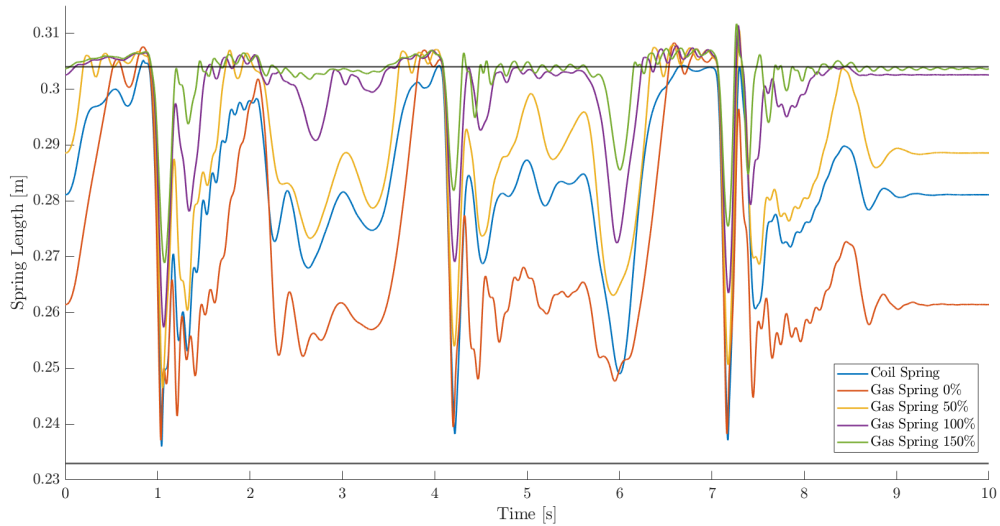


Figure 5.16: Spring length for the acceleration responses in time for suspension design seat A with different springs and settings

To investigate the shock mitigating characteristics for the proposed design and the original design, the peak accelerations in the horizontal and vertical direction are calculated and shown in table 5.5. Furthermore, the shock transmissibility factors for the accelerations in the vertical direction are calculated using the peak accelerations of the deck level acceleration record. The shock transmissibility factors are shown in table 5.6. In tables 5.5 and 5.6, a non-linear trend is observed between the seat level accelerations in the vertical direction and the initial pressure of the gas-spring. Based on the results, it is expected for this trend to continue for gas-spring with a setting of more than 150 %. A unexpected result is the seat level accelerations in the horizontal direction of the gas-spring with the setting of 0%. The peak accelerations of this suspension in the horizontal direction are larger than it measured for the coil spring, but in the vertical direction larger peak accelerations are observed with the coil spring.

Table 5.5: Peak accelerations of the seat level acceleration response per wave impact for suspension design seat A with different springs and settings

Suspension		Vertical Direction [g]			Horizontal Direction [g]		
Spring	Setting [%]	Wave Impact 1	Wave Impact 2	Wave Impact 3	Wave Impact 1	Wave Impact 2	Wave Impact 3
Coil	-	17.71	5.89	11.24	3.76	1.29	2.45
Gas	0	13.69	6.58	9.28	5.12	3.03	4.34
Gas	25	8.15	3.52	5.05	3.96	1.41	2.73
Gas	50	5.67	2.51	3.41	2.91	1.04	1.67
Gas	75	4.63	2.03	2.81	2.14	0.78	1.98
Gas	100	3.63	1.69	2.27	1.66	0.73	2.07
Gas	125	3.11	1.54	2.17	1.38	0.96	2.29
Gas	150	2.76	1.48	1.87	1.17	1.23	2.24

Table 5.6: Shock transmissibility factors for the accelerations in the vertical direction per wave impact for suspension design seat A with different springs and settings

Suspension		Shock Transmissibility Factor [-]		
Spring	Setting [%]	Wave Impact 1	Wave Impact 2	Wave Impact 3
Coil	-	7.84	3.22	4.91
Gas	0	6.06	3.6	4.05
Gas	25	3.61	1.92	2.21
Gas	50	2.51	1.37	1.49
Gas	75	2.05	1.11	1.23
Gas	100	1.61	0.92	0.99
Gas	125	1.38	0.84	0.95
Gas	150	1.22	0.81	0.82

5.4.2. Probability of Injury

In the previous section, the change of the shock mitigating characteristics for different springs and settings was reviewed by analysing the shock transmissibility factors. However, this analysis is considered to be insufficient, because lower shock transmissibility factors do not necessarily result in a lower probability of injury. In addition to the peak acceleration, parameters such as the pulse duration, pulse shape and jerk also influence the probability of injury. These parameters are not taken into account when the performance is only measured with the shock transmissibility factors. Therefore, the resulting seat level accelerations should also be analysed with various injury models in order to check whether the performance of the suspension design really did improve. In this research, the DRI and the modified evaluation methods of ISO 2631 Part 5 are implemented. Both evaluation methods are explained in chapter 3. First, the seat level accelerations are analysed with the DRI and subsequently with the modified evaluation methods of ISO 2631 Part 5.

In the DRI method, the seat level accelerations are used to calculate the maximum compression of the spine during the excitation period. Normally, the DRI method would calculate the maximum spinal compression for a single shock, but the seat level acceleration contains three individual wave impacts. Therefore, the three largest values DRI describing the maximum spinal compression per wave impact were used. In table 5.7, the DRI values per wave impact in the acceleration record are shown for suspension design seat A with different springs and settings. By comparing the resulting DRI values with figure 3.4, it is concluded that exposure to these seat level accelerations would not result in spinal injury. Although, the seat level acceleration contains large acceleration spikes, the duration of these spikes is so short that they do not result in a hazardous compression of the spine. A very important note on these results is that the DRI does not take repetitive loading into account. According to this method, one could be exposed to these seat level accelerations for an infinitely long time and still no spinal injury would result.

Next, the seat level accelerations are analysed with the modified evaluation methods of ISO 2631 Part 5. With these methods the lumbar acceleration in the vertical and horizontal direction are calculated. Through the Palmgren-miner fatigue theory, repetitive loading is taken into account. Additionally, the ultimate strength of the lumbar spine is incorporated with an optimized age-dependent coefficient based on gender. In this research, the operator is assumed to be at age of 24 years who is exposed to these accelerations for half an hour a day, 30 days a year for two consecutive years. The resulting risk factor and the probability of injury according to the standard method and modified evaluation methods of ISO 2631 Part 5 are shown in table 5.8. For the modified method of ISO 2631 Part 5, two cases are calculated in which the operator has a male or female gender.

Table 5.7: DRI values for the acceleration response in the vertical direction per wave impact for suspension design seat A with different springs and settings

Suspension		Dynamic Response Index [-]		
Spring	Setting [%]	Wave Impact 1	Wave Impact 2	Wave Impact 3
Coil	-	7.04	3.02	4.44
Gas	0	7.92	4.99	5.93
Gas	25	6.93	3.45	4.50
Gas	50	5.77	2.46	3.27
Gas	75	4.77	2.00	2.58
Gas	100	4.01	1.69	2.16
Gas	125	3.42	1.85	2.43
Gas	150	3.00	1.99	2.47

Table 5.8: Risk factor and probability of injury according to the ISO method and the modified ISO method for lumbar accelerations in both the horizontal and the vertical direction for suspension design seat A with different springs and settings

Suspension		ISO		Modified ISO			
Spring	Setting [%]	R [-] (neutral)	Probability (neutral)	R [-] (male)	Probability [%] (male)	R [-] (female)	Probability [%] (female)
Coil	-	3.17	high	2.95	99.56	2.76	100.0
Gas	0	3.34	high	3.11	99.81	2.90	100.0
Gas	25	2.96	high	2.75	98.85	2.57	100.0
Gas	50	1.84	high	1.71	69.19	1.60	99.87
Gas	75	1.41	high	1.31	42.78	1.22	91.56
Gas	100	1.19	medium	1.11	29.72	1.04	73.95
Gas	125	1.05	medium	0.97	21.64	0.91	56.18
Gas	150	0.94	medium	0.87	16.32	0.81	41.97

In table 5.8, the risk factors for both evaluation methods are approximately of the same magnitude across different springs and settings, but major deviations are shown in the probability of injury. The standard evaluation expresses the probability of injury in terms of low, moderate or high, but fails to report the according risk in another form such as percentages. The Weibull injury risk model gives alarmingly high values for the probability of injury. The probability of injury values illustrate the high risk of injury to which the HSC operators are exposed. Furthermore, the results highlight the probability of injury differences between sexes. This confirms once more that the gender of a person should be taken into account when assessing spinal injury as a result of WBV and RS. An important note on the results of the modified evaluation methods of ISO 2631 Part 5 is that the models do not include healing over the course of time [5]. This is expected to have a significant contribution as the accumulated damage will decrease in between periods of exposure to the WBV and RS [5]. Furthermore, the modified risk factor and Weibull injury risk model are still dependant on the RNN model as shown in figure 3.6. This model is not ideal as it is only validated for seat level acceleration peaks up to 4 [g], while these are easily exceed in the dynamic simulations as shown by table 5.5.

6

Conclusion & Recommendations

In this chapter, the research questions are answered based on the results obtained from the research. Additionally, the limitations and the implications of the results are discussed. Finally, recommendations for further research will be given.

6.1. Conclusion

The problem identified in the literature study [27] and described in section 1.3 consists of three parts. First, in prior research the shock mitigating seat suspension designs are analysed with either simplistic or specific which limits the applicability of these models to other suspension designs. Second, a half-sine approximation is often used to approximate the wave impact accelerations while the validity of this approximation can be questioned. Additionally, the importance of wave impact durations for testing and designing is neglected. Third, most prior research did not include a suitable injury model to evaluate the accelerations, to which the operators are exposed, and their relation with risk of injury and adverse health effects. Therefore, the main objective of the research is to prevent injuries of high speed marine craft operators resulting from repetitive wave impacts by incorporating an injury model in the analyses of various suspension principles in the design of Shock Mitigating Seats (SMS). Based on the main objective, the following main research question was formulated:

How can injuries experienced by the crew on high speed craft caused by wave impacts be modeled in the analyses of various suspension principles in the design of shock mitigating seats?

In addition to the main research question, three research questions were defined in order to conduct research specifically on the three parts of the problem.

1. *How can the analyses of various suspension principles for shock mitigating seat designs be improved by integrating highly non-linear elements in the computer program such as a gas-spring element that includes the effect of bottoming?*

For the analyses of various suspension principles in the design of shock mitigating seats, a computer program was developed which was based on the finite element method in combination with the total Lagrangian approach. The program has three DOF and allows input accelerations in the surge, heave and pitch directions. Therefore, the computer program is able to analyse various suspension designs with coupled forward and vertical motions. The phenomena that cause shock amplification are bottoming and dynamic amplification. Dynamic amplification is the result of a pulse-period mismatch, while bottoming is the result of an insufficient stroke length leading to metal-on-metal contact. The sudden mechanical shock in the suspension leads to large acceleration spikes that can exceed the wave impact acceleration levels. In prior research, bottoming was seldom implemented in

the element. Only in a few studies, the effect was implemented yet in a rudimentary way by instantaneously increasing the stiffness. Therefore, two spring elements in this research were derived that included bottoming in a more complex form. The coil spring element and gas-spring element were derived such that their stiffness-elongation or force-displacement curves increased according to a cubic transition function when the deformed length approached the extreme lengths of the element. In comparison to the implementation of bottoming in prior research, this cubic increase is expected to be more realistic. The implementation of the various highly non-linear elements in combination with the more complicated form of bottoming enables the possibility to analyse a wide range of suspension principles for shock mitigating designs and show more realistic behaviour of bottoming during dynamic simulations. As a result, the analyses of various suspension principles for shock mitigating seat designs are improved.

2. *Which existing injury model is suitable to relate the physical loads experienced on high speed craft to the injuries of the crew, and how can this model be incorporated in the model?*

Various studies were analysed to identify the most common injury (locations) and adverse health effects. The results showed that the most common injury locations are the lower back, knees and shoulders. However, the cause-effect relationship or correlation of the exposure to WBV and RS to injuries and adverse health effects is not yet clear. Research showed that the human tolerance to shocks depends on the magnitude, duration and shape of the acceleration pulse, but also on the direction in which the acceleration is applied and the jerk. Based on the reviewed literature, the two existing injury criteria to assess spinal injury which seem to be appropriate are (1) the dynamic response index and (2) the evaluation methods from ISO 2631 Part 5. However, both evaluation methods still have their limitations. The main limitation of the dynamic response index is that the criteria does not account for or is validated for repetitive loading, while the spinal injuries of high speed marine craft operators are often the result of multiple wave impacts over a longer period of time. The main limitation of the evaluation methods from ISO 2631 Part 5 is that it is not validated for wave impacts with seat level acceleration peaks larger than 4 [g] while seat level acceleration peaks exceeding 10 [g] have been reported and were confirmed in the case study. Additionally, the standard risk factor has no proven correlation with injury risks. Based on the limitations of both injury models, the ISO 2631 Part 5 method is most likely the best suitable injury criterion. The evaluation method can be improved by implementing a metamodel based on a lumped mass human body or by implementing a modified risk factor with an optimized age-dependent coefficient based on the gender of a person in combination with a Weibull injury risk model. In this research, the dynamic response index and the evaluation methods from ISO 2631 Part 5 with the modified risk factor and the Weibull injury risk model were implemented in order to predict the probability of spinal injury.

3. *What simplified floor level acceleration pulse is a realistic representation of the accelerations experienced in wave impacts events at high speed?*

For testing and designing purposes the half-sine approximation is often used to approximate the rigid body acceleration pulse of the wave impact phase. Additionally, testing requirements state that a single impact duration of 100 [ms] without much argumentation. First, the validity of the half-sine approximation was reviewed with a single DOF mass-spring-damper model and full scale measurements of wave impacts. The measured acceleration record consisted of three wave impacts with a varying peak acceleration of approximately 1.8 [g] to 2.3 [g] and an impact duration of approximately 90 [ms] to 230 [ms]. The results showed that the half-sine approximation is a reasonable approximation for the wave impact phase only. However, in the definition of the half-sine approximation the resulting accelerations of buoyancy, hydrodynamic lift, thrust and drag beyond the wave impact phase are ignored. The results showed that these accelerations have a significant influence on the required stroke during a wave impact event. The accelerations result in a larger compression of the spring, which increases both the required stroke and the probability of bottoming. Therefore, the

half-sine approximation should not be used blindly without considering this major drawback. For designing purposes, it is recommended to disregard the half-sine approximation since it underestimates the probability of bottoming. Second, the importance of the wave impact duration was investigated. In prior research, an extensive set of full-scale wave impact measurements was gathered. The data showed that for wave impacts the peak acceleration varies from 1 [g] to 7 [g] and the impact duration varies from 100 [ms] to 450 [ms]. Variation in these measurements is the result of variable craft weight, impact angle, wave height, speed, deadrise and location of the impact. With the the half-sine approximation and the extensive set of data it was shown that severity of real wave impacts may be seriously underestimated when a single impact duration is taken. For testing purposes, the half-sine approximation offers some advantages, but is recommended that the value of the impact duration is varied for a realistic range of impact durations based on the expected operating conditions. This may require a reconfiguration of the test apparatus and involve high costs.

Based on the results of the three questions, it is concluded that the injuries and adverse health effects can be modeled by implementing spinal injury models, based on the seat level acceleration response taking repetitive loading of WBV and RS into account. Using a more complicated computer program that allows three DOF in the surge, heave and pitch direction and additionally integrates highly non-linear elements including the effect of bottoming, the seat level accelerations of various suspension principles in the design of shock mitigating seats can be calculated more accurately. Any suspension design can now be analysed with injury models and the probability of injuries determined based on the expected operating conditions of the craft and crew.

Using the results of the main research question and the additional research questions, a case study was conducted for a FRISC of the Royal Netherlands Navy. The objective of the case study was to demonstrate the possibilities offered by the computer program and the injury evaluation methods. Based on prior research, two shock mitigating seat designs were reviewed. The suspension of seat A is based on a parallelogram of pinned truss elements in combination with a coil spring and a damper while the suspension of seat B is based on parallel (composite) leaf spring clamped on both ends in combination with a damper. Unfortunately, the suspension design of seat B is not well described in the literature which led to an inaccurate model. A design based on the suspension of seat A using a gas-spring instead of a coil spring was proposed. The first and foremost reason for this alteration is that the gas-spring may prevent seat level acceleration spikes resulting from bottoming as the stiffness increases gradually. The proposed design was analysed with dynamic simulations in which the initial pressure of the gas-spring was varied while the geometry and the weight of the operator remained constant. The results were compared with the standard suspension design of seat A and showed that the seat level acceleration spikes can be significantly reduced if the initial pressure of the gas-spring is properly adjusted to the weight of the operator. For the most severe wave impact of the acceleration record, the shock transmissibility factor was reduced from 7.84 [-] to 1.22 [-]. This result indicates that the shock pulse is still not mitigated, but the amplification is significantly reduced. Furthermore, the resulting seat level accelerations were evaluated with the implemented injury models. An operator of the age of 24 years who is exposed to the accelerations for half an hour a day, 30 days a year for two consecutive years was assumed. According to the modified evaluation method of ISO 2631 Part 5, the probability of injury for a male operator was reduced from 99.5 % to 16.3 %. For a female operator the probability of injury was reduced from 100.0 % to 42.0 %. Therefore, the implementation of a gas-spring in the suspension design of seat A is concluded to be a viable option for the mitigation of hazardous levels of WBV and RS.

6.2. Limitations

In this section, the limitations of the computer program, research methods and the results are discussed.

6.2.1. Limitations of the Computer Program

The developed software used for the static and dynamic analysis has the following limitations:

1. The equations of motion for both the static and dynamic analysis are based on the total Lagrangian approach. In this approach the deformed structure is determined based from the reference configuration, which is the undeformed structure. A more accurate approach would be the updated Lagrangian approach, which calculates the new deformation from the current configuration. However, this approach is more complicated and compute-intensive.
2. The large rotation beam element can only be used for static analysis. Therefore, for the dynamic analyses the only option is the non-linear Euler-Bernoulli beam element. However, the use of this element for structures experiencing large deformations is limited as the element is based on the small angle approximation. Furthermore, a cubic transition function was used to represent bottoming in the coil spring and gas-spring elements. This cubic transition is expected to be more realistic than increasing the stiffness instantaneously, but it may still not be representative enough for bottoming in practice.
3. The computer program allows three DOF in the surge, heave and pitch direction. However, based on the human tolerance to shocks and the injury models it is concluded that the accelerations in other directions increase the probability of injury even more. Therefore, an extension of the computer program to six DOF allows for a more accurate analyses of the performance of SMS and the resulting probability of injury for operators.
4. The static simulations can only be performed with force loading. The implementation of prescribed displacements can be beneficial as it enables simulations and analyses of snap-through behaviour and the equilibrium path in the unstable region.

6.2.2. Limitations of the Review on Injury Models

The extensive literature review on the resulting injuries and adverse health effects shows a few limitations.

1. The most referenced standards and some injury models to evaluate the human exposure to WBV and RS were reviewed. The cause-effect relationship or the correlation of the physical loads and the resulting injuries and adverse health effects remains difficult to define. Almost all injury models and criteria are based on either *in vitro* studies or on experiments with restricted acceleration levels. Therefore, it is difficult to accurately describe the probability of injury for repetitive loading and high accelerations levels. As a result, the obtained risk of injury values may not be accurate.
2. In an attempt to improve both the commonly referenced standards and the injury models, various literature on reducing the drawbacks and deficiencies was studied. One of these improvements was a promising metamodel based on a Madymo (TNO, Inc.) simulation of a lumped mass system. However, this metamodel is not published in the literature. The implementation of this metamodel may improve the evaluation method of ISO 2631 Part 5. In this research, the standard RNN model was used which was only validated for seat level accelerations with a peak acceleration up to 4 [g].

6.2.3. Limitations of the Study on Wave Impact Accelerations

In the research on the wave impact excitation pulse and the review of the half-sine approximation, various assumptions and available data limited the analyses.

1. The analyses was mostly limited by the availability of full-scale experimental data of wave impacts. In literature, an extensive data set of full-scale wave impacts was found, but the data did not include pulse shapes. An acceleration record of a KNRM lifeboat was obtained which provided the required pulse shapes in order to review the half-sine approximation. However, the acceleration record only consisted of three wave impacts with impact durations varying from approximately 90 [ms] to 230 [ms] and peak accelerations from 1.8 [g] to 2.3 [g]. The resulting findings and conclusions are based on these data sets and may not be valid for strongly deviating full-scale experimental data.

2. For the sake of time and simplicity, the review of the half-sine approximation was conducted with a single DOF mass-spring-damper model that did not include the effect of bottoming and had natural frequencies in the range of 1 [Hz] to 3 [Hz]. It was assumed that these results are valid for more complex models with similar natural frequencies.

6.2.4. Limitations of the Case Study

During the case study a number of simplification and assumptions, limited the analyses of the SMS designs.

1. The models for seat A and seat B are based on the models used and described in prior research. The research that focused on seat A provided a very accurate description of the suspension of seat A and the values used for the analyses. Therefore, the model of seat A used in this research can be confidently called as fairly accurate. The research of seat B did not describe the suspension as accurate and contradicting values were reported. This had a direct negative influence on the accuracy of the model of seat B and this was observed during static simulations of the suspension.
2. For the dynamic simulations several assumptions had to be made regarding the weight of a typical operator for a FRISC and the required height of the seat. Eventually, the values from prior research were reused and for the height of the seat the average height that the suspension would allow was used.
3. A major limitation for the case study was the available time in the remainder of the research project. Many more simulations and analyses of various models could have been conducted, but this would require a huge amount of effort and time. Therefore, the case study was limited to a very general case in which mostly average values were used.

6.3. Implications

In practice, two scenarios can occur in which the results of this research can be of value.

In the first scenario, the computer program and results can be used by a shock mitigating seat designer, engineer or researcher. The seat designer, engineer or researcher can use the computer program and the highly non-linear elements to investigate suitable suspension designs for the mitigation of the deck level accelerations. Additionally, alterations of existing suspension designs can be investigated. The performance of these designs can be analysed by evaluating the seat level accelerations with the proposed injury models to see whether the design performs sufficiently or lacks in performance. An additional benefit of this program is that many simulations can be made and used to optimize a design before producing the first prototype and testing this design with either sea trials or in a laboratory. As a result, the need for many expensive iterations of a design becomes unnecessary. Therefore, the method and results have the possibility to save time and reduce high costs in the design process of a SMS.

In the second scenario, the computer program and results can be used by engineers working for the materials department of various maritime organizations. When the crew and passengers of HSC craft suffer from fatigue and injuries and the need to reduce the physical loads arises, then shock mitigation seating may provide a solution. Various shock mitigating seat designs are developed by commercial companies and can be bought 'off the shelf'. Before buying several seats and extensively testing them based on the expected operating conditions, the engineers now have the possibility to accurately analyse the performance of various designs for representative wave impacts and determine the suitability of a design for the intended craft. Furthermore, the method can assist in defining new guidelines within the maritime organizations for the crew and operators of HSC which limit the exposure of the personnel to the physical loads and therefore limit the probability of injury to an acceptable level. The acceptable level of risk of injury may vary per company or per country depending on regulations or ethical beliefs. A whole discussion about ethical considerations can be held, but that does not fit within the scope of this thesis.

6.4. Recommendations

Based on the described limitations of the computer program and the research methods, several recommendations are made for the application of the results and for further research.

6.4.1. Current Implementation

The following recommendations should be taken into account when the results of this research are used when analysing SMS.

- For the analyses of various suspension principles, highly non-linear elements incorporating the effect of bottoming should be implemented as bottoming results in a high probability of injury.
- In analyses of a suspension design, the natural frequencies of the suspension and the periods of the excitation pulses should be reviewed in order to prevent dynamic amplification of the deck level accelerations.
- To determine the probability of injury resulting from a single severe shock, the dynamic response index is suitable. For repetitive loading, the modified evaluation methods ISO 2631 Part 5 are recommended as these take repetitive loading, gender and age into account for the probability of injury.
- When determining the probability of injury, the age and gender of the person should be taken into account as these variables have significant influence on the ultimate strength of the lumbar spine and the resulting probability of injury.
- For seat testing purposes, the half-sine approximation can be used as it offers some advantages as the method allows to easily and quickly generate various wave impacts, but it is recommended to vary both the impact duration and peak acceleration in order to represent a wide range of wave impacts.
- For seat designing purposes, it is recommended to disregard the half-sine approximation and to use full-scale measurements as the half-sine approximation underestimates the probability of bottoming which is the cause for seat level acceleration spikes.

6.4.2. Additional Research

The following recommendations indicate possible further research topics which may contribute to an improvement of the analyses of SMS and the experienced injuries of HSC operators.

- For both static and dynamic analysis, the use of a commercial computer program implementing the derived highly non-linear finite elements is recommended unless the computer program developed in this research is improved. The commercial computer programs tend to be more user friendly and use more efficient or accurate numerical methods to calculate the deformations.
- An in depth study could be conducted to bottoming behaviour in coil spring and gas-spring elements. In this research a cubic transition curve was used, but it is suspected that the accuracy of this approximation could be improved further.
- During research on human tolerance to shocks, the natural frequency of the human body in a seated or standing position was shortly discussed. Some literature indicated that the natural frequency of the human body should be avoided to avoid resonance in the body, but no scientific proof was provided. It remains unclear whether the natural frequency of the human body should be avoided and no literature with convincing arguments was found.
- After reviewing numerous literature, the cause-effect relationship or correlation of the exposure to WBV and RS and the resulting injuries and adverse health effects is still not yet clear. Further research could be conducted in order to define this relation.

-
- A drawback of the DRI injury model is that the weight of additional equipment can invalidate the model. Therefore, an investigation of an advanced human model which has the possibilities to add additional weight to the upper torso or head to increase the accuracy of the lumbar accelerations could be conducted. It is expected that a heavier upper torso influences the probability of spinal injury.
 - Before the half-sine approximation can be used for designing purposes, it should be improved such that the neglected accelerations beyond the wave impact phase which cause the approximation to underestimate bottoming are incorporated.

References

- [1] International Organization for Standardization. *ISO 2631: Mechanical vibration and shock. Evaluation of human exposure to whole-body vibration. Part 5: Method for evaluation of vibration containing multiple shocks*, first edition, 2004.
- [2] A. Eiband. Human tolerance to rapidly applied acceleration: a summary of literature. Technical report, National Aeronautics and Space Administration, Jun 1959.
- [3] J.W. Brinkley, , and J.T. Shaffer. Dynamic simulation techniques for the design of escape systems: Current applications and future air force requirements. Technical report, Aerospace Medical Research Laboratory, 1971.
- [4] R.T. Lynch, D.M. McDonough, and T. Keon. An update to the dynamic response index (dri) model for use in assessing seat performance in military ground vehicles. In *Safe Symposium*, Oct 2012.
- [5] A.L. Schmidt, G. Paskoff, B.S. Shender, and C. Bass. Risk of lumbar spine injury from cyclic compressive loading. *SPINE*, 37(26):E164–E1621, Dec 2012.
- [6] M.R. Riley, T.W. Coats, and H. Murphy. Acceleration response mode decomposition for quantifying wave impact load in high-speed planing craft. Technical report, Navel Surface Warfare Center Carderock Division, Apr 2014.
- [7] T. Coe et al. Development of an international standard for comparing shock mitigating boat seat performance. *Innovation in Small Craft Technology*, Apr 2016.
- [8] Habbeke Shipyard. Valentijn class, jun 2020. <https://habbeke.nl/project/valentijn-class/>.
- [9] A.W. Vredeveltdt. private communication, Jul 2020. TNO Netherlands.
- [10] S. Vredeveltdt. Analyse van de huidige schokdempende stoelen op de friscs: Modelleren en orientatie op tekortkomingen. Bachelor’s thesis, Netherlands Defence Academy, Mar 2016.
- [11] K. Olausson. *On Evaluation and Modelling of Human Exposure to Vibration and Shock on Planing High-Speed Craft*. Licentiate thesis, KTH - Royal Institute of Technology, 2015.
- [12] W. Ensign, J.A. Hodgdon, W.K. Prusaczyk, S. Ahlers, D. Shapiro, and M. Lipton. A survey of self-reported injuries among special boat operators. Technical Report 00-48, Naval Health Research Center, San Diego, California, USA, 2000.
- [13] R.M. Gollwitzer and R.S. Peterson. Repeated water entry shocks on high-speed planing boats. Report css/tr-96-27, Naval Surface Warfare Center Panama City Dahlgren Division, 1995.
- [14] W.C.J. Boef. Launch and impact of free fall lifeboats. *Ocean Engineering*, 30(4):139–159, Oct 1992.
- [15] J.T. Somers, D. Gohmert, and J.W. Brinkley. Application of the brinkley dynamic response criterion to spacecraft transient dynamic events. TM-2013-217380-REV1 Johnson Space Center Houston, National Aeronautics and Space Administration, Mar 2017.
- [16] K. Stouten. Redesigning the Jockey Seat for fast planing crafts: Integration of composite resilient mounting. Master’s thesis, Delft University of Technology, Nov 2016.
- [17] K. Alausson. Vibration mitigation for high speed craft. Master’s thesis, Centre for Naval Architecture Royal Institute of Technology, Stockholm, Sweden, Sep 2012.

- [18] Defensie. Frisc-motorboot, 2019. <https://www.defensie.nl/onderwerpen/materieel/schepen/frisc-motorboot-fast-raiding-interception-and-special-forces-craft>.
- [19] S. Myers et al. Effectiveness of suspension seats in maintaining performance following military high-speed boat transits. *Human Factors*, pages 264–276, 2012.
- [20] C. Bass, R. Salzar, A. Ziemba, S. Lucas, and R. Peterson. The modeling and measurement of humans in high speed planing boats under repeated vertical impacts. In *International IRCOBI Conference on the Biomechanics of Impact*, pages 397–408, Sep 2005.
- [21] B.J. Cameron, J.B. Morrison, D.G. Robinson, G. Roddan, P. Eng, and M.J.N. Springer. Development of a standard for the health hazard assessment of mechanical shock and repeated impact in army vehicles. Technical report, US Army Medical Research and Materiel Command Fort Detrick, Dec 1997.
- [22] K. Garme, L. Burstrom, and J. KutenKeuler. Measures of vibration exposure for a high-speed craft crew. *Journal of Engineering for the Maritime Environment*, 225(4):338–349, 2011.
- [23] K. Olausson and K. Garme. Prediction and evaluation of working conditions on high-speed craft using suspension seat modelling. *Part M: Journal of Engineering for the Maritime Environment*, Proceedings of the Institution of Mechanical Engineers, 2014.
- [24] K. Olausson and K. Garme. Simulation-based assessment of hsc crew exposure to vibration and shock. *Proceedings of the 12th International Conference on Fast Sea Transportation*, 2013.
- [25] M. Razola, K. Olausson, K. Garme, and A. Rosen. On high-speed craft acceleration statistics. *Ocean Engineering*, 114:115–133, Mar 2016.
- [26] J. Marshall, T. Coats, and M.R. Riley. The rationale, assumptions, and criteria for laboratory test requirements for evaluating the mechanical shock attenuation performance of marine shock isolation seats. Technical Report NSWCCD-80-TR-2018/015, Navel Surface Warfare Center Carderock Division, Aug 2018.
- [27] N. van den Nieuwenhuijzen. Shock mitigating seats on high speed marine craft. Literature Study, Aug 2020.
- [28] M.R. Riley, K.D. Haupt, H.C. Neil Ganey, and T.W. Coats. Laboratory test requirements for marine shock isolation seats. Technical report, Navel Surface Warfare Center Carderock Division, May 2015.
- [29] NAVSEA. Laboratory test requirements for evaluating the mechanical shock attenuation performance of marine shock isolation seats. Technical Report T9006-AE-TRQ-010, Navel Surface Warfare Center Carderock Division, Feb 2019.
- [30] M.R. Riley, K.D. Haupt, and H.P. Murphy. An investigation of wave impact duration in high-speed planing craft in rough water. Technical report, Navel Surface Warfare Center Carderock Division, Apr 2014.
- [31] International Organization for Standardization. *ISO 2631: Mechanical vibration and shock. Evaluation of human exposure to whole-body vibration. Part 1: General Requirements*, second edition, 1997.
- [32] P.R. Payne. Method to quantify ride comfort and allowable accelerations. *Aviation Space and Environmental Medicine*, Jan 1978.
- [33] D.P. Allen, D.J. Taunton, and R. Allen. A study of shock impacts and vibration dose values onboard highspeed marine craft. *Transactions of the Royal Institution of Naval Architects Part A: International Journal of Maritime Engineering*, 150(3), Jan 2008.

- [34] J. Ullman. Slamming standards. *Professional BoatBuilder*, 149, Jun 2014.
- [35] J. Ullman. Tackling human impact exposure on high-speed boats. *Ship and Boat International*, Nov 2014.
- [36] T. R. Chandrupatla and A. D. Belegundu. *Introduction to Finite Elements in Engineering*. Pearson, fourth edition, 2011.
- [37] J. Fish and T. Belytschko. *A First Course in Finite Elements*. Wiley, 2008.
- [38] A.B. Shiflet and G.W. Shiflet. *Introduction to Computational Science*. Princeton University Press, 2006.
- [39] N. van den Nieuwenhuijzen. Analyse van het torsietrillingsgedrag in de aandrijflijn van een schip. Bachelor's thesis, Netherlands Defence Academy, Apr 2018.
- [40] M. Petyt. *Introduction to finite element vibration analysis*. Syndicate of the University of Cambridge, 1990.
- [41] F.S. Tse, I.E. Morse, and R.T. Hinkle. *Mechanical vibrations theory and applications*. Prentice Hall, second edition, 1978.
- [42] S.S. Rao. *The Finite Element Method in Engineering*. Butterworth-Heinemann, sixth edition, 2018.
- [43] S.S. Rao. *Mechanical Vibrations*. Pearson, fourth edition, 2005.
- [44] R.D. Cook, D.S. Malkus, M.E. Plesha, and R.J. Witt. *Concepts and Applications of Finite Element Analysis*. John Wiley and Sons, fourth edition, Oct 2001.
- [45] J.W.S. Rayleigh. *The Theory of Sound*, volume 1 and 2. Dover Publications, second edition, 1894.
- [46] S. Krenk. *Non-linear Modeling and Analysis of Solids and Structures*. Cambridge University Press, 2009.
- [47] R. de Borst, M.A. Crisfield, J.J.C. Remmers, and C.V. Verhoosel. *Non-linear Finite Element Analysis of Solids and Structures*. Wiley, second edition, 2012.
- [48] A.K. Chopra. *Dynamics of Structures Theory And Applications to Earthquake Engineering*. Prentice Hall, fourth edition, 2012.
- [49] M.J. Jordan, H.N. Shapiro, D.D. Boettner, and M.B. Bailey. *Principles of Engineering Thermodynamics*. Wiley, eight edition, 2015.
- [50] Royal Netherlands Army. Beproeversrapport trillingsmetingen frisc en boston whaler. Technical report, Directie Materiele Instandhouding, 2014.
- [51] A.S.W. Leung, C.C.H. Chan, J.J.M. Ng, and P.C.C. Wong. Factors contributing to officers' fatigue in high-speed maritime craft operations. *Applied Ergonomics*, 37:565–576, 2006.
- [52] B. Cripps, S. Rees, H. Philips, C. Cain, D. Richards, and J. Cross. Development of a crew seat system for high speed rescue craft. In *7th International Conference on Fast Sea Transportation*, 2003.
- [53] M.J. Griffin. *Handbook of Human Vibration*. Academic Press, 1990.
- [54] J.M. Randall, R.T. Matthews, and M.A. Stiles. Resonant frequencies of standing humans. *Ergonomics*, 40(9):879–886, 1997.
- [55] T.E. Fairley and M.J. Griffin. The apparent mass of the seated human body: vertical vibration. *Journal of Biomechanics*, 22:81–94, 1989.

- [56] The European Parliament and the council of the European Union. Directive 2002/44/ec on the minimum health and safety requirements regarding the exposure of workers to the risks arising from physical agents (vibration). *Official Journal of the European Communities*, L177:13–19, 2002.
- [57] International Maritime Organization. *HSC-Code 2000 International code of safety for High-Speed Craft*, second edition, 2009.
- [58] Maritime and Coastguard Agency. *Marine Guidance Note MGN 436 Whole-body vibration: Guidance on Mitigating Against the Effects of Shocks and Impacts on Small Vessels.*, Sep 2011.
- [59] R. Peterson, E. Pierce, B. Price, and C. Bass. Shock mitigation for the human on high speed craft: Development of an impact injury design rule. In *TO AVT Symposium on Habitability of Combat and Transport Vehicles: Noise, Vibration and Motion*, 2004.
- [60] C. Bass, S. Lucas, R. Salzar, and W. Pilkey. Human biodynamics modeling (mk v seated). Planing boats 2, University of Virginia, 2003.
- [61] C. Bass, A. Ziemba, R.S. Peterson, and B. Price. Assessment of spinal impact injury from high speed craft loading. SAVIAC 75th Shock and Vibration Symposium, Oct 2004.
- [62] C. Bass, R. Salzar, J. Ash, A. Ziemba, S. Lucas, R. Peterson, E. Pierce, and B. Price. Dynamics models for the assessment of spinal injury from repeated impact in high speed planing boats. In *International IRCOBI Conference on the Biomechanics of Injury*, pages 397–400, Sep 2007.
- [63] C. Bass, R. Salzar, J. Ash, A. Ziemba, S. Lucas, R. Peterson, and E. Pierce. Development of dynamics models for assessing spinal dynamics and injury from repeated impact in high speed planing boats. In *SAE World Congress & Exhibition*, 2008.
- [64] International Maritime Organization. International convention for the safety of life at sea (solas), Nov 1974.
- [65] V. Kumar, V.H. Saran, and V. Guruguntla. Study of vibration dose value and discomfort due to whole body vibration exposure for a two wheeler drive. In *National Conference on Machines and Mechanisms*, 2013.
- [66] M.A. Miner. Cumulative damage in fatigue. *Applied Mechanics*, 12(3), 1945.
- [67] A. Fatemi and L. Yang. Cumulative fatigue damage and life prediction theories: a survey of the state of the art for homogeneous materials. *International Journal of Fatigue*, 20(1):9–34, Jan 1998.
- [68] M.C.Y. Niu. *Airframe Structural Design: Practical Design Information And Data On Aircraft Structures*. Hong Kong Conmilit Press LTD., second edition, 1999.
- [69] N.L. Post, S.W. Case, and J.J. Lesko. Modeling the variable amplitude fatigue of composite materials: A review and evaluation of the state of the art for spectrum loading. *International Journal of Fatigue*, 30(12):2064–2086, Dec 2008.
- [70] S.P. Zhu, H.Z. Huang, and Z.L. Wang. Fatigue life estimation considering damaging and strengthening of low amplitude loads under different load sequences using fuzzy sets approach. *International Journal of Damage Mechanics*, 2011.
- [71] Z. Peng, H.Z. Huang, J. Zhou, and Y.F. Li. A new cumulative fatigue damage rule based on dynamic residual s-n curve and material memory concept. *Metals*, 8(456), 2018.
- [72] W. Hwang and K.S. Han. Cumulative damage models and multi-stress fatigue life prediction. *Composite Materials*, 20(2):125–153, 1986.

- [73] H. Gao, H.Z. Huang, S.P. Zhu, Y.F. Li, and R. Yuan. A modified nonlinear damage accumulation model for fatigue life prediction considering load interaction effects. *The Scientific World Journal*, 2014.
- [74] H.L. Leve. Cumulative damage theories. In A.F. Madayag, editor, *Metal Fatigue: Theory and Design*, pages 170–203. John Wiley and Sons, 1969.
- [75] J.B. Morrison, D.G. Robinson, J.J. Nicol, G. Roddan, S.H. Martin, M.JN. Springer, B.J. Cameron, and J.P. Albano. A biomechanical approach to evaluating the health effects of repeated mechanical shocks. models for aircrew safety assessment: Use, limitations and requirements. NATO RTO Human Factors and Medicine Panel, 1999.
- [76] P.R. Payne and E.L. Stech. Dynamic models of the human body. Amrl-tr-66-157, Aerospace Medical Research Laboratory Wright-Patterson Air Force Base, Nov 1969.
- [77] NATO Standardization Agency. Procedures for evaluating the protection level of armoured vehicles. Aep-55, North Atlantic Treaty Organization, 2014.
- [78] J.W. Brinkley. Personnel protection concepts for advanced escape system design. In *Human Factors Considerations in High Performance Aircraft*, 1984.
- [79] C. Bass. The injury mechanics associated with shock mitigation. In *Mult-Agency Craft Conference*, 2002.
- [80] R. Happee, M. Hoofman, A. van den Kroonenberg, P. Morsink, and J. Wismans. A mathematical human body model for frontal and rearward seated automotive impact loading. Stapp Car Crash Conference, 1998.
- [81] R. Happee, S. Ridella, A. Najef, P. Morsink, R. de Lange, R. Bours, and J. van Hoof. Mathematical human body models representing a mid size male and a small female for frontal, lateral and reward impact loadings. IRCOBI Conference, Sep 2000.
- [82] M. Riley, T. Coats, K. Haupt, and D. Jacobson. The characterization of individual wave slam acceleration responses for high-speed craft. In *American Towing Tank Conference*, Aug 2010.
- [83] M.R. Riley and T.W. Coats. A simplified approach for analyzing accelerations induced by wave impacts in high-speed planing craft. In *The Third Chesapeake Powerboat Symposium*, Jun 2012.
- [84] A. Rosen and K. Garme. Model experiment addressing the impact pressure distribution on planing craft in waves. *International Journal of Small Craft Technology*, 146 Part B1, 2004.
- [85] K. Garme, A. Rosen, and J. Kutteneuler. In detail investigation of planing pressure. In *HYDRALAB 3 Joint User Meeting*, Feb 2010.
- [86] N.H. Jasper. Dynamic loading of a motor torpedo boat (yp 110) during high speed operation in rough water. David Taylor Model Basin Report C-175, Sep 1949.
- [87] D. Blount and D. Hankley. Full scale trials and analysis of high performance planing craft data. *Society of Naval and Marine Engineers*, 1976.
- [88] M.R. Riley and T.W. Coats. Development of a method for computing wave impact equivalent static accelerations for use in planing craft hull design. In *The Third Chesapeake Powerboat Symposium*, Jun 2012.
- [89] KNRM. Valentijn klasse, Jun 2020. <https://www.knrm.nl/reddingboten/valentijn-klasse>.
- [90] M.R. Riley, K.D. Haupt, and H.P. Murphy. Test specification guide for electrical and electronic equipment to withstand wave impacts in planing craft. Report nswccd-tm-23-2012/03, Naval Surface Warfare Center, Jan 2012.

- [91] P. Buxbaum. Easing the ride: How much can you mitigate shocks on the water. U.s. coast guard forum volume 2 issue 2, KMI Media Group, May 2010.
- [92] American Society of Testing and Materials. *Standard Test Method for Simulated Drop of Loaded Containers by Shock Machines*, Apr 2009. D5487.
- [93] Department of Defense Test Method Standard. *Environmental Engineering Considerations of Laboratory Tests*, Oct 2008. MIL-S-810G Method 516.6 Shock.
- [94] Department of Defense Test Method Standard. *Electronic and Electrical Component Parts*, Oct 2008. MIL-STD-202G Method 213B Shock.
- [95] N.J. Mansfield. *Human Response to Vibration*. CRC Press, 2005.
- [96] I.M. Daniel and O. Ishai. *Engineering mechanics of composite materials*. Oxford University Press Inc, second edition, 2006.
- [97] R.P. Notenboom. *Nonlinear Mode Interaction For Thin Imperfect Anisotropic Circular Cylindrical Shells Under Different Loading Conditions*. PhD thesis, Delft University of Technology, Dec 2006.
- [98] C Kassapoglou. *Design and Analysis of Composite Structures*. John Wiley & Sons Inc, second edition, 2013.
- [99] R. L. Burden and J.D. Faires. *Numerical Analysis*. Brooks/Cole, ninth edition, 2010.
- [100] W. Gautschi. *Numerical Analysis*. Birkhauser, second edition, 2011.
- [101] R.C. Hibbeler. *Mechanics of Materials*. Pearson, ninth edition, 2013.
- [102] P. Nanakorn and L.N. Vu. A 2d field-consistent beam element for large displacement analysis using the total lagrangian formulation. *Finite Elements in Analysis and Design*, 42(14-15):1240–1247, Oct 2006.
- [103] Klaus-Jurgen Bathe. *Finite Element Procedures In Engineering Analysis*. Prentice-Hall, 1982.
- [104] Z. P. Bazant and L. Cedolin. *Stability of Structures: Elastic, Inelastic, Fracture and Damage Theories*. World Scientific, first edition, 2010.
- [105] K.M. Hsiao and F. Y. Hou. Nonlinear finite element analysis of elastic frames. *Computers & Structures*, 26(4):693–701, 1987.
- [106] H.B. Coda and M. Greco. A simple fem formulation for large deflection 2d frame analysis based on position description. *Computer Methods in Applied Mechanics and Engineering*, 193(33-35):3541–3557, Aug 2004.
- [107] K. Mattiasson. Numerical results from large deflection beam and frame problems analysed by means of elliptic integrals. *International Journal for Numerical Methods in Engineering*, 17(1):145–153, Jan 1981.



Root-Finding Algorithms

The root-finding problem is a very common problem in numerical approximation. The process of a root-finding problem involves finding the solution of equation with the form $f(x) = 0$ for a given continuous differentiable function f . The function f can be defined as the difference between two arbitrary functions, for example $f(x) = g(x) - h(x)$. The root-finding problem is not necessarily limited to a single continuous function, for the roots of system of equations may be needed to find as well. For the root-finding problem, special algorithms are developed that are called root-finding algorithms. Root-finding algorithms are not always able to find the roots of given functions, but that does not mean that no roots exist. Most root-finding algorithms use iterations and a start value to solve the equations. As the number of iterations is limited, the algorithm provides a approximation to the root and not an exact solution. The error of the approximation (i.e. tolerance) can usually be defined by the user of the algorithm. The number of iterations needed to meet the required tolerance depends on the convergence rate [99].

A.1. Newton-Raphson Method

The root-finding algorithm Newton-Raphson method, also known as Newton's method, is named after Isaac Newton (1641-1727) and Joseph Raphson (1648-1715) and is one of the most powerful and well-known numerical methods for solving a root-finding problem. The basic idea of this method is to start with an initial approximation of the root x_0 , preferably close to the root, and to approximate the real root x_r by using the tangent line of the function. The tangent line of the function is calculated with theories from calculus. With the tangent line, an better approximation x_{n+1} , compared to the initial approximation, of the real root can be determined. Suppose that $f(x) \in C^2[a, b]$, where f is a continuous differentiable function with real values and $x_0 \in [a, b]$, such that $f'(x_0) \neq 0$ and $|x - x_0| \ll 1$. Consider, the first Taylor polynomial for $f(x)$ expanded about x_0 and evaluated at x [99] [100].

$$f(x) = f(x_0) + (x - x_0) \cdot f'(x_0) + \frac{(x - x_0)^2}{2} \cdot f''(x_0) \quad (\text{A.1})$$

Since $f(x) = 0$, the equation becomes

$$0 = f(x_0) + (x - x_0) \cdot f'(x_0) + \frac{(x - x_0)^2}{2} \cdot f''(x_0) \quad (\text{A.2})$$

The Newton-Raphson method is derived with the assumption that $|x - x_0| \ll 1$, meaning that $(x - x_0)^2$ is even smaller and can be omitted. Therefore, the equation is approximately

$$0 \approx f(x_0) + (x - x_0) \cdot f'(x_0) \quad (\text{A.3})$$

Solving this equation for x gives

$$x \approx x_0 - \frac{f(x_0)}{f'(x_0)} \equiv x_{n+1} \quad (\text{A.4})$$

From this derivation the Newton-Raphson method originates. The method starts with an initial approximation and generates a sequence as $\{x_n\}_{n=0}^{\infty}$, by

$$x_n = x_{n-1} - \frac{f(x_{n-1})}{f'(x_{n-1})} \text{ for } n \geq 1 \quad (\text{A.5})$$

The stopping technique inequalities in the application of this model for a number of iterations N and a given tolerance criteria $\epsilon > 0$ is described as

$$|f(x_N)| \leq \epsilon \quad (\text{A.6})$$

A disadvantage of this inequality is that it gives no information of the actual error $|x_r - x_N|$. However, this maximum value of the error can be influenced by altering the tolerance criterion [100].

The rate of convergence for the Newton-Raphson method is quadratic, but in order to have this rate a number of assumptions must be satisfied. Some of these advantages and disadvantages to those assumptions are: [99]

- An accurate initial approximation is needed, otherwise the assumption $|x - x_0| \ll 1$ is not true, meaning that the $(x - x_0)^2$ can not be omitted. Therefore, the first iterations are made with very small force scale factor, which gradually increases by small steps.
- The stopping technique inequality used gives no information of the resulting error, when the tolerance criterion is satisfied. However, this can be limited somewhat by defining a small tolerance and the final error is not that important in this application as long as it is small.
- One of the major drawbacks of the method is the need to know the value of the derivative of f at each approximation. The derivatives will be calculated with the finite difference method using a small step size.
- When a stationary point of the function is encountered, the derivative of the function will be equal to zero. The algorithm will stop and no approximation is found. To prevent problems with a stationary point, the finite difference method will make use of three points and use a polynomial.
- For a system of non-linear equations, the Jacobian matrix is needed to calculate the derivatives. Calculating the Jacobian and inverting it every matrix costs a lot of computing power. This can be reduced by using the result of a linear approximation sequence as an initial approximation for the non-linear iteration sequence.

In this research the Newton-Raphson method will be used for the static analysis. The residue function, equation (2.21), is a function of the displacements and the force scale vectors, such that $\vec{R} \in (\vec{Q}, \lambda)$. For the initial value ($k = 0$) of the displacements $\vec{Q}^{(k)}$, the equilibrium equation is not satisfied as $|\vec{R}^{(k)}(\vec{Q}^{(k)}, \lambda)| \neq \vec{0}$. Suppose that

$$\vec{Q}^{(k+1)} = \vec{Q}^{(k)} + \Delta\vec{Q}^{(k)} \quad (\text{A.7})$$

is a solution, so that

$$|\vec{R}^{(k+1)}(\vec{Q}^{(k+1)}, \lambda)| \approx \vec{0} \leq \vec{\epsilon} \quad (\text{A.8})$$

where ϵ is the defined tolerance criteria. Then,

$$\vec{R}^{(k+1)} \approx \vec{R}^{(k)} + \Delta\vec{R}^{(k)} \quad (\text{A.9})$$

and

$$\Delta\vec{R}^{(k)} = \left[\frac{\partial \vec{R}}{\partial \vec{Q}_i} \right] \Delta\vec{Q}^{(k)} = [J] \Delta\vec{Q}^{(k)} \quad (\text{A.10})$$

where $[J]$ is the Jacobian matrix. From this equation it follows that the correction for the displacement is given by

$$\Delta\vec{Q}^{(k)} = -[J]^{-1} \vec{R}^{(k)} \quad (\text{A.11})$$

Then, the new displacements vector can be determined according to

$$\vec{Q}^{(k+1)} = \vec{Q}^{(k)} - [J]^{-1} \vec{R}^{(k)} \quad (\text{A.12})$$

Using this result the new residue vector can be calculated and its value is with the defined tolerance criteria.

$$|\vec{R}^{(k+1)}(\vec{Q}^{(k+1)}, \lambda)| \leq \bar{\epsilon} ? \quad (\text{A.13})$$

If the tolerance criteria is not satisfied, the method is to be repeated. The Jacobian matrix in this algorithm has the form of

$$[J] = \left[\begin{array}{cccc} \frac{\partial \vec{R}(\vec{Q}, \lambda)}{\partial Q_1} & \frac{\partial \vec{R}(\vec{Q}, \lambda)}{\partial Q_2} & \dots & \frac{\partial \vec{R}(\vec{Q}, \lambda)}{\partial Q_N} \end{array} \right] \quad (\text{A.14})$$

Every column vector of the Jacobian is calculated with the finite difference method. With this method the derivatives of differential equations can be approximated. Using three points of a function f , the points f_0 , f_{-h} and f_{+h} , the derivative in f_0 can be approximated by plotting a polynomial through these points and calculating the average slope. In this calculation a small step size of h is used.

$$f'_0 = \frac{\frac{f_0 - f_{-h}}{h} + \frac{f_{+h} - f_0}{h}}{2} = \frac{f_{+h} - f_{-h}}{2h} \quad (\text{A.15})$$

For the static analyses, the derivatives are thus calculated by

$$\frac{\partial \vec{R}(\vec{Q}, \lambda)}{\partial Q_i} = \frac{\vec{R}((\vec{Q} + \Delta Q_i), \lambda) - \vec{R}((\vec{Q} - \Delta Q_i), \lambda)}{2h} \quad (\text{A.16})$$

B

Derivation of the Internal Forces for Standard Finite Elements

In this appendix the internal forces of the standard finite elements are derived from the potential energy formulations.

B.1. Non-Linear Beam Element

In this research, the potential energy of an element U_e is considered to be equal to the elastic strain energy. The strain energy of a volume of the element is defined as [42]

$$U_e = \frac{1}{2} \iiint_{Vol} \sigma \epsilon dV \quad (\text{B.1})$$

The potential energy is always positive as the stress and strain will always be in the same direction. As the material is homogeneous and behaves in a linear-elastic manner, Hooke's law can be used to simplify the expression. The Hooke's law, equation (B.2), for a linear elastic material states that the the strain in a material is linearly proportional to the applied stress using the modulus of elasticity (E) [101].

$$\sigma = E\epsilon \quad (\text{B.2})$$

This simplification is not valid for an element which experiences large deformations (i.e. plastic deformation). Substituting the Hooke's law in the potential energy equation and splitting the integral over the volume in a integral over the length and a integral over the cross-section gives

$$U_e = \frac{1}{2} \int_{x=0}^L \iint_A E\epsilon^2 dA dx \quad (\text{B.3})$$

B.1.1. Axial Strain

In figure B.1, a beam element with a length (L) and a point P are shown [42]. The deformed beam element has a horizontal displacement, vertical displacement and rotation. The horizontal and vertical displacement are a function of x , while the rotation is constant along the length of the beam. The shape functions for the local horizontal ($u(x)$) and vertical ($v(x)$) displacements can be defined as [42]

$$\begin{aligned} u(x) &= u_1 + \left(\frac{u_2 - u_1}{L} \right) x \\ v(x) &= v_1 + \left(\frac{v_2 - v_1}{L} \right) x \end{aligned} \quad (\text{B.4})$$

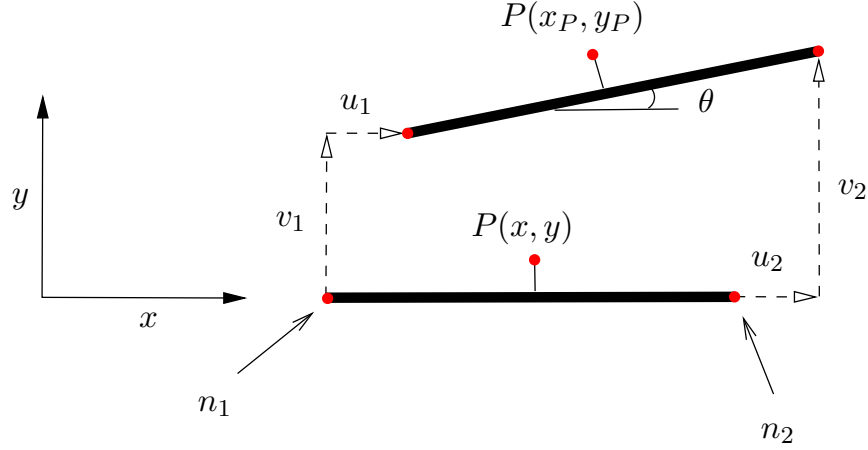


Figure B.1: Deformed beam element

The derivatives of these functions with respect to the horizontal coordinate are

$$\begin{aligned} u_x &= \frac{u_2 - u_1}{L} \\ v_x &= \frac{v_2 - v_1}{L} \end{aligned} \quad (\text{B.5})$$

Using these derivatives, the length of a deformed differential element with an unit length can be rewritten to [47]

$$L = \sqrt{(1 + u_x^2) + v_x^2} \quad (\text{B.6})$$

and the trigonometric functions as a function of the deformed length [102].

$$\begin{aligned} \cos \theta &= \frac{1 + u_x}{\sqrt{(1 + u_x)^2 + v_x^2}} \\ \sin \theta &= \frac{v_x}{\sqrt{(1 + u_x)^2 + v_x^2}} \\ \tan \theta &= \frac{v_x}{1 + u_x} \end{aligned} \quad (\text{B.7})$$

For an arbitrary point P on the beam, the new position can be described as

$$\begin{aligned} x_P &= x + u - y \sin \theta \\ y_P &= v + y \cos \theta \end{aligned} \quad (\text{B.8})$$

where u and v are a function of x, y . With these equations the displacement gradient matrix can be written as [102]

$$[F] = \begin{bmatrix} \frac{\partial x_P}{\partial x} & \frac{\partial x_P}{\partial y} \\ \frac{\partial y_P}{\partial x} & \frac{\partial y_P}{\partial y} \end{bmatrix} = \begin{bmatrix} 1 + u_x & -\sin \theta \\ v_x & \cos \theta \end{bmatrix} \quad (\text{B.9})$$

The Green-Lagrange strain matrix is defined as [47]

$$[E] = \begin{bmatrix} \epsilon_{xx} & \epsilon_{xy} \\ \epsilon_{yx} & \epsilon_{yy} \end{bmatrix} = \frac{1}{2} [F]^T [F] - [I] \quad (\text{B.10})$$

The rotation matrix is defined as

$$[R] = \begin{bmatrix} \cos \theta & \sin \theta \\ -\sin \theta & \cos \theta \end{bmatrix} \quad (\text{B.11})$$

A matrix $[\hat{F}]$ can be defined which can be simplified with the trigonometric functions to

$$[\hat{F}] = [R][F] = \begin{bmatrix} \frac{(1+u_x)^2}{\sqrt{(1+u_x)^2+v_x^2}} + \frac{v_x^2}{\sqrt{(1+u_x)^2+v_x^2}} & 0 \\ 0 & 1 \end{bmatrix} = \begin{bmatrix} \sqrt{(1+u_x)^2+v_x^2} & 0 \\ 0 & 1 \end{bmatrix} \quad (\text{B.12})$$

As the rotation matrix is orthogonal the Green-Lagrange strain can be rewritten to

$$[E] = \frac{1}{2}[F]^T[R]^T[R][F] - [I] = \frac{1}{2}[\hat{F}]^T[\hat{F}] - [I] \quad (\text{B.13})$$

Another matrix $[L]$ is defined as

$$[L] = [\hat{F}] - [I] = \begin{bmatrix} \sqrt{(1+u_x)^2+v_x^2} - 1 & 0 \\ 0 & 0 \end{bmatrix} = [L]^T \quad (\text{B.14})$$

With the matrix $[L]$ this the Euler-Lagrange strain becomes [102] [46]

$$[E] = \frac{1}{2}[\hat{F}]^T[\hat{F}] - [I] = \frac{1}{2}([L][L]^T + [L]^T + [L]) \approx [L] \quad (\text{B.15})$$

The term $[L][L]^T$ is neglected, because the strains are assumed to be small $u_x, v_x \ll 1$ [47]. The only non-zero component in the strain matrix is the axial strain which is

$$\epsilon_{xx} = \epsilon_a = \sqrt{1+2u_x+u_x^2+v_x^2} - 1 \quad (\text{B.16})$$

The Taylor polynomial series is used to simplify the expression of the axial strain [47]. The function $\sqrt{1+\mu}$ can be expressed as

$$\sqrt{1+\mu} = 1 + \frac{1}{2}\mu - \frac{1}{8}\mu^2 + \sum_{n=3}^{\infty} \mu^n (-1)^{n-1} \frac{(2n-3)!}{n!(n-2)!2^{2n-2}} \quad (\text{B.17})$$

according to the Taylor series of

$$\sum_{n=0}^{\infty} x^n \frac{f^{(n)}(0)}{n!} = \sum_{n=0}^{\infty} x^n (-1)^{n-1} \frac{(2n-3)!}{n!(n-2)!2^{2n-2}} \quad (\text{B.18})$$

If $\mu \ll 1$ is true, then $\mu^2 \approx 0$. Therefore, it is assumed that the function can be approximated as

$$\sqrt{1+\mu} \approx 1 + \frac{1}{2}\mu \quad (\text{B.19})$$

With this approximation, the expression for the axial strain simplifies to [47] [42]

$$\epsilon_a = u_x + \frac{1}{2}u_x^2 + \frac{1}{2}v_x^2 \quad (\text{B.20})$$

B.1.2. Bending Strain

The dimensions of the cross-section of the beam are much smaller than the length $b, t \ll L$ such that the beam is considered slender. The cross-sectional plane remains perpendicular to the neutral axis when deforming such that shear deformations in the deformation of the beam are excluded [103].

In figure B.2, a differential element of the beam element before and after deformation due to a bending load is shown. In this figure, the horizontal axis is placed on the neutral axis of the beam. As the differential element deforms, the angle between cross-sections at different locations becomes $d\theta$ and the slope of the beam is θ . The radius of curvature ρ is defined as the distance from the center of curvature to the arc dx . Any arc of the differential element other than dx is subjected to strain. The strain of an arbitrary arc ds can be calculated according to

$$\epsilon = \frac{ds' - ds}{ds} = \frac{ds' - dx}{dx} = \frac{(\rho + y)d\theta - \rho d\theta}{\rho d\theta} = \frac{y}{\rho} \quad (\text{B.21})$$

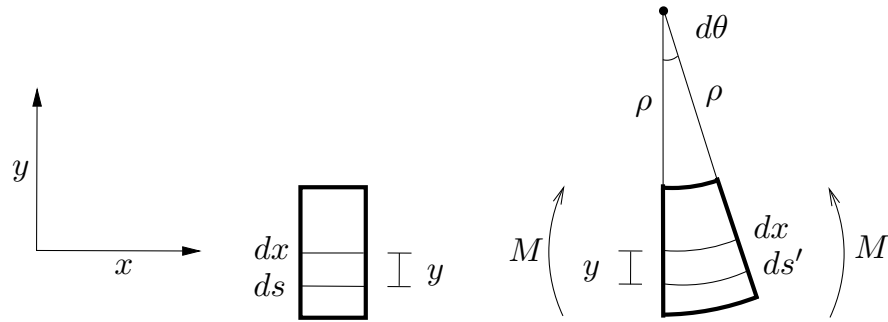


Figure B.2: Deformed differential beam element due to bending

With Hooke's law (B.2) and the flexure formula which describes the bending stress in a beam under a bending moment $\sigma = \frac{-My}{I}$ the radius of curvature can be calculated according to

$$\frac{1}{\rho} = \frac{M}{EI} \quad (\text{B.22})$$

This equation is called the moment-curvature relationship. Another method to describe the radius of curvature is from its relation with the arc length and the angle of the arc.

$$\rho d\theta = ds \rightarrow \rho \frac{d\theta}{dx} = \frac{ds}{dx} \quad (\text{B.23})$$

The relation is derived based on figure B.3. Where the slope of the arc is defined as $\tan(\theta) = \frac{dy}{dx}$ and is

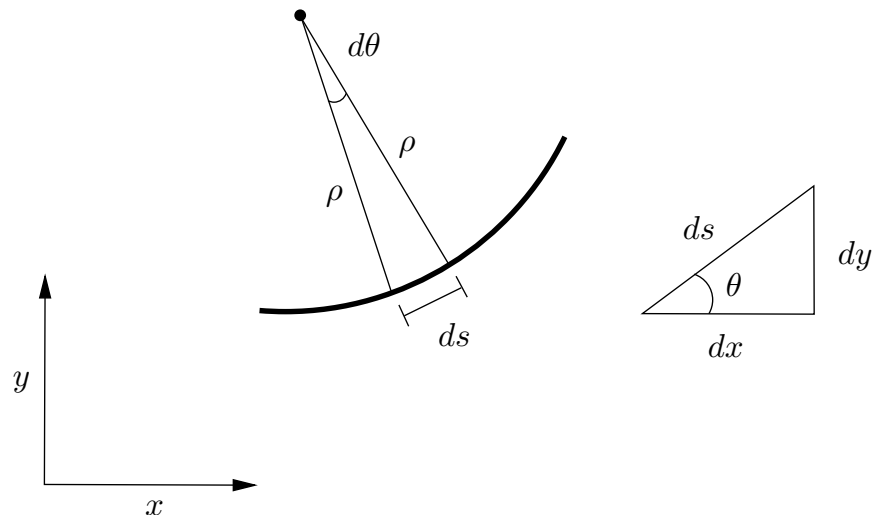


Figure B.3: Relation between radius of curvature and arc length

differentiated to

$$\frac{d\theta}{dx} = \frac{\frac{d^2y}{dx^2}}{1 + \left(\frac{dy}{dx}\right)^2} \quad (\text{B.24})$$

The arc length is calculated with Pythagorean theorem and rewritten to

$$\frac{ds}{dx} = \sqrt{1 + \left(\frac{dy}{dx}\right)^2} \quad (\text{B.25})$$

From these equations follows the expression for the radius of curvature [101].

$$\frac{1}{\rho} = \frac{\frac{d^2y}{dx^2}}{\left[1 + \left(\frac{dy}{dx}\right)^2\right]^{\frac{3}{2}}} \quad (\text{B.26})$$

For the beam element, the shape function for the vertical displacement along the beam $v(x)$ is substituted for the curve displacement function y .

$$\frac{1}{\rho} = \frac{\frac{d^2v}{dx^2}}{\left[1 + \left(\frac{dv}{dx}\right)^2\right]^{\frac{3}{2}}} \quad (\text{B.27})$$

It is assumed that the displacements $u_x \ll 1$ and slope $\tan(\theta) \approx \theta$ of the deformed beam are small such that the angle in figure B.1 can be approximated as

$$\tan \theta = \frac{v_x}{1 + u_x} \rightarrow \theta \approx v_x \quad (\text{B.28})$$

This approximation is known as the small angle approximation. If the angle is $\theta \ll 1$, then the term v_x^2 in equation (B.27) is negligible. Therefore, the expression for the radius of curvature simplifies to

$$\frac{1}{\rho} = \frac{d\theta}{dx} \approx \frac{dv_x}{dx} \quad (\text{B.29})$$

Combining this result with the strain for an arbitrary arc at a distance y the expression becomes

$$\frac{\epsilon}{y} \approx \frac{dv_x}{dx} \quad (\text{B.30})$$

From which follows that the strain is [42]

$$\epsilon = y\epsilon_b \approx yv_{xx} \quad (\text{B.31})$$

Therefore, the bending strain in a beam element is approximately equal to second derivative of the shape function for the vertical displacement. The shape function for the local vertical displacement and displacement is expressed as [42]

$$v(x) = a_0 + a_1x + a_2x^2 + a_3x^3 \quad (\text{B.32})$$

The shape function for the rotation can be derived by the approximation that $\theta = v_x$.

$$\theta(x) = a_1 + 2a_2x + 3a_3x^2 \quad (\text{B.33})$$

For the shape functions, the following boundary conditions are valid for a beam subjected to a bending moment.

$$x = \begin{cases} 0, & v_1 = a_0 \\ 0, & \theta_1 = a_1 \\ L, & v_2 = a_0 + a_1L + a_2L^2 + a_3L^3 \\ L, & \theta_2 = a_1 + 2a_2L + 3a_3L^2 \end{cases} \quad (\text{B.34})$$

Using the boundary conditions, the coefficients a_0, a_1, a_2 and a_3 can be determined. The shape function for the local vertical displacements including the rotation of the nodes results in

$$v(x) = v_1 + \theta_1 x + \left(-\frac{3(v_1 - v_2)}{L^2} - \frac{(2\theta_1 + \theta_2)}{L} \right) x^2 + \left(\frac{2(v_1 - v_2)}{L^3} + \frac{(\theta_1 + \theta_2)}{L^2} \right) x^3 \quad (\text{B.35})$$

B.1.3. Internal Forces

As the beam element supports both axial loads and bending loads, the total strain of the beam element consists of the axial strain and the bending strain.

$$\epsilon = \epsilon_a + y\epsilon_b \quad (\text{B.36})$$

As the axial strain and bending strain are not a function of the cross-section and the modulus of elasticity is not a function of the cross-section and constant over the length of the element, the potential energy simplifies to

$$U_e = \frac{1}{2} E \int_x \left(\epsilon_a^2 \iint_A dA + 2\epsilon_a \epsilon_b \iint_A y dA + \epsilon_b^2 \iint_A y^2 dA \right) dx \quad (\text{B.37})$$

The beam element is considered from the neutral axis of the element. Therefore, the vertical coordinate in the total strain of the beam element is equal to zero. The integrals over the cross-section therefore simplify to

$$\begin{aligned} \iint_A dA &= A \\ \iint_A y dA &= 0 \\ \iint_A y^2 dA &= I \end{aligned} \quad (\text{B.38})$$

The total potential energy of the beam element results in

$$U_e = U_a + U_b = \frac{1}{2} EA \int_{x=0}^L \epsilon_a^2 dx + \frac{1}{2} EI \int_{x=0}^L \epsilon_b^2 dx \quad (\text{B.39})$$

This equation shows that the potential energy of the beam element consists of the potential energy due to axial strain U_a and bending strain U_b . Both the axial strain and bending strain are a function of the horizontal coordinate. In order to calculate the internal forces of the non-linear beam element, the expression for the potential energy is rewritten to

$$U_e = \frac{1}{2} EAL \int_{\xi=0}^1 \epsilon_a^2 d\xi + \frac{1}{2} EIL \int_{\xi=0}^1 \epsilon_b^2 d\xi \quad (\text{B.40})$$

Where $\xi = \frac{x}{L}$. In these equation, the displacements are made non-dimensional using the length of the bar. The local internal forces of the beam element are determined by calculating the partial derivatives of the potential energy with respect to the local displacements. Displacements and rotations in the local coordinate system with the lowercase letter q . Where q is a vector which has the form of $(u_1, v_1, \theta_1, u_2, v_2, \theta_2)$ and $\bar{q}_i = \frac{q_i}{L}$.

$$\frac{\partial U_e}{\partial \bar{q}_i} = EAL \int_{\xi=0}^1 \epsilon_a \frac{\partial \epsilon_a}{\partial \bar{q}_i} d\xi + EIL \int_{\xi=0}^1 \epsilon_b \frac{\partial \epsilon_b}{\partial \bar{q}_i} d\xi \quad (\text{B.41})$$

The integrals have the form of

$$\int_{\xi=0}^1 \epsilon_a \frac{\partial \epsilon_a}{\partial \bar{q}_i} d\xi = \int_{\xi=0}^1 (e_0 + e_1\xi + e_2\xi^2 + e_3\xi^3 + e_4\xi^4) (c_0 + c_1\xi + c_2\xi^2 + c_3\xi^3 + c_4\xi^4) d\xi \quad (\text{B.42})$$

The product of the two polynomials within the integral produces an polynomial of the eight order. For the integrals of the bending strain, the polynomial is only of the fourth order.

The non-dimensional displacements are transformed back to normal displacements using the length of the beam.

$$\frac{\partial U_e}{\partial q_j} = \frac{1}{L} \frac{\partial U_e}{\partial \bar{q}_i} \quad (\text{B.43})$$

Figure B.4 , shows the beam element in the global coordinate system. Displacements and rotations in the global coordinate system are indicated with the uppercase letter Q . The local coordinate system is at an angle α compared to the global coordinate system. With the angle of the beam element, the internal forces

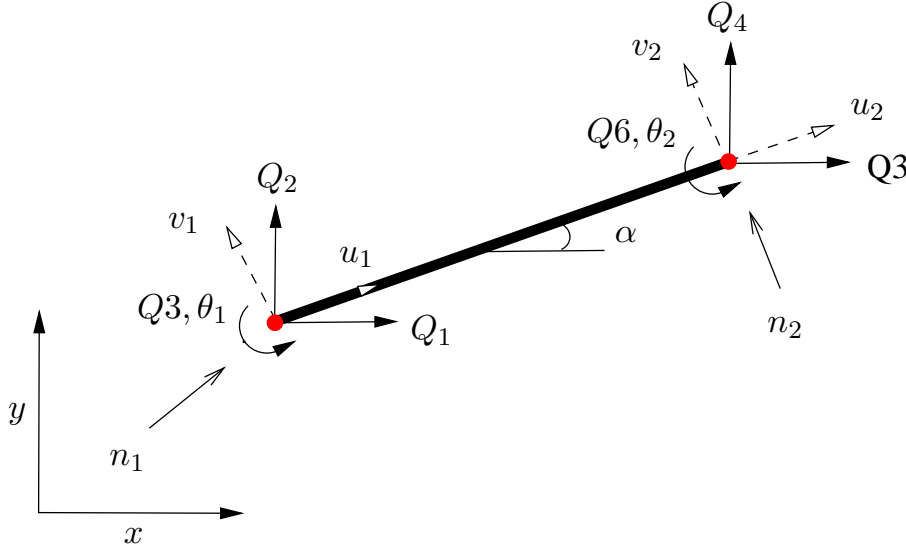


Figure B.4: Beam element in the global coordinate system

in the global coordinate system are calculated according to [44] [42]

$$\begin{aligned} \frac{\partial U_e}{\partial Q_1} &= \frac{\partial U_e}{\partial q_1} \cos \alpha - \frac{\partial U_e}{\partial q_2} \sin \alpha & \frac{\partial U_e}{\partial Q_4} &= \frac{\partial U_e}{\partial q_4} \cos \alpha - \frac{\partial U_e}{\partial q_5} \sin \alpha \\ \frac{\partial U_e}{\partial Q_2} &= \frac{\partial U_e}{\partial q_1} \sin \alpha + \frac{\partial U_e}{\partial q_2} \cos \alpha & \frac{\partial U_e}{\partial Q_5} &= \frac{\partial U_e}{\partial q_4} \sin \alpha + \frac{\partial U_e}{\partial q_5} \cos \alpha \\ \frac{\partial U_e}{\partial Q_3} &= \frac{\partial U_e}{\partial q_3} & \frac{\partial U_e}{\partial Q_6} &= \frac{\partial U_e}{\partial q_6} \end{aligned} \quad (\text{B.44})$$

The resulting internal forces of the non-linear beam element are summed into an internal forces vector for the complete system according to

$$\frac{\partial U}{\partial Q_i} = \sum \frac{\partial U_e}{\partial Q_j} \quad (\text{B.45})$$

Where $j = 3n_1 - 3 + i$ with $i = 1, 2, 3$ for nodal point one and where $j = 3n_2 - 6 + i$ with $i = 4, 5, 6$ for nodal point two.

B.2. Linear Beam Element

A simplified version of the non-linear beam element is the linear beam element. A linear beam element can be used when the local horizontal displacement is not influenced by the local vertical displacement of the beam due to bending. The deformed length only depends on the local displacements in the horizontal direction.

Therefore, the non-linear terms in the axial strain (B.20) are neglected and the axial strain reduces to

$$\epsilon_a = u_x \quad (\text{B.46})$$

The bending strain is unchanged and remains

$$\epsilon_b \approx v_{x,x} \quad (\text{B.47})$$

As a result of the simplified axial strain the potential energy can be simply calculated with

$$U_e = \frac{1}{2}EA\epsilon_a^2 + \frac{1}{2}EI \int_{x=0}^L \epsilon_b^2 dx \quad (\text{B.48})$$

as the axial strain is not a function of the horizontal coordinate. No substitution with the dimensionless length ξ is required in order to solve the integral for the bending strain. The internal forces are calculated with

$$\frac{\partial U_e}{\partial q_i} = EA\epsilon_a \frac{\partial \epsilon_a}{\partial q_i} + EI \int_{x=0}^L \epsilon_b \frac{\partial \epsilon_b}{\partial q_i} dx \quad (\text{B.49})$$

The internal forces in the local coordinate system are transformed to internal forces in the global coordinate system according to (B.44). Subsequently, these forces are summed for the complete system according to (B.45).

B.3. Non-Linear Bar Element

A bar element is similar to a beam element, except the dimensions of the cross-section are such that the bar element can only support axial loads. Therefore, this bar element can only be used in specific parts of structures where only axial loads are present.

For the non-linear bar element, the total strain consists only of the axial strain.

$$\epsilon = \epsilon_a = u_x + \frac{1}{2}u_x^2 + \frac{1}{2}v_x^2 \quad (\text{B.50})$$

Where the shape function for the vertical displacement and rotation (B.35) is simplified to

$$v(x) = v_1 + \left(\frac{v_2 - v_1}{L} \right) x \quad (\text{B.51})$$

as the the nodal points do not have a rotation and the bar can not support bending loads. Therefore, the potential energy of the element only consists of the potential energy due to axial strain.

$$U_e = U_a \quad (\text{B.52})$$

The potential energy due to axial strain can be calculated with

$$U_a = \frac{1}{2}EA \int_{x=0}^L \epsilon_a^2 dx = \frac{1}{2}EA\epsilon_a^2 \quad (\text{B.53})$$

From which the internal forces are calculated according to

$$\frac{\partial U_e}{\partial q_i} = EA\epsilon_a \frac{\partial \epsilon_a}{\partial q_i} \quad (\text{B.54})$$

Where q has the form of (u_1, v_1, u_2, v_2) . Figure B.5, shows the bar element in the global coordinate system. The figure also shows that the nodal points do not have a rotation as the element can not support bending loads. The internal forces in the local coordinate system are transformed to internal forces in the

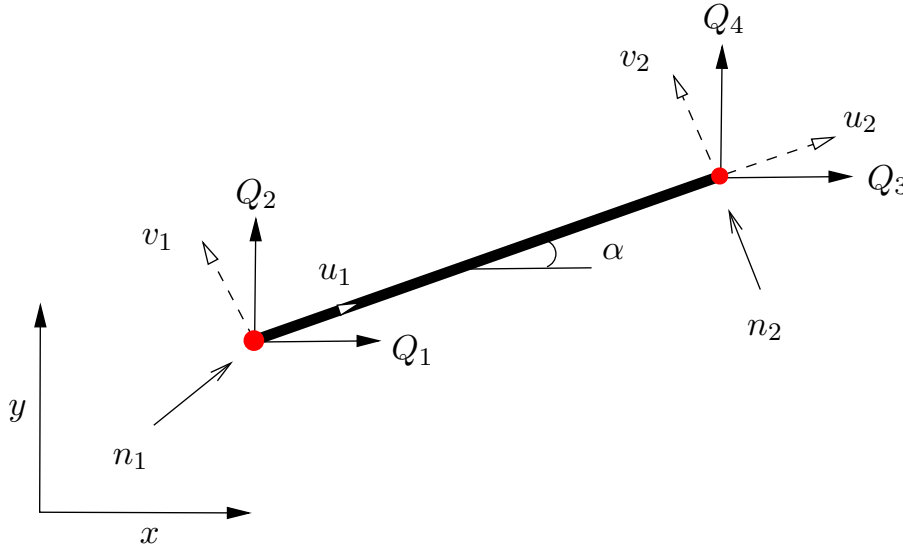


Figure B.5: Bar element in the global coordinate system

global coordinate system according to (B.44). Subsequently, these forces are summed for the complete system according to (B.45).

B.4. Linear Bar Element

A simplified version of the non-linear bar element is the linear bar element. The linear bar element can be used when only axial loads are applied and when the local horizontal displacement is not influenced by the local vertical displacement. The deformed length of the bar element depends on the local displacements in the horizontal direction.

For the linear bar element, the total strain consists of the linear terms in the axial strain [103] [44] [42].

$$\epsilon = \epsilon_a = u_x \quad (\text{B.55})$$

The rest of the derivation for the internal forces of the linear bar element follows the derivation of the non-linear bar element, but the vector q has the form of (u_1, u_2) .

B.5. Large Rotation Beam Element

For the non-linear beam element, the small angle approximation (B.28) was used to derive the shape function for the vertical displacement. A more complex and accurate shape function can be derived when this approximation is not made.

If the small angle approximation is not valid, then the strain is equal to

$$\epsilon = y\epsilon_b = y \frac{d\theta}{dx} \quad (\text{B.56})$$

The derivative of the $\tan \theta$ is calculated according to

$$\frac{d \tan \theta}{dx} = \frac{d \tan \theta}{d\theta} \frac{d\theta}{dx} \quad (\text{B.57})$$

with $\tan \theta = \frac{v_x}{1 + u_x}$. Following from these equations $\frac{d\theta}{dx}$ can be derived as

$$\frac{d\theta}{dx} = \cos^2(\theta) \frac{d \tan \theta}{dx} \quad (\text{B.58})$$

where [102]

$$\frac{d \tan \theta}{dx} = \frac{v_{xx}(1 + u_x) - v_x u_{xx}}{(1 + u_x)^2} \quad (\text{B.59})$$

Based on the shape function of the horizontal displacement (B.4), the term u_{xx} is equal to zero. Therefore, the final expression for the bending strain is [102]

$$\epsilon_b = \frac{d\theta}{dx} = \frac{v_{xx}(1 + u_x)}{(1 + u_x)^2 + v_x^2} \quad (\text{B.60})$$

The shape function for the local vertical displacement is again expressed as (B.32). For the shape functions, the following boundary conditions are valid.

$$x = \begin{cases} 0, & v_1 = a_0 \\ 0, & v_{1x} = a_1 \\ L, & v_2 = a_0 + a_1L + a_2L^2 + a_3L^3 \\ L, & v_{2x} = a_1 + 2a_2L + 3a_3L^2 \end{cases} \quad (\text{B.61})$$

With

$$\begin{aligned} v_{1x} &= (1 + u_x) \tan \theta_1 \\ v_{2x} &= (1 + u_x) \tan \theta_2 \end{aligned} \quad (\text{B.62})$$

The resulting shape function of the local vertical displacement is

$$\begin{aligned} v(x) &= v_1 + \frac{1}{L}((L + u_2 - u_1) \tan \theta_1)x \\ &+ \frac{1}{L^2} (3(v_2 - v_1) - (L + u_2 - u_1)(2 \tan \theta_1 + \tan \theta_2)) x^2 \\ &+ \frac{1}{L^3} (2(v_1 - v_2) + (L + u_2 - u_1)(\tan \theta_1 + \tan \theta_2)) x^3 \end{aligned} \quad (\text{B.63})$$

If the deformations and angle would small such that $u_x \ll 1$ and $\tan \theta \approx \theta$ were valid, then the expression for the shape function would simplify to equation (B.35), which is the shape function for the vertical displacement based on the small angle approximation.

The potential energy of the beam is calculated with (B.40), where the displacements are expressed as the dimensionless length ξ . For the internal forces, the potential energy is partially derived to the local displacements according to (B.41).

In an attempt to solve the integrals, both the axial strain and bending strain are differentiated to one of the six displacement directions.

$$\frac{\partial \epsilon_a}{\partial \bar{q}_i} = \frac{\partial u_x}{\partial \bar{q}_i} + u_x \frac{\partial u_x}{\partial \bar{q}_i} + v_x \frac{\partial v_x}{\partial \bar{q}_i} \quad (\text{B.64})$$

$$\frac{\partial \epsilon_b}{\partial \bar{q}_i} = \frac{\frac{\partial v_{xx}}{\partial \bar{q}_i}(1 + u_x) + v_{xx} \frac{\partial u_x}{\partial \bar{q}_i}}{(1 + u_x)^2 + v_x^2} - 2 \frac{v_{xx}(1 + u_x) \left((1 + u_x) \frac{\partial u_x}{\partial \bar{q}_i} + v_x \frac{\partial v_x}{\partial \bar{q}_i} \right)}{\left((1 + u_x)^2 + v_x^2 \right)^2} \quad (\text{B.65})$$

The resulting integrals can not be solved directly. Based on the assumption that the term $(1 + u_x)^2 + v_x^2$ always is nonzero, the integrals do not have asymptotic behaviour. Therefore, the integrals will be solved using numerical integration. A suitable numerical integration method is the Gaussian quadrature method. The Gaussian quadrature method solves the integrals according to [99]

$$\int_{\xi=0}^1 f(\xi) d\xi \approx \frac{1}{2} \sum_{i=1}^N f(\xi_i) w_i \quad (\text{B.66})$$

where

$$\xi_i = \frac{1 + \eta_i}{2} \quad (\text{B.67})$$

The Gaussian quadrature method divides the points for evaluation of the integral in an optimal way. The number of points can be adjusted to the required precision of the results [99].

Once the internal forces in the local coordinate system are calculated, they are transformed to internal forces in the global coordinate system according to (B.44). Subsequently, these forces are summed for the complete system according to (B.45).

C

Validation of Standard Finite Elements

In this appendix the finite elements of the model are validated on the basis of test cases from literature. For each element, the most important results from the literature will be shown as well as the results obtained using the finite elements.

C.1. Bar Element

The linear bar element of the program is not validated through a test case obtained from literature as this element is easy to validate by hand calculations for a structure with few elements. The non-linear bar element is validated with a Von Mises truss test case. This validation is discussed in the next section.

C.1.1. Von Mises Truss

In this section, the non-linear bar element will be validated with a Von Mises truss obtained from literature [104] [46] [47]. The Von Mises truss structure is shown in figure C.1.

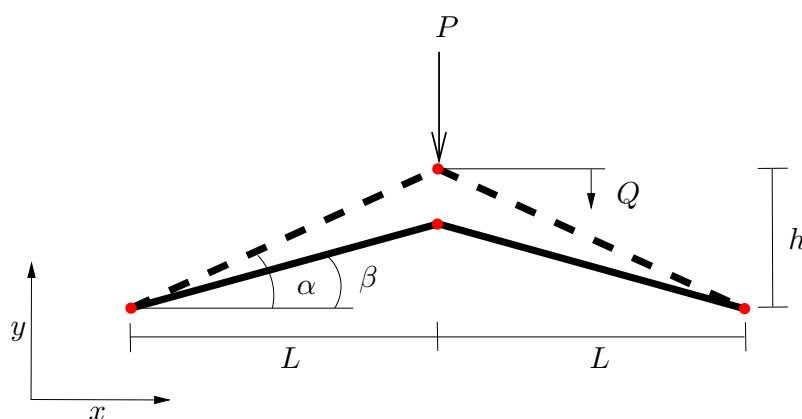


Figure C.1: Schematic representation of the Von Mises truss

The Von Mises truss consists of two linear elastic bar elements with equal specific properties and the same length. Both bars are pinned on one end and connected with each other on the other end. The Euler buckling load is assumed to be large enough to prevent the bars from ever buckling. As an increasing vertical load is applied to the joint, both bars will gradually deform until the structure shows snap-through

behaviour. A snap-through is a phenomenon where the structure quickly deforms from one stable equilibrium state to another stable equilibrium state under a marginal increase of the applied force.

First, the analytical derivation of the Von Mises truss is shown [104]. The length of the bars in the Von Mises truss can be determined with the half-span width and the initial angle of the bar.

$$L_b = \frac{L}{\cos \alpha} \quad (\text{C.1})$$

The axial strain of the bars is [46] [47]

$$\epsilon = \frac{L'_b - L_b}{L_b} = \frac{\cos \alpha}{\cos \beta} - 1 \quad (\text{C.2})$$

With a definition for the strain, the potential energy is expressed as

$$\Pi = U - PQ = \frac{EAL}{\cos \beta} \left(\frac{\cos \alpha}{\cos \beta} - 1 \right)^2 - PL(\tan \alpha - \tan \beta) \quad (\text{C.3})$$

By differentiation, the equilibrium condition can be obtained.

$$\frac{\partial \Pi}{\partial \beta} = \frac{1}{\cos^2 \beta} [2EA(\cos \alpha \tan \beta - \sin \beta) + P] = 0 \quad (\text{C.4})$$

Which means that equilibrium is achieved when

$$P = 2EA(\sin \beta - \cos \alpha \tan \beta) \quad (\text{C.5})$$

By another differentiation, the extreme values of the force P for a certain β are determined.

$$\frac{\partial P}{\partial \beta} = 2EA \left(\cos \beta - \cos \alpha \frac{1}{\cos^2 \beta} \right) = 0 \quad (\text{C.6})$$

From which follows

$$\cos \beta = (\cos \alpha)^{\frac{1}{3}} \quad (\text{C.7})$$

Therefore the critical deformed angle β_{crit} , indicating the limit point, is

$$\beta_{\text{crit}} = \cos^{-1}(\cos \alpha)^{\frac{1}{3}} \quad (\text{C.8})$$

Accordingly, the critical load and the critical vertical displacement can be calculated with

$$P_{\text{crit}} = 2EA(\sin \beta_{\text{crit}} - \cos \alpha \tan \beta_{\text{crit}}) \quad (\text{C.9})$$

$$Q_{\text{crit}} = h - L \tan \beta_{\text{crit}} \quad (\text{C.10})$$

In figure C.2, the equilibrium path for the Von Mises truss is shown. The stable and unstable region of the equilibrium path are indicated with the green and red lines above the equilibrium path. With a snap-through, the deformed Von Mises truss snaps from the stable equilibrium at β_{crit} to the static equilibrium at $-\beta_{\text{crit}}$.

The finite element program used in this research and described in this report is only able to accurately calculate the values until the limit point and no values in the unstable region of the equilibrium path. If one wants to calculate the force/displacement beyond the limit point in the unstable region of the equilibrium path, one should apply displacement loading instead of force loading [47]. In order to validate the non-linear bar element the results of the analytical derivation and the finite element results are compared. For the bar element, the following specific properties are used: a modulus of elasticity of $E = 1.28 \cdot 10^9$ [N·m⁻²] and a cross-sectional area A of 1.0 [m²]. Per bar only one element was used and the tolerance for the Newton-Raphson method is set to $\epsilon \leq 1 \cdot 10^{-8}$ [-]. The number of scale factors to gradually increase to load was $\lambda = 1 \cdot 10^5$ [-]. Three different cases were used, in which the initial height of the joint varied for the values $h = 5.0$ [m], $h = 1.0$ [m] and $h = 0.1$ [m]. The results are shown in tables C.1 and C.2.

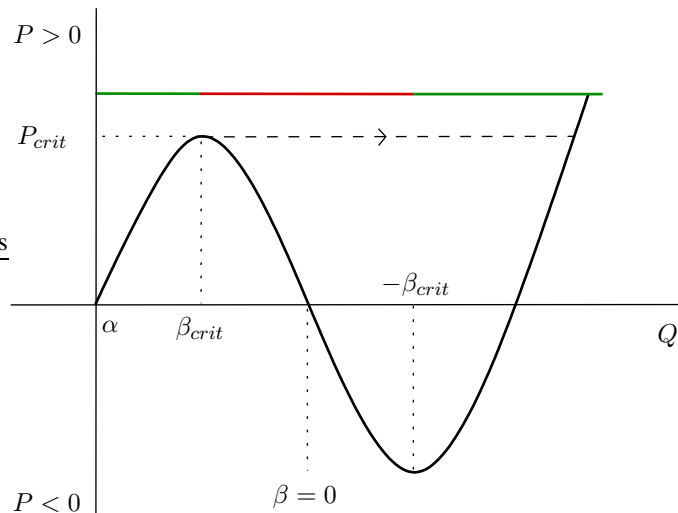


Figure C.2: Von Mises truss equilibrium path including snap-through behaviour

Tables C.1 and C.2 show that the results for a smaller initial height have a lower error value for both the critical load and the critical deformed angle. This can be explained by the fact that in the derivation of the bar element, an approximation is made using a Taylor polynomial which is valid for small deformations. Therefore, the approximation more valid for lower initial heights, a smaller initial angle leading to smaller errors.

Table C.1: Von Mises truss critical load results

Test case	Analytic result [N]	FEM result [N]	Error [%]
A	$4.91 \cdot 10^7$	$4.41 \cdot 10^7$	10.31
B	$4.88 \cdot 10^5$	$4.85 \cdot 10^5$	0.50
C	$4.93 \cdot 10^2$	$4.93 \cdot 10^2$	0.01

Table C.2: Von Mises truss critical displacement results

Test case	Analytic result [m]	FEM result [m]	Error [%]
A	2.22	2.11	4.89
B	$4.24 \cdot 10^{-1}$	$4.22 \cdot 10^{-1}$	0.43
C	$4.23 \cdot 10^{-2}$	$4.22 \cdot 10^{-2}$	0.25

C.2. Beam Element

In this section both the linear beam element and the non-linear beam element are validated. The linear beam element is validated through a comparison with an analytical derivation of the suspension design of seat B, see figure 5.4a. The analytical derivation is based on the virtual work method. The non-linear beam element is validated with test cases obtained from literature.

C.2.1. Beam Deflection Formulae

In this section, the linear beam element will be validated through a comparison with an analytical derivation of the parallel leaf spring of seat B, see figure 5.4a. A schematic representation of seat B is shown in figure C.3. In this schematic representation, the parallel leaf spring is modelled as parallel beam elements with the same specific properties. At points A and B, the beams are clamped and the element at point P is considered as a rigid. Three loads are applied to the body: a force in the horizontal direction, a force in the vertical direction and a moment.

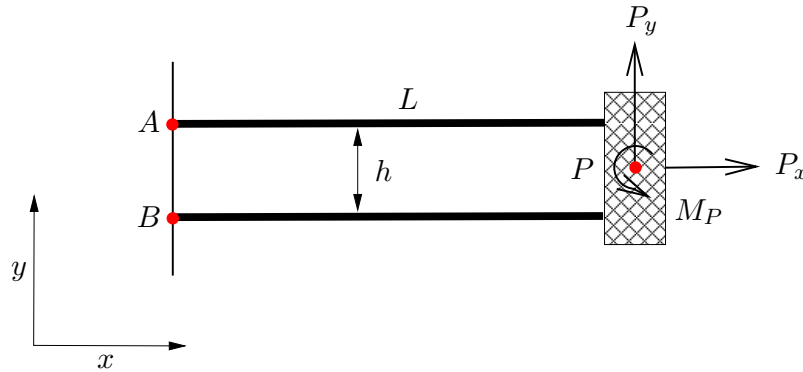


Figure C.3: Schematic representation of the simplified suspension of seat B

When comparing this figure with figure 5.4a it is noticeable that the parallel leaf spring in figure C.3 is not under an angle, which simplifies the derivation. To determine the behaviour of the parallel leaf spring when it is under an angle, one can simply apply the forces at the angle of interest. The objective of the analytical derivation is to determine for which conditions the rotation of the rigid body is approximately equal to zero. The rigid body represents the seat on which the person sits and this seat should have minimal rotation while experiencing vertical displacements.

As point A and B are clamped, reaction forces will occur. These forces are indicated with H for horizontal forces, V for vertical forces and M for moments. The equilibrium equations for this structure are

$$\begin{aligned}
 \rightarrow \sum = 0 & \quad -H_A - H_B + P_x = 0 \\
 +\uparrow \sum = 0 & \quad V_A + V_B + P_y = 0 \\
 \zeta + \sum = 0 & \quad M_B + P_y L - P_x \frac{h}{2} + M_P + M_A + H_A h = 0
 \end{aligned} \tag{C.11}$$

In these equilibrium equations there are six unknown reaction forces, while there are only three equilibrium equations. Therefore, the structure is statically indeterminate to the third degree. The virtual work method is applied to solve this problem. The reaction forces at point B are replaced with known forces, see figure C.4.

In addition, displacements requirements are derived that state that the horizontal displacement, vertical displacement and rotation of point B are equal to zero $u_B, v_B, \theta_B = 0$. The normal force, shear force and moment as a function of an arbitrary coordinate along the beam are derived.

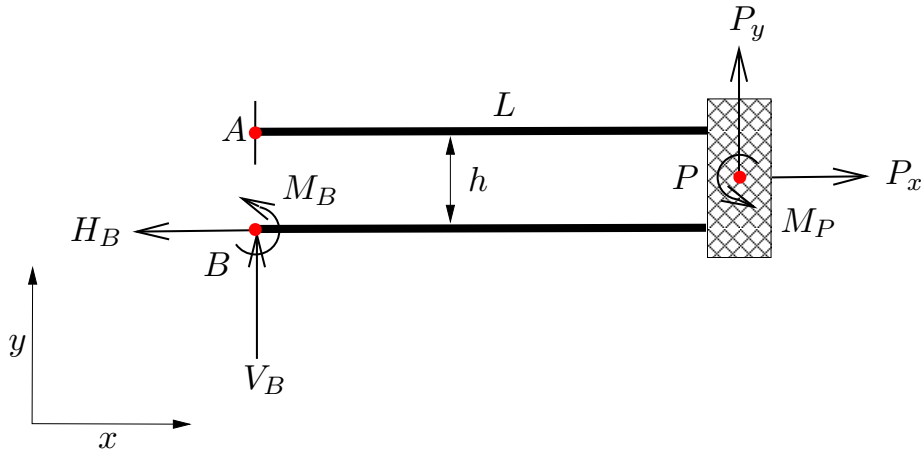


Figure C.4: Seat B suspension model application of virtual work method

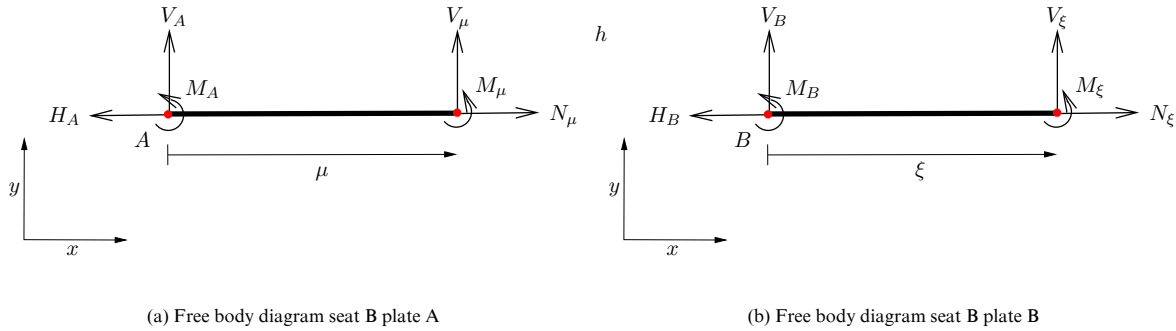


Figure C.5: Seat B suspension model free body diagrams

Starting with point A based on the Free Body Diagram (FBD) shown in figure C.5a.

$$\begin{aligned}
 \sum \rightarrow &= 0 & N(\xi) &= -H_A \\
 \sum \uparrow &= 0 & V(\xi) &= V_A \\
 \sum \curvearrowright &= 0 & M(\xi) &= M_A - V_A \xi
 \end{aligned}
 \tag{C.12}$$

In combination with the equilibrium equations the functions result in

$$\begin{aligned}
 N(\xi) &= -P_x + H_B \\
 V(\xi) &= -P_y - V_B \\
 M(\xi) &= \xi P_y + \xi V_B - M_B - P_y L - \frac{1}{2} P_x h - M_P + h H_B
 \end{aligned}
 \tag{C.13}$$

The same is done starting from point B, based on the FBD shown in figure C.5b.

$$\begin{aligned}
 \sum \rightarrow &= 0 & N(\mu) &= -H_B \\
 \sum \uparrow &= 0 & V(\mu) &= V_B \\
 \sum \curvearrowright &= 0 & M(\mu) &= -V_B \mu + M + B
 \end{aligned}
 \tag{C.14}$$

According to Castigliano's second theorem the horizontal displacement, vertical displacement and rotation of point B can be calculated. The theorem states that the displacement of a point is equal to the first

partial derivative of the strain energy with respect to the force acting on that point in the direction of the displacement [101].

$$\Delta = \int_0^L \frac{N}{EA} \frac{\partial N}{\partial P} + \frac{M}{EI} \frac{\partial M}{\partial P} dx \quad (\text{C.15})$$

Note that in these formula the shear in the beams is neglected as the beams are assumed to be long and slender. The results are the displacements of point B as a function of the forces in point B and the forces in point P . The expressions can be rewritten to the resulting forces in point B .

$$\begin{aligned} H_B &= \frac{P_x}{2} + \frac{LAhP_y}{2Ah^2 + 8I} + \frac{AhM_P}{Ah^2 + 4I} \\ V_B &= -\frac{P_y}{2} \\ M_B &= -\frac{L(Ah^2 + 8I)P_y}{4Ah^2 + 16I} - \frac{2IM_P}{Ah^2 + 4I} \end{aligned} \quad (\text{C.16})$$

These results are substituted in the equilibrium equations (C.11). There are still six unknown reaction forces, but there are six equations to solve the problem which means that the problem is now statically determined. The displacements and rotation of point P can be calculated with Castigliano's second theorem similar to equation (C.15). The final result of these calculations are the displacements and rotation as a function of the applied loads at point P .

$$\begin{aligned} u_P &= \frac{LP_x}{2EA} \\ v_P &= \frac{L^2((16P_yL + 24M_P)I + ALP_yh^2)}{24EI(Ah^2 + 4I)} \\ \theta_P &= \frac{L(P_yL + 2M_P)}{E(Ah^2 + 4I)} \end{aligned} \quad (\text{C.17})$$

In these equations, it is visible that the distance between the parallel beams is of great importance as the relation with the vertical displacement and the rotation is quadratic. For very small values of h the contribution to the bending stiffness would be negligible. For h in converging to small values, the parallel beams would have the same results as if the beams were placed side by side meaning the total cross-sectional area and the moment of inertia are multiplied by a factor two.

In order to compare the results of the analytical derivation and the finite element results, values for the geometric properties have been obtained from literature [16]. The length of the beam is $L = 0.6$ [m], the thickness $t = 0.008$ [m] and the width $b = 0.15$ [m] resulting in a cross-sectional area of $A = 0.0012$ [m²] and an area moment of inertia of $I = 6.4 \cdot 10^{-9}$ [m⁴]. Furthermore, it is assumed that the modulus of elasticity is $E = 200 \cdot 10^9$ [N · m⁻²] and the distance between the parallel beams $h = 0.12$ [m]. The rigid body connecting the parallel beams is modelled as two beam elements with a modulus of elasticity $E = 200 \cdot 10^{14}$ [N · m⁻²] which is many times larger than the modulus of elasticity of the beams. The tolerance for the Newton-Raphson method and the equilibrium equations is set to $\epsilon = 1.0 \cdot 10^{-3}$ [-]. The parallel beams are modelled with one element each. Increasing the number of elements gives a larger accuracy of the results. The result are shown in tables C.3, C.4 and C.5.

Table C.3: Seat B suspension model horizontal force displacement results

$P_x = 1.0 \cdot 10^8$ [N]	Analytic result	FEM result	Error [%]
u_P [m]	0.125	0.125	0.002
v_P [m]	0	0	0
θ_P [rad]	0	0	0

Table C.4: Seat B suspension model vertical force displacement results

$P_y = -3.0 \cdot 10^3$ [N]	Analytic result	FEM result	Error [%]
u_P [m]	0	0	0
v_P [m]	-0.0211	-0.0211	$9.69 \cdot 10^{-5}$
θ_P [rad]	$-3.12 \cdot 10^{-4}$	$-3.11 \cdot 10^{-4}$	0.0112

Table C.5: Seat B suspension model bending moment displacement results

$M_P = -3.0 \cdot 10^5$ [Nm ⁻¹]	Analytic result	FEM result	Error [%]
u_P [m]	0	0	0
v_P [m]	-0.0312	-0.0312	-0.0113
θ_P [rad]	-0.104	-0.104	0.226

In addition, the linear beam element is tested with numerous standard beam deflection formulae and the results were very accurate compared to the results of the analytical formulae. Multiple simulations have been made with constant loading conditions where the distance between the parallel beams is varied. The applied loading conditions are $P_x = 0.0$ [N], $P_y = -3000$ [N] and $M_P = -3000$ [N]. The results are shown in figure C.6. In this figure it is visible that the rotation of the rigid body increases as the distance between the

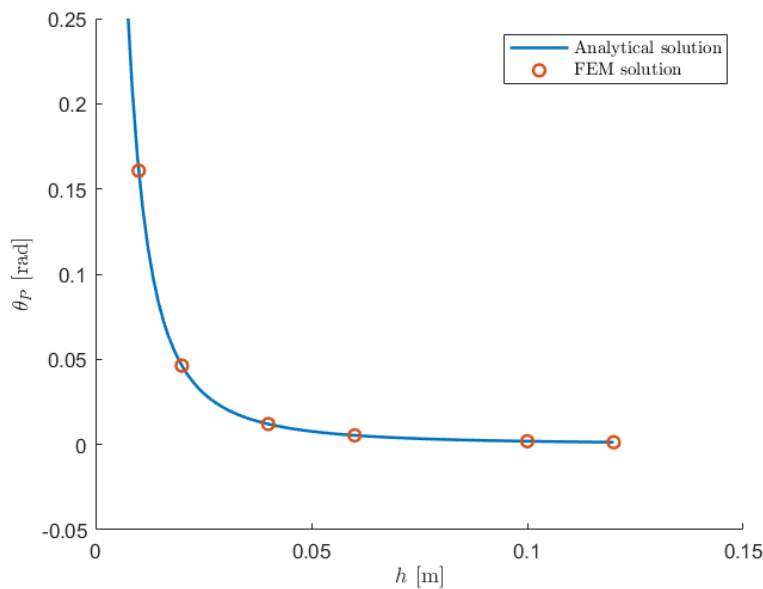


Figure C.6: Seat B suspension model rotation of the rigid body

parallel beams becomes smaller than $h = 0.1$ [m]. The shape of the curve is quadratic, which was expected based on the analytical formulations. Furthermore, the analytical solution and finite element solution are an exact match. As mentioned earlier, when the distance between the beams decreases the beams start to show similar behaviour to a single beam with doubled cross-sectional area and area moment of inertia as if the parallel beams would be side to side. As a result, the parallel beams start to deform differently to when the distance between the beam is sufficiently large. Two of the test cases from figure C.6 are shown in figures C.7a and C.7b.

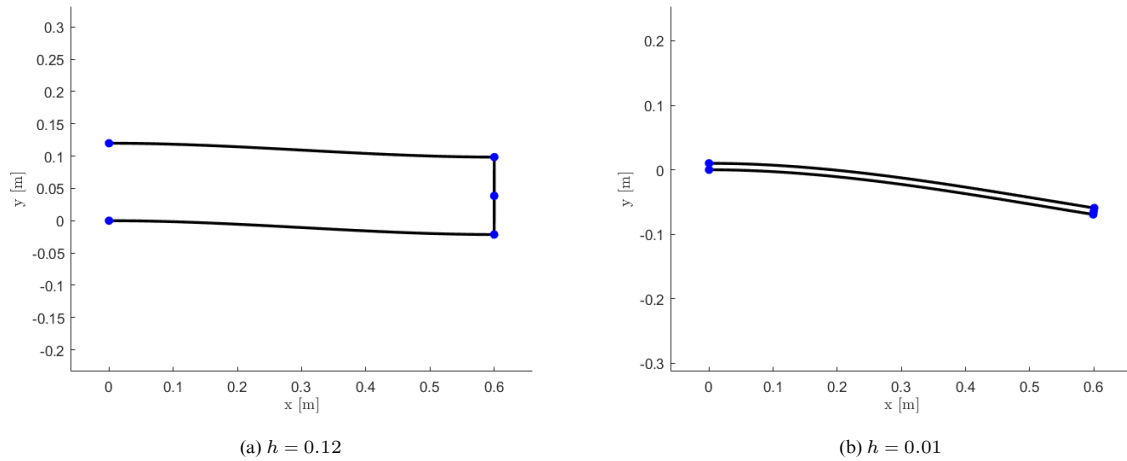


Figure C.7: Seat B suspension model deformation for different values of h

It is recommended that for further research and testing with the parallel leaf spring that the rotation of any rigid body as a function of the distance between the plates is reviewed. The rotation of the seat should be kept at a minimum as any rotation will increase the travelled distance of the seat and may cause discomfort for the person sitting on it.

C.2.2. Portal Frame

In this section, the non-linear beam element will be validated through test case obtained from literature [105]. The article describes an formulation of a non-linear beam including a co-rotational with small deflection beam theory which removes the restriction of small rotations between successive increments [105] [46]. For solving the non-linear equilibrium equations, the Newton-Raphson method is used in combination with a constant arc length control method. Important assumptions are that the nodal rotational angles are assumed to be small and the membrane strain along the deformed beam axis is assumed to be constant. When the co-rotational element is derived, multiple structures are tested and the results are compared with other literature. One of these test cases is shown in figure C.8, where a portal frame consisting of three beams is loaded.

In the figure C.9, multiple curves are drawn for different values of n , which describes the relative magnitude of the horizontal force in point B of the portal frame. Note that the values are shown in imperial units. The authors compared their results with the results of an existing study to show that their approach for the non-linear beam element needed less increments to acquire satisfactory accuracy. The authors used a tolerance of $\epsilon = 1.0 \cdot 10^{-4}$ for the equilibrium equations and varied the discretization of each member in the portal frame from one to four beam elements. The beam elements in the structure have a length of $L = 120.0$ [in], modulus of elasticity of $E = 30.0 \cdot 10^3$ [ksi], area moment of inertia of $I = 310.1$ [in⁴] and a cross-sectional area of $A = 11.77$ [in²]. In the finite element program, multiple simulations have been made while increasing the number of beam elements per member. In figure C.9, the finite element results for a discretization of ten beam elements per member are shown. In figure C.10, the deformed portal frame is shown for the various values of force nP . The figures show that when the force nP increases, the horizontal deflection of point B increases. Additionally, due to the combination of the increasing sideways force the top beam starts to deform as well.

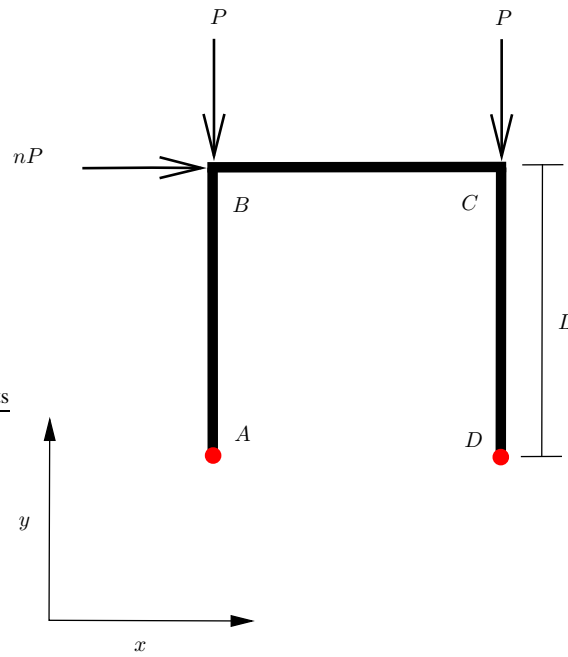


Figure C.8: Schematic representation of the portal frame

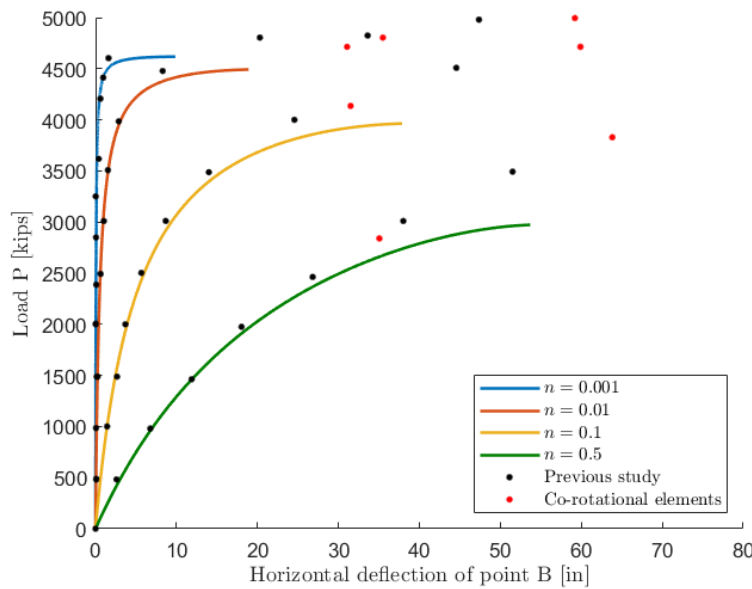


Figure C.9: Portal frame load-deflection curves for different values of n

When comparing the finite element results with the results from the article, strong deviations are noticed in the curves for an increasing horizontal force in point B. The curves were supposed to continue at the point where they are plotted in the figure, however the finite element program was not able to converge to a solution. After a thorough review of the program and the test case, it was concluded that the program was not able to converge to a solution due to the fact that the rotation of the element increases strongly for only a small increase of the applied load. Another important noticeable difference is the deviation of the curves with relation the data points. The deviation in the results is due to the small angle approximation made in

the derivation of the non-linear beam element. In the area for relative small deformations, the FEM results better match the results from the literature. It is recommended for further research that the deflections and rotations of the beam elements are monitored if results start deviating or deflections increase to significant values.

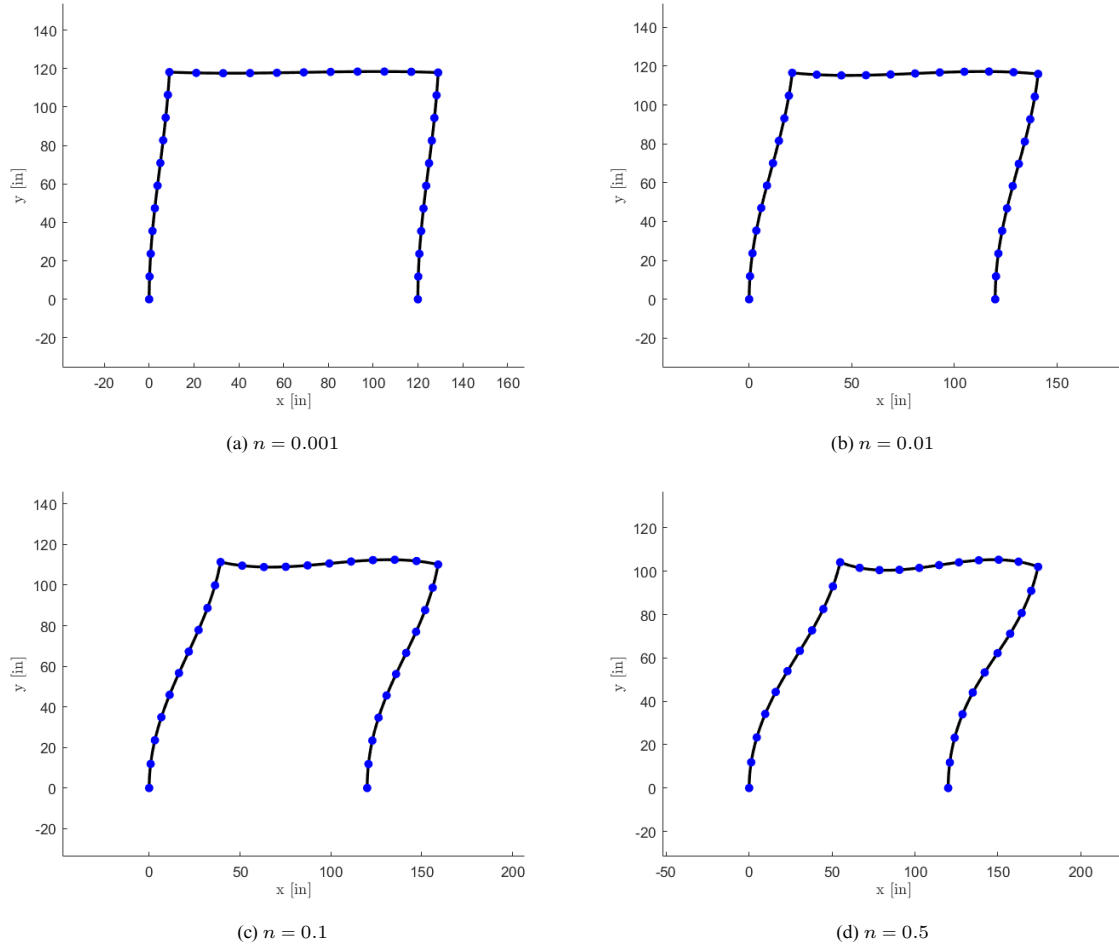


Figure C.10: Portal frame deformation for different values of n

C.2.3. Diamond Frame

In this section, the non-linear beam element will be validated through another test case obtained from literature [106] [107]. Both articles review the same structure as a test case, which is an diamond consisting of four members and a load is applied to the upper joint and lower joint. The structure is shown in figure C.11. In the first article a geometrical non-linear formulation based on position description is presented to solve large deflection problems. The principle of minimum potential energy and Euler-Bernoulli kinematics are adopted [106]. In the second article, exact results for some large deflection beam and frame problems are provided in a diagram form and in tabular form, which can be used to validate finite element methods. These structures are analysed by means of elliptic integrals. The results are based on elements which are linear elastic, ignore axial and shear deformations and have uniform cross-sections [107].

For the simulation, the non-linear beam elements have a length of $L = 1.0$ [m], modulus of elasticity of $E = 1.0$ [$\text{N} \cdot \text{m}^{-2}$], area moment of inertia of $I = 1.0$ [m^4] and a cross-sectional area of $A = 1000$ [m^2] [106]. In addition, the diamond frame structure is simplified based on symmetry conditions. For each

member in the diamond frame structure a discretization of ten beam elements was applied. In the figures C.12a and C.12b, the deformed diamond frame structures for tensile and compressive loading are shown. In the figures C.13, C.14 and C.15 the results of the finite element program are plotted as well as the results from the literature [107].

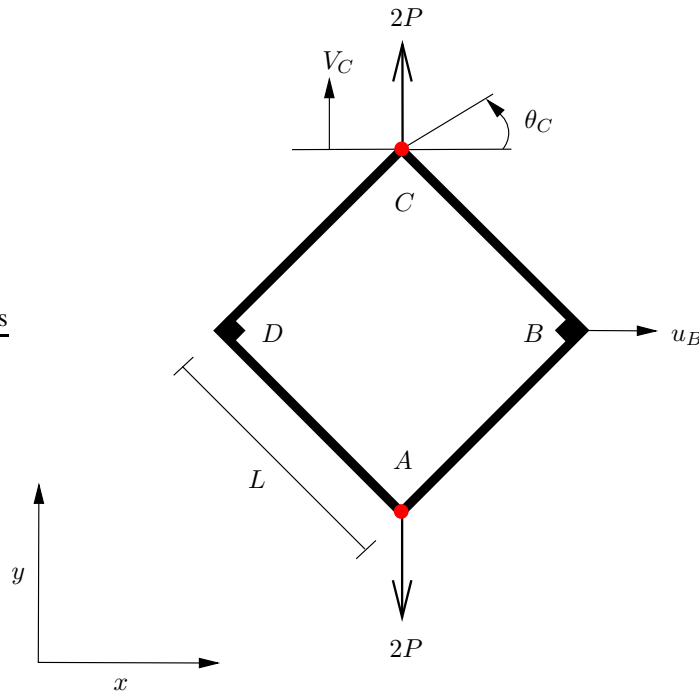


Figure C.11: Schematic representation of the diamond frame

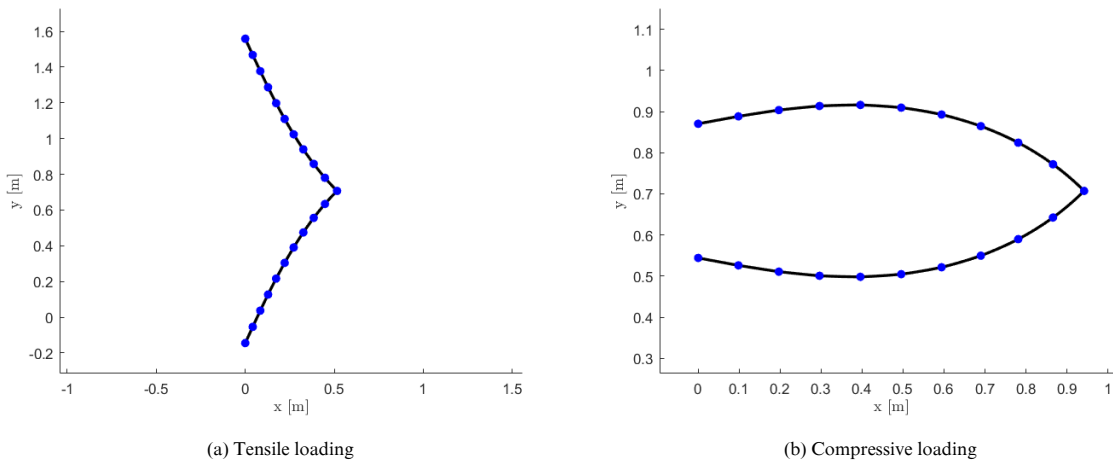


Figure C.12: Diamond frame deformation for different types of loading

In the figures it is visible that for a relative small loads the results match with the exact solutions from the literature. When the diamond frame structure is subjected to tensile forces curve continues to the maximum load shown in the plot. However, when the diamond frame structure is subjected to compressive forces the

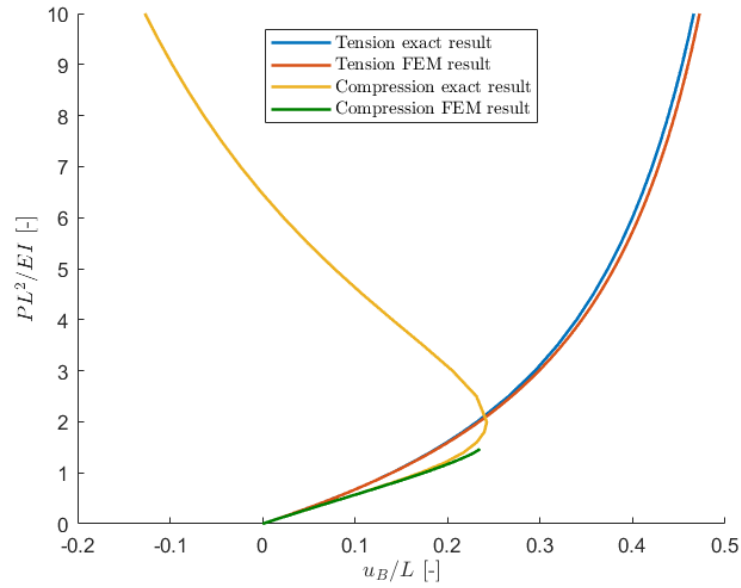


Figure C.13: Diamond frame horizontal displacement of point B

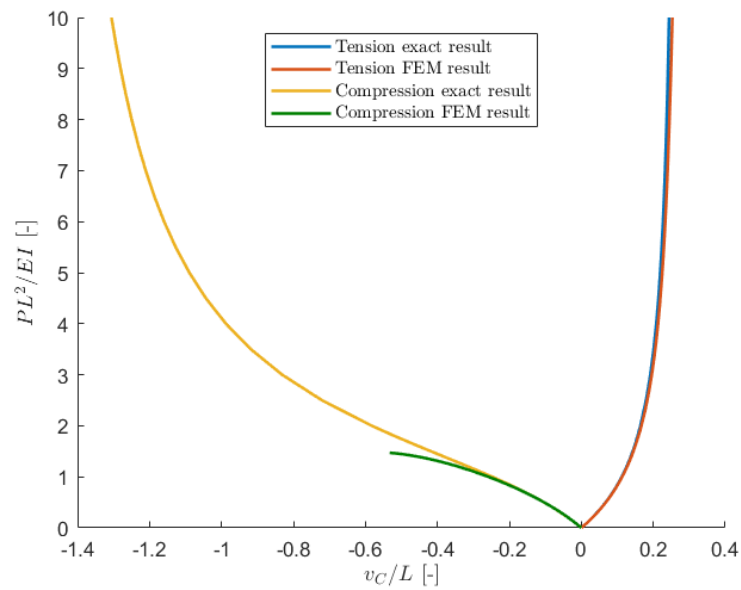


Figure C.14: Diamond frame vertical displacement of point C

curve ends at relative low forces. This is a result of the finite element program which is unable to converge to a solution as in the compression case the forces causes the beam elements to deform with large deflections. This behaviour was expected considering the results of the application of the finite element program to the portal frame in the previous section. For the larger tensile loads in the figures a small difference between the exact solution and the finite element results is visible. Therefore, an more in depth convergence study was conducted. In figure C.16, the results of the convergence study are shown.

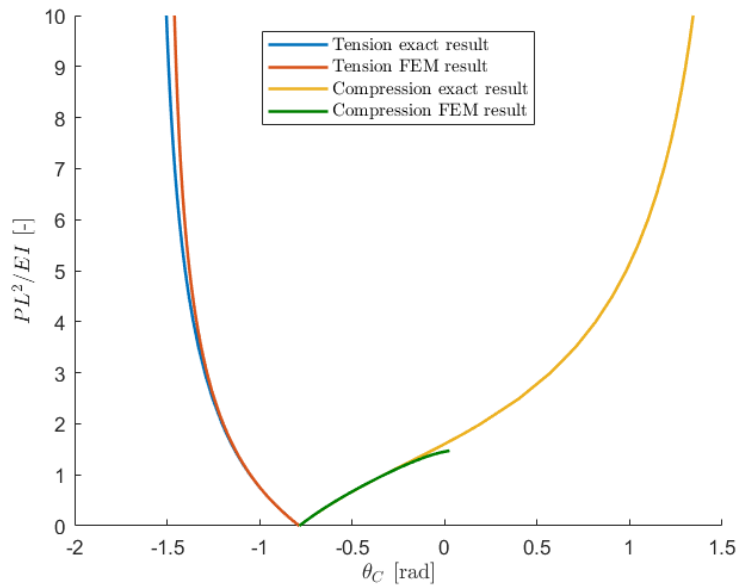


Figure C.15: Diamond frame rotation of point C

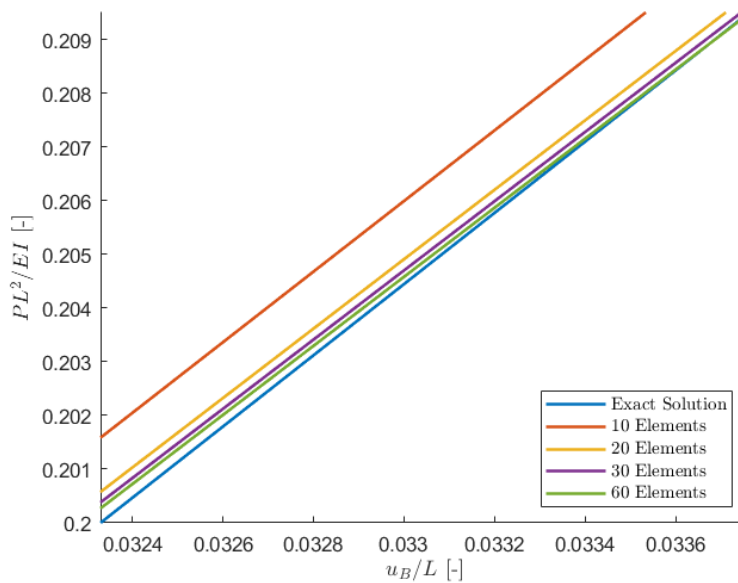


Figure C.16: Diamond frame convergence study results

In the figure C.16, the axis are zoomed in on the part for smaller deflections ($u_B < 0.04$ [m]). The figure shows that for an increasing number of elements, the finite element results converge to the exact solution provided by the literature. As the number of elements decreases, the structure behaves stiffer and has less deflection. The intersection between the curves of the finite element results and the exact solution have no physical meaning. Concluding from the convergence study and the results from the finite element program, the difference in the curves for larger deflections is a result of the limitations of the non-linear bar element due to the small angle approximation. If one wants to acquire more accurate results, then the use high order and more complex elements incorporating large deflections is recommended.

C.3. Large Rotation Beam Element

In this section, the large rotation beam element is validated with two test cases obtained from literature [106] [107]. First, a cantilever beam with an end point load is analysed. Then, the diamond frame is again analysed and the results are compared with the results of the standard non-linear beam element.

C.3.1. Cantilever Beam

The cantilever beam is fixed on one end and at the other end a vertical load is applied. The beam elements in the structure have a length of $L = 1.0$ [m], modulus of elasticity of $E = 1.0$ [$\text{N}\cdot\text{m}^{-2}$], area moment of inertia of $I = 1.0$ [m^4] and a cross-sectional area of $A = 1000$ [m^2]. In figures C.18a and C.18b the non-dimensional horizontal displacement and vertical displacement are plotted against the non-dimensional applied vertical force. In the figures, multiple curves are shown for an increasing number of elements. Figure C.17, shows the deformed cantilever beam for a discretization of 4 and 25 elements. As expected, the results for an increasing number of elements converge to the exact solution. The large rotation beam element is concluded to produce the desirable results.

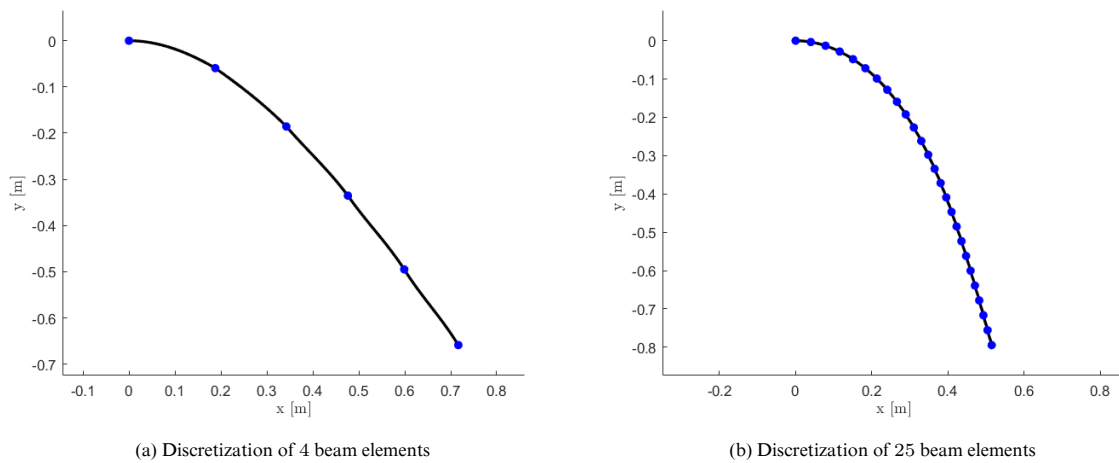
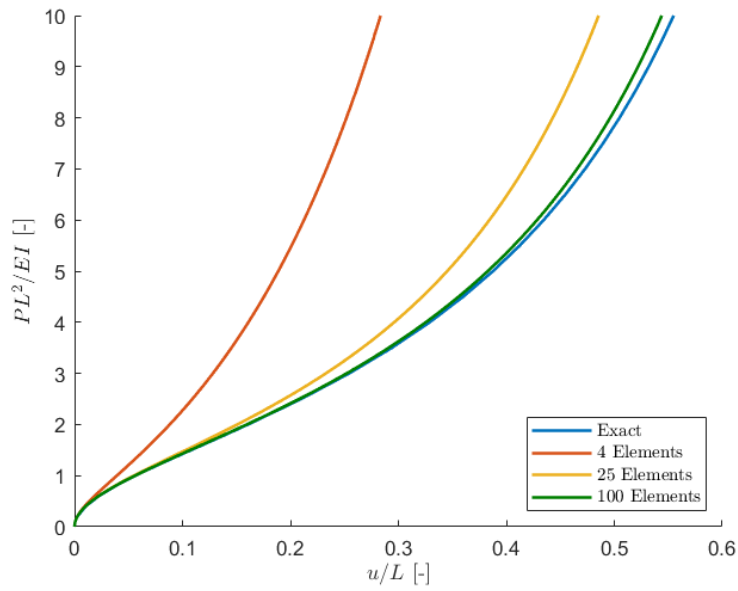


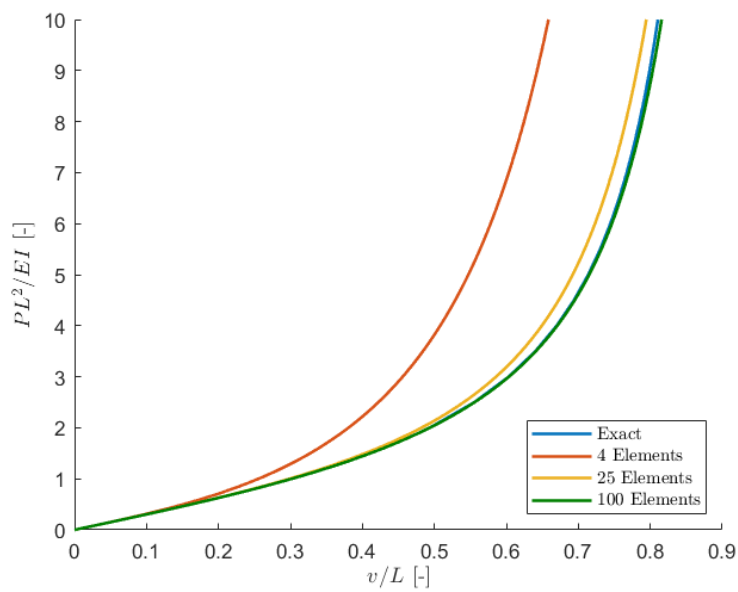
Figure C.17: Cantilever beam deformation for different discretizations

C.3.2. Diamond Frame

The same properties for the structure are used as in the simulations with the standard non-linear beam element. With test case of the cantilever beam in the previous section, the large rotation beam element was already validated. With the test case of the diamond frame, the results of the standard non-linear beam element and the large rotation beam element can be compared. In the figures C.19a and C.19b the non-dimensional horizontal displacement and vertical displacement plotted against the non-dimensional force in the tensile loading case. The red and the yellow curves display the results of the standard non-linear beam element and the large rotation beam element. The blue curve shows the exact results from literature [107]. For each analysis, the number of elements used to model the diamond frame is sixty. As can be seen in the figures, the results at larger deformations are more accurately approximated by the large rotation beam element compared to the standard non-linear beam element. Therefore, this element is recommended when large deformations and rotations occur in deformed structures during static analysis.

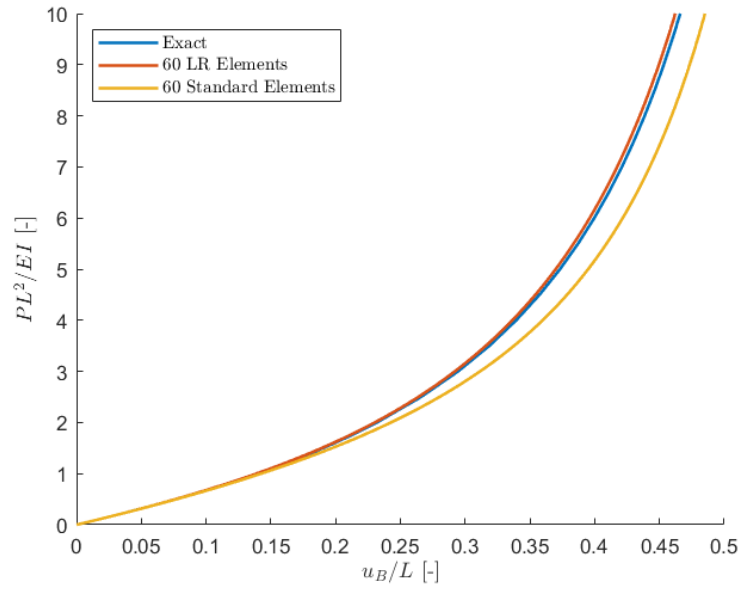


(a) Horizontal displacement

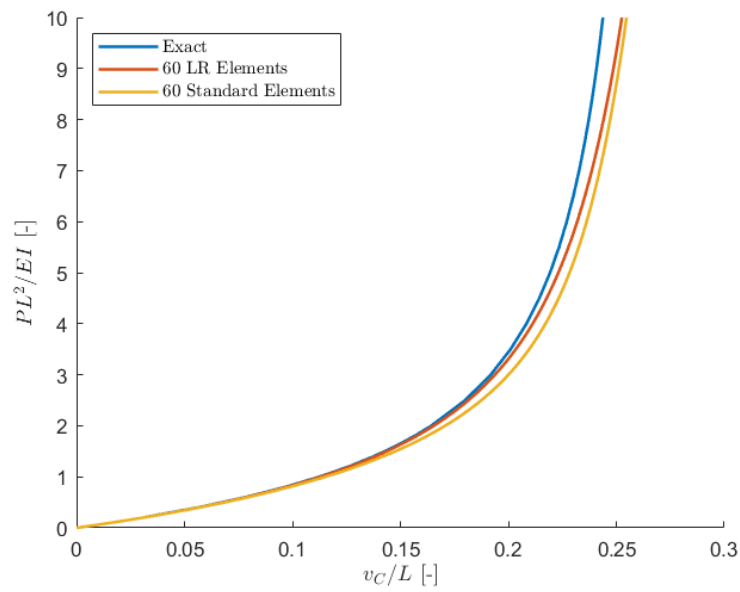


(b) Vertical displacement

Figure C.18: Cantilever beam with end point load displacements



(a) Horizontal displacement of point B



(b) Vertical displacement of point C

Figure C.19: Diamond frame deformation for different beam elements

D

Derivation of the Internal Forces for Special Finite Elements

In this appendix the internal forces of the special finite elements are derived from the potential energy formulations.

D.1. Damper Element

A damper element dissipates kinetic energy by converting the energy into heat via viscous friction (Rayleigh damping). The compression or extension motion of the damper is resisted by the damper force, which is approximately proportional to the opposite direction of the velocity [43] [44].

The Rayleigh dissipation function for a damper element is defined as [45]

$$R = \frac{1}{2}c\dot{\Delta L}^2 \quad (\text{D.1})$$

Where c is the damping coefficient and $\dot{\Delta L}$ the change in elongation over time. The damping coefficient is regarded as a constant value for the specific damper.

D.1.1. Non-Linear Damper

For the non-linear damper, the elongation is defined as

$$\Delta L = L' - L_0 = \sqrt{(L + u_2 - u_1)^2 + (v_2 - v_1)^2} - L_0 \quad (\text{D.2})$$

The change of elongation over time is

$$\dot{\Delta L} = \frac{d\Delta L}{dt} = \frac{(L + u_2 - u_1)(\dot{u}_2 - \dot{u}_1) + (v_2 - v_1)(\dot{v}_2 - \dot{v}_1)}{\sqrt{(L + u_2 - u_1)^2 + (v_2 - v_1)^2}} \quad (\text{D.3})$$

The damper force in the local coordinate system is calculated according to

$$R_F = \frac{\partial R}{\partial \dot{q}_i} = c\dot{\Delta L} \frac{\partial \dot{\Delta L}}{\partial \dot{q}_i} \quad (\text{D.4})$$

Where q is has the form of (u_1, v_1, u_2, v_2) . With the angle of the damper element, the damper forces in the global coordinate system are calculated according to

$$\begin{aligned} \frac{\partial R}{\partial \dot{Q}_1} &= \frac{\partial R}{\partial \dot{q}_1} \cos \alpha - \frac{\partial R}{\partial \dot{q}_2} \sin \alpha & \frac{\partial R}{\partial \dot{Q}_4} &= \frac{\partial R}{\partial \dot{q}_4} \cos \alpha - \frac{\partial R}{\partial \dot{q}_5} \sin \alpha \\ \frac{\partial R}{\partial \dot{Q}_2} &= \frac{\partial R}{\partial \dot{q}_1} \sin \alpha + \frac{\partial R}{\partial \dot{q}_2} \cos \alpha & \frac{\partial R}{\partial \dot{Q}_5} &= \frac{\partial R}{\partial \dot{q}_4} \sin \alpha + \frac{\partial R}{\partial \dot{q}_5} \cos \alpha \end{aligned} \quad (\text{D.5})$$

The damper forces of all dampers are summed in the damper force vector of the global coordinate system (R_F) according to

$$\frac{\partial R}{\partial Q_j} = \sum \frac{\partial R}{\partial Q_i} \quad (\text{D.6})$$

Where $j = 3n_1 - 3 + i$ with $i = 1, 2$ for nodal point one and where $j = 3n_2 - 6 + i$ with $i = 4, 5$ for nodal point two.

D.1.2. Linear Damper

For the linear damper, the non-linear terms in the elongation are neglected. Therefore, the elongation becomes

$$\Delta L = L' - L_0 = L + u_2 - u_1 - L_0 \quad (\text{D.7})$$

Then the change in elongation over time is defined as

$$\dot{\Delta L} = \frac{d\Delta L}{dt} = \dot{u}_2 - \dot{u}_1 \quad (\text{D.8})$$

Substituting in the expression of the Rayleigh dissipation function and rewriting it to matrix-vector form gives the local specific damping matrix $[c]$.

$$R = \frac{1}{2} (\dot{u}_1 \quad \dot{v}_1 \quad \dot{u}_2 \quad \dot{v}_2) \begin{bmatrix} c & 0 & -c & 0 \\ 0 & 0 & 0 & 0 \\ -c & 0 & c & 0 \\ 0 & 0 & 0 & 0 \end{bmatrix} \begin{pmatrix} \dot{u}_1 \\ \dot{v}_1 \\ \dot{u}_2 \\ \dot{v}_2 \end{pmatrix} \quad (\text{D.9})$$

This matrix can be transformed to the global specific damping matrix $[C]$ using the rotation matrix according to

$$[C] = [R]^T [c] [R] \quad (\text{D.10})$$

Where the rotation matrix is defined as

$$[R] = \begin{bmatrix} \cos \theta & \sin \theta & 0 & 0 \\ -\sin \theta & \cos \theta & 0 & 0 \\ 0 & 0 & \cos \theta & \sin \theta \\ 0 & 0 & -\sin \theta & \cos \theta \end{bmatrix} \quad (\text{D.11})$$

The damping force (R_F) in the global coordinate system is calculated by

$$R_F = [C] \vec{Q} \quad (\text{D.12})$$

E

Derivation of the Mass Matrices for the Finite Elements

In this appendix the mass matrices of the finite elements are derived from the kinetic energy formulations.

E.1. Beam Element

The kinetic energy of a mass is defined as [42]

$$T_e = \iiint_{Vol} \rho v^2 dV \quad (E.1)$$

A differential element of mass is defined as $dm = \rho dA dx$. Then, the expression of kinetic energy for the beam becomes

$$T_e = \frac{1}{2} \rho \int_{x=0}^L \iint_A v^2 dA dx \quad (E.2)$$

From the coordinates (B.8) for an arbitrary point P on the beam in combination with the small angle approximation (B.28) the velocity of a differential element of mass of the beam due to bending is defined as

$$v^2 = \dot{x}^2 + \dot{y}^2 = (\dot{u} - y\dot{\theta})^2 + \dot{v}^2 = \dot{u}^2 - 2y\dot{\theta} + \dot{v}^2 + y^2\dot{\theta}^2 \quad (E.3)$$

This formulation of the velocity includes the velocity of the mass from the neutral axis of the element due to bending. Substituting the velocity in the expression for the kinetic energy gives

$$T_e = \frac{1}{2} \rho \int_{x=0}^L \left(\dot{u}^2 + \dot{v}^2 \iint_A dA - \iint_A 2y\dot{\theta} dA + \dot{\theta}^2 \iint_A y^2 dA \right) dx \quad (E.4)$$

The beam elements are considered from the neutral axis of the element itself. Therefore, the integrals over the cross-section become equal to

$$\begin{aligned} \iint_A y^2 dA &= I \\ \iint_A dA &= A \\ \iint_A 2y\dot{\theta} dA &= 0 \end{aligned} \quad (E.5)$$

Then, the kinetic energy for the beam element simplifies to

$$T_e = \frac{1}{2} \rho A \int_{x=0}^L (\dot{u}^2 + \dot{v}^2) dx + \frac{1}{2} \rho I \int_{x=0}^L \dot{\theta}^2 dx \quad (\text{E.6})$$

Where \dot{u}, \dot{v} and $\dot{\theta}$ are the derivatives of the shape functions u (B.4), v (B.35) and θ (B.28) with respect to time.

$$\begin{aligned} \dot{u}(x) &= \dot{u}_1 + \left(\frac{\dot{u}_2 - \dot{u}_1}{L} \right) x \\ \dot{v}(x) &= \dot{v}_1 + \dot{\theta}_1 x + \left(-\frac{3(\dot{v}_1 - \dot{v}_2)}{L^2} - \frac{\dot{\theta}_2 + 2\dot{\theta}_1}{L} \right) x^2 + \left(\frac{2(\dot{v}_1 - \dot{v}_2)}{L^3} + \frac{\dot{\theta}_2 + \dot{\theta}_1}{L^2} \right) x^3 \\ \dot{\theta}(x) &= \frac{d}{dt} \left(\frac{dv}{dx} \right) \end{aligned} \quad (\text{E.7})$$

The kinetic energy of the beam element results in

$$T_e = \frac{1}{2} \vec{q}^T [m] \vec{q} \quad (\text{E.8})$$

Where \vec{q} is has the form of $(\dot{u}_1, \dot{v}_1, \dot{\theta}_1, \dot{u}_2, \dot{v}_2, \dot{\theta}_2)$. Where $[m]$ is the local specific mass matrix and is expressed as [42]

$$[m] = \rho A L \begin{bmatrix} \frac{1}{3} & 0 & 0 & \frac{1}{6} & 0 & 0 \\ 0 & \frac{13}{35} + \frac{6I}{5AL^2} & \frac{11L}{210} + \frac{I}{10AL} & 0 & \frac{9}{70} - \frac{6I}{5AL^2} & -\frac{13L}{420} + \frac{I}{10AL} \\ 0 & \frac{11L}{210} + \frac{I}{10AL} & \frac{11L}{105} + \frac{I}{15A} & 0 & \frac{13L}{420} - \frac{I}{10AL} & -\frac{13L}{140} - \frac{I}{30A} \\ \frac{1}{6} & 0 & 0 & \frac{1}{3} & 0 & 0 \\ 0 & \frac{9}{70} - \frac{6I}{5AL^2} & \frac{13L}{420} - \frac{I}{10AL} & 0 & \frac{13}{35} + \frac{6I}{5AL^2} & -\frac{11L}{210} - \frac{I}{10AL} \\ 0 & -\frac{13L}{420} + \frac{I}{10AL} & -\frac{13L}{140} - \frac{I}{30A} & 0 & -\frac{11L}{210} - \frac{I}{10AL} & \frac{11L}{105} + \frac{I}{15A} \end{bmatrix} \quad (\text{E.9})$$

This matrix can be transformed to the global specific mass matrix $[M]$ using the rotation matrix according to

$$[M] = [R]^T [m] [R] \quad (\text{E.10})$$

Where the rotation matrix is defined as

$$[R] = \begin{bmatrix} \cos \theta & \sin \theta & 0 & 0 & 0 & 0 \\ -\sin \theta & \cos \theta & 0 & 0 & 0 & 0 \\ 0 & 0 & 1 & 0 & 0 & 0 \\ 0 & 0 & 0 & \cos \theta & \sin \theta & 0 \\ 0 & 0 & 0 & -\sin \theta & \cos \theta & 0 \\ 0 & 0 & 0 & 0 & 0 & 1 \end{bmatrix} \quad (\text{E.11})$$

E.2. Bar Element

As the bar can only support axial loads, no rotation is present in the element. Therefore, the velocity of the differential element of mass of the bar element is simplified from (E.3) to

$$v^2 = \dot{u}^2 + \dot{v}^2 \quad (\text{E.12})$$

In this expression it is visible that the rotation along the length of the beam is not present. The \dot{u} and \dot{v} are the derivatives of the shape functions u and v (B.4) with respect to time.

$$\begin{aligned} \dot{u}(x) &= \dot{u}_1 + \left(\frac{\dot{u}_2 - \dot{u}_1}{L} \right) x \\ \dot{v}(x) &= \dot{v}_1 + \left(\frac{\dot{v}_2 - \dot{v}_1}{L} \right) x \end{aligned} \quad (\text{E.13})$$

The shape functions can be rewritten in matrix-vector form as

$$\dot{u}(x) = (\dot{u}_1 \quad \dot{u}_2) \begin{pmatrix} 1 - \frac{x}{L} \\ \frac{x}{L} \end{pmatrix} = \left(1 - \frac{x}{L} \quad \frac{x}{L}\right) \begin{pmatrix} \dot{u}_1 \\ \dot{u}_2 \end{pmatrix} \quad (\text{E.14})$$

$$\dot{v}(x) = (\dot{v}_1 \quad \dot{v}_2) \begin{pmatrix} 1 - \frac{x}{L} \\ \frac{x}{L} \end{pmatrix} = \left(1 - \frac{x}{L} \quad \frac{x}{L}\right) \begin{pmatrix} \dot{v}_1 \\ \dot{v}_2 \end{pmatrix} \quad (\text{E.15})$$

As the velocity of the volume element consists of the velocity in the local horizontal (u) and local vertical (v) direction, the expression for the kinetic energy becomes

$$T_e = \frac{1}{2} \rho A \int_{x=0}^L (\dot{u}^2 + \dot{v}^2) dx = \frac{1}{2} \vec{q}^T [m] \vec{q} \quad (\text{E.16})$$

Where \vec{q} is has the form of $(\dot{u}_1, \dot{v}_1, \dot{u}_2, \dot{v}_2)$. In which the local specific mass matrix $[m]$ is [42]

$$[m] = \left(\frac{\rho AL}{6}\right) \begin{bmatrix} 2 & 0 & 1 & 0 \\ 0 & 2 & 0 & 1 \\ 1 & 0 & 2 & 0 \\ 0 & 1 & 0 & 2 \end{bmatrix} \quad (\text{E.17})$$

This variation of the local specific mass matrix for a bar element is commonly called as the consistent mass matrix [44] [42] Another variant is the lumped mass matrix, where the mass of the bar is located at the nodes. The lumped mass matrix is therefore a diagonal matrix [44] [42]. The lumped mass matrix variant is

$$[m]_{lumped} = \left(\frac{\rho AL}{2}\right) \begin{bmatrix} 1 & 0 & 0 & 0 \\ 0 & 1 & 0 & 0 \\ 0 & 0 & 1 & 0 \\ 0 & 0 & 0 & 1 \end{bmatrix} \quad (\text{E.18})$$

The local specific mass matrix can be transformed to the global specific mass matrix using the rotation matrix which is defined as

$$[R] = \begin{bmatrix} \cos \theta & \sin \theta & 0 & 0 \\ -\sin \theta & \cos \theta & 0 & 0 \\ 0 & 0 & \cos \theta & \sin \theta \\ 0 & 0 & -\sin \theta & \cos \theta \end{bmatrix} \quad (\text{E.19})$$

E.3. Large Rotation Beam Element

For the large rotation beam element, the velocity of the differential element of mass is defined as (E.3). The shape functions of the large rotation beam element are (B.4) and (B.63). The derivatives of these shape functions with respect to time are

$$\dot{u}(x) = \dot{u}_1 + \left(\frac{\dot{u}_2 - \dot{u}_1}{L}\right) x \quad (\text{E.20})$$

$$\begin{aligned} \dot{v}(x) &= \dot{v}_1 + \frac{1}{L} ((L + u_2 - u_1) \tan \dot{\theta}_1) x \\ &+ \frac{1}{L^2} (3(\dot{v}_2 - \dot{v}_1) - (L + u_2 - u_1)(2 \tan \dot{\theta}_1 + \tan \dot{\theta}_2)) x^2 \\ &+ \frac{1}{L^3} (2(\dot{v}_1 - \dot{v}_2) + (L + u_2 - u_1)(\tan \dot{\theta}_1 + \tan \dot{\theta}_2)) x^3 \end{aligned} \quad (\text{E.21})$$

In the derivative of the shape function for the vertical displacement non-linear behaviour is visible. The shape function is dependant on the horizontal displacements. This shows that the mass matrix of the large rotation beam element is non-linear, which means that mass matrix must be recalculated for each time step in the dynamic analysis. This would lead to a significant increase of the computation time and of the required computational power. Therefore, in this research the large rotation beam element will only be used for static analysis.

E.4. Point Mass

A point mass is defined as a mass at a single node or point. This very simple element can be used to add mass on specific nodes in a structure. The kinetic energy of a point mass is

$$T_e = \frac{1}{2} \vec{q} [m] \vec{q} \quad (\text{E.22})$$

Where \vec{q} is has the form of (\dot{u}_1, \dot{v}_1) and the local specific mass matrix is [44] [42]

$$[m] = \begin{bmatrix} m & 0 \\ 0 & m \end{bmatrix} \quad (\text{E.23})$$

The local specific mass matrix of a point mass is equal to the global specific mass matrix.

E.5. Special Finite Elements

The kinetic energy formulations for the special finite element (coil-spring, damper, gas-spring) are based on the lumped mass matrix (E.18) from the derivation of the bar element.

$$[m] = \left(\frac{m}{2}\right) \begin{bmatrix} 1 & 0 & 0 & 0 \\ 0 & 1 & 0 & 0 \\ 0 & 0 & 1 & 0 \\ 0 & 0 & 0 & 1 \end{bmatrix} \quad (\text{E.24})$$

In this formulation, the mass of the special finite elements is divided over the nodes and the result is a diagonal matrix. The corresponding rotation matrix is

$$[R] = \begin{bmatrix} \cos \theta & \sin \theta & 0 & 0 \\ -\sin \theta & \cos \theta & 0 & 0 \\ 0 & 0 & \cos \theta & \sin \theta \\ 0 & 0 & -\sin \theta & \cos \theta \end{bmatrix} \quad (\text{E.25})$$

F

Validation of the Dynamic Program

In this appendix, the dynamic analysis program is validated. First, an single DOF mass-spring-damper model is described. The model is used to validate the dynamic analysis of linear elements and to determine which numerical integration method from MATLAB should be used to solve the ODE's. Then, the equations of motion for a simplified suspension design are derived of which the motions are non-linear due to the non-linear geometric properties. These equations of motion are used to validate the results of the non-linear elements and the ODE solvers.

F.1. Single DOF Mass-Spring-Damper Model

In figure F.1, a schematic representation of the mass-spring-damper model is shown. The figure shows that the model consists of three masses, two coil springs and one damper. This simplified model resembles an drop weight with a SMS mounted on it.

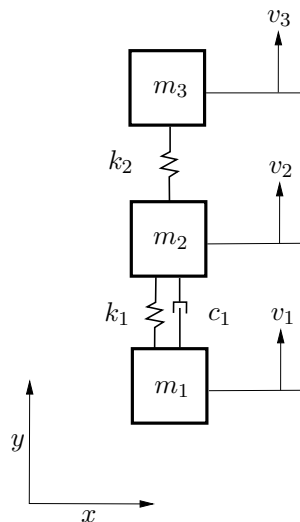


Figure F.1: Single DOF mass-spring-damper model

The equations of motion for a damped system, are derived with the Euler-Lagrange equation.

$$\frac{d}{dt} \left(\frac{\partial \mathcal{L}}{\partial \dot{q}_j} \right) - \frac{\partial \mathcal{L}}{\partial q_j} + \frac{\partial R}{\partial \dot{q}_j} = \frac{\partial W}{\partial q_j} \quad (\text{F.1})$$

With the Lagrange equation

$$\mathcal{L} = T - U \quad (\text{F.2})$$

Where T is the kinetic energy of the masses and U the potential energy is equal to the elastic energy of the springs. The kinetic energy is

$$T = \sum \frac{1}{2} m_j v_j^2 = \frac{1}{2} m_1 v_1^2 + \frac{1}{2} m_2 v_2^2 + \frac{1}{2} m_3 v_3^2 \quad (\text{F.3})$$

The spring potential energy is

$$U = \sum \frac{1}{2} k_j \Delta L_j^2 = \frac{1}{2} k_1 (v_2 - v_1)^2 + \frac{1}{2} k_2 (v_3 - v_2)^2 \quad (\text{F.4})$$

The Rayleigh damping is [45]

$$R = \sum \frac{1}{2} c_j \dot{\Delta L}_j^2 = \frac{1}{2} c_1 (\dot{v}_2 - \dot{v}_1)^2 \quad (\text{F.5})$$

The work done by external forces on the masses is defined as

$$W = P_1 v_1 + P_2 v_2 + P_3 v_3 \quad (\text{F.6})$$

Substituting all results in the Euler-Lagrange equation gives [44]

$$\begin{bmatrix} m_1 & 0 & 0 \\ 0 & m_2 & 0 \\ 0 & 0 & m_3 \end{bmatrix} \begin{pmatrix} \ddot{v}_1 \\ \ddot{v}_2 \\ \ddot{v}_3 \end{pmatrix} + \begin{bmatrix} -c_1 & -c_1 & 0 \\ -c_1 & c_1 & 0 \\ 0 & 0 & 0 \end{bmatrix} \begin{pmatrix} \dot{v}_1 \\ \dot{v}_2 \\ \dot{v}_3 \end{pmatrix} + \begin{bmatrix} -k_1 & -k_1 & 0 \\ -k_1 & (k_1 + k_2) & -k_2 \\ 0 & -k_2 & -k_2 \end{bmatrix} \begin{pmatrix} v_1 \\ v_2 \\ v_3 \end{pmatrix} = \begin{pmatrix} P_1 \\ P_2 \\ P_3 \end{pmatrix} \quad (\text{F.7})$$

From which the acceleration of the masses can be calculated according to

$$\begin{pmatrix} \ddot{v}_1 \\ \ddot{v}_2 \\ \ddot{v}_3 \end{pmatrix} = \begin{bmatrix} m_1 & 0 & 0 \\ 0 & m_2 & 0 \\ 0 & 0 & m_3 \end{bmatrix}^{-1} \left(- \begin{bmatrix} -c_1 & -c_1 & 0 \\ -c_1 & c_1 & 0 \\ 0 & 0 & 0 \end{bmatrix} \begin{pmatrix} \dot{v}_1 \\ \dot{v}_2 \\ \dot{v}_3 \end{pmatrix} - \begin{bmatrix} -k_1 & -k_1 & 0 \\ -k_1 & (k_1 + k_2) & -k_2 \\ 0 & -k_2 & -k_2 \end{bmatrix} \begin{pmatrix} v_1 \\ v_2 \\ v_3 \end{pmatrix} + \begin{pmatrix} P_1 \\ P_2 \\ P_3 \end{pmatrix} \right) \quad (\text{F.8})$$

In this expression, it is shown that the accelerations are a function of the displacements. In order to solve the differential equations, the three second order differential equations are rewritten to two six first order differential equations as

$$Y = \begin{pmatrix} v_1 \\ v_2 \\ v_3 \\ \dot{v}_1 \\ \dot{v}_2 \\ \dot{v}_3 \end{pmatrix} \quad \text{and} \quad \dot{Y} = \begin{pmatrix} \dot{v}_1 \\ \dot{v}_2 \\ \dot{v}_3 \\ \ddot{v}_1 \\ \ddot{v}_2 \\ \ddot{v}_3 \end{pmatrix} \quad (\text{F.9})$$

The vector \dot{Y} is the derivative of the vector Y . To solve these differential equations an ODE solver of MATLAB is used. The types of solvers and the most suitable one for this application will be discussed in the next section.

If the acceleration of one the masses is prescribed in any way, for example the measured data of a wave impact is used for the acceleration of mass m_1 , then this data is to be substituted for the according acceleration (\ddot{v}_1).

The equations of motion for the undamped system without external loads acting on it are

$$\begin{bmatrix} m_1 & 0 & 0 \\ 0 & m_2 & 0 \\ 0 & 0 & m_3 \end{bmatrix} \begin{pmatrix} \ddot{v}_1 \\ \ddot{v}_2 \\ \ddot{v}_3 \end{pmatrix} + \begin{bmatrix} k_1 & -k_1 & 0 \\ -k_1 & (k_1 + k_2) & -k_2 \\ 0 & -k_2 & k_2 \end{bmatrix} \begin{pmatrix} v_1 \\ v_2 \\ v_3 \end{pmatrix} = \begin{pmatrix} 0 \\ 0 \\ 0 \end{pmatrix} \quad (\text{F.10})$$

or in a more convenient notation

$$[M]\ddot{v} + [K]v = 0 \quad (\text{F.11})$$

The expression for the displacement and acceleration of a harmonic vibration are

$$v = U \cos(\omega t) \quad (\text{F.12})$$

$$\ddot{v} = -\omega^2 U \cos(\omega t) \quad (\text{F.13})$$

Substituting these values in the equations of motion of the free undamped equations of motion gives

$$([K] - \omega^2[M])U \cos(\omega t) = 0 \quad (\text{F.14})$$

The trivial solution of this equation is $\cos(\omega t) = 0$. This solution is ignored as the equations of motion should apply for every time step. Thus, $\cos(\omega t) \neq 0$ should be true. The resulting expression is [44] [42]

$$([K] - \omega^2[M])U = 0 \quad (\text{F.15})$$

Next, both sides are multiplied with the inverse mass matrix and λ is substituted for ω^2 .

$$([M]^{-1}[K] - \lambda[I])U = 0 \quad (\text{F.16})$$

In this equation, λ is the eigenvalue and U is the according eigenvector. The determinant of this equation gives the characteristic polynomial. With this polynomial the eigenvalues and eigenvectors are calculated. The roots of this polynomial represent the eigenvalues of the matrix $[M]^{-1}[K]$.

For this single degree to freedom mass-spring-damper model three different eigenvalues exist. The lowest eigenvalue, with the value of zero, describes the movement of the system as a rigid body. The other eigenvalues, which are nonzero, describe the present vibration modes. These values are dependant on the stiffnesses of the various springs. The value of the eigenvalues will influence the results of the ODE solvers.

The damping ratio ζ describes at what rate the oscillations decay from one excitation to the next one. This ratio is usually defined as [44]

$$\zeta = \frac{c}{c_{crit}} = \frac{c}{2 \cdot \sqrt{k \cdot m}} \quad (\text{F.17})$$

Where c_{crit} is the critical damping coefficient. The damping ratio depends on the damping present in the system. Without damping the system would oscillate indefinitely. If the damping ratio is less than one, the system is underdamped and the motion is oscillatory until it decays completely [44]. If the damping ratio in the system is greater than one, the system is overdamped and the mass would return to its starting position without oscillating [44]. When the damping ratio is equal to unity, the damping is equal to the critical damping coefficient and the system returns to its starting position with minimal amount of time required. This form of damping in the system is known as critically damped.

For the validation tests, drop tests are simulated by dropping the seat from a static equilibrium. In this static equilibrium the springs are already compressed due to the weight of the masses. The drop tests are simulated by giving the whole seat model an initial constant downward speed which is equal to the integral of the prescribed excitation pulse over time that is applied to the base of the seat. This mimics the free fall of the drop weight until it impacts a wave or the ground. After the impact, the prescribed acceleration of remains zero as the base of the seat is in rest after the impact.

With these simulated drop tests, multiple simulations were made where the linear spring and damper elements and the effect of bottoming were validated independently. The tests showed satisfying results. The most important observations of these tests were

- For a spring with an increasingly large stiffness compared to the other spring, its motion behaviour starts to resemble that of a rigid body.

- Springs with a large stiffness generate vibrations with a high frequency and lead to eigenvalues with large values.
- Large masses have large inertia and this is shown in their motion which is not influenced as a result of any present high frequency vibrations.

Further results of this model are not shown in this report as the model is trivial. Additional results of the dynamic analysis program will be shown in the last section of this appendix. The results shown later will be more interesting as it is validated with a more complex model which has non-linear motions.

F.2. MATLAB ODE Solvers

The dynamic analysis is performed by solving the equations of motion with an ODE solver of MATLAB. the MATLAB toolbox offers various ODE solvers for different problems types and with varying accuracy. In this section, two of the ODE solvers are discussed; the ODE45 and ODE15s solver.

The ODE45 solver is based on explicit Runge-Kutta of the fourth/fifth order, the Dormand-Prince method. The solver combines a fourth order and fifth order method and requires six function evaluations per step. This solver is a single-step solver as it only need the solution of the preceding time step to calculate the solution of the immediate time step. The ODE45 solver is usually the go-to solver for many problems, but may fail for very stiff problems.

The ODE15s solver is based on the backward differentiation formulas, also known as Gear's method. The solver uses formulas of the one to fifth order. This solver is a multi-step solver as it needs the solutions of several preceding time steps to calculate the solution of the immediate time step. This ODE solver is more suitable to solve stiff differential equations.

Both the ODE45 solver and ODE15s solvers use a variable time step routine which bases the time step for each step on both the absolute and relative errors. The routine reduces the step size for the solution until the value of the local error meets both tolerance limits. The default values of these tolerances are 10^{-3} for the relative error and 10^{-6} for the absolute error. These values can be altered by the user. For two random values X and Y , the the relative error (RelTol) is defined as

$$\text{RelTol} = \frac{\text{abs}(X - Y)}{\min(\text{abs}(X), \text{abs}(Y))} \quad (\text{F.18})$$

and the absolute error (AbsTol) is defined as

$$\text{AbsTol} = \text{abs}(X - Y) \quad (\text{F.19})$$

The input of the ODE solvers is vector \dot{Y} containing the expression for the acceleration, the time span and the initial conditions. The output of the ODE solvers is the the same time span with the default step size and the vector Y containing the displacement and velocity for each according time step. The acceleration per time step can later be calculated with the results of the ODE solver. If the minimal step size is defined in the time span input, the output will have the same time span and step size. The ODE solver does not solve the differential equations on these time steps, but calculates the solutions on these time steps before returning the output using polynomial interpolation.

For the dynamic analysis program it is important to choose the right ODE solver. The choice of solver influences the required computing power and simulation time, but also the accuracy of the results. As previously mentioned, the ODE45 solver can have trouble with solving stiff differential equations, while the ODE15s solver has less problems. This problem was also encountered with the simulations of the single degree of freedom mass-spring-damper model from the previous section. In these simulations, spring elements with very large stiffnesses were used. These stiff elements led to large eigenvalues which resulted in

vibrations with a very high frequency. These vibrations formed a problem for the ODE45 solver, because this method is a single-step solver. As the ODE45 is a single-step solver it needs the solution of the preceding time step to calculate the solution of the immediate time step. As there is a vibration with a very high frequency present in the signal, the ODE45 solver continuously reduces the step size to such small values that the simulation time increases drastically or the solver may even fail to solve the differential equations. The ODE15s solver provides a solution to this problem as it is a multi-step solver. As the ODE15s solver is a multi-step solver, the solver is able to keep a relative larger time step while the results are within the limits of the tolerances. The solver uses multiple preceding solutions and a polynomial to calculate the solution of the immediate time step. A downside of this method is that it does not accurately describe the high frequency vibrations.

During the simulations made in this research it is known that the very high frequencies in the signal are a result of very stiff elements and they are considered as not that interesting compared to the relative large motions of the seat or the masses. Thus, the high frequency vibrations are a form of noise on the signal. Therefore, neglecting the very high frequency vibrations by the ODE15s solver is considered to be acceptable.

For very stiff differential equations, the output signal of the ODE15s solver will still contain vibration noise. This noise makes it difficult to compare to large motions of any structure to the motions of a signal without any noise. Therefore, additional measures are taken to reduce the amount vibration noise. The following method is based on a method from NAVSEA which was reviewed in the literature study [6]. First, the fast Fourier transform is applied to the output signal of the ODE solver. This transformation shows what frequencies are present within the signal. This transformation will clearly show the difference between the frequency of the interesting large motions and the frequency of the vibration noise. Subsequently, a low-pass filter is applied to the signal. The cutoff frequency can be based on the fast Fourier transform. This low-pass filter will filter all frequencies above the cutoff frequency from the signal. The literature of NAVSEA suggests that a cutoff frequency of 10 Hz usually suffices for craft less than 100 feet long [6].

With the ODE15s solver and the application of the low-pass filter, the required computing power and simulation time are limited while the results remain accurate. The resulting filtered signal is much easier to analyse and easier to compare to other simulations. The low-pass filter function in MATLAB automatically compensates for the delay.

F.3. Equations of Motion for Seat A

In order to validate the dynamic analysis program, the equations of motion for a simple suspension design based on a parallelogram of pinned truss elements are analytically derived. The suspension design is shown in figure F.2. The suspension design consists of three linear bars, a non-linear spring and a non-linear damper. The non-linear spring and non-linear damper are mounted between points A and C. Linear bar elements are mounted between points AB, BC and CD. All elements are connected with pinned joints. Nodes A and D have a pinned connection mounted on a non-moving body. The linear bar elements have such a stiffness, that they are regarded as rigid bodies. Therefore, only the spring and damper element will deform under loading conditions. Only point B and point C have a mass, all other elements are regarded as having no mass. A load P is applied in the vertical direction of point C.

The equations of motion are derived with the Euler-Lagrange equation. The displacements, velocities and accelerations are expressed as a function of the motion of point A. The coordinates of all points are

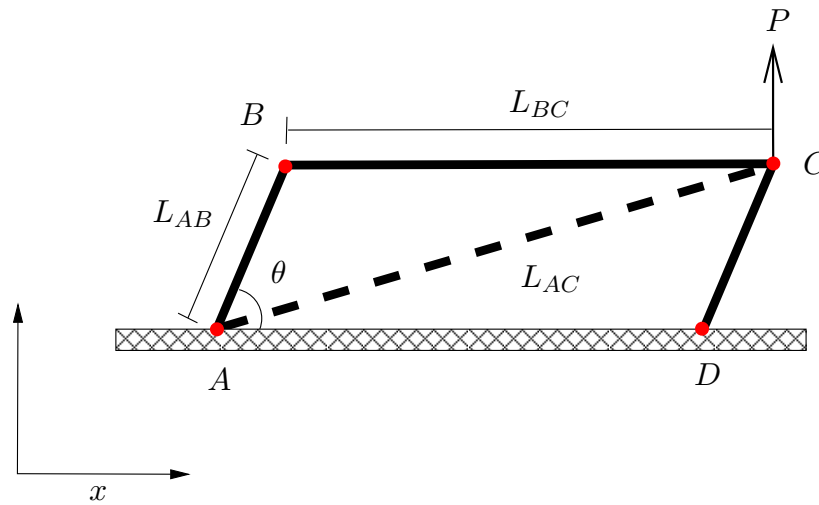


Figure F.2: Schematic representation of the simplified suspension of seat A

expressed as

$$\begin{aligned}
 x_B &= L_{AB} \cos(\theta) \\
 y_B &= L_{AB} \sin(\theta) \\
 x_C &= L_{BC} + L_{AB} \cos(\theta) \\
 y_C &= y_B \\
 x_D &= L_{BC} \\
 y_D &= y_A
 \end{aligned} \tag{F.20}$$

When deriving the coordinates with respect to time in order to calculate the velocities and accelerations. The velocities and accelerations of the coordinates for the upper part of the suspension design (seat) and the lower part of the suspension design (base) are equal. For point B , the velocity and acceleration are

$$\begin{aligned}
 \dot{x}_B &= -L_{AB} \dot{\theta} \sin(\theta) \\
 \dot{y}_B &= L_{AB} \dot{\theta} \cos(\theta) \\
 \ddot{x}_B &= -L_{AB} \ddot{\theta} \sin(\theta) - L_{AB} \dot{\theta}^2 \cos(\theta) \\
 \ddot{y}_B &= L_{AB} \ddot{\theta} \cos(\theta) - L_{AB} \dot{\theta}^2 \sin(\theta)
 \end{aligned} \tag{F.21}$$

The Euler-Lagrange equation (F.1) is used to derive the equations of motion for a damped system. The derivatives of the each term with respect to angle (θ) and angular velocity ($\dot{\theta}$) are required.

The kinetic energy is

$$T = \sum \frac{1}{2} m_j v_j^2 = \frac{1}{2} (m_B + m_C) (\dot{x}_B^2 + \dot{y}_B^2) = \frac{1}{2} (m_B + m_C) L_{AB}^2 \dot{\theta}^2 \tag{F.22}$$

The gravitational potential energy is

$$U_g = \sum m_j g h_j = (m_B + m_C) g y_B = (m_B + m_C) g L_{AB} \sin(\theta) \tag{F.23}$$

The spring potential energy is

$$U_v = \frac{1}{2} k \Delta L^2 \tag{F.24}$$

In which

$$\Delta L = L_{AC} - L_0 \quad (\text{F.25})$$

Where L_0 is the undeformed length of the spring. The length of the spring is calculated according to

$$L_{AC} = \sqrt{(x_C - x_A)^2 + (y_C - y_A)^2} = \sqrt{L_{AB}^2 + 2L_{AB}L_{BC} \cos(\theta) + L_{BC}^2} \quad (\text{F.26})$$

The Rayleigh damping is defined as

$$R = \frac{1}{2}c\dot{\Delta L}^2 \quad (\text{F.27})$$

In which

$$\dot{\Delta L} = -\frac{L_{AB}L_{BC}\dot{\theta} \sin(\theta)}{L_{AC}} \quad (\text{F.28})$$

The external work by load P is

$$W = \sum F_i s_i \delta W = P y_C = P L_{AB} \sin(\theta) \quad (\text{F.29})$$

The derivative of the external load is

$$\frac{\partial W}{\partial \theta} = P L_{AB} \cos(\theta) \quad (\text{F.30})$$

The result of the Euler-Lagrange equation can be rewritten to an expression for the angular acceleration ($\ddot{\theta}$).

$$\ddot{\theta} = -\frac{1}{(m_B + m_C)L_{AB}^2} \left((m_B + m_C)g L_{AB} \cos(\theta) - k \Delta L \frac{L_{AB}L_{BC} \sin(\theta)}{L_{AC}} + c \frac{L_{AB}^2 L_{BC}^2 \dot{\theta} \sin(\theta)^2}{L_{AC}^2} - P L_{AB} \cos(\theta) \right) \quad (\text{F.31})$$

The expression for the angular acceleration shows all the individual terms that determine the value of acceleration. Assume that the simplified suspension design operates in the angle range of $10^\circ \leq \theta \leq 80^\circ$.

The first term between the parentheses originates from the gravitational potential energy. The only variables in this term are the masses ($m_B + m_C$) as all other parameters are constants. As all variables and parameters in this term are positive assuming an angle of $10^\circ \leq \theta \leq 80^\circ$, then this term always decreases the acceleration.

The second term in between the parentheses originates from the spring potential energy. The variables in this term are the spring stiffness (k) and the undeformed length of the spring (L_0). The contribution of this term depends on the values of ΔL . If for any angle $\Delta L \geq 0$, then this term counteracts the weight of the masses and increases the acceleration. If for any angle $\Delta L \leq 0$, then the term will add to the weight of the masses and decrease the acceleration. The spring stiffness can be used to amplify or reduce the value of this term.

The third term in between the parentheses originates from the Rayleigh damping. The only variable in this term is the Rayleigh damping coefficient (c). This term dissipates energy proportional with the angular velocity. This term has no contribution to the static equilibrium of the suspension. Note that it does contribute to the angular acceleration in dynamic simulations. The term counteracts the angular acceleration depending on the sign of the angular velocity.

The last term in between the parentheses is from the work done by the external load. The only variable in this term is the external load itself. The direction of the external determines the sign and thus how this term will contribute to the angular acceleration. As positive external load will pull point C in the upward vertical direction and result in an increase of the angular acceleration. A negative external load will push

point C in the downward vertical direction and result in a decrease of the angular acceleration.

In this suspension design, the elongation of the spring must balance with the weight of the masses and the external load if it has a negative sign. With an ODE solver, the angle, angular velocity and angular acceleration are calculated from the equations of motion. Using these results, the motions, velocities and accelerations of all other points are determined.

F.4. Validation of the Dynamic Program

In this section, the dynamic analysis program will be validated with the equations of motion for the suspension design derived in the previous section. First, the non-linear damping element, non-linear spring element and bottoming were validated independently. These simulations showed satisfying results. In this section, only the simulation which includes all these elements and bottoming is shown as this is the most interesting and complex simulation. In figure F.3, the deformed suspension design from the dynamic analysis program is shown. The suspension as shown in the figure is in static equilibrium. For a more detailed figure and description of the suspension design, take a look at figure F.2 and the according section.

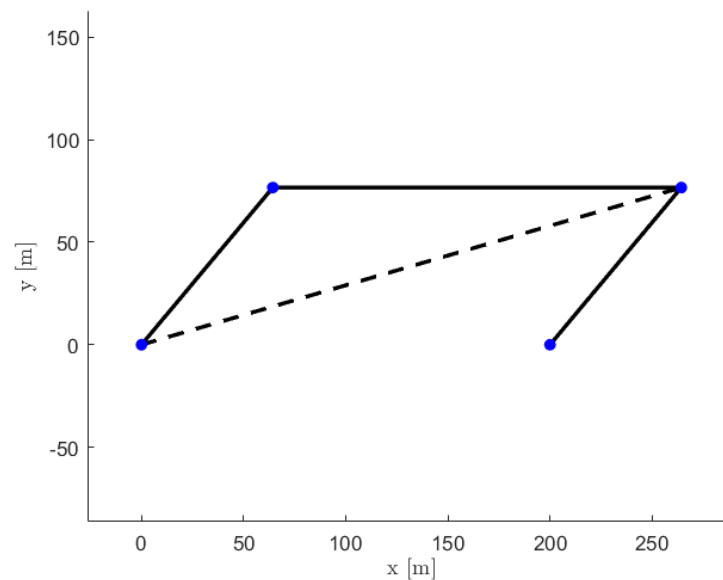


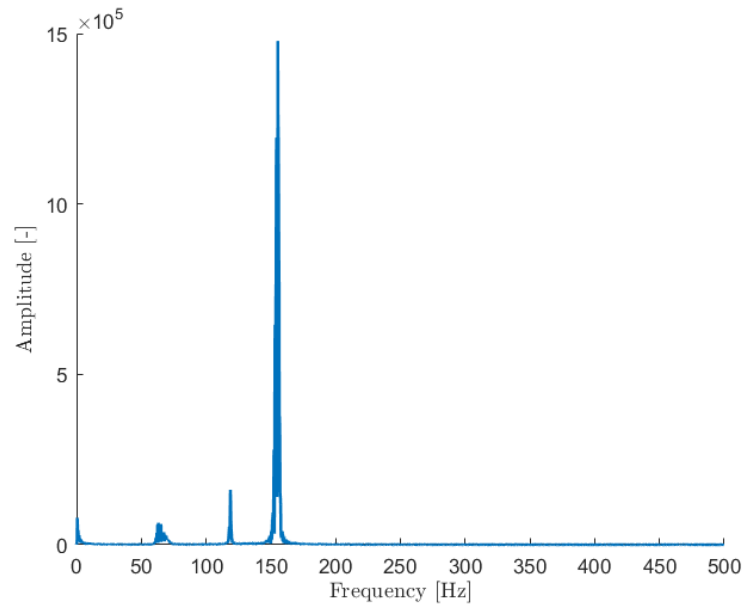
Figure F.3: Seat A suspension model deformation

The linear bar elements between points AB , BC and CD have a modulus of elasticity of $E = 1.0 \cdot 10^9$ [$\text{N} \cdot \text{m}^{-2}$] and cross-sectional area of $A = 1.0$ [m^2]. The length of the bar between points AB is $L_{AB} = 100.0$ [m] and the length of the bar between points BC is $L_{BC} = 200.0$ [m]. The non-linear spring element between points AC has a stiffness $K = 1500$ [$\text{N} \cdot \text{m}^{-1}$], a undeformed length of $L_0 = 275.0$ [m], a minimum length of $L_{min} = 1.0$ [m] and a maximum length of $L_{max} = 281.0$ [m]. If the spring bottoms, the stiffness of the elements is multiplied by a factor two. The non-linear damper element between points AC has a damping coefficient of $C = 100.0$ [$\text{N} \cdot \text{s} \cdot \text{m}^{-1}$]. The masses at both point B and C are $m_B = m_C = 18$ [kg]. None of the other elements has a mass. At point C , a vertical load is applied with the value of $P = -5000.0$ [N]. The static equilibrium with the external load is at an angle of $\theta = 44.71^\circ$. Without the external load, the equilibrium is at an angle of $\theta = 49.88^\circ$.

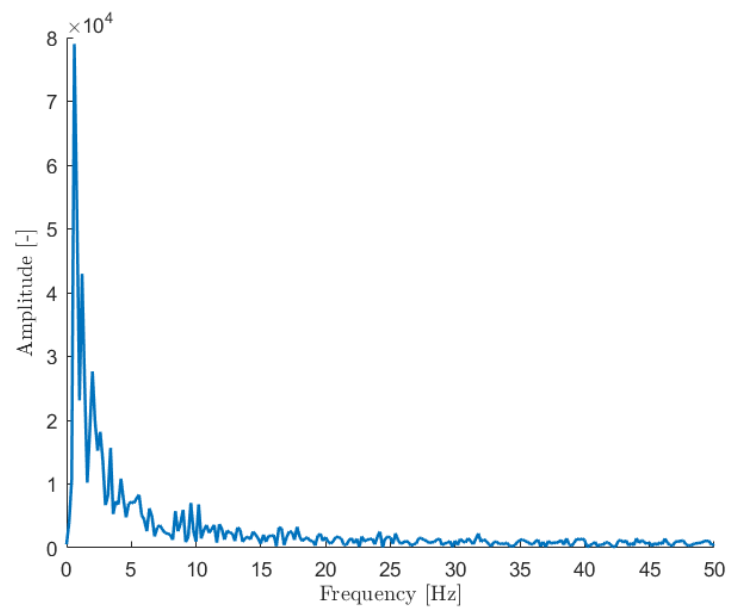
For the dynamic analysis, the simulation starts from the static equilibrium without an external load. At time $t = 0$ [s], the external load is applied and the suspension will deform over time due to the impact and converge to the static equilibrium with the external load.

For the simulation, the ODE15s solver of MATLAB is used with the default error tolerances. The time step size is set to $\Delta t = 0.001$ [s] and the total simulation lasts five seconds. The results are then filtered with a low-pass filter. The displacement and velocity are filtered using a cutoff-frequency of 10 [Hz] and the acceleration with a cutoff-frequency of 5 [Hz]. The acceleration is filtered with a smaller frequency to remove most of the vibrations and ease the comparison in the figures.

In figure F.4a, the FFT of the vertical acceleration of point C is shown. The FFT shows large amplitude peaks at the frequencies around 60 [Hz], 120 [Hz] and 150 [Hz]. The high frequencies are a result of the stiff elements used in the structure and will cause high frequency vibrations. These vibrations are not so interesting for the motion of the structure as these vibrations have little influence on the deformation of the structure. In figure F.4b, the same FFT is shown but it is zoomed in on the range of frequencies between 0 and 50 [Hz]. In this figure, the amplitude peaks at the lower frequencies are better visible. These lower frequencies are related to the larger motions of the structure. These motions are more interesting when analysing the SMS and validating the program. Based on the figures, the a cutoff frequency of 10 [Hz] for the low-pass filters is used.



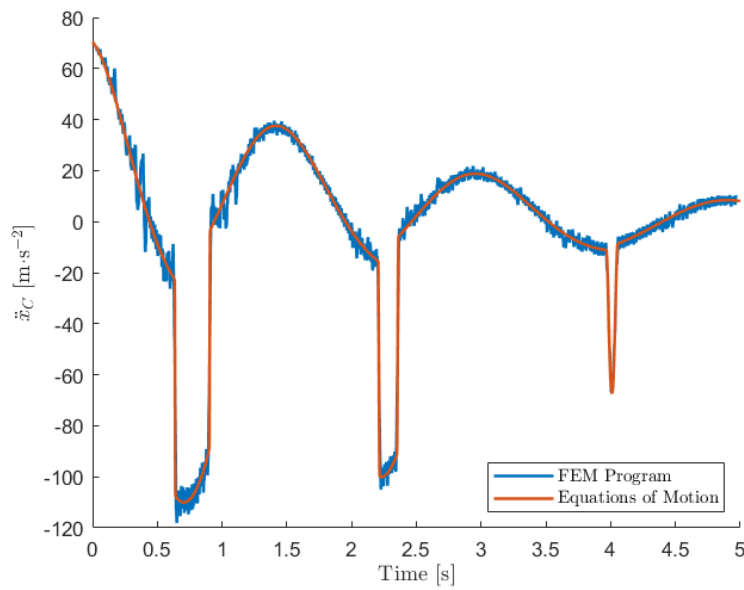
(a) Original FFT



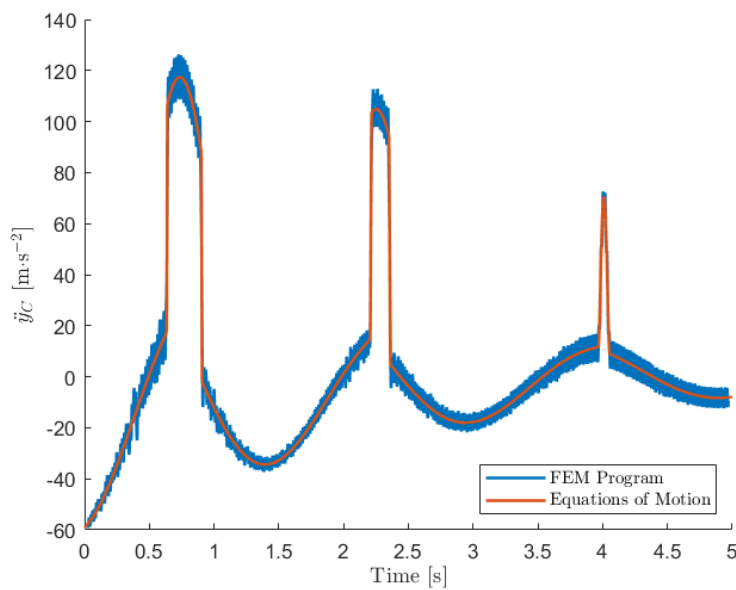
(b) Zoomed in FFT

Figure F.4: Seat A suspension model FFT of the vertical acceleration

As previously mentioned, the simulation starts from a static equilibrium and at the start of the simulation an external load is applied. This external load causes the suspension to deform, such that it compresses the parallelogram but extends the spring and damper. In figures F.5a and F.5b, the horizontal and vertical acceleration of point C is plotted in time. In these figures, both the results of the FEM program and the equations of motion are plotted. In the results of the FEM program there are still some vibrations visible after filtering. Although vibrations are still present, the results are very satisfying as the general motions of the structure coincide. In the figures, large jumps in the accelerations to higher values are visible. This is the phenomenon known as bottoming. As the spring is extended to its maximum length, the stiffness doubles and the acceleration values increase drastically. Bottoming should therefore be prevented at all times on SMS.



(a) Horizontal acceleration



(b) Vertical acceleration

Figure F.5: Seat A suspension model acceleration of the seat in time

In figure F.6, the length of the spring is plotted in time. Note that the maximum length of the spring is defined at 281 [m]. The figure clearly shows that at $t = 0$ the length of the spring starts to increase as was expected. In the first peak it crosses the threshold of the maximum length. This could be prevented by increasing the stiffness beyond this threshold with a larger factor instead of doubling the stiffness. In practice, once the SMS bottoms the spring is not able to extend or compress any further. In this plot, the vibrations have such small deformation amplitudes that they are almost not visible. This again illustrates that the high frequency accelerations have negligible influence on the deformations or displacements.

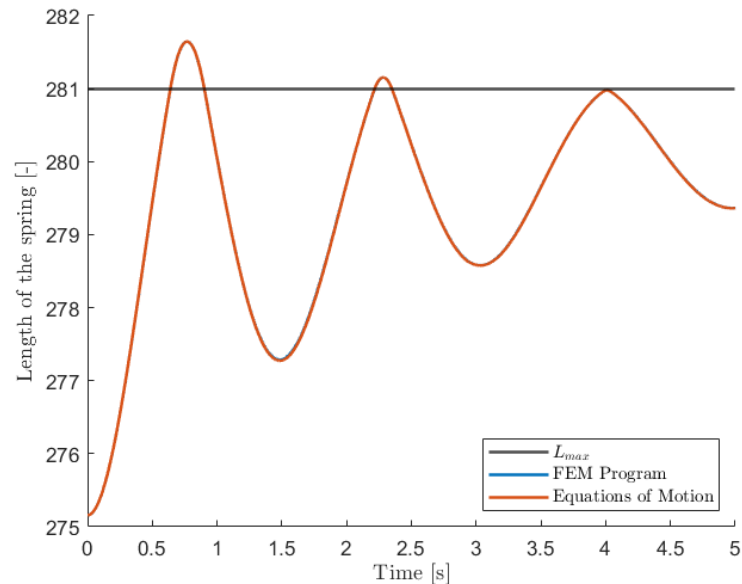
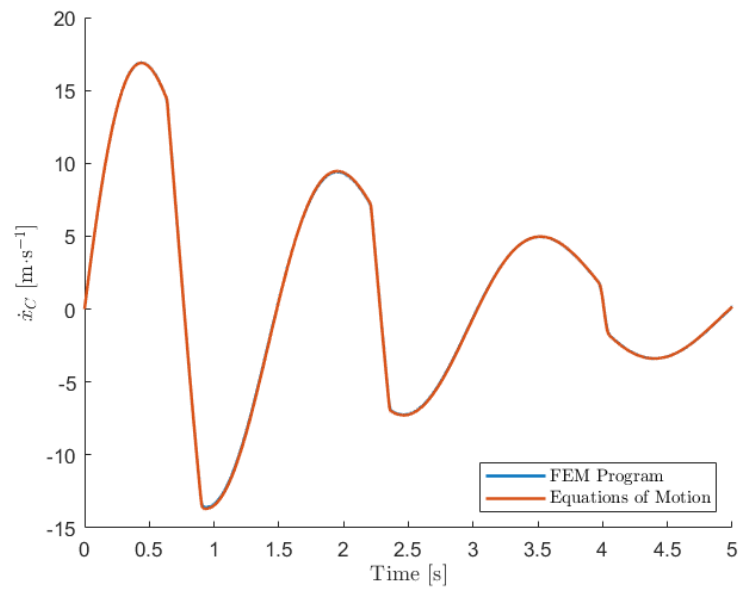
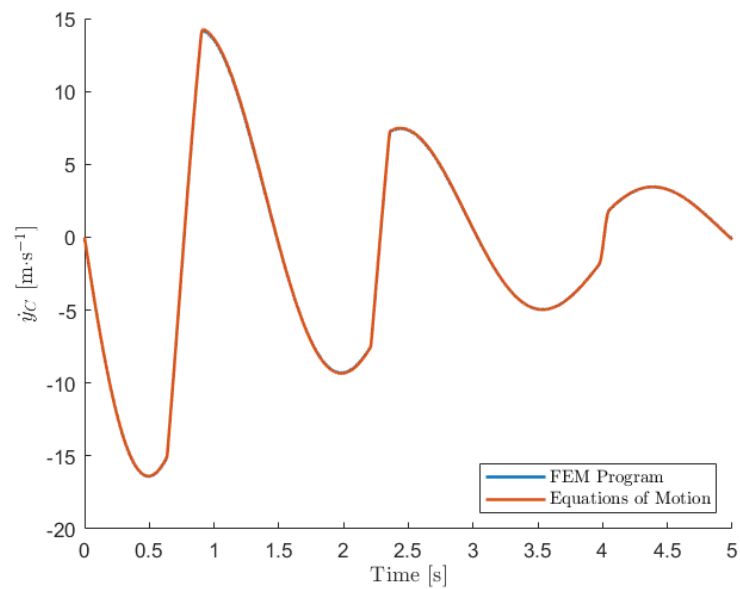


Figure F.6: Seat A suspension model length of the spring in time

In the figures F.7a and F.7b, the horizontal and vertical position in time shown. In the figures F.8a and F.8b, the horizontal and vertical position in time shown. The results of both the velocity and position of point C match with the results of the equations of motion. In the results of the FEM program, the vibrations are almost not visible on this axis system as the amplitude is very small compared to the relative large amplitude motions. In the time trace of the velocity of point C , the effect of bottoming is clearly visible as the gradient of the curve abruptly changes. The change of the gradient is not noticeable in the position time trace, which is expected according to the basic kinematics theory. Based on the presented results, the dynamic program is considered to be validated and ready for the application on SMS designs.

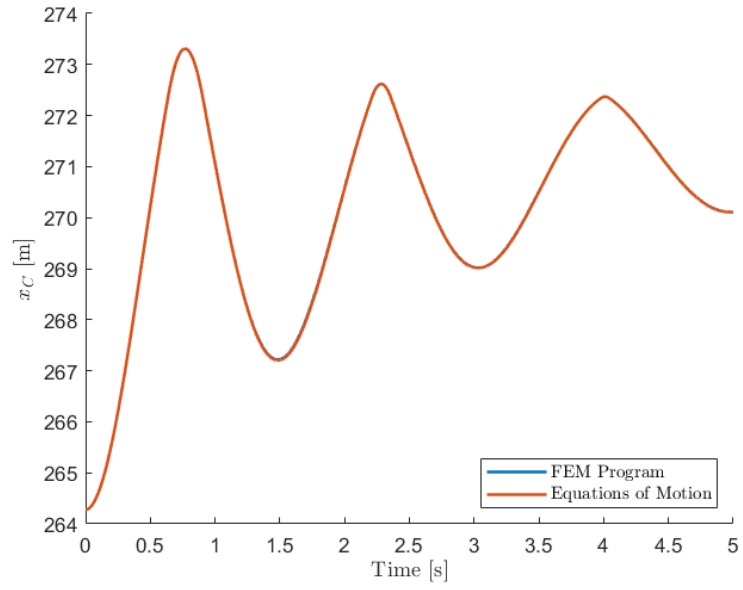


(a) Horizontal velocity

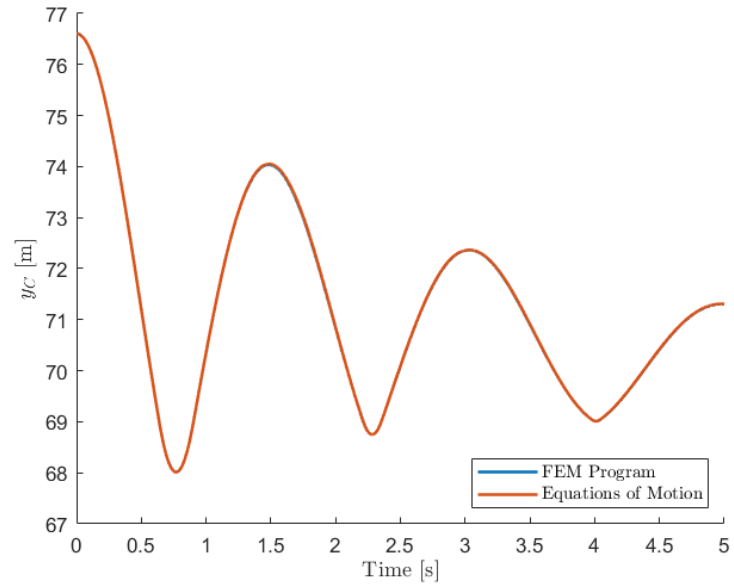


(b) Vertical velocity

Figure F.7: Seat A suspension model velocity of the seat in time



(a) Horizontal position



(b) Vertical position

Figure F.8: Seat A suspension model position of the seat in time